JOHANNES GUTENBERG UNIVERSITÄT MAINZ

Inorganic nanoparticles as models for prebiotic enzymes

Dissertation

zur Erlangung des Grades

„Doktor der Naturwissenschaften“

im Promotionsfach Chemie

am Fachbereich Chemie, Pharmazie, Geographie und Geowissenschaften

der Johannes Gutenberg-Universität Mainz

Melanie Viel

geboren in Bonn

Mainz, 2021

Dekan: [redacted]

Erster Berichterstatter: [redacted]

Zweiter Berichterstatter: [redacted]

Tag der mündlichen Prüfung:

Erklärung:

Die vorliegende Arbeit wurde in der Zeit März 2018 bis März 2021 unter der Betreuung von Herrn [redacted] am Departement Chemie der Johannes Gutenberg – Universität Mainz durchgeführt.

Hiermit erkläre ich, dass die vorliegende Arbeit selbstständig verfasst und keine anderen als die angegebenen Quellen und Hilfsmittel verwendet wurden. Alle Ausführungen, die wörtlich oder sinngemäß aus anderen Quellen übernommen wurden, sind als solche gekennzeichnet.

Mainz, den 18.03.2021

_____

Melanie Viel

Danksagung:

Als erstes möchte ich mich bei [redacted] für die Möglichkeit, die Dissertation in seiner Arbeitsgruppe anzufertigen bedanken. Ebenfalls für die Betreuung, Unterstützung und zahlreichen Diskussionen. Besonders bedanken möchte ich mich für die Freiheit, mit der er mich hat meine Forschungsarbeit gestalten lassen und gleichzeitig für das Vertrauen, das er mir damit entgegengebracht hat.

Ich bedanke mich bei der gesamten Arbeitsgruppe, bestehend aus ehemaligen und aktuellen Mitarbeitern. Allen Dank voraus gilt [redacted], [redacted] und [redacted], die mir sowohl fachlich jederzeit mit Rat und Tat zur Seite standen, Mut machten und unterstützten, aber auch privat für alle Angelegenheiten ein offenes Ohr hatten. [redacted] möchte ich explizit für die Anfertigungen von HR-TEM und EDX-Messungen danken, sowie für das Korrekturlesen dieser Arbeit. [redacted] danke ich besonders für die konstruktiven Diskussionen bezüglich der Kinetik-Messungen und dem Korrekturlesen. [redacted] möchte ich für die zahlreichen Gespräche rund um meine Dissertation danken. Sie waren ideenreich, ermutigend und haben an vielen Stellen zum Gelingen der Arbeit beigetragen.

Ich bedanke mich bei der ehemaligen Katalyse-Gruppe bestehend aus [redacted] und [redacted] und der aktuellen BioNano-Gruppe bestehend aus [redacted] und [redacted] für die Diskussionen rund um unsere Forschungsarbeit.

Danken möchte ich auch allen Kartenspielern, die jederzeit für geistige Auflockerung in den Mittagspausen gesorgt haben, als uns das noch möglich war.

Ich bedanke mich bei [redacted] für viele offene und ehrliche Gespräche.

Vielen Dank an die gesamte [redacted]. Es war eine aufregende Zeit mit euch, die mich geprägt hat und einen Teil zu meiner persönlichen Entwicklung beigetragen hat.

Ein besonderer Dank gilt [redacted], dem Herzstück des Arbeitskreises. Danke für die Übernahme aller bürokratischen und organisatorischen Aufgaben. Aber vor allem danke ich für ihr offenes Ohr!

[redacted] möchte ich für Rat und Tat rund um die NMR-Analytik und die Durchführung der Messungen während der Corona-Zeit bedanken.

Mein Dank gilt auch dem [redacted], das uns das Arbeiten erst möglich macht.

Ich danke [redacted] und [redacted] für die Messung der Röntgendiffraktogramme.

Mein Dank gilt auch den Studenten, die ich während meiner Doktorarbeit betreuen durfte, und die alle ein Teil dieser Erfahrung waren. Danke, dass ihr zu meiner Forschungsarbeit beigetragen habt.

Ich danke ganz besonders [redacted] und [redacted]. Ihr seid meine Felsen in der Brandung. Danke für eure Nachsicht, Geduld und grenzenlose Unterstützung. Ihr gebt mir Rückhalt in schwierigen Zeiten und weicht nie von meiner Seite. Danke, dass ihr da seid.

Zusammenfassung:

Die vorliegende Dissertation beschäftigt sich mit Nanopartikeln als Enzymmimetika im Kontext der präbiotischen Evolution. Enzyme sind essentiell für alle Lebensformen und deshalb bei Fehlfunktionen auch häufig involviert in komplexe Krankheitsbilder. Da sie so bedeutend sind für das Leben wird neben der Isolierung und der Aufreinigung schon länger an ihrer Nachahmung geforscht. Neben beispielsweise metallorganischen Komplexen, Polymeren und Cyclodextrinen sind anorganische Nanopartikel immer mehr in den Fokus gerückt.

Anorganische Nanopartikel weisen im Vergleich zu natürlichen Enzymen Vorteile wie die Stabilität gegenüber Temperatur- und pH-Wert-Änderungen auf und sind zudem vergleichsweise günstig herstellbar. Im Hinblick auf die präbiotische Entwicklung der ersten Lebensformen könnten anorganischen Oberflächen eine zentrale Rolle gespielt haben. Wähdören die ersten Lebensformen gebildet haben, deren strukturellen Eigenschaften noch sehr einfach gewesen sein müssen, könnten anorganische Oberflächen als Katalysatoren fungiert haben.

Die vorliegende Arbeit beschäftigt sich mit Nanopartikeln als Enzymmimetika im Hinblick auf die Darstellung einer Reaktionskaskade. Hierzu ist die Dissertation in drei Projekte unterteilt.

Das erste Projekt beschäftigt sich explizit mit der Nachahmung des Enzyms Peroxidase und dem Aktivitätsnachweise mittels verschiedener Untersuchungen. Es wurden Nanopartikel mit drei verschiedenen Zusammensetzungen untersucht: Hämatit-Nanopartikel, Magnetit-Nanopartikel und synthetisch neu entwickelte Pseudobrookit-Nanopartikel. Alle drei Nanopartikel wurden drei verschiedenen Untersuchungen – dem ABTS-, dem TMB- und dem AR-Assay – unterzogen und ihre katalytischen Eigenschaften bezüglich der ermittelten kinetischen Parameter, der Michaelis-Menten Konstante und der maximalen Reaktionsgeschwindigkeit, bewertet. Herausgearbeitet werden konnte, dass die Wahl der Untersuchungsmethode maßgeblich über den Nachweis der enzymanalogen Aktivität, aber auch über die kinetischen Parameter entscheidet.

Das zweite Projekt setzt sich intensiv mit der Synthese von heteromultimeren Nanopartikeln zur Nachahmung einer Reaktionskaskade mittels einer Nanostruktur auseinander. Die Reaktionskaskade beinhaltet die photokatalytische

Produktion von Wasserstoffperoxid mithilfe eines Nanopartikels, das durch Diffusion zu einem Peroxidase-nachahmenden Nanopartikel gelangt, wo es mittels dessen katalytischen Aktivität zu Wasser umgesetzt wird. Die Darstellung heterotrimerer Nanostrukturen wie TiO_2@Au@Fe_3O_4 und ZnO@Au@Fe_3O_4 wird diskutiert. Bei der Überprüfung der katalytischen Eigenschaften konnten Au@Fe_3O_4 Janus Partikeln bessere Eigenschaften nachgewiesen werden als den Fe_3O_4 Nanopartikeln des ersten Projektes. Ebenso zeigten Au@ZnO Janus Partikel hinsichtlich der photokatalytischen Produktion von Wasserstoffperoxid bessere Ergebnisse als reine ZnO Nanopartikel. Neben der Darstellung heteromultimerer Nanostrukturen mittels heterogener Nukleation und epitaxialem Wachstum wurde auch ein Ansatz über Oberflächenfunktionalisierung erprobt. Der bifunktionelle Ligand 4-(11-Mercaptoundecyl)benz-1,2-diol verfügt über eine Thiolgruppe, die sich zur Funktionalisierung von Gold-Nanopartikeln eignet, als auch über eine Katecholgruppe, die bekannt ist für ihre Fähigkeit Fe_3O_4 und TiO_2 Nanopartikel zu funktionalisieren. Die Struktur des Liganden und aller Zwischenstufen wurden mittels NMR-Experimenten vollständig aufgeklärt bevor er zur Synthese von heterotrimeren Nanostrukturen genutzt wurde.

Das dritte Projekt beschäftigt sich mit der Synthese sogenannter Nanorasseln. Hier bilden Hämatit-Nanopartikel den Kern der Nanorasseln, die umhüllt sind von einer mesoporösen Silikahülle, in der die Hämatit-Nanopartikel frei schwimmen können. Die Silikahülle stellt hierbei ein Analogon zur Zellmembran von Archaeen dar, während der Hämatit-Nanopartikel ein Enzymmimetikum darstellt. Auf der Außenseite der Silikahülle sind Titan(IV)-oxid Nanopartikel ankondensiert die zur photokatalytischen Erzeugung von Wasserstoffperoxid genutzt werden können. Produziertes Wasserstoffperoxid gelangt mittels Diffusion durch die mesoporöse Silikahülle in das Innere der Nanorassel, wo es an der Oberfläche des Hämatit-Nanopartikels umgesetzt werden kann. Mithilfe einer Farbreaktion kann dieser Umsatz nachgewiesen werden. Durch diese Nanorassel kann eine Reaktionskaskade anhand eines zellähnlichen anorganischen Modells dargestellt werden, das der Struktur einer sehr frühen Lebensform ähnelt.

Abstract:

This dissertation deals with nanoparticles as enzyme mimics in the context of prebiotic evolution. Enzymes are essential for all forms of life and are therefore often involved in complex diseases if they malfunction. Because they are so important for life, research has long been conducted into their imitation, in addition to their isolation and purification. In addition to organometallic complexes, polymers and cyclodextrins, inorganic nanoparticles have increasingly become the focus of attention.

Compared to natural enzymes, inorganic nanoparticles have advantages such as stability against changes in temperature and pH value and can also be produced comparatively cheaply. With regard to the prebiotic development of the first life forms, inorganic surfaces may have played a central role. While the first life forms were formed, whose structural properties must still have been very simple, inorganic surfaces could have acted as catalysts.

The present thesis deals with nanoparticles as enzyme mimics with regard to the representation of a reaction cascade. For this purpose, the dissertation is divided into three projects.

The first project explicitly deals with the mimicry of the enzyme peroxidase and the proof of activity by means of various investigations. Nanoparticles with three different compositions were investigated: Haematite nanoparticles, magnetite nanoparticles and synthetically newly developed pseudobrookite nanoparticles. All three nanoparticles were subjected to three different assays - the ABTS, the TMB and the AR assay - and their catalytic properties were evaluated with respect to the determined kinetic parameters, the Michaelis-Menten constant and the maximum reaction rate. It could be worked out that the choice of the examination method decides decisively on the proof of the enzyme-analogue activity, but also on the kinetic parameters.

The second project focuses intensively on the synthesis of heteromultimeric nanoparticles to mimic a reaction cascade using a nanostructure. The reaction cascade involves the photocatalytic production of hydrogen peroxide using a nanoparticle, the hydrogen peroxide diffuses to a peroxidase-mimicking nanoparticle where it is converted to water by its catalytic activity. The preparation

of heterotrimeric nanostructures such as TiO_2@Au@Fe_3O_4 and ZnO@Au@Fe_3O_4 is discussed. When the catalytic properties were tested, Au@Fe_3O_4 Janus particles were shown to have better properties than the Fe_3O_4 nanoparticles of the first project. Similarly, Au@ZnO Janus particles showed better results than pure ZnO nanoparticles with respect to the photocatalytic production of hydrogen peroxide. Besides the preparation of heteromultimeric nanostructures *via* heterogeneous nucleation and epitaxial growth, an approach *via* surface functionalisation was also tested. The bifunctional ligand 4-(11-mercaptoundecyl)benzene-1,2-diol has a thiol group suitable for functionalising Au nanoparticles as well as a catechol group known for its ability to functionalise Fe_3O_4 and TiO_2 nanoparticles. The structure of the ligand and all intermediates were fully elucidated by NMR experiments before it was used to synthesise heterotrimeric nanostructures.

The third project deals with the synthesis of so-called nanorattles. Here, hematite nanoparticles form the core of the nanorattles, which are encased in a mesoporous silica shell in which the hematite nanoparticles can float freely. The silica shell is an analogue of the cell membrane of archaea, while the hematite nanoparticle is an enzyme mimic. TiO_2 nanoparticles are condensed on the outside of the silica shell and can be used for the photocatalytic production of hydrogen peroxide. Produced hydrogen peroxide diffuses through the mesoporous silica shell into the interior of the nanorattle, where it can be converted on the surface of the hematite nanoparticle. This conversion can be detected with the help of a colour reaction. Through this nanorattle, a reaction cascade can be represented using a cell-like inorganic model that resembles the structure of a very early life form.

List of abrreviations

(HR)-TEM	(high resolution) – transmission electron microscopy
1-ODE	1-octadecene
ABTS	2,2'-azino-di-(3-ethylbenzthiazoline-6-sulphonic acid)
Al_2O_3	aluminium oxide
$AlCl_3$	aluminium(III) chloride
AR	Amplex™ Red, Amplifu™ Red, 10-Acetyl-3,7-Dihydroxyphenoxazin
ATP	adenosine triphosphate
Au	gold
BA	benzyl alcohol
BET	Brunauer-Emmett-Teller
CaO	calcium oxide
CeO_2	cerium dioxide
CLSM	confocal laser scanning microscopy
COSY	correlation spectroscopy
Cu	copper
Cyt C	cytochrome C
DMSO	dimethyl sulphoxide
DNA	deoxyribonucleic acid
Fe	iron
Fe_2O_3	iron(III) oxide
Fe_2TiO_5	pseudobrookite
Fe_3O_4	iron(II,III) oxide
FOX	ferrous oxidation-Xylenol orange
H_2	hydrogen
H_2O	water
H_2O_2	hydrogen peroxide
HMBC	heteronuclear multiple bond correlation
HRP	horseradish peroxidase

HSQC	heteronuclear single bond coherence
IR	infrared
JP	Janus particle
K_2O	potassium oxide
K_M	Michaelis-Menten constant
KSAc	potassium thioacetate
LUCA	last universal common ancestor
$MgAl_2O_4$	magnesium aluminate, spinel
MnO	manganese(II) oxide
MQW	milli Q water
$NaBH_4$	sodium borohydride
NH_3	ammonia
NMR	nuclear magnetic resonance
NPs	nanoparticles
Pb	lead
RNA	ribonucleic acid
ROS	reactive oxygen species
rRNA	ribosomal ribonucleic acid
S	sulphur
$SOCl_2$	sulphonyl chloride
SOD	superoxide dismutase
THF	tetrahydrofuran
TiO_2	titanium dioxide
TMB	3,3',5,5'-tetramethylbenzidine
V_{max}	maximum velocity
XO	xylenol orange
XRD	x-ray diffraction
ZnO	zinc(II) oxide, zincite
ZnS	zinc(II) sulphide

List of content

Introduction 1

One day all children ask their parents "why is the sky blue?" or “where do the colours of the rainbow come from?" and the answer is: because of light scattering and refraction. The blue sky could be explained by the Rayleigh light scattering. While sunlight appears white, in reality it is composed of light of different wavelengths, which for the human eye appears isolated in different colours. This light corresponds to electromagnetic radiation of certain wavelengths and represents the complete light spectrum visible to the human eye, including UV radiation (which is not visible for the human eye). When light penetrates the ozone layer and enters the atmosphere, it is scattered by the smallest gas molecules (e.g. N_2 and O_2) contained in the atmosphere. These gas molecules are very small compared to the wavelength of the light emitted by the sun, so that this scattering process is called Rayleigh scattering. While the sun is at its zenith and the path of the light through the atmosphere is short, a large part of the short-wave electromagnetic radiation is refracted, the sky appears blue. At sunrise and sunset, however, the path of light through the atmosphere is longer, the blue component of the light on this path is reduced by the scattering and the sky appears red.[1] The formation of a rainbow can be explained by the refraction of light. Already Isaac Newton discovered that white light can be refracted at a prism and split in such a way that monochromatic light rays can be observed. The same thing happens when a rainbow is created. In this case the light is not refracted directly at a prism, but at raindrops, because water is also able to refract light.[2]

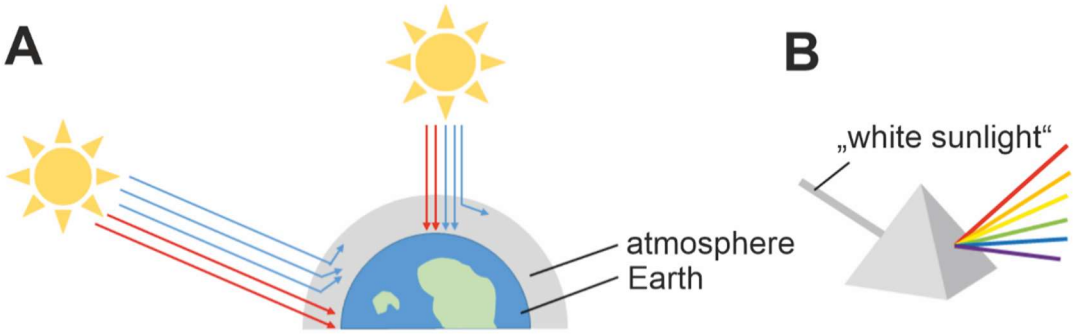

Figure 1: Light scattering and refraction. A: Schematic representation of the scattering of sunlight on its way through the atmosphere to Earth as a function of distance, resulting in the observation of different sky colours. (The schematic representation is not to scale.) B: Refraction of light by a prism resulting in the separation into the spectral colours.

Children have many questions. And we are also able to answer many of their questions, but one question remains unanswered to this day: "How was life created?" Certainly, the question from the mouth of a child is perfectly justified, but from the mouth of a scientist it could be strongly criticised. Again and again there are disputes between clergymen and scientists but this should not be the subject of the present work, nor should it attack anyone in his or her opinion and religious views. It should also be said in advance that the present work cannot answer this question either, but it should nevertheless give an overview of previous research and provide new food for thought: While scientists have devoted a great deal of attention to the question of how nucleobases and peptides are formed starting from amino acids and how amino acids were formed before, the influence of metal ions on the formation of new molecules has often been neglected. In this work, the influence of inorganic matter on the origin of life and the first biochemical metabolic processes will be examined. For this purpose, inorganic metal-containing nanoparticles have been used as a model for minerals and rocks, in order to investigate their influence on the formation of living organisms in more detail. Previous work has already assumed that minerals and rocks, as heterogeneous catalysts, could have played a decisive role in the origin of life. This hypothesis is now to be taken up here in order to develop models with which basic reactions and reaction cascades that may have contributed to the origin of life a long time ago, can be imitated.[3]

The origin of life 2

Already Anaximander, a Greek philosopher who lived from 610 to 547 BC, dealt with the question what the origin of the world was, as well as about the origin of life.[4] Therefore, it is a question that has occupied mankind for at least 2500 years, but this question has yet to be answered. Searching through literature, the next major theories, which still form the basis of current research today, are found in the year 1924. In 1924 Alexander Ivanovich Oparin published his first book which dealt with the question of the origin of life. However, this book was only available in Russian and therefore did not receive much international attention.[5] In 1936 Oparin's book *Origin of life* was published (in English in 1938) and well received and discussed among scientists, as it was the first book that tried to explain the origin of life from a chemical point of view.[6] Following the research in this field, Oparin's publications have laid a foundation on which many scientists have continued to build their research. While Anaximander pursued the theory of panspermia, which states that life forms simply existed in space and were brought to Earth by meteorites only transferring the question to another planet, *Oparin* assumed that the first life forms emerged through evolutionary processes and self-organisation.[4,7] Oparin's hypothesis comprises four assumptions about the prebiotic atmosphere:[4]

1. The atmosphere was reductive and consisted mainly of methane, nitrogen, hydrogen and water.

2. There were different forms of energy in the atmosphere, such as electrical discharges, solar radiation and volcanic heat, which contributed to the formation of organic matter.

3. These organic compounds accumulated in oceans and lakes (primitive hydrosphere); forming the so-called primordial soup.

4. The first forms of life formed spontaneously from the primordial soup.

Although Oparin's hypothesis was pioneering, it left many questions unanswered (e.g. origin of chirality). Nevertheless, it was possible to postulate a basic sequence

of evolutionary steps, accepted by scientists from various disciplines (Figure 2), but the details of the individual steps remain to be investigated.

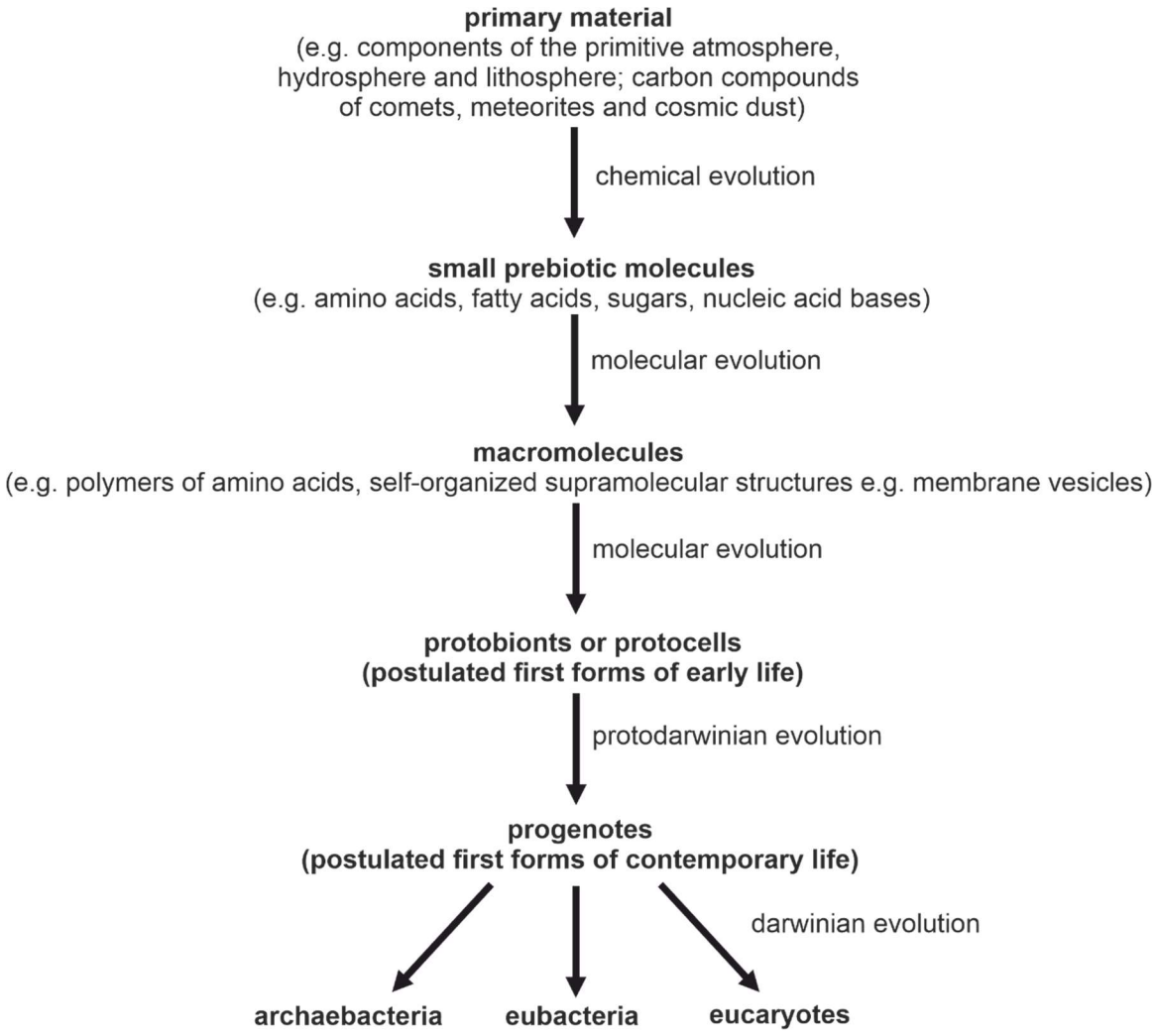

Figure 2: Postulated evolutionary steps; starting from simple molecules *via* prebiotic structures to the cells of today. Based on [4].

Figure 2 shows a schematic representation of the postulated evolutionary steps starting with the source materials (e.g. methane, hydrogen, nitrogen and water from the simple atmosphere). It is assumed that the first prebiotic molecules (e.g. amino acids) have formed out of these molecules. From these macromolecules were formed, for example by condensation reactions. Macromolecules then built up protobionts or protocells, which are considered to be the first postulated living forms of the early life. Through evolutionary development, these first potential life forms developed into progenotes, which are regarded as the first life forms of contemporary life. Finally the three domains of life known to us today developed:

the archaebacteria, the eubacteria and the eucaryotes, whose further development can be represented in the phylogenetic tree of life.

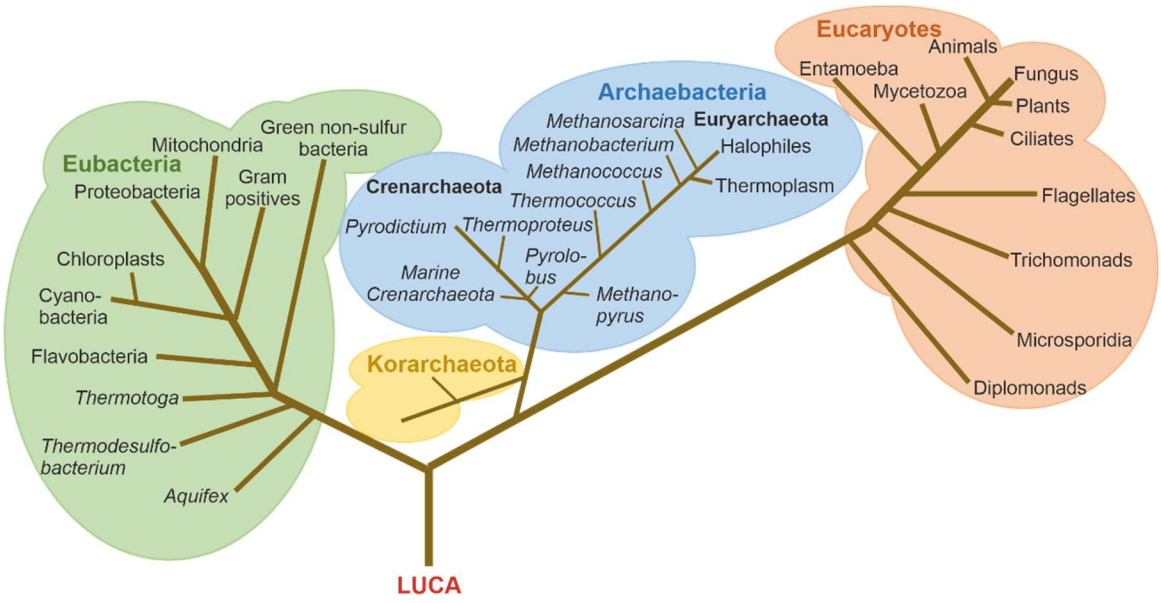

Figure 3: Phylogenetic tree of life of the three domains of contemporary life. Based on [8,9].

The phylogenetic tree gives an overview of the relationship between the three domains based on the analogies of the sequences of ribosomal ribonucleic acids (rRNA).[8] According to Woese, who began isolating rRNA from some bacteria in the mid-1970s, analysing their base sequence and providing the basis for the phylogenetic tree, the basic message of the phylogenetic tree is that the nature of existence is represented by the root and that primary organismic lines emerged from the root.[8,10] The root of the phylogenetic family tree leads to LUCA - the last universal common ancestor.[9] But LUCA does not seem to be a single defined life form from which all other living beings originate, but rather a pool of many living beings, which exchanged their genetic information.[11,12]

As it can be seen, the subject of the origin of life is very complex and employs scientists from various disciplines. Important and ground-breaking results have already been collected, forming the basis for new experiments. And yet the question of the origin of life is still not absolutely clearly defined.

The following chapters will focus especially on the chemical experiments and aspects of this field of research.

2.1. Miller-Urey experiment

The Miller-Urey Experiment, conducted in 1953, is a highly regarded experiment to test the hypothesis of how life could have originated on Earth. It is still considered ground-breaking today, is taught in schools and universities reproduced many times.

Figure 4 shows the schematic structure of the apparatus used in this experiment.

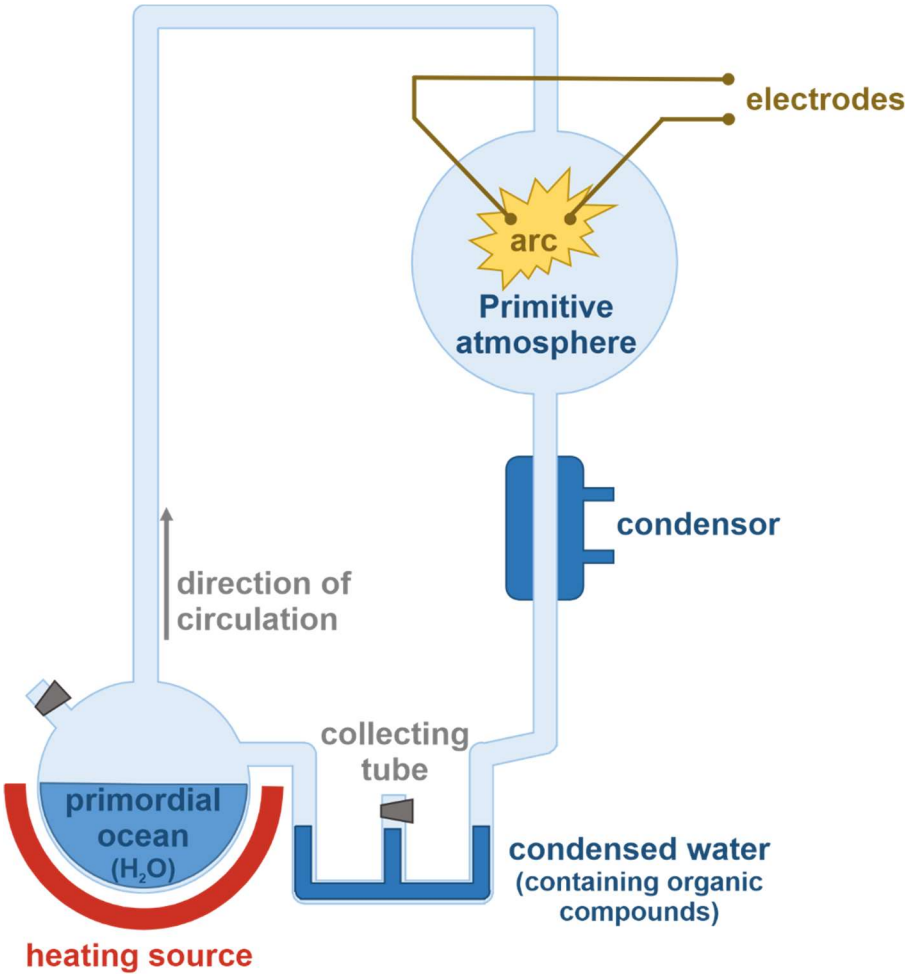

Figure 4: Schematic drawing of the experimental setting of the Miller-Urey experiment. Based on [13].

Miller and Urey assumed that the primordial atmosphere was reductive and consisted mainly of methane, but also of some extent of hydrogen (H_2), water (H_2O) and ammonia (NH_3). They tried to simulate the conditions of the primordial atmosphere in a closed experimental setting by introducing the gases they suspected into the system and boiling water in a flask connected to the setting. The gas phase, which is supposed to represent the primordial atmosphere, is supplied with energy by means of an electric arc (comparable to solar radiation) over a

period of one week. By external cooling, parts of the gas phase can be condensed. In the condensed water, organic molecules such as aldehydes and cyanides, but also amino acids (mainly alanine and glycine; both in D- and L- conformation), and in the gas phase mainly carbon monoxide and nitrogen could be detected.[14]

Ferus et al. reported that in a modified reproduction of the Miller-Urey experiment it was possible to synthesise formamide from carbon monoxide and ammonia, which can decompose into cyanide, hydrogen and amine radicals under the assumed conditions of the original atmosphere. From these radicals 2,3-diaminofumaronitrile (1) could be produced, which can dimerise to 4-amino-5-cyanoimidazole (2). Also the pyrimidine bases cytosine (5) and uracil (6) can be formed. From 4-amino-5-cyanoimidazole (2) the purine bases adenine (3) and guanine (4) can also be obtained.[15]

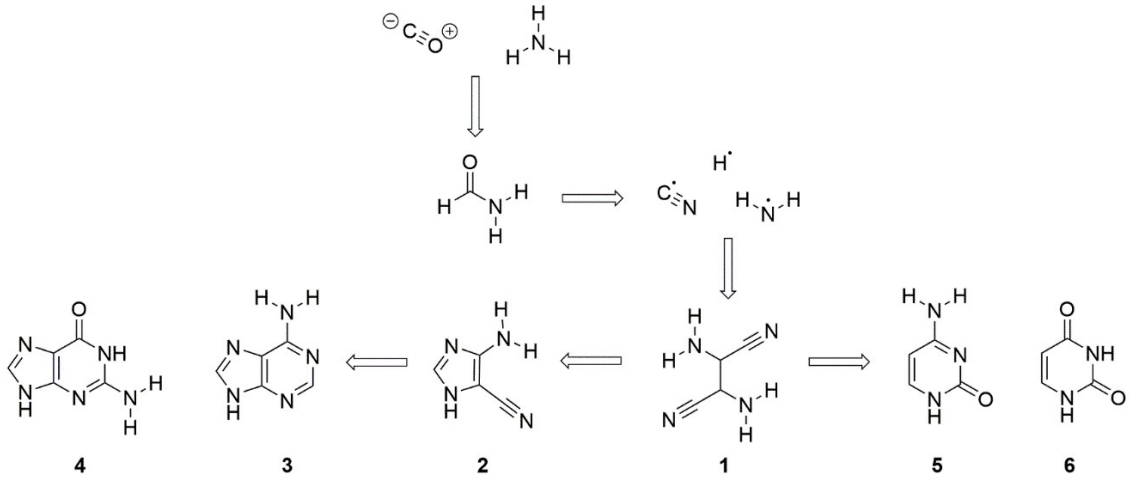

Figure 5: Reaction scheme of the modified Miller-Urey experiment with the nucleobases adenine (3), guanine (4), cytosine (5) and uracil (6) as products. Based on [15].

In summary, the Miller-Urey experiment was one of the most ground-breaking experiments for understanding how life could have been created on Earth. Especially for questions concerning organic chemistry and biochemistry, first ideas could be suggested. At the same time, the experiment provided a good basis for targeted organic syntheses, e.g. the Strecker synthesis.[13]

2.2. Iron sulphur compounds

Despite the great insights gained from the Miller-Urey experiment, Günter Wächtershäuser devoted himself to two equal important questions in 1988. In his opinion, the influence of photochemical energy as well as inorganic redox potential should also be considered, because anaerobic photoautotrophy is only known from eubacteria, anaerobic chemolithoautotrophy only from archaebacteria. Therefore he made the hypothesis that the origin of life is energetically coupled with exergonic pyrite formation.[16]

Table 1: Overview of the free Gibbs energies ΔG_f^0 that contribute to pyrite formation.[17]

chemical compound	ΔG_f^0
$FeS_{2(s)}$ – Pyrite	-160.1 kJ mol^{-1}
$FeS_{(s)}$	-93.8 kJ mol^{-1}
$H_2S_{(aq)}$	-27.9 kJ mol^{-1}
$FeS_{(s)} + H_2S_{(aq)} \rightarrow FeS_{2(s)} + H_{2(g)}$	-38.4 kJ mol^{-1}

Based on this theory, Wächtershäuser sketches the known citrate cycle under reductive conditions as a possible citrate cycle of archaebacteria. He shows how the enzyme-catalysed partial steps could hypothetically have been catalysed by pyrite, hydrogen sulphide and carbon dioxide.[17] His hypothesis is supported from today's perspective by the recognition of the biological importance of iron-sulphur clusters. For example, a [3Fe-4S]-system is known from aconitase which, in interaction with a labile [4Fe-4S]-form, is significantly involved in the equilibrium between citrate and isocitrate *via Z*-aconitate.[18] But there are also arguments against Wächtershäuser´s theory. On one hand, it is assumed that the environmental conditions outlined by Wächtershäuser are too sulphurous. On the other hand, partial steps of the citrate cycle can also occur in the absence of iron carbide and sulphide, but in the presence of nickel sulphate. A further significant counterargument is that the reductive citrate cycle is a very specialised metabolic pathway, which is mainly known from carbon dioxide fixation. However, there are no known cells that receive the energy for the synthesis of adenosine triphosphate (ATP) from this metabolic pathway alone.[19]

Continuing, Wächtershäuser hypothesised on a first and very early selection mechanism. Assuming the energetic coupling between pyrite formation and the origin of life and Wächtershäuser's hypothesis that the first life forms might have originated on pyrite surfaces, it can be assumed that organisms formed before cellular structures developed. Knowing that the majority of biomolecules are negatively charged, he assumed that the mineral surfaces on which the first organisms are said to have developed must be positively charged in order for the biomolecules to be attached. Taking electrostatic interactions into account, he concluded that the positive charges must be associated with polyvalent cations (Mg^{2+}, Ca^{2+}, Fe^{2+}, Mn^{2+}, Zn^{2+}). At the same time, he also discusses that when a biomolecule interacts with a surface, the potential detachment must be taken into account. Apart from the strength of the electrostatic interaction, there is always the possibility of separation through protonation or hydrolysis of a functional end group or through decarboxylation. The probability of a bound biomolecule being detached is most unlikely at a neutral pH. He assumed that the first metabolism must have taken place under these conditions, since the condition of neutral pH is conserved in today's living organisms, though there are exceptions. Nevertheless, even under these conditions there is still the possibility of a biomolecule being detached from a surface. Whether a biomolecule is bound to a surface, is determined by the equilibrium reaction between synthesis rate of the biomolecule and the detachment from the surface. At this point, Wächtershäuser assumed a first selection mechanism. This is because the more negative charges a biomolecule presents, the greater the electrostatic interaction with the surface, and hence, the lower the probability that the biomolecule will be detached from the surface. This provides an initial explanation for the existence of ribonucleic acids (RNA), deoxyribonucleic acids (DNA) and coenzymes.[20]

Following the experiments of Miller and Urey, Wächtershäuser was thus able to provide a theory on the origin of life, which on the one hand provided a first approach to selection, but on the other hand also included inorganic matter for the first time. His hypothesis was also important because it considered the existence of anaerobic photoautotrophy and anaerobic chemolithotrophy.[16,21]

2.3. Hydrothermal vents

Despite the findings of Wächtershäuser, his theories and results were never embedded in a geological context. Research on hydrothermal vents in the mid-ocean ridge led to the thesis that geological sites could be the place where life originated.[21]

Hydrothermal vents are underwater springs, often found on adjoining continental plates and are distinguished between vents originating from a magmatic source and those originating from an alkaline source. Due to their phenotypes, they are often referred to as black smoker, lost city systems and white smoker.[22,23]

In the following, a short overview of all three forms will be given and the similarities and differences will be worked out.

2.3.1. Black smoker

Black smokers are an impressive natural phenomenon that can be observed especially on the mid-ocean ridge. These are hydrothermal springs under stone formations, from which black smoke is emitted intermittently. This effect occurs when seawater enters the hot basalt and comes into close contact with the magma zone directly below the sea floor. It is heated there, accumulates with volcanic gases und builds an explosive mixture. On the way back to the seawater it incorporates minerals. When it gets in contact with cold seawater, minerals (especially metal sulphides) precipitate, so that black clouds can be observed inside the ocean. The water ejected from the vents has a temperature up to 405 °C, an acidic pH value (2-3), a strong reducing effect and it contains metals, hydrogen and hydrogen sulphide in addition to metal sulphides. It also contains methane and magmatic carbon dioxide.[3,22]

2.3.2. Lost city systems

In 2000 the so-called lost city systems were discovered. These are also hydrothermal vents whose chimneys are mainly made of carbonates. They can reach a height of up to 60 m and are located on ultramafic seafloor.[3] Ultramafic

seafloor is a soil that consists of more than 90 percent mafic minerals. These include magmatic rocks with dark minerals such as olivine, pyroxene, phlogopite, chlorite, amphibole and biotite, but also light minerals such as zircon, apatite, melilith, titanite, magnetite and ilmenite.[24,25]

Table 2: Overview of minerals contained in ultramafic soils with molecular formula and classification in the case of silicates.[24–27]

name	classification	molecular formula
olivine	nesosilicate	$(Mg,Mn,Fe)_2[SiO_4]$
pyroxene	chain silicate	ABX_2O_6 with mainly: A = Mg^{2+},Fe^{2+},Mn^{2+} B = Mg^{2+},Fe^{2+},Mn^{2+},Ca^{2+} X = Si^{4+}
phlogopite	phyllosilicate	$KMg_3[(F,OH)_2\|AlSi_3O_{10}]$
chlorite	phyllosilicate	$(Fe,Mg,Al,Zn)_6(Si,Al)_4O_{10}(OH)_8$
amphibole	chain silicate	$A_{0-1}B_2C_5X_8O_{22}(OH)_2$ with mainly: A = vacancy, Na^+, K^+, B = Ca^{2+},Na^+,Mg^{2+},Fe^{2+},Mn^{2+},Li^+ C = Mg^{2+},Fe^{2+},Mn^{2+},Li^+ X = Si^{4+}
biotite	phyllosilicate	$K(Mg,Fe,Mn)_3[(OH,F)_2\|Al,Fe,Ti]Si_3O_{10}$
zircon	nesosilicate	$Zr[SiO_4]$
apatite		$Ca_5[(F,Cl,OH)\|(PO_4)_3]$
melilith	sorosilicate	$(Ca,Na)_2(Mg,Al)[Si_2O_7]$
titanite	nesosilicate	$CaTi[O\|SiO_4]$
magnetite		Fe_3O_4
ilmenite		$FeTiO_3$

In contrast to black smokers, lost city systems are not located near submarine volcanoes. Nevertheless, even in Lost City systems water is heated up to 200 °C by convection (heat is dissipated from the rock). The surrounding rock contains iron and magnesium and is dominated by olivine. The released water has a high

pH value (9-11) and a temperature up to 91 °C. It is rich in hydrogen, methane and lower hydrocarbons. In contrast to the black smokers, however, it contains almost no carbon dioxide. When the water is released, the high pH on contact with seawater causes carbonates to precipitate, which leads to the formation of carbonate-containing chimneys. Serpentinisation can also be observed in lost city systems.[3] Serpentinisation describes the process by which rocks rich in olivine and pyroxene react with water to produce magnetite, hydroxides and serpentine, releasing hydrogen - shown in the following reaction equations.[28]

$$Fe_2SiO_4 + 5\ Mg_2SiO_4 + 9\ H_2O \rightarrow 3\ Mg_3Si_2O_5(OH)_4 + Mg(OH)_2 + Fe(OH)_2 \quad \textbf{(1)}$$

$$Mg_2SiO_4 + MgSiO_3 + 2\ H_2O \rightarrow Mg_3Si_2O_5(OH)_4 \quad \textbf{(2)}$$

$$3\ Fe(OH)_2 \rightarrow Fe_3O_4 + 2\ H_2O + H_2 \quad \textbf{(3)}$$

The hydrogen release during serpentinisation is discussed as an energy source that may have contributed to the creation of life.[29] This is the reason why Lost City systems are discussed as places for the emergence of first life forms.

2.3.3. White smoker

White smokers are also hydrothermal vents which expel saturated hydrothermal liquid at a temperature of 250 °C to 300 °C. This also ejects baryte and silica, which causes the white colour. In contact with cold ocean water, sulphate salts also precipitate. The chimneys are very rich in iron (Fe), sulphur (S), lead (Pb) and zinc sulphide (ZnS).[30] These inorganic compounds are discussed as catalysts for the origin of life. ZnS for example are known for their photocatalytic properties. They are able to product different organic compounds.[31] Fe and S are discussed as source of energy (see chapter 2.2). In the following table the most important features of the three hydrothermal systems are summarised.

Table 3: Comparison of black smoker, lost city systems and white smoker.

	black smoker	lost city system	white smoker
origin	volcanic	ultramafic seafloor	volcanic
released water temperature	270 - 380 °C	40 - 91 °C	250 - 300 °C
pH	2 to 3	9 to 11	basic
released water colour	black	colourless	white
metals contained	iron, manganese	iron, magnesium	barium ($BaSO_4$), silica (SiO_2)
solved gases	H_2, H_2S, magmatic CO_2	H_2, CH_4, lower C_nH_{2n+2}	H_2, H_2S, magmatic CO_2
chimney substance	Fe, S_x, PbS, ZnS	carbonates	Fe, S_x, PbS, ZnS
serpentinisation	x	✓	x

One of the most important differences that needs to be emphasised is that black and white smokers are based on volcanic activity, while the lost city systems are located away from volcanic areas and are based on ultramafic seafloors. Also, the temperature of ejected water is significantly lower in lost city systems than in volcanic based smokers. In terms of pH, lost city systems are similar to white smokers, while in terms of metals they are closer to black smokers. It is also important to note that serpentinisation is only characteristic for the lost city systems, which produces molecular hydrogen, which is discussed as the energy source for the origin of life.

2.4. Tectonic fault systems

Fault systems are areas where tectonic activity has caused fractures or cracks in the rock, causing rock formations to shift relative to each other and the formation of so called fault areas.[32] Mayer and Schreiber developed a model for the origin of life taking into account a hypothetical crustal profile of the Earth. They assume a 20 km thick crust, whose temperature increases by 40 °C per kilometre depth. Within this crust they distinguished three different zones, which differ mainly in their temperature and pressure conditions. This is accompanied by different phase states of water and carbon dioxide, considered as main components in their

model.[33] Since the model is based on the existence of different phases of water and carbon dioxide and different phase transitions, the phase diagrams of both components are briefly introduced here.

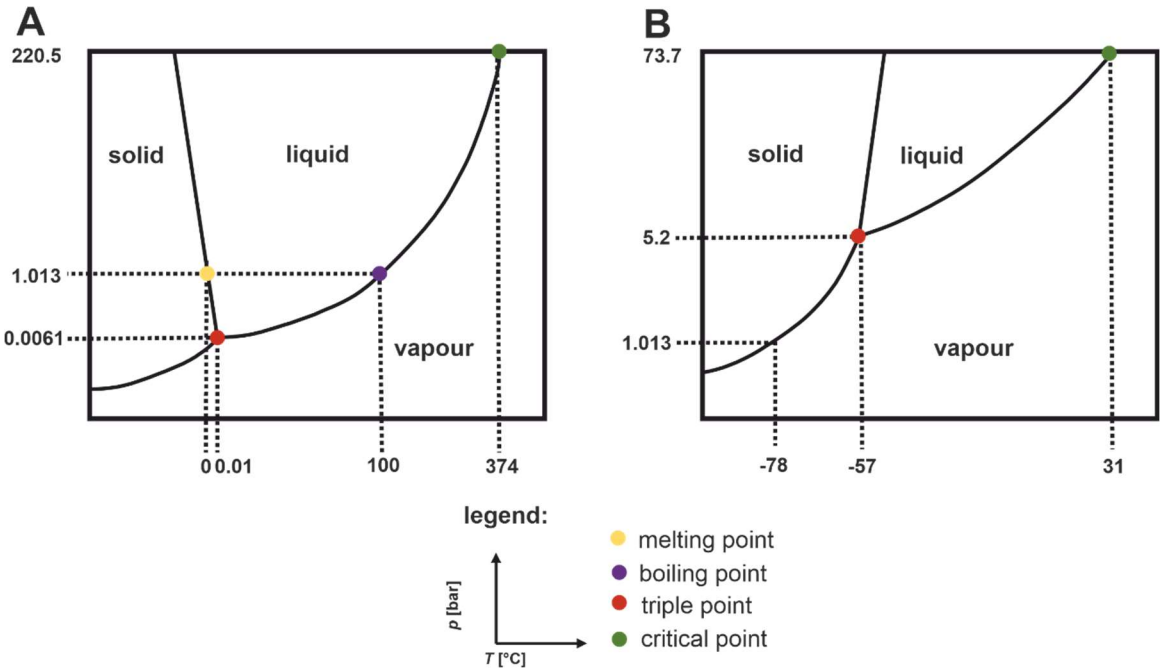

Figure 6: Phase diagrams. A: of water. B: of carbon dioxide. Based on [27]. (not scaled)

Figure 6 shows the phase diagrams of water and carbon dioxide. Particularly marked are the prominent points, such as the triple point and the critical point. If the pressure and temperature of the critical point are exceeded, a substance goes into a supercritical state. In this state it is no longer possible to differentiate between gas and liquid. This supercritical state is assumed for both water and carbon dioxide in Mayer and Schreiber's model in the deeper layers of the Earth's crust in.

The following Table 4 lists the different zones with their parameters and the respective states of the two components. For a distance of less than 1 km, the coexistence of subcritical water and subcritical carbon dioxide is applied.[33]

Table 4: Overview of the assumed different zones of the hypothetical crustal profile and their properties.

		1	2	3
distance	< 1 km	1 – 5 km	5 – 10 km	10 – 20 km
temperature	< 40 °C	40 – 200 °C	200 – 400 °C	400 – 800 °C
pressure	< 74 bar		up to 1 kbar	1 – 2 kbar
H_2O	subcritical	subcritical	sub-/supercritical	supercritical
CO_2	subcritical	supercritical	supercritical	supercritical

On the basis of this model, it is assumed that prebiotic molecules were formed at different levels of this model Earth crust depending on the availability of the necessary educts. In addition, it is assumed that catalysts in form of siliceous and metallic surfaces have had an influence on the formation of these molecules. The transfer of these molecules to upper layers or to the Earth's surface is said to have been promoted by tectonic activity, and hereby promotes the rise of supercritical carbon dioxide, which forms bubbles.[33,34] It is assumed that this carbon dioxide extracted organic, non-polar molecules from subcritical water and thus transported them to upper levels.[33]

Schreiber and Mayer also assume that among the formed organic molecules there are also amphiphilic molecules which can form a monolayer on the outside of the carbon dioxide bubbles. While the carbon dioxide bubbles shrink when the bubbles rise, because the water is enriched with carbon dioxide when aqueous media pass through, the monolayers remain intact. It is assumed that this is how the first prebiotic cell precursors could have formed. After the inclusion of organic molecules, subsequent reactions could have taken place within these compartments, controlled by pressure and temperature conditions that act on the system when migrating through the zones. When the bubbles reach the surface of the carbon dioxide-enriched water, they collapse and release their contents. The organic molecules contained in the structures are thus available for reactions at the upper areas of defect systems.[33] Continuing, they also present a model that cyclically represents the formation of vesicles under consideration of the changing environmental conditions.[35]

Peroxidase mimics | 3

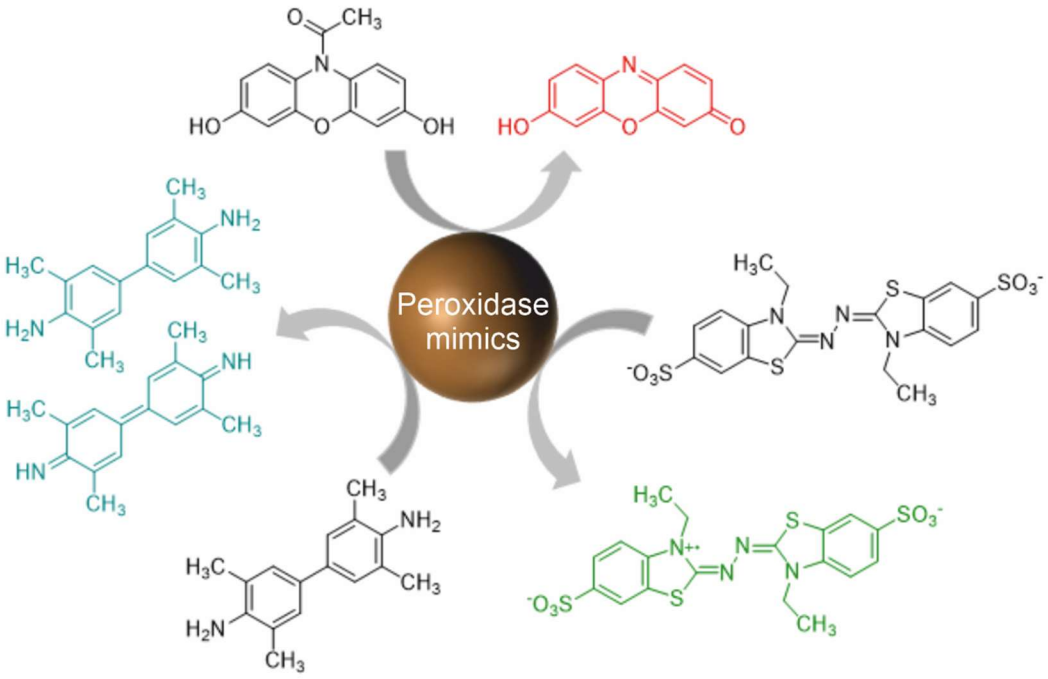

The aim of this chapter is to study the peroxidase activity of different nanoparticles. Hematite, magnetite and pseudobrookite nanoparticles are examined and compared with respect to their catalytic activity. In addition, different assays will be used and evaluated based on the results.

3.1. Theoretical background

This chapter deals with nanoparticles as mimics for the enzyme peroxidase. The nanoparticles used in this work will be examined and compared for their activity with respect to peroxidase and various assays. For a better understanding, nanoparticles as enzyme mimics will be discussed in advance. Furthermore, peroxidase will be explained in detail and the different assays for activity determination will be discussed. Finally, the underlying compounds of the nanoparticles will be discussed.

3.1.1. Nanoparticles as enzyme mimics

Enzymes are biological catalysts of enormous importance for every living organism. This is underlined by the fact that a quarter of the human genome encodes enzymes.[36] This is also the reason why researchers have been working for many years on the analysis of enzymes with regard to their structure and functionality, but also their imitation using metal complexes, polymers, cyclodextrins, porphyrins, supramolecules and biomolecules.[37–42] A striking example with evolutionary relevance is carboanhydrase. Carboanhydrase is an enzyme that catalyses reversibly the formation of hydrogen carbonate from carbon dioxide. This is particularly important for aerobic organisms. The enzyme has a divalent zinc ion in its active centre, which is essential for its catalytic activity.[36] Three isoforms of carbonic anhydrase are known, the α-form being found mainly in human beings, the β-form in higher plants and some bacterial species and the γ-form mainly presented in archaebacteria. It is assumed that all three isoforms have developed in convergent evolution, because no sequence matches could be found during their investigation. However, the zinc ion in the active centre is a conserved structural unit. While the zinc ion in the α-form is coordinated by three histidine residues, it is stabilised in the β-form by one histidine and two cysteine residues. In the γ-form, there are three zinc-containing centres which are structurally similar to the α-form, although the zinc ions are located in the area between the three subunits. In addition, the γ-form has a structural motif that could not be detected in the other two forms - a left-handed β-helix.[36,43] This example

illustrates the importance of carboanhydrase for almost all life forms, in addition to the relevance of the bivalent zinc ion as Lewis acid for catalytic activity. Since there are no sequence matches between the three isoforms, it can be assumed that evolutionary processes have produced three times a carbonic anhydrase containing a zinc ion in the active centre, which emphasised the importance of inorganic matter for the existence of life.

Since the significant involvement of metal ions in the active centre of many enzymes is well known, many researchers have made it their business to imitate this catalytic activity with various model compounds. For example, the well-known enzymes peroxidase and catalase contain iron ions, haloperoxidase contains vanadium and superoxide dismutase could contain copper and zinc, iron, manganese or nickel ions in their active centres.[44–47] The question is how to mimic these enzymes. Gao et al. reported in 2007 that the peroxidase function can be mimicked with magnetite nanoparticles.[48] Since then, research on nanoparticles as enzyme mimics, so called nanozymes, has been of great interest. Besides the fact that nanoparticles can imitate enzymes, nanoparticles have some significant advantages over enzymes. For example, the iron and molybdenum containing enzyme nitrogenase catalyses the formation of ammonia from molecular nitrogen under physiological conditions by consuming ATP, which would be of great interest as an alternative to the Haber-Bosch process if it could be mimicked with nanoparticles.[49] In the Haber-Bosch process, ammonia is synthesised on an industrial scale from molecular hydrogen and molecular nitrogen. This process already uses iron(II,III) oxide (Fe_3O_4) as a catalyst, from which α-Fe is formed by adding promoters (e.g. aluminium(III) oxide (Al_2O_3), calcium oxide (CaO), potassium oxide (K_2O)) at 400 °C, and which is then involved in the catalysis of the reaction.[27] A comparison shows that while one reaction takes place under physiological conditions, the other reaction takes place at temperatures of 400 °C to 500 °C and at a pressure of 250 bar to 350 bar. Isolating the nitrogenase in large quantities would not only be very labour-intensive, but also costly. Alternatively, the enzyme could also be produced biotechnologically, although enzymes are not particularly stable biomolecules. Even small changes in the pH value, but also temperature increases lead to the denaturation of the enzyme. In oxidative environments, disulphide bridge bonds can also be irreversibly cleaved, so that the

secondary to quaternary structure of the enzyme is destroyed and the activity of the enzyme is lost.[36,50] Nanoparticles on the other hand, can be produced in large quantities at comparatively low cost and are then stable with respect to various parameters. Thus, nanoparticles can be used in some cases both in acidic and basic media, but also at high and low temperatures. In Table 5, the advantages and disadvantages of enzymes and nanoparticles are compared again.[51]

Table 5: Advantages and disadvantages of enzymes and nanozymes in comparison.[51]

	enzymes	**nanozymes**
advantages	high metabolic rate high specificity diversity	high efficiency stable high diversity of compounds low priced
disadvantages	expensive low stability	physiological compatibility low specificity

Since Gao's publication, many more nanoparticles with intrinsic enzyme activities have been found and studied in more detail. A few prominent examples are Fe_3O_4 as peroxidase mimic, manganese(II) oxide (MnO) as superoxide dismutase (SOD) mimic, iron(III) oxide (Fe_2O_3) as catalase mimic, cerium(IV) dioxide (CeO_{2-x}) as haloperoxidase mimic and copper-iron (CuFe) nanoparticles as tyrosinase mimic and are listed in Table 6 below.

Table 6: Overview of examples of nanomaterials with enzyme-like activity (R = organic residue, X^- = Cl^-, Br^-, I^-)[18,48,52–55].

nanomaterial	**enzyme-like activity**	**catalysed reaction**	
Fe_3O_4	peroxidase	$H_2O_2 + RH_2 \rightarrow 2\ H_2O + R$	**(4)**
MnO	superoxide dismutase	$2\ O_2^{\cdot-} + 2\ H^+ \rightarrow H_2O_2 + O_2$	**(5)**
Fe_2O_3	catalase	$2\ H_2O_2 \rightarrow O_2 + 2\ H_2O$	**(6)**
CeO_{2-x}	haloperoxidase	$X^- + H_2O_2 + RH + H^+ \rightarrow RX + 2\ H_2O$	**(7)**
CuFe	tyrosinase	$C_9H_{11}O_3N \rightarrow C_9H_{11}O_4N \rightarrow C_9H_9O_4N$	**(8)**

Clearly, the prominent examples of enzyme mimics are in all cases catalysed redox reactions. The catalysis of hydrolysis or acid-base reactions is still a great challenge.

Ultimately, however, nanozymes are particularly interesting in application. Applications are conceivable, for example, in the environment for the detection of organic environmental pollution, in microbiology as antimicrobial and antifouling treatment, but also in biomedicine as an *in vitro* application for the biosensoring of biomarkers, but also as an *in vivo* application for imaging and therapy.[56–58]

3.1.2. Peroxidase

Peroxidase is an enzyme belonging to the class of oxidoreductases, and its task is to reduce peroxides by oxidation of a reducing agent (e.g. iodide or glutathione).[59] This is particularly important for living organisms, as hydrogen peroxide is toxic, being able to induce oxidative damage (for example in DNA, ribonucleic acid (RNA) or to amino acids, proteins and enzymes) and thus leads to long-term consequences, such as the development of cancer and diseases caused by enzyme defects. However, it must be said that hydrogen peroxide is also important because it acts as a second messenger.[60] This underlines why this molecule must be subject to strict control. It can be produced by reversing the catalase reaction, but it can also be destroyed by reaction with peroxidase (or catalase).

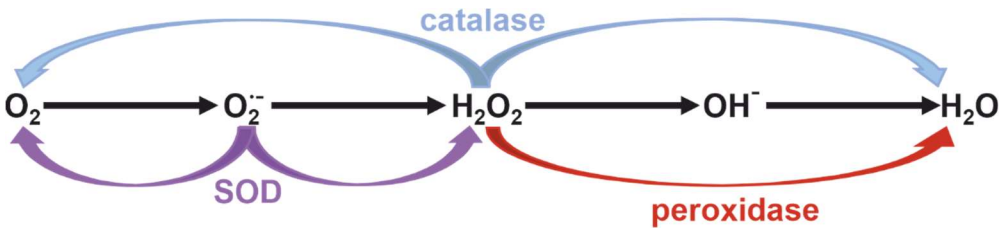

Figure 7: Overview of the catalysed reactions of catalase, SOD and peroxidase. Based on [58].

Figure 7 gives an overview of the enzyme-catalysed reactions of oxygen to water *via* various intermediates, of which the superoxide radical and hydrogen peroxide belong to the reactive oxygen species (ROS). The corresponding reaction equations are shown in Table 6.

Peroxidase enzymes are divided into two different classes: haem and non-haem containing enzymes. This thesis will focus on haem containing peroxidases which are divided in four superfamilies: peroxidase – catalase, peroxidase – cyclooxygenase, peroxidase – chlorite dismutase and peroxidase – peroxygenase. These superfamilies are divided in several other families so that approximately 1286 members of these four superfamilies are known today.[61] Prominent examples are the horseradish peroxidase (HRP), myeloperoxidase, lignin peroxidase and cytochrome c (Cyt C) peroxidase.[62–65] It is supposed that the four superfamilies evoluted independently from each other.[61]

Already several groups have worked on the elucidation of the catalysis mechanism of peroxidases. If the mechanism could be elucidated it will not only enlarge the knowledge of this enzyme group, but also makes it easier to mimic peroxidases. In the following Figure 8, the proposed catalysis mechanism of the HRP is shown on the basis of hydrogen peroxide and 2,2'-azino-di-(3-ethylbenzthiazoline-6-sulphonic acid) (ABTS) as substrates.

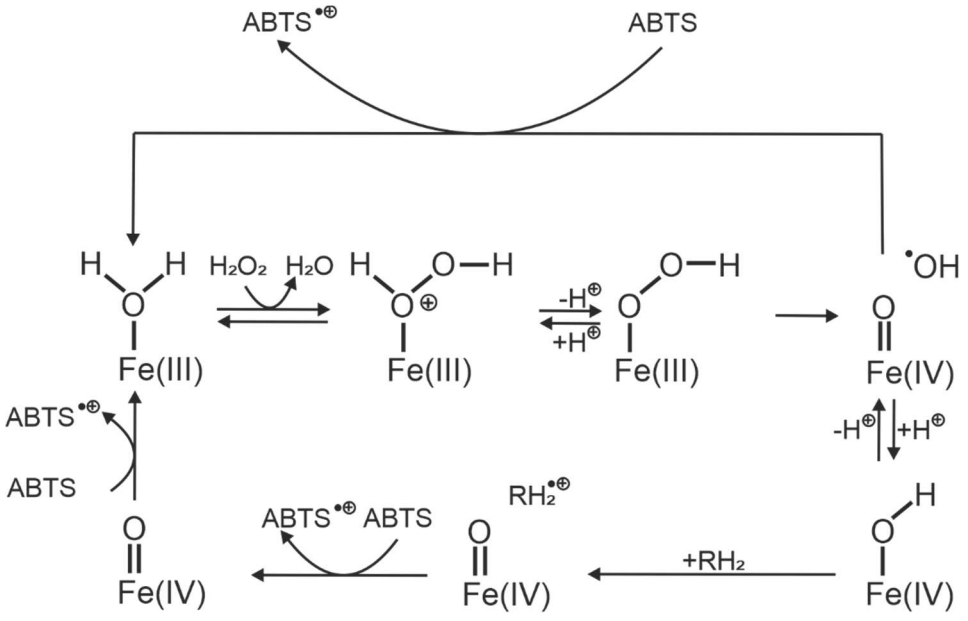

Figure 8: Proposed catalysis mechanism of HRP on the basis of ABTS as substrate. Based on [66] and [18].

It is expected that in the absence of hydrogen peroxide the catalytic active iron(III) ion in the active centre of the enzyme is complexed by a water molecule. This water molecule is exchanged in the presence of hydrogen peroxide (H_2O_2). By deprotonation a peroxo species is formed, which splits under homolysis into a

ferryl(IV) haem species and a hydroxyl radical. The formed hydroxyl radicals and the protonated ferryl(IV) species are able to oxidise other proteins, which can react with ABTS molecules.

The motivation behind imitating the enzyme peroxidase is obvious, considering that hydrogen peroxide must be strictly controlled in every organism. If excess hydrogen peroxide cannot be destroyed, it causes oxidative damage so severe that no living being would be viable in the long term. However, the use of nanoparticles as peroxidase mimics in living organisms is not yet conceivable due to the discussed toxicity of nanoparticles. The application for the detection of biomarkers, however, does not pose a problem.[67,68] For example, Fe_3O_4 nanoparticles in cooperation with the enzyme glucose oxidase can be used to quantitatively determine the amount of glucose contained in a sample. If the glucose oxidase converts glucose, one mole of hydrogen peroxide is formed per mole of glucose. This can be converted by the Fe_3O_4 nanoparticles by means of a colour reaction, so that the amount of hydrogen peroxide converted is proportional to the colour intensity. For example, the determination of blood sugar values can be carried out.[69]

In connection with the development of the first living organisms and the origin of life, minerals, such as magnetite, hematite or pseudobrookite may have been essential to destroy hydrogen peroxide, while the first life forms were not evolutionarily developed to the point of having enzymes. Alternative protection systems must have been essential for the genesis of life.

3.1.3. Hematite, Magnetite and Pseudobrookite

With the consideration of the enzyme peroxidase and the knowledge that its active centre contains iron ions, it seems obvious to investigate iron-containing nanoparticles regarding their catalytic activity with respect to this enzyme. This section is intended to provide a brief overview of the compounds on which the nanoparticles examined in this chapter are based.

Hematite is the most common iron oxide and is the α-modification of iron (III) oxide, which is well known for its red-brown colour. Also it is presumed to be the most

stable iron oxide under standard conditions.[70] It is antiferromagnetic and has a Néel temperature of 955 K. The crystal structure of hematite is derived from corundum. Hematite is mainly used as a colour pigment.[71]

Iron(II,III) oxide, also called magnetite, crystallises in an inverse spinel structure. This structure is derived from the naturally occurring mineral magnesium aluminate $MgAl_2O_4$, also called spinel. Magnetite nanoparticles are known to be superparamagnetic.[72]

Iron(II,III)-oxide nanoparticles are already being extensively researched because of their morphological variability and their wide range of applications. In addition to spherical Fe_3O_4 nanoparticles, cubic and elongated cubic Fe_3O_4 nanoparticles have already been synthesised.[73,74] They are used as electrical conductors, their inverse spinel structure enables them to exchange electrons between Fe^{2+} and Fe^{3+} species, as well as in biomedicine as magnetic resonance imaging contrast agent, tissue-specific drug delivery systems and in hyperthermia treatment.[27,75]

Pseudobrookite (Fe_2TiO_5) crystallises in an orthorhombic structure with the space group B_{bmm}.[76] It is best known as a pigment with colours ranging from yellow-pink to red to brown, resulting from the fact that the pseudobrookite forms isomorphic mixed crystals with magnesium and aluminium.[77]

3.1.4. Peroxidase Assays

To determine peroxidase activity, various photometric assays can be used, all based on colour reactions. Three different methods will be presented here, which are based on the use of three different educts and their respective advantages and disadvantages will be worked out.

ABTS-Assay

ABTS forms a colourless solution in water in dilution, which can be oxidised to a metastable radical cation under the influence of peroxidase and in the presence of hydrogen peroxide.[78] This makes the solution appear green and absorbs at

405 nm with additional absorption bands at 395 nm, 640 nm and 725 nm as well as an absorption shoulder at 580nm.[78,79]

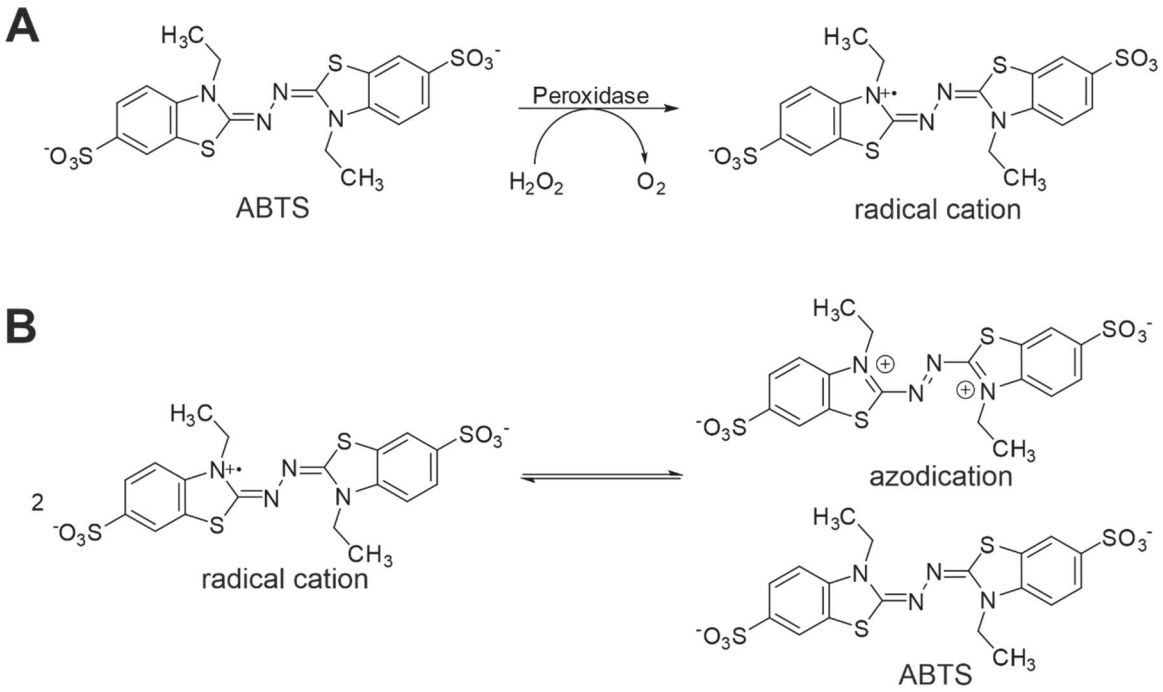

Figure 9: Reaction equation for the reaction of ABTS with hydrogen peroxide under catalysis of peroxidase or a peroxidase mimic. A: Reaction of ABTS to the metastable radical cation. B: Disproportionation of the radical cation into the azodication and ABTS.

However, the radical cation can also disproportionate to an azodication. This reaction proceeds very slowly, which is a problem if weakly active materials would be examined, because the measurements would have to be carried out over hours. It is also a problem in isolation, purification and analysis of the product and makes the investigation of feedback inhibition more difficult.[78] A green colouration of the ABTS solution is observed under the influence of light, so that the solution must always be freshly prepared and handled under exclusion of light.

TMB-Assay

The activity of peroxidase or peroxidase mimics can also be quantified using 3,3´,5,5´-tetramethylbenzidine (TMB). The oxidation of TMB with hydrogen peroxide under the catalysis of peroxidase is a two-step electron transfer. The reaction product is a diimine that appears yellow in solution and absorbs at a wavelength of 450 nm. The two-step reaction involves a radical cation. Two radical cations can react in a redox reaction to the educt TMB and to the final product (the

diimine). Together they build a charge transfer complex with a characteristic absorption at the wavelengths of 370 nm and 652 nm.[80,81]

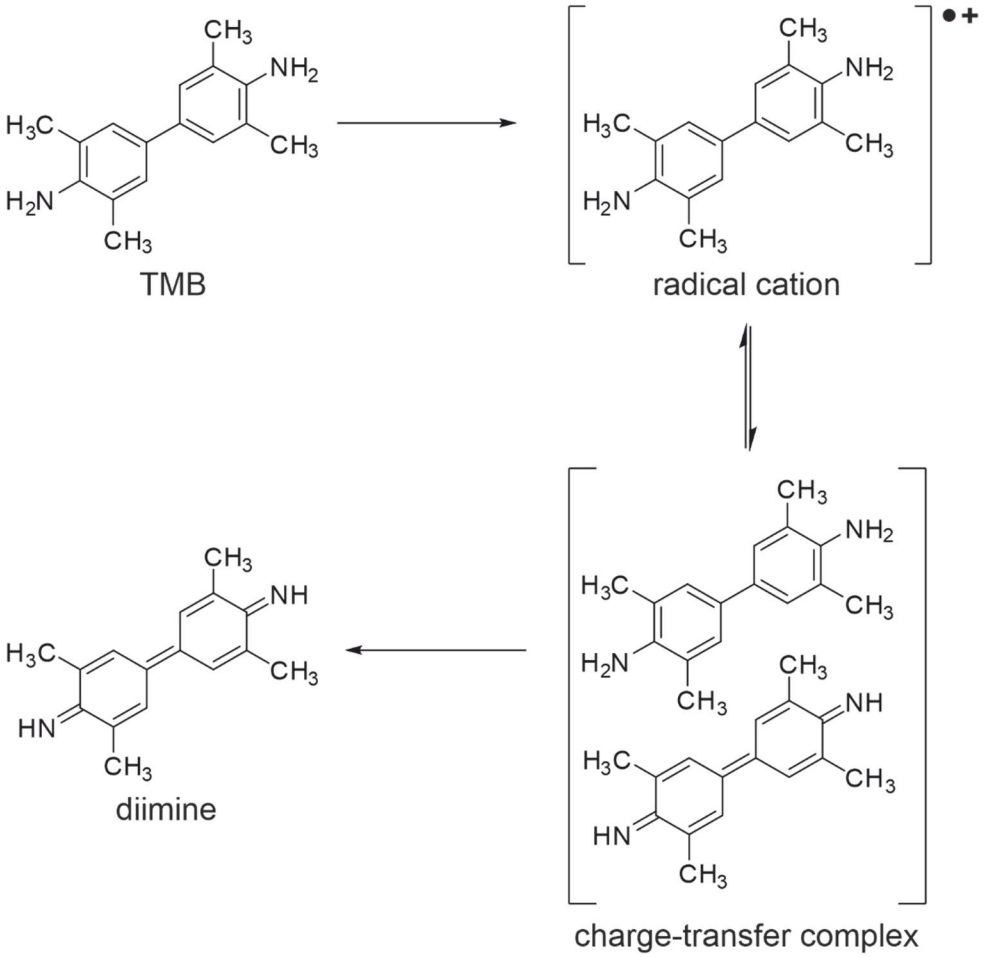

Figure 10: Reaction equation for the reaction of TMB with hydrogen peroxide under catalysis of peroxidase or a peroxidase mimic.

A special feature of this method is the possibility to observe the process of the reaction photometrically *via* the intermediate product. However, TMB is hardly soluble in water, so that dimethyl sulphoxide (DMSO) or a water-DMSO mixture must be used. Strict pH control is also important for this assay. The final diimine product is only formed in the acidic milieu.

Amplex Red™-Assay

10-Acetyl-3,7-dihydroxyphenoxazine (AR) is a molecule for the determination of peroxidase activity, also known as Amplex™ Red or Amplifu™ Red. If the colourless AR is oxidised by peroxidase catalysis with hydrogen peroxide, the

fluorescent resorufin (emission at 590 nm) is formed.[82] A characteristic absorption band can be detected at a wavelength of 572 nm.[83,84] However, the fluorescent product resorufin can be further oxidised in a subsequent reaction to resazurin, a N-oxide that no longer has fluorescent properties, but an absorption band at 603 nm.[85,86]

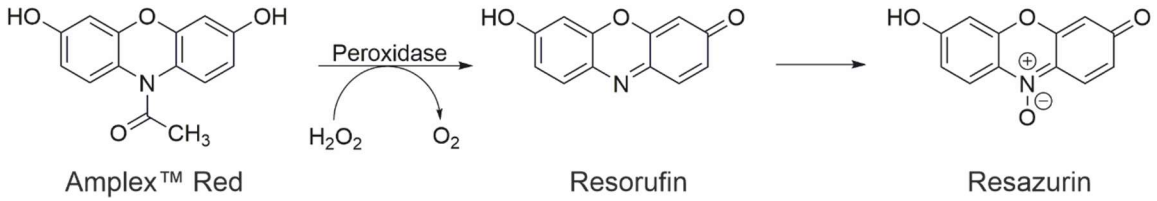

Figure 11: Reaction equation for the reaction of AR with hydrogen peroxide under catalysis of peroxidase or a peroxidase mimic.

Of particular interest with this method is the fluorescence of the resulting product, which makes the method particularly interesting for biomedical applications using confocal laser scanning microscopy (CLSM).[87] However, even this educt is not soluble in water alone, so that ethanol or an ethanol-water mixture is needed. However, stoichiometry must also be taken into account for this reaction, as it is known that the product resorufin can be further oxidised to resazurin, which is no longer fluorescent.

In conclusion, it can be summarised that all three methods are useful and have their right to exist. However, all three methods also have shortcomings or challenges in their application. In chapter 3.2, three different types of nanoparticles with intrinsic peroxidase activity will be investigated with these three methods to show the advantages and disadvantages of these methods and to discuss the resulting divergent results.

3.2. Results and discussion

In this part the three formerly introduced types of nanoparticles will be discussed in detail. First the synthesis of the nanoparticles will be explained shortly, before they will be characterised intensively. The characterisation includes x-ray diffraction (XRD) patterns, transmission electron microscopy (TEM) images and BET (Brunauer-Emmett-Teller) measurements and the discussion of their morphology and their sizes. Furthermore, the catalytic properties of the nanoparticles in three different peroxidase assays will be examined. At the end the kinetic measurements will be summarised and compared. The advantages and disadvantages of the different assays will be pointed out respective their possible application.

3.2.1. Synthesis and characterisation of hematite nanoparticles

Hematite spindle-shaped nanoparticle synthesis was performed as described by *Daniel*.[88] For this purpose, iron(III) chloride was hydrolysed in the presence of potassium dihydrogen phosphate in aqueous solution under reflux. Nanoparticles with an average length of 449.9 nm ± 79.0 nm and an average width of 76.2 nm ± 11.6 nm were obtained.

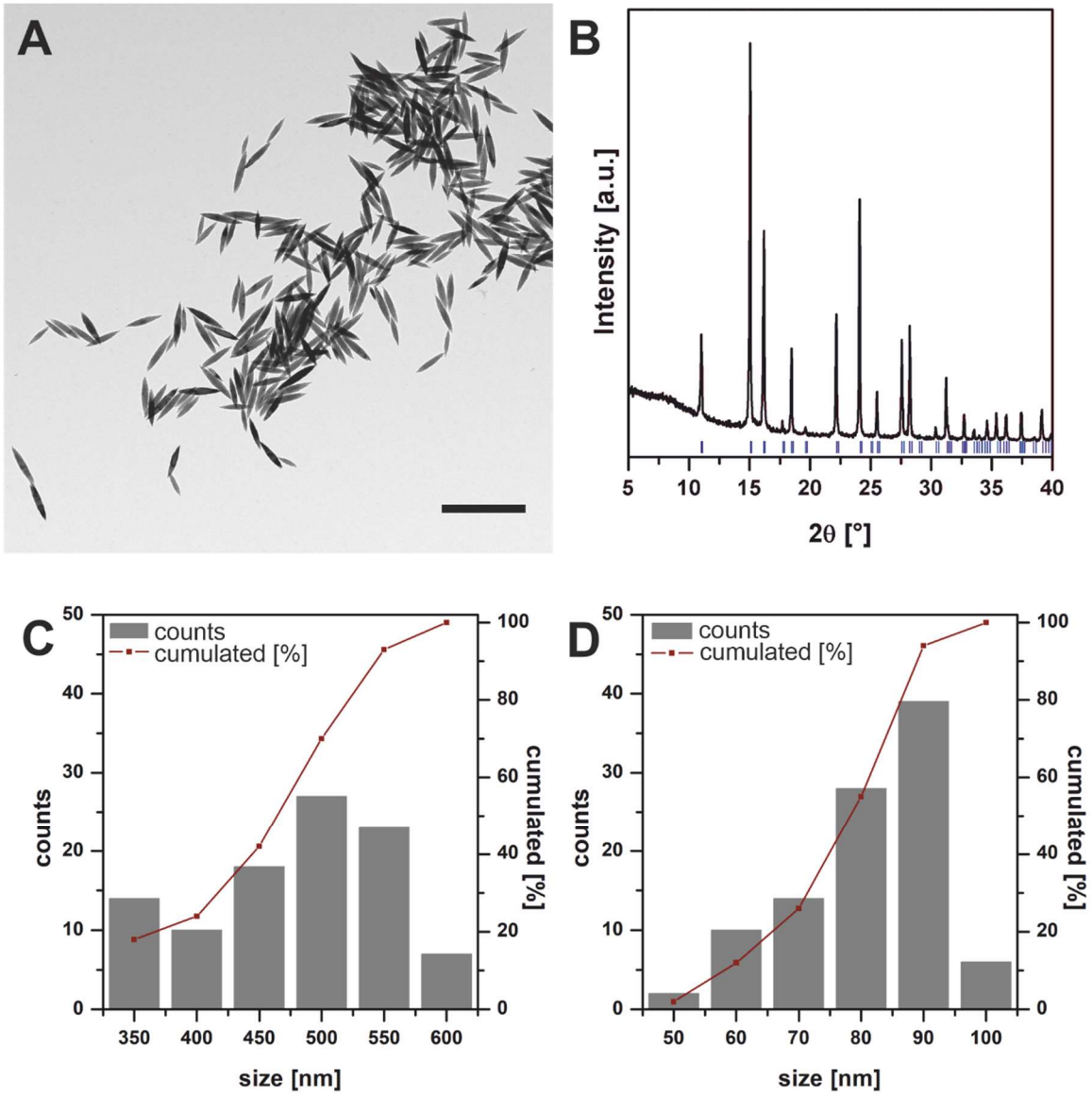

Figure 12: Characterisation of hematite nanoparticles. A: TEM image of the synthesised nanoparticles (scale bar 1 µm). B: XRD pattern (black) with literature reflexes (blue) (JCDPS card 99-504-2341). C: Histogram of the length of the nanoparticles. D: Histogram of the width of the nanoparticles.

Figure 12A shows a characteristic TEM image of spindle shaped hematite nanoparticles, while the Figure 12C and D show the histograms of the measured lengths and widths of the particles seen in the TEM image. The XRD pattern (Figure 12B) confirms the existence of hematite as the phase of the nanoparticles. The BET surface area is 21.300 $m^2 g^{-1}$ (see 3.5).

In the following the catalytic properties of the hematite nanoparticles will be discussed.

3.2.2. Kinetics of hematite nanoparticles

After complete characterisation, the hematite nanoparticles were subjected to kinetic investigations regarding their peroxidase-like activity. They were examined using the ABTS, TMB and AR assay described in section 3.1.4.

First kinetic measurements with different amounts (150 µg and 50 µg) of hematite nanoparticles were performed with the ABTS assay.

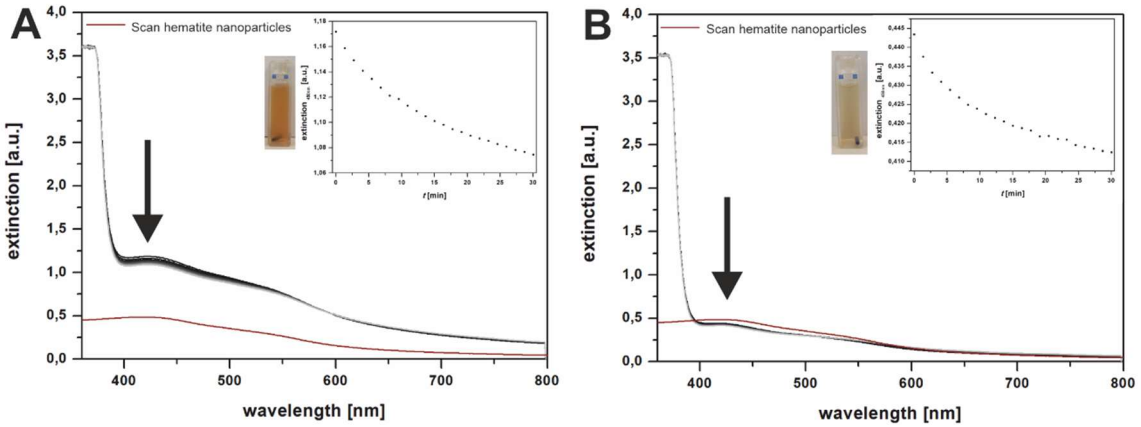

Figure 13: ABTS kinetic measurements of hematite nanoparticles. A: Measurement with a total amount of 150 µg hematite nanoparticles. Red line corresponds to the scan of the hematite nanoparticles. Inlay of the extinction change during the kinetic measurement at 405 nm. B: Measurement with a total amount of 50 µg hematite nanoparticles. Inlay of the extinction change during the kinetic measurement at 405 nm.

In both cases, the measurements show a decrease in absorbance at a wavelength of 405 nm (illustrated by the inlays in A and B, which show the change in absorbance over time at a wavelength of 405 nm). This seems strange at first, because in case of a peroxidase-like activity an increase in the absorbance at this wavelength is expected. However, the UV-Vis scan of the hematite nanoparticles shows that the nanoparticles have a self-absorption in the wavelength range around 405 nm. Despite the circulation in the cuvette caused by stirring, it can be assumed that some of the nanoparticles precipitate, which causes a decrease in the observed absorbance. If the measurement is carried out with a significantly lower amount of hematite nanoparticles (Figure 13B), it can be observed that the background absorbance is significantly reduced, but no increase in absorbance at a wavelength of 405 nm can be detected. Therefore, based on these measurements, it can be concluded that the hematite nanoparticles regarding the ABTS assay do not exhibit intrinsic peroxidase activity. Afterwards kinetic measurements with TMB were performed.

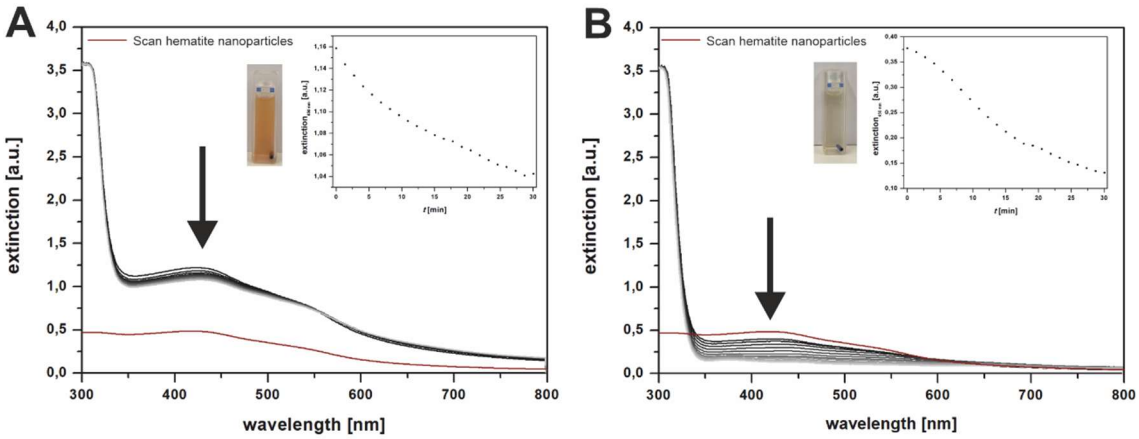

Figure 14: TMB kinetic measurements of hematite nanoparticles. A: Measurement with a total amount of 150 µg hematite nanoparticles. Red line corresponds to the scan of the hematite nanoparticles. Inlay of the extinction change during the kinetic measurement at 450 nm. B: Measurement with a total amount of 50 µg hematite nanoparticles. Red line corresponds to the scan of the hematite nanoparticles. Inlay of the extinction change during the kinetic measurement at 450 nm.

In this case a decrease in intensity can be observed regardless of the amount of hematite nanoparticles used too. The product of this assay can be detected at a wavelength of 450 nm. However, no increase in absorbance is detectable in this range in which the measurements were performed. Here, it can also be assumed that the nanoparticles partially precipitate despite circulation and are thus responsible for the decrease in absorbance due to their self-absorption in the measured wavelength range. Afterwards kinetic measurements with AR were performed.

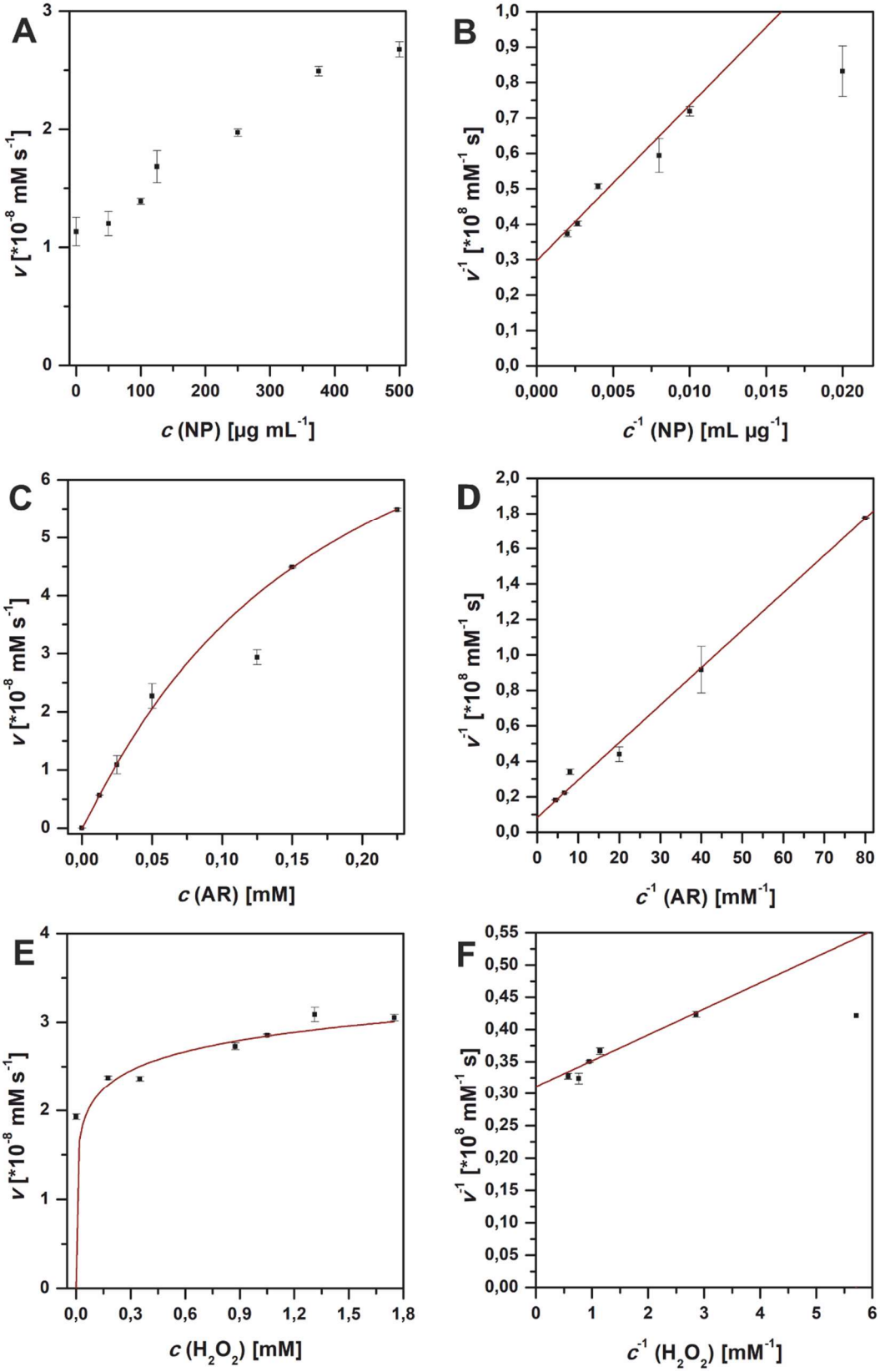

Figure 15: Kinetic measurements of hematite nanoparticles using the AR assay. (A, C and E – Michaelis-Menten kinetics; B, D and F - Lineweaver-Burk presentation; variation of the amount of nanoparticles (A and B), AR (C and D) and hydrogen peroxide (E and F)).

Figure 15 shows the kinetic measurements of the hematite nanoparticles using AR as dye substrate. Typical Michaelis-Menten kinetics are shown as well as the resulting Lineweaver-Burk diagrams. The results are like expected. Figure 15 A and B show the variation of the amount of nanoparticles used in the measurements while keeping the substrates hydrogen peroxide and AR constant. It is apparent that the bigger the amount of hematite nanoparticles in the measurements gets, the higher the activity gets. A linear correlation could be detected. In Figure 15A the Michaelis-Menten diagram shows a linear graph, so the Lineweaver-Burk diagram does not give any further information. In case of the variation of the concentration of AR a typical hyperbolic graph could be seen (Figure 15C). The linearised form of this graph is shown in Figure 15D. With the aid of the function of this linear graph the kinetic parameters like the Michaelis-Menten constant K_M and the maximum velocity v_{max} of the reaction could be calculated. K_M is 0.2522 ± 0.0002 mM while v_{max} is $1.1945*10^{-7} \pm 0.0007*10^{-7}$ mM s^{-1}. The measurements of the variation of hydrogen peroxide show the typical graphical trend as well. The kinetic parameters resulting from the Lineweaver-Burk graph are K_M 0.130 ± 0.006 mM and v_{max} $3.21*10^{-8} \pm 0{,}03*10^{-8}$ mM s^{-1}. Compared to the biochemistry and the characterisation of enzymes the natural substrate of the hematite nanoparticles is hydrogen peroxide since the Michaelis-Menten constant regarding the hydrogen peroxide is lower than the constant respective the AR.

In conclusion the experiments show that in case of hematite nanoparticles the choice of assay should be considered. With the ABTS and TMB assay no peroxidase-like activity of hematite nanoparticles could be detected because of the colour of the nanoparticles. However, with the AR assay the activity could be measured. In the following table the kinetic parameters are summarised.

Table 7: Kinetic parameters of hematite nanoparticles obtained from three different peroxidase assays with Lineweaver-Burk graphs.

	v_{max} [mM s^{-1}]	K_M [mM]
ABTS	-	-
TMB	-	-
AR	$1.1945*10^{-7} \pm 0.0007*10^{-7}$	0.2522 ± 0.0002
H_2O_2 (AR)	$3.21*10^{-8} \pm 0{,}03*10^{-8}$	0.130 ± 0.006

An evaluation of the catalytic activity of the hematite nanoparticles will be made at the end of this chapter in consideration of the other types of nanoparticles.

3.2.3. Synthesis and characterisation of magnetite nanoparticles

Magnetite nanoparticles with a size of 22 nm ± 5 nm were synthesised using a hot injection method on the basis of the synthesis of gold-iron(II,III) oxide (Au@Fe_3O_4) Janus particles used in chapter 4. Iron(0) pentacarbonyl was injected to a solution containing 1-octadecene, oleylamine and oleic acid at 120 °C. With increasing temperature the iron(0) pentacarbonyl was decomposed. Oleylamine was used as reducing agent while oleic acid was the surfactant.

In order to obtain magnetite nanoparticles of low dispersity, the synthesis was optimised by varying the amounts of oleylamine and oleic acid. The best result was used for further experiments. Despite the still quite high dispersity, these nanoparticles were deliberately selected and not nanoparticles of another synthesis route in order to be able to compare them with nanoparticles of the same synthesis route later in this work.

In Figure 16 the main analytic data respective the nanoparticle synthesis is presented. Figure 16A shows a TEM image of the spherical magnetite nanoparticles. The XRD pattern in Figure 16B verifies the presence of magnetite as only iron oxide phase. C shows the particle size distribution of hundred measured nanoparticles.

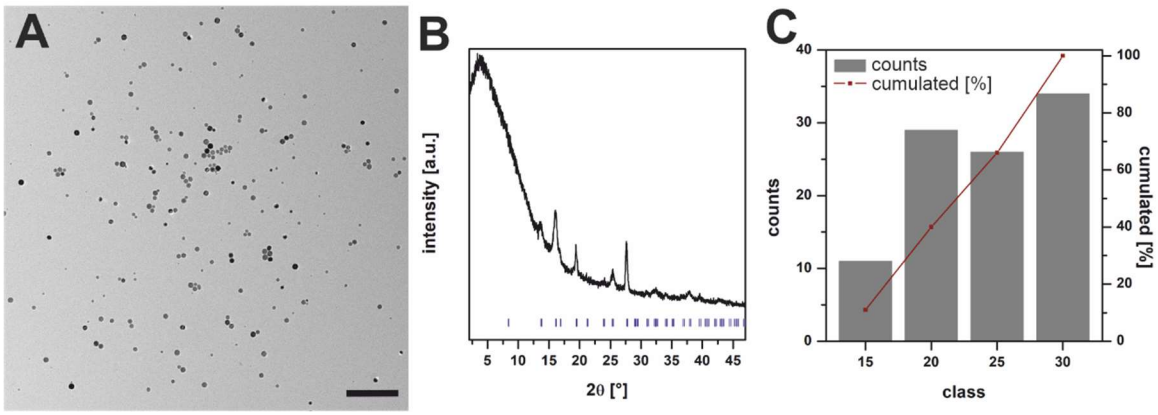

Figure 16: Characterisation of magnetite nanoparticles. A: TEM image of the synthesised nanoparticles (scale bar 250 nm). B: XRD pattern (black) with literature reflexes (blue) (JCDPS card 96-900-2317). C: Histogram of the diameter of the nanoparticles.

In the following the catalytic properties of the magnetite nanoparticles will be discussed.

3.2.4. Kinetics of magnetite nanoparticles

First scanning kinetic measurements with the substrates ABTS and TMB were performed to prove if the synthesised magnetite nanoparticles have an intrinsic peroxidase-like activity.

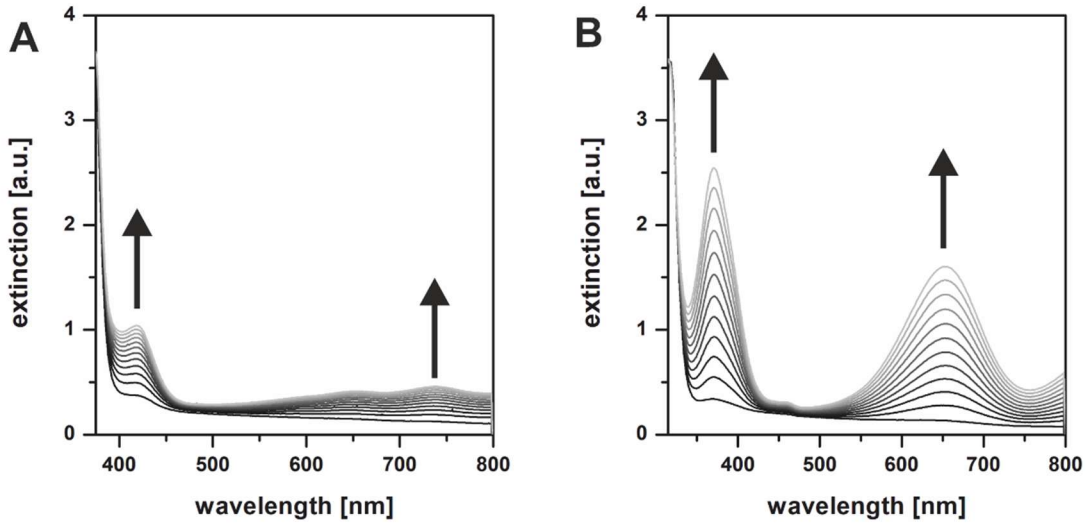

Figure 17: Scanning kinetic measurements of magnetite nanoparticles over 30 minutes using ABTS (A) and TMB (B).

Figure 17 shows the scanning kinetic measurements of the magnetite nanoparticles using ABTS (Figure 17A) and TMB (Figure 17B) as substrates. In both cases a change in the absorption spectra is detectable. In the case of ABTS as substrate an increase in the absorption at a wavelength of 420 nm and in the range of 600 nm to 800 nm is measurable while in case of the TMB an absorption increase is detectable at wavelengths of 370 nm and 652 nm. Both measurements indicate that the synthesised nanoparticles can mimic the enzyme peroxidase. Figure 17B indicates that in the case of the measurement with TMB as dye substrate only the charge-transfer complex is formed.

Afterwards, Michaelis-Menten kinetic analysis were executed to evaluate the kinetic performans of the nanoparticles regarding three different assays. The first assay to be considered is the ABTS assay.

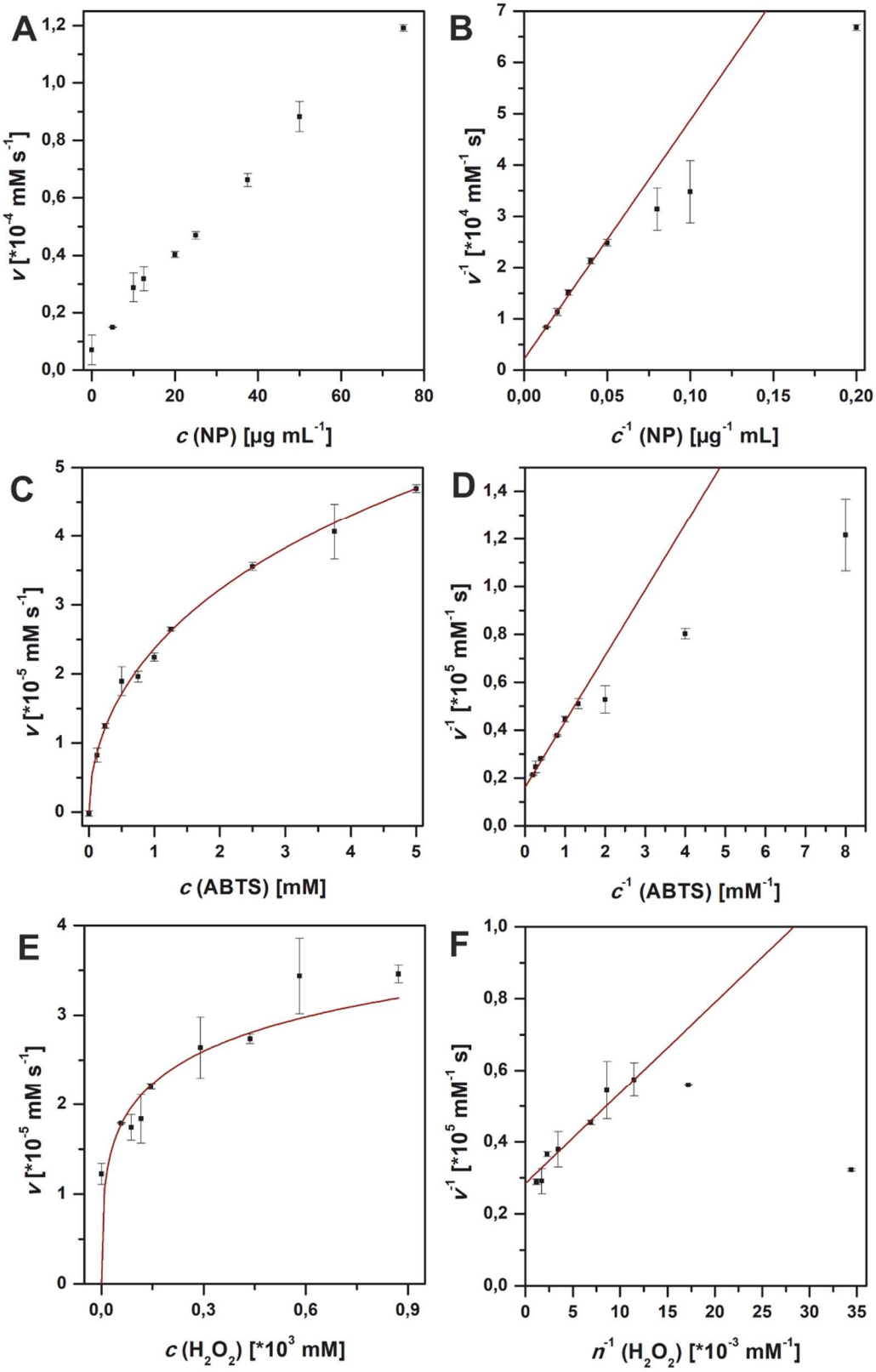

Figure 18: Kinetic measurements of magnetite nanoparticles using the ABTS assay. (A, C and E – Michaelis-Menten kinetics; B, D and F - Lineweaver-Burk presentation; variation of the amount of nanoparticles (A and B), ABTS (C and D) and hydrogen peroxide (E and F)).

Figure 18 shows the graphs of the Michaelis-Menten kinetics and Lineweaver-Burk depositions of magnetite nanoparticles with the dye substrate ABTS. As expected, the hyperbolic behaviour of the Michaelis-Menten kinetics is detectable with the variation of ABTS and hydrogen peroxide. In case of variation of the amount of nanoparticles, a linear increase of the reaction rate is visible depending on the concentration of nanoparticles in the measured solution. This can be explained by the fact that with increasing concentration of the nanoparticles a larger number of nanoparticles is available for catalysis. A larger number of nanoparticles is equivalent to an effectively larger surface area with more active sites. More active sites lead to an increase in the reaction rate. The linear behaviour of the graph (Figure 18A) can be explained by the fact that, assuming that each nanoparticle has the same properties (same surface area, same number of active sites), each nanoparticle has the same activity. This means the reaction rate is linearly dependent to the amount of nanoparticles used. From the linearised Michaelis-Menten kinetics, i.e. the Lineweaver-Burk graphs (Figure 18D and F), the kinetic parameters can be determined from the ordinate section and the intersection of the graph with the abscissa. Not all measuring points were included in the linear fit, since no slope can be detected in the saturation during linearisation. Furthermore, the slope of the hyperbola decreases towards saturation.

Table 8: Kinetic parameters of magnetite nanoparticles obtained from the ABTS assay with Lineweaver-Burk graphs.

	v_{max} [mM s^{-1}]	K_M [mM]
ABTS	$6.2*10^{-5} \pm 0.1*10^{-5}$	1.717 ± 0.007
H_2O_2	$3.51*10^{-5} \pm 0.09*10^{-5}$	89 ± 3

The kinetic parameters obtained from Lineweaver-Burk graphs are concluded in Table 8. It can be stated that v_{max} in relation to ABTS is almost twice as large as in the case of hydrogen peroxide. At the same time, K_M is significantly smaller in relation to ABTS than in relation to hydrogen peroxide. From a biochemical point of view, this suggests that ABTS is the natural substrate of the nanoparticle.

Subsequently, the same investigations were performed with TMB as dye substrate and the same kinetic parameters were determined.

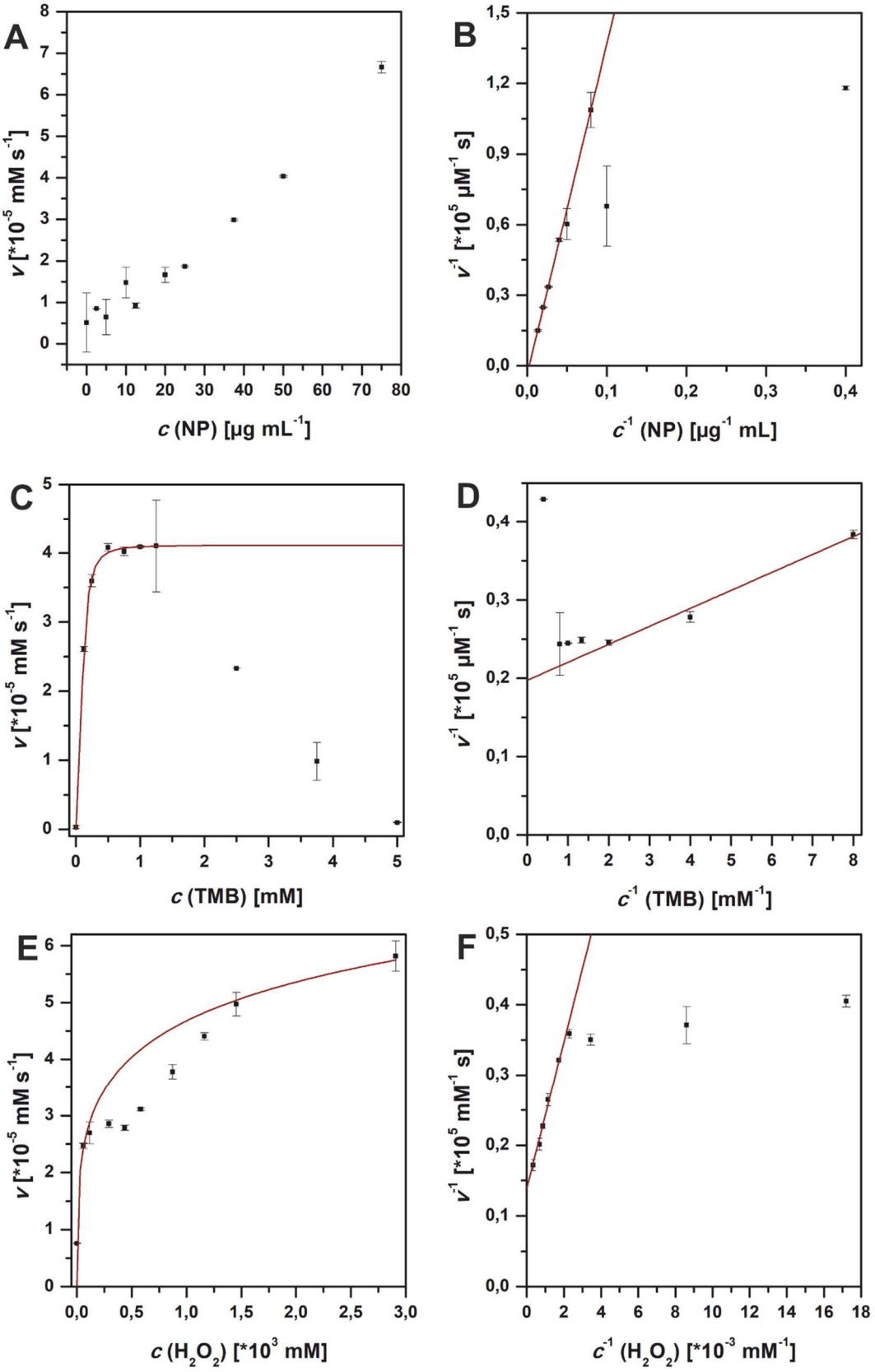

Figure 19: Kinetic measurements of magnetite nanoparticles using the TMB assay. (A, C and E – Michaelis-Menten kinetics; B, D and F - Lineweaver-Burk presentation; variation of the amount of nanoparticles (A and B), TMB (C and D) and hydrogen peroxide (E and F)).

Figure 19 shows the Michaelis-Menten kinetics and Lineweaver-Burk graphs of magnetite nanoparticles with TMB as dye substrate. A linear trend within the Michaelis-Menten kinetics can be observed by varying the concentration of the nanoparticles used (Figure 19A). In the case of variation of the TMB concentration (Figure 19C), a strong increase of the reaction rate with increasing TMB concentration is observed at the beginning, but decreases rapidly at concentrations higher than 1.5 mM. This seems to be surprising at first, but during these measurements it could be observed that the solutions did not turn blue-green, but instead took on a yellow colour. This is particularly interesting, because with increasing concentration of TMB the charge-transfer complex is no longer formed as product, but the final end product, the yellow appearing diimine. Consequently, it can be assumed that by increasing the TMB concentration, the equilibrium of the reaction (see Figure 10) is shifted in favour of the diimine. This is not optimal in the case of a Michaelis-Menten kinetic, where the measurement is deliberately carried out till v_{max} is reached. The values were not taken into account in the Michaelis-Menten fit. For the Lineweaver-Burk graph, the measurement data above a TMB concentration of 1.5 mM was deliberately omitted because of the subsequent reaction, in order not to further falsify the kinetics parameters. In this case, the kinetic parameters have to be considered critically, because it is not clear from the measurements whether the diimine was already formed during the previous measurements. At a wavelength of 370 nm, this is not detectable and the yellow colour is visually superimposed by the blue-green colour of the charge-transfer complex as long as this complex is the main product. If the diimine is formed at the same time, the measured absorbance increase at 370 nm would be reduced, because while the charge-transfer complex is formed, the complex molecules continue to react. This would have the consequence that the reaction rate determined from this would assume a lower value. Consequently, in this case it cannot be assumed with certainty that the reaction rates correspond to the actual rates, or that they would not assume higher values. The resulting kinetic parameters can therefore be particularly error-prone which, however, cannot be represented purely mathematically. The Michaelis-Menten kinetics under variation of the hydrogen peroxide concentration again shows a hyperbolic behaviour (Figure 19E). Using the Lineweaver-Burk graph (Figure 19F) the kinetic

parameters could be determined. As already described above, not all measured values were included in the linear fit for the reasons mentioned above.

Table 9: Kinetic parameters of magnetite nanoparticles obtained from the TMB assay with Lineweaver-Burk graphs.

	v_{max} [mM s^{-1}]	K_M [mM]
TMB	$5.1*10^{-5} \pm 0.1*10^{-5}$	0.116 ± 0.003
H_2O_2	$7.2*10^{-5} \pm 0.3*10^{-5}$	750 ± 3

The kinetic parameters obtained from Lineweaver-Burk graphs are concluded in Table 9. While the values for v_{max} in this assay related to TMB and hydrogen peroxide do not differ that much, the deviations of the K_M values are all the greater. The K_M value related to TMB is over 6000 times greater than the value related to hydrogen peroxide. Consequently, from a biochemical point of view, the affinity of the nanoparticles to the dye molecule is greater than to hydrogen peroxide.

Subsequently, the same investigations were performed with AR as dye substrate and the same kinetic parameters were determined.

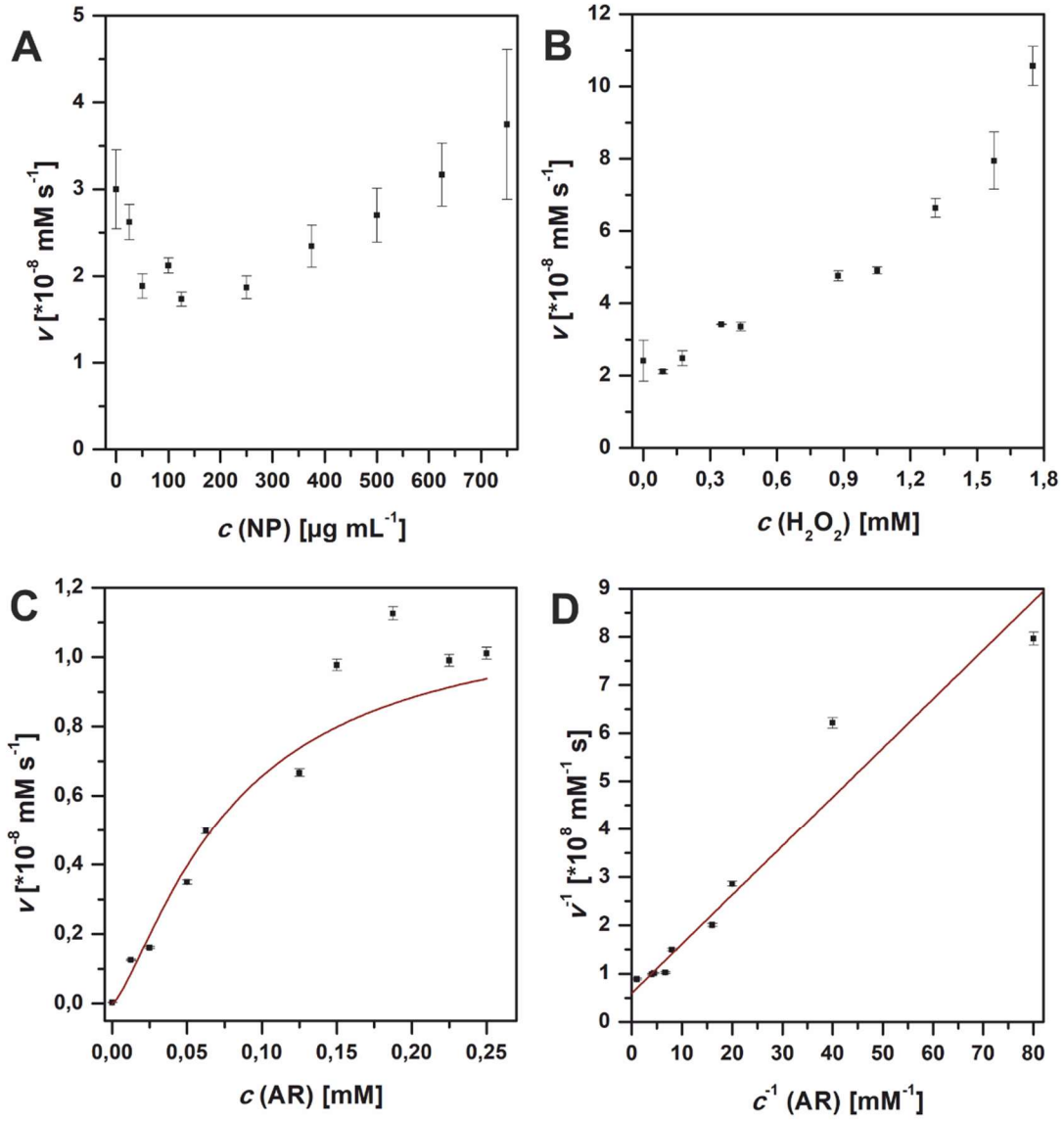

Figure 20: Kinetic measurements of magnetite nanoparticles using the AR assay. (A, B and C – Michaelis-Menten kinetics; D - Lineweaver-Burk presentation of C; variation of the amount of nanoparticles (A), AR (C and D) and hydrogen peroxide (B)).

Figure 20 shows the Michaelis-Menten kinetics of magnetite nanoparticles using AR as dye substrate. It is noticeable that the variation of the nanoparticle concentration does not show a linear behaviour as in the previous kinetics (see Figure 20A). At low concentrations the reaction rate decreases compared to the measurement without nanoparticles and only at higher concentrations it increases again. It should also be noted that the blank value is only exceeded at a nanoparticle concentration of over 600 µg ml^{-1}. It can be assumed that in this case not the fluorescent resorufin is produced, but the non-fluorescent resazurin. This explains the decrease of the reaction speed, which is based on the decrease of the

fluorescence intensity. However, with a look at the graph as a whole, it becomes clear that this is unlikely, since higher concentrations of nanoparticles produce a fluorescent species. However, a reduction of resazurin to resorufin cannot be assumed under the given conditions. It can rather be assumed that the nanoparticles interact with the resulting product resorufin but also with the educt AR *via* the phenolic hydroxyl groups. Two hypotheses can be made here: On one hand it could be assumed that the interaction between the substrate and the nanoparticle is sterically unfavourable for catalysis, so that the molecule cannot be converted. However, this contradicts the formation of resorufin at higher nanoparticle concentrations. On the other hand, one could assume that the AR molecules are converted to resorufin on the surface of the nanoparticle, but remain there and interact with the nanoparticles *via* the phenolic hydroxyl groups. The resulting proximity of the fluorescent molecules to each other leads to quenching effects, so that a decrease in fluorescence intensity can be measured. Only at higher nanoparticle concentrations an increase in fluorescence intensity can be measured, since the reaction speed is significantly higher due to the larger amount of available nanoparticles. As a result, more substrate molecules reacted simultaneously at the magnetite nanoparticles and at the same time more resorufin molecules are exchanged for unreacted substrate molecules at the nanoparticle surface, so that the fluorescent molecules can diffuse faster and free in the reaction solution and the quenching effect is cancelled.

Figure 20B shows the Michaelis-Menten kinetics under variation of the hydrogen peroxide concentration. An almost linear relationship between the hydrogen peroxide concentration and the reaction rate can be seen. This cannot be matched at all with the observation in the measurements with ABTS as dye substrate. However, it supports the previous hypothesis of the reaction and interaction of the dye AR with the surface of the magnetite nanoparticles. The linear behaviour of the graph (Figure 20B) can be explained by diffusion. If there is an interaction between the phenolic hydroxyl groups of the resorufin and thus quenching effects that are only overcome by exchanging the resorufin for unreacted AR molecules at the surface of the magnetite nanoparticles, this process is diffusion-limited. It can be assumed that the diffusion rate is constant, so that the same number of molecules on the surface of the nanoparticles can be exchanged per time unit. If more of the

hydrogen peroxide is available by increasing the concentration of the hydrogen peroxide, diffusion is not accelerated, but the diffusion path can be reduced by increasing the supply so that the reaction is shifted towards the product according to the principle of Le Chatelier. The faster exchange of molecules by a higher supply of hydrogen peroxide increases the reaction rate so that a linear relationship between the reaction rate and the hydrogen peroxide concentration can be established.

The variation of the AR concentration leads to an almost hyperbolic curve of the graph (Figure 20C). This observation can be combined with the previous explanations for the other two measurements. As with the measurement with hydrogen peroxide, it can be assumed that with increasing dye concentration the diffusion path is reduced and thus, a faster exchange of fluorescent molecules against substrate molecules can take place. If the concentration of dye is low enough, the molecules will still interact with the magnetite nanoparticles, but there will be no quenching effects, since the low concentration also minimises the interaction of AR molecules with each other. Using the Lineweaver-Burk graph (Figure 20F) the kinetic parameters could be determined.

Table 10: Kinetic parameters of magnetite nanoparticles obtained from the AR assay with Lineweaver-Burk graphs.

	v_{max} [mM s^{-1}]	K_M [mM]
AR	$1.68*10^{-8} \pm 0.03*10^{-8}$	0.1711 ± 0.0006
H_2O_2	-	-

The kinetic parameters obtained from Lineweaver-Burk graphs are concluded in Table 10. Kinetic parameters could not be determined for the conversion of hydrogen peroxide because the kinetic does not obey the rules of Michaelis-Menten kinetics but presents a linear relationship. The parameters for the conversion of the dye are listed.

It can be summarised that all three assays led to three completely different results with respect to the measurement curves but also to the kinetic parameters. While in the case of the ABTS assay all graphical representations were as expected, in the TMB assay follow-up reactions could be observed and in the AR assay

interactions between dye substrate and nanoparticles could be suspected. In the following table all determined kinetic parameters are summarised.

Table 11: Kinetic parameters of magnetite nanoparticles obtained from three different peroxidase assays with Lineweaver-Burk graphs.

	v_{max} [mM s^{-1}]	K_M [mM]
ABTS	$6.2*10^{-5} \pm 0.1*10^{-5}$	1.717 ± 0.007
TMB	$5.1*10^{-5} \pm 0.1*10^{-5}$	0.116 ± 0.003
AR	$1.68*10^{-8} \pm 0.03*10^{-8}$	0.1711 ± 0.0006
H_2O_2 (ABTS)	$3.51*10^{-5} \pm 0.09*10^{-5}$	89 ± 3
H_2O_2 (TMB)	$7.2*10^{-5} \pm 0.3*10^{-5}$	750 ± 3
H_2O_2 (AR)	-	-

Looking at Table 11, the magnitude of the maximum reaction speed of the AR conversion is particularly striking. The reaction proceeds significantly slower than the conversion of the two dyes ABTS and TMB. Otherwise, the values determined for v_{max} are of the same order of magnitude, but a general trend cannot be recognised. While no K_M value for hydrogen peroxide could be determined using the AR assay, this could be done using the other two assays. Nevertheless, the determined values could not be more different. The K_M value resulting from the TMB assay is more than eight times greater than that obtained by the ABTS assay. However, this could also be due to the observed subsequent reaction. Yet, when comparing the K_M values related to hydrogen peroxide with those related to the dye substrates, it is clear that the values related to the dyes are significantly lower. From a biochemical point of view, this means that the nanoparticles have a greater affinity to the dye molecules than to hydrogen peroxide. Comparing the K_M values of the dye molecules with each other, it is noticeable that the value related to ABTS is greater by a factor of 10 than the other two. While TMB is a non-polar, non-charged dye, ABTS is particularly distinguished by the salt form used. ABTS is polar and charged. This could influence the interaction with the nanoparticles. Nevertheless, taking all results into account, it is clear that the ABTS assay is the most suitable assay for magnetite nanoparticles.

3.2.5. Synthesis and characterisation of pseudobrookite nanoparticles

The pseudobrookite nanoparticles were produced in an ultrasonic synthesis using iron(II) acetate as iron precursor and titanium isopropoxide. The product resulted after decomposition was centrifuged and calcined. The resulting powder was characterised *via* XRD, TEM, high resolution-TEM (HR-TEM), BET and UV-Vis measurements.

Figure 21 shows the most important analytic data for characterisation of the new synthesised compound. The TEM image shows particles whose size is in the nano range. An unambiguous determination of the size is not possible due to the different sizes of the particles and the partly not clearly recognisable particle edges. Therefore, no histograms are generated for this type of particle.

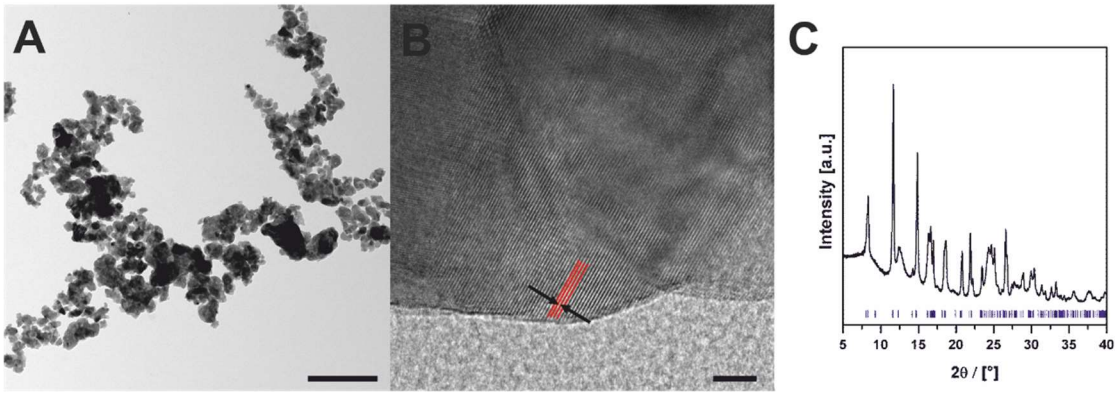

Figure 21: Characterisation of pseudobrookite nanoparticles. A: TEM image of the synthesised nanoparticles (scale bar 250 nm). B: HR-TEM (scale bar 5 nm). Red lines show the lattice planes with measured distances of 0.1425 nm. C: XRD pattern of synthesised pseudobrookite nanoparticles (black) with references (blue) (JCDPS card 96-200-2319).

The TEM image (Figure 21A) shows an agglomerate of nanoparticles with non-uniform morphologies. While the XRD pattern (Figure 21C) indicates the existence of pseudobrookite nanoparticles, the HR-TEM image (Figure 21B) which makes it possible to measure the lattice plane distances supports the results of the XRD pattern. The lattice plane distances marked in the image (red lines with black arrows) exhibit a distance of 0.1425 nm which indicates the presentation of the [154] plane.[89] The BET surface area of the pseudobrookite nanoparticles is 7.887m² g^{-1}.

In the subsequent experiments the kinetic properties respective the peroxidase-like activity were examined.

3.2.6. Kinetics of pseudobrookite nanoparticles

First scanning kinetic measurements with the substrates ABTS and TMB were executed to prove if the synthesised pseudobrookite nanoparticles exhibit an intrinsic peroxidase-like activity.

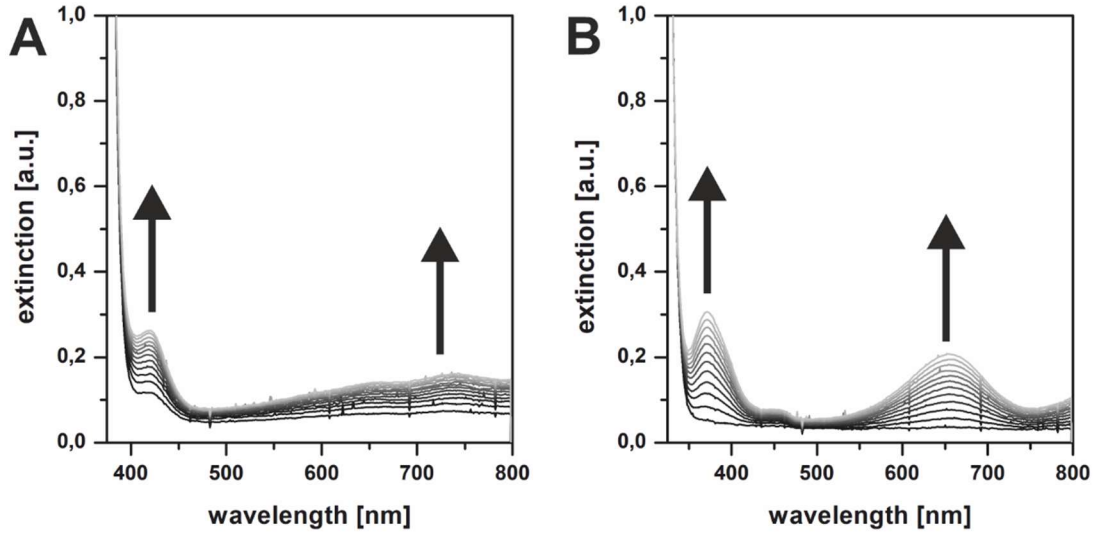

Figure 22: Scanning kinetic measurements of pseudobrookite nanoparticles over 30 minutes using ABTS (A) and TMB (B).

Figure 22 shows the scanning kinetic measurements of the pseudobrookite nanoparticles using ABTS (Figure 22A) and TMB (B) as substrates. Both measurements show a change in the absorption spectra. In the case of ABTS as substrate an increase in the absorption at a wavelength of 420 nm and in the range of 600 nm to 800 nm is detectable, while in case of the TMB an absorption increase is measurable at wavelengths of 370 nm and 652 nm which indicates that only the charge-transfer complex is built. Both measurements indicate that the synthesised nanoparticles can mimic the enzyme peroxidase.

Afterwards Michaelis-Menten kinetic analysis were executed to evaluate the kinetic performans of the nanoparticles regarding three different assays, starting with the ABTS assay.

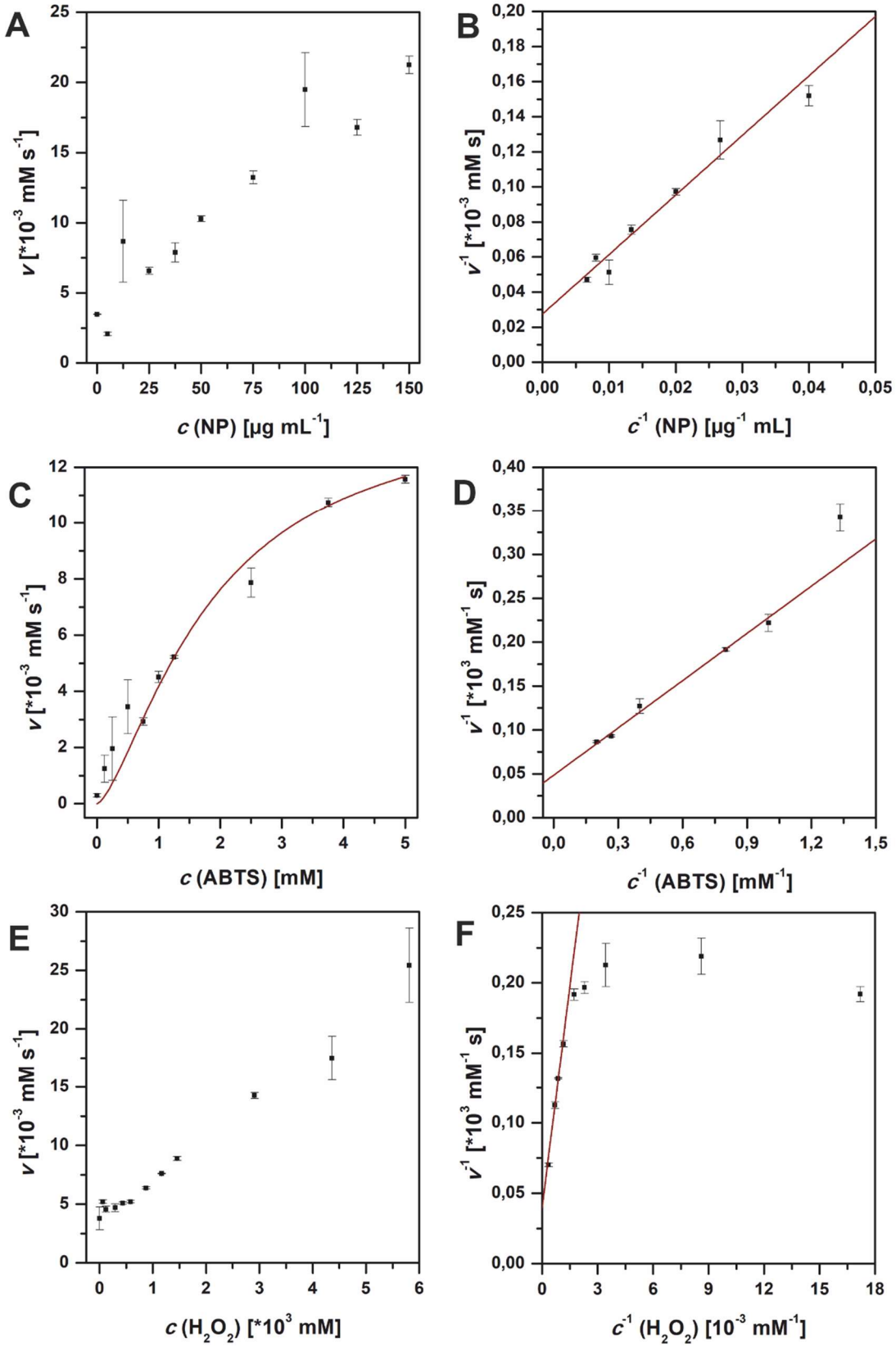

Figure 23: Kinetic measurements of pseudobrookite nanoparticles using the ABTS assay. (A, C and E – Michaelis-Menten kinetics; B, D and F - Lineweaver-Burk presentation; variation of the amount of nanoparticles (A and B), ABTS (C and D) and hydrogen peroxide (E and F)).

Figure 23 shows the Michaelis-Menten kinetics and Lineweaver-Burk graphs of pseudobrookite nanoparticles in the ABTS assay. As discussed above, the linear relationship between the concentration of nanoparticles and the reaction rate can be observed (Figure 23A). The Michaelis-Menten kinetics of the variation of the dye substrate concentration shows the typical hyperbolic curve (Figure 23C), whereas no maximum reaction rate can be achieved under variation of the hydrogen peroxide concentration (Figure 23E). Nevertheless, even in this case a decrease of the slope with an increase of the hydrogen peroxide concentration can be seen, so that it can be assumed that the maximum reaction rate could still be reached at even higher hydrogen peroxide concentrations. In this case, higher concentrations were not used, since half of the volume was already concentrated hydrogen peroxide solution when measuring with the highest concentration. If the concentration is increased further, the buffering effect can no longer be guaranteed. The kinetic parameters obtained from the Lineweaver-Burk graphs are summarised in the following table.

Table 12: Kinetic parameters of pseudobrookite nanoparticles obtained from the ABTS assay with Lineweaver-Burk graphs.

	v_{max} [mM s^{-1}]	K_M [mM]
ABTS	0.020 ± 0.001	3.6 ± 0.2
H_2O_2	0.025 ± 0.001	2632 ± 66

The kinetic parameters obtained from Lineweaver-Burk graphs are concluded in Table 12. It can be summarised that the maximum reaction rates in relation to ABTS and hydrogen peroxide are almost equal. However, the K_M values show significant differences. For example, the K_M value based on hydrogen peroxide is over 700 times greater than that based on ABTS. Consequently, from a biochemical point of view, the affinity of the nanoparticles to the dye molecule is greater than to hydrogen peroxide.

Subsequently, the same investigations were performed with TMB as dye substrate and the same kinetic parameters were determined.

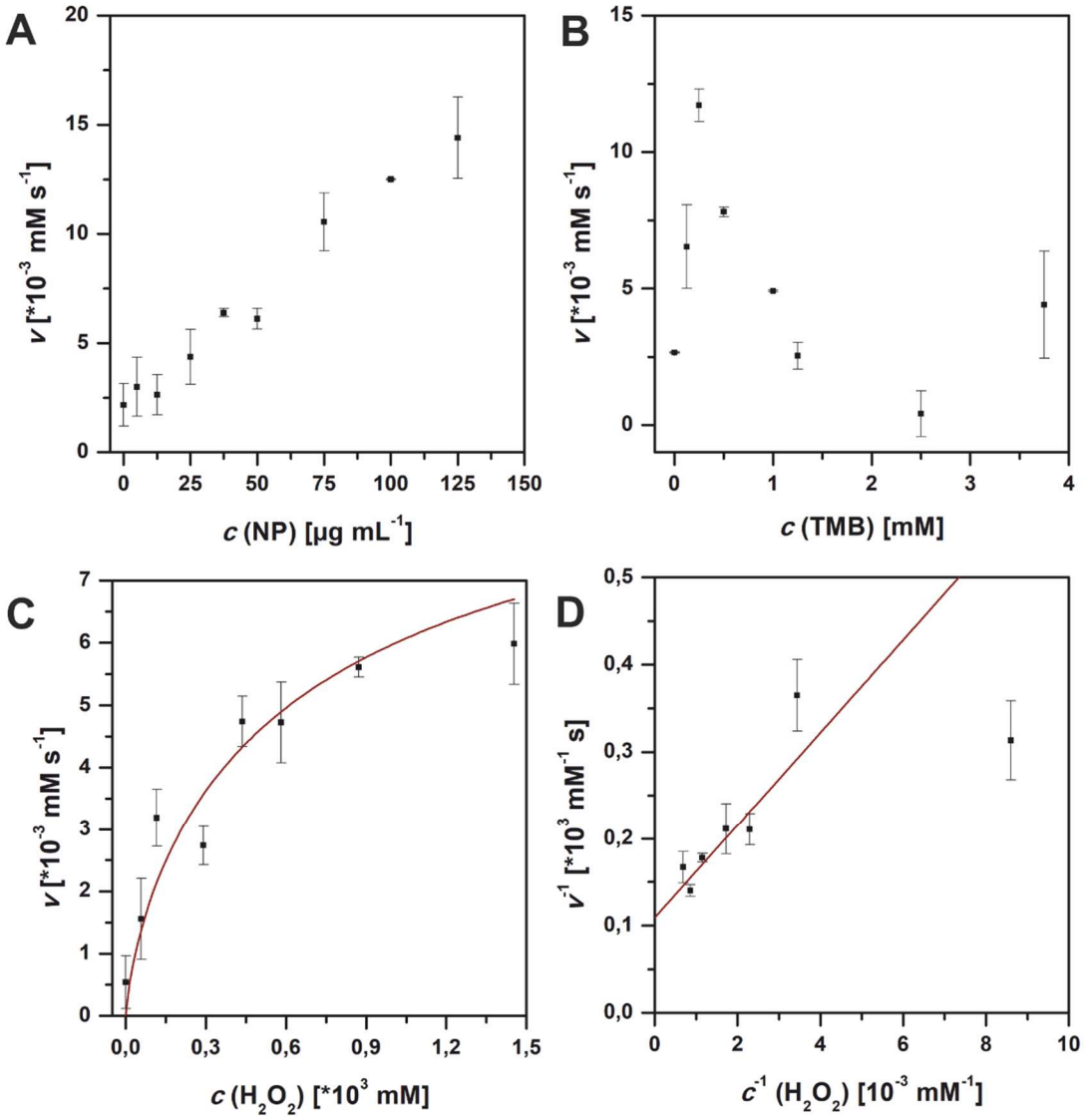

Figure 24: Kinetic measurements of pseudobrookite nanoparticles using the TMB assay. (A, B and C – Michaelis-Menten kinetics; D - Lineweaver-Burk presentation of C; variation of the amount of nanoparticles (A), TMB (B) and hydrogen peroxide (C and D)).

Figure 24 shows the Michaelis-Menten kinetics and Lineweaver-Burk diagrams of the pseudobrookite nanoparticles in the TMB assay. The variation of the nanoparticle concentration shows the expected and previously discussed linear relationship between nanoparticle concentration and reaction rate (Figure 24A). In the case of variation of the TMB concentration, an increase in the reaction rate can be observed first and then a decrease (Figure 24B). Also, in this case it could be observed that the solutions with higher TMB concentrations took on a yellow and not a blue-green colour. Consequently, as already discussed in section 3.2.4, the diimine was formed in this case as the final end product too. When varying the

hydrogen peroxide concentration, which is the most interesting measurement in the case of peroxidase mimics, a hyperbolic curve of the graph of the Michaelis-Menten kinetics can be observed (Figure 24C). From the linearised plot (Figure 24D) the kinetic parameters could be determined.

Table 13: Kinetic parameters of pseudobrookite nanoparticles obtained from the TMB assay with Lineweaver-Burk graph.

	v_{max} [mM s^{-1}]	K_M [mM]
TMB	-	-
H_2O_2	0.009 ± 0.001	487 ± 50

The kinetic parameters obtained for hydrogen peroxide from Lineweaver-Burk graphs are concluded in Table 13. With the help of the measurement data in this case only v_{max} and K_M could be determined with respect to hydrogen peroxide. However, it can be stated that in this case the error of the K_M value is comparatively large compared to previously determined parameters. Kinetic parameters regarding TMB could not be determined because the kinetics do not obey the rules of Michaelis-Menten kinetics because of the mentioned follow-up reaction.

Subsequently, the same investigations were performed with AR as dye substrate and the same kinetic parameters were determined.

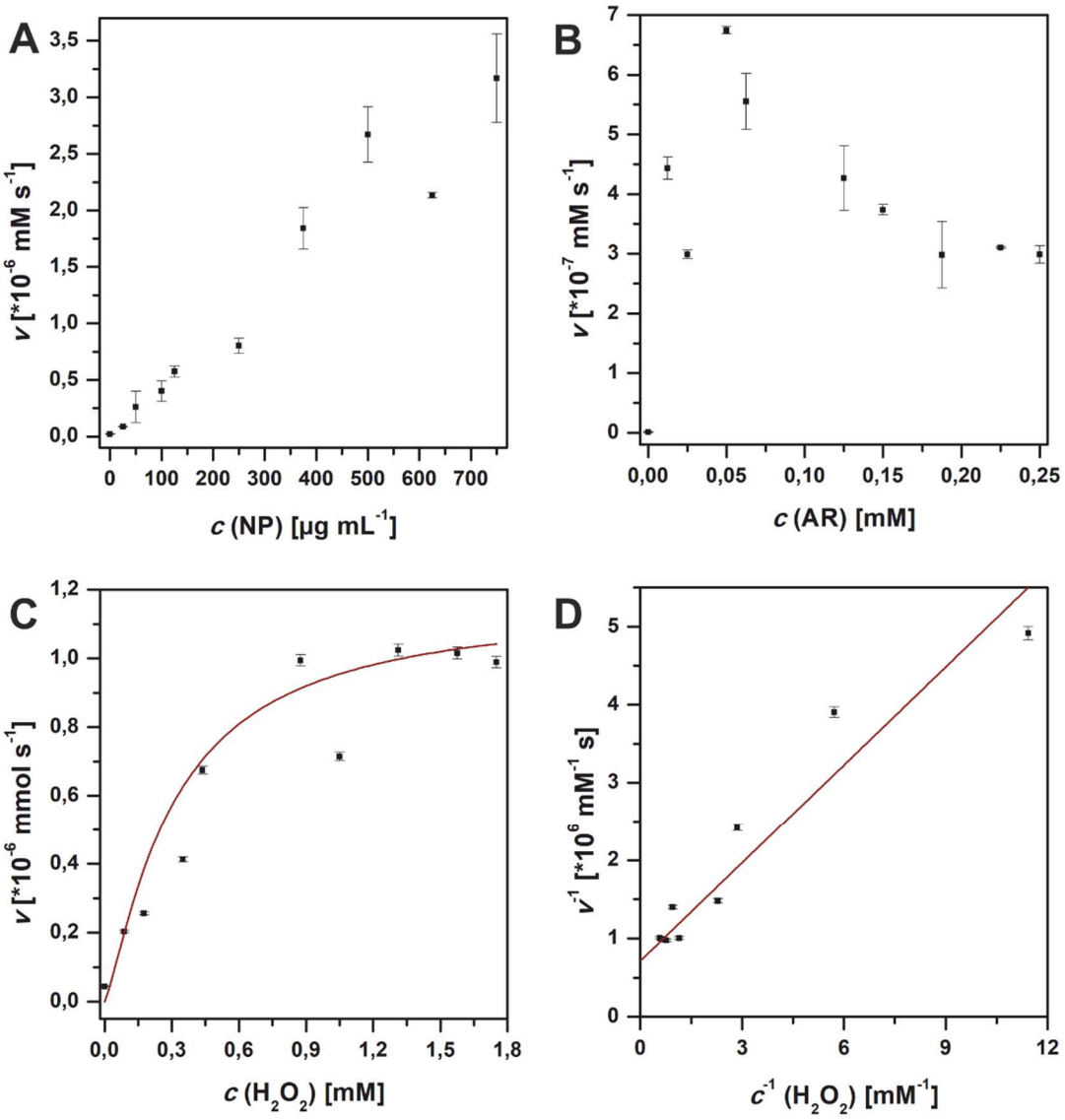

Figure 25: Kinetic measurements of pseudobrookite nanoparticles using the AR assay. (A, B and C – Michaelis-Menten kinetics; D: Lineweaver-Burk presentation of C; variation of the amount of nanoparticles (A), AR (B) and hydrogen peroxide (C and D)).

Figure 25 shows the Michaelis-Menten kinetics and Lineweaver-Burk diagrams of pseudobrookite nanoparticles in the AR assay. Figure 25A shows the linear relationship between nanoparticle concentration and reaction rate as in previous measurements. Figure 25B shows the reaction rate as a function of the dye substrate concentration. It is noticeable that first an increase in the reaction rate is observed, but then a decrease at concentrations greater than 0.05 mM. It must be assumed that the fluorescent resorufin was further oxidised under the present conditions to the non-fluorescent resazurin. This reduces the measured fluorescence intensity and thus affects the reaction rate. The data of the

measurement series of the variation of the hydrogen peroxide concentration (Figure 25C) shows the expected hyperbolic behaviour. Figure 25D shows the linearised values.

Using the Lineweaver-Burk graph (Figure 25D) the kinetic parameters for hydrogen peroxide could be determined.

Table 14: Kinetic parameters of pseudobrookite nanoparticles obtained from the AR assay with Lineweaver-Burk graphs.

	v_{max} [mM s^{-1}]	K_M [mM]
AR	-	-
H_2O_2	$1.10*10^{-6} \pm 0.01*10^{-6}$	0.588 ± 0.004

The kinetic parameters obtained from Lineweaver-Burk graphs are concluded in Table 14. Kinetic parameters could not be determined for the conversion of AR because the kinetics do not obey the rules of Michaelis-Menten kinetics but presents a linear relationship. The parameters for the conversion of hydrogen peroxide are listed.

It can be summarised that also in this case all three assays led to different results. While the Michaelis-Menten kinetics with variation of the nanoparticle and hydrogen peroxide concentration showed the expected graphical progression, this was not always the case with variation of the dye substrate concentration. The parameters determined are listed in the following table.

Table 15: Kinetic parameters of pseudobrookite nanoparticles obtained from three different peroxidase assays with Lineweaver-Burk graphs.

	v_{max} [mM s^{-1}]	K_M [mM]
ABTS	0.020 ± 0.001	3.6 ± 0.2
TMB	-	-
Amplex™ Red	-	-
H_2O_2 (ABTS)	0.025 ± 0.001	2632 ± 66
H_2O_2 (TMB)	0.009 ± 0.001	487 ± 50
H_2O_2 (AR)	$1.35*10^{-6} \pm 0.02*10^{-6}$	0.487 ± 0.003

Only kinetic parameters concerning the conversion of the ABTS could be determined. When looking at the parameters related to hydrogen peroxide, it is noticeable that the values of the parameters determined from the AR assay are of a completely different order of magnitude than those of the other assays. While values of the same order of magnitude can be determined for v_{max} in the ABTS and TMB assay, the values for K_M of the three assays cannot be more different.

For the pseudobrookite nanoparticles it is not very easy to call one of the assays "the right one" or "the best one". While in the TMB and AR assay it cannot be excluded that parallel to the conversion of the AR to resorufin and the TMB to the charge-transfer complex, further oxidation to resazurin and the diimine occurs, the ABTS assay does not show the desired hyperbolic behaviour of the Michaelis-Menten application by varying the hydrogen peroxide concentration. This shows clearly the importance of always questioning and examining the performed assays in detail.

3.2.7. Comparison of the nanoparticles and the assays

Finally, the question about what can be learned from the previous measurements remains. It could be seen that the hematite nanoparticles allegedly have no activity similar to peroxidase. However, if one uses the correct assay for this type of particle, this catalytic activity can be easily detected in hematite nanoparticles and even expressed in kinetic parameters. In the case of the magnetite and pseudobrookite nanoparticles, all three assays were apparently feasible. In the case of magnetite nanoparticles, it has already been discussed that the ABTS assay is probably the most appropriate assay. In the case of the pseudobrookite nanoparticles none of the assays has been clearly identified. Probably the TMB assay is preferable in this case. The ABTS assay did not show the expected variation in hydrogen peroxide concentration. In the AR assay, the fluorescent product appears to have turned into non-fluorescent resazurin. To continue measuring at the higher hydrogen peroxide concentrations, one would have to switch to UV-Vis measurements and find an agreement between fluorescence and absorption measurements in the evaluation. This is particularly difficult for higher ordered reactions. In addition to the two different measurement methods, it must

also be taken into account that the substrate AR is the most expensive of the three dye educts. At the same time, one would have to work with significantly higher concentrations of the dye for absorption measurements than for fluorescence measurements. The TMB assay has similar problems as the AR assay, that the charge-transfer complex is subject to a reaction to the diimine, but this would be detectable with absorption measurements. In this case, one would not have to use another method, but could carry out further experiments without an additional device. Furthermore, the reaction remains a higher order reaction, which makes the measurements and its evaluation more complex, but is the simpler and cheaper alternative compared to the AR assay.

The following table summarises again all obtained kinetic parameters of the three different nanoparticles and the three different assays.

Table 16: Overview of all determined kinetic parameters of the three nanoparticles (hematite, magnetite, pseudobrookite) regarding the three different assays (ABTS, TMB, AR).

		hematite		magnetite		pseudobrookite	
		v_{max} [mM s^{-1}]	K_M [mM]	v_{max} [mM s^{-1}]	K_M [mM]	v_{max} [mM s^{-1}]	K_M [mM]
ABTS	ABTS	-	-	$6.2*10^{-5} \pm 0.1*10^{-5}$	1.717 ± 0.007	0.020 ± 0.001	3.6 ± 0.2
	H_2O_2	-	-	$3.51*10^{-5} \pm 0.09*10^{-5}$	89 ± 3	0.025 ± 0.001	2632 ± 66
TMB	TMB	-	-	$5.1*10^{-5} \pm 0.1*10^{-5}$	0.116 ± 0.003	-	-
	H_2O_2	-	-	$7.2*10^{-5} \pm 0.3*10^{-5}$	750 ± 3	0.009 ± 0.001	487 ± 50
AR	AR	$1.1945*10^{-7} \pm 0.0007*10^{-7}$	0.2522 ± 0.0002	$1.68*10^{-8} \pm 0.03*10^{-8}$	0.1711 ± 0.0006	-	-
	H_2O_2	$3.21*10^{-8} \pm 0,03*10^{-8}$	0.130 ± 0.006	-	-	$1.35*10^{-6} \pm 0.02*10^{-6}$	0.487 ± 0.003

By looking at Table 16, it becomes clear that none of the three assays performed makes it possible to compare the three types of nanoparticles examined. There is (already strongly limited by the hematite) no assay that provides all desired kinetic parameters for all three nanoparticle types. Comparing the hematite nanoparticles with the pseudobrookite nanoparticles, the AR assay data suggests that the hematite nanoparticles are the ones with the higher affinity for hydrogen peroxide. However, the reaction rate of the hematite nanoparticles is significantly lower with respect to hydrogen peroxide than that of the pseudobrookite. Comparing the magnetite and pseudobrookite nanoparticles with respect to their K_M values relative to hydrogen peroxide in the ABTS and TMB assays, the results cannot be more different. While according to the ABTS assay, the magnetite nanoparticles have the greater affinity for hydrogen peroxide, according to the TMB assay the pseudobrookite nanoparticles have the greater affinity for hydrogen peroxide. However, it can be stated that in the case of the ABTS and TMB assays, all maximum reaction rates determined are in the same order of magnitude. It can also be uniformly stated that the lower K_M values could be determined from both assays with respect to the dye substrates. However, comparable kinetic parameters could not be determined for any nanoparticle type with different assays.

3.3. Conclusion

From the conducted investigations it is clear how critical the results from Michaelis-Menten kinetics performed with nanoparticles have to be considered. All three performed assays have their right to exist - without the AR assay for example the peroxidase-like activity of hematite nanoparticles would not be detectable. However, care must be taken when comparing nanoparticles with each other. The question of subsequent and side reactions within the assay must always be critically examined. The possible interaction of nanoparticles with the substrate or with the resulting product must always be considered. For the comparison of the kinetic performance of nanoparticles within a laboratory all three assays can be useful, but if a comparison with foreign measurement results is to be made, the reaction conditions and the measurement results should be carefully checked.

3.4. Experimentals

3.4.1. Materials

(9*Z*)-Octadecenoic acid (oleic acid, OAc, $C_8H_{34}O_2$, technical grade 90 %, Sigma-Aldrich), 1-octadecene (1-ODE, $C_{18}H_{36}$, technical grade, 90 %, Sigma-Aldrich), 2,2′-azino-bis(3-ethylbenzothiazoline-6-sulfonic acid) diammonium salt (ABTS, $C_{18}H_{24}N_6O_6S_4$, 98 %, Alfa Aesar), 3,3´,5,5´-tetramethylbenzidine (TMB, $C_{16}H_{20}N_2$, ≥99 %, Sigma-Aldrich), acetic acid (CH_3COOH, 100 %, VWR), acetone (C_3H_6O, technical, Sigma-Aldrich), amplifu™ red (AR, $C_{14}H_{11}NO_4$, ≥98 %, Sigma-Aldrich), cyclohexane (C_6H_6, 99.5 %, Fisher), ethanol (C_2H_5OH, 99 %, Fisher), ethylene glycole (EG; $C_2H_6O_2$, anhydrous, 99.8 %, Sigma-Aldrich), hydrogen peroxide (H_2O_2, 35 %, pure, Roth), iron(0) pentacarbonyl ($Fe(CO)_5$, Sigma-Aldrich; >99.99% trace metals basis), iron(II) acetate ($Fe(CH_3COO)_2$, >90 %, TCI), iron(III) chloride hexahydrate ($FeCl_3 \cdot 6H_2O$, 97 %, abcr), oleylamine ($C_{18}H_{37}N$, > 50 %, TCI), potassium dihydrogen phosphate (KH_2PO_4, 99 %, Sigma-Aldrich), sodium acetate ($NaCH_3COO$, >99.5 %, Roth), tetrahydrofurane (THF, C_4H_8O, 99.8 %, Fisher), tetramethylammonium hydroxide ($N(CH_3)_4OH$, 25 wt % in methanol, Sigma-Aldrich), titanium(IV) isopropoxide ($C_{12}H_{28}O_4Ti$, 98 %, Acros).

3.4.2. Synthesis

Synthesis of hematite nanoparticles

Iron(III) chloride hexahydrate (2,7 g, 10 mmol) and potassium dihydrogen phosphate (27,7 mg, 0,2 mmol) were dissolved in water (500 mL) and refluxed for 72 h. After cooling to room temperature the hematite nanoparticles were precipitated with THF and collected *via* centrifugation (9000 rpm, 10 min).[88]

Synthesis of magnetite nanoparticles

A solution containing 1-octadecen (20 mL), oleylamine (4 mL, 12.2 mmol) and oleic acid (4 mL, 12.6 mmol) was heated to 120 °C in 10 minutes. The temperature was hold for 20 minutes. At the end of this period iron(0) pentacarbonyl (0.1 mL, 0.7 mmol) was injected. The solution was heated up to 310 °C in 30 minutes. The temperature was kept constant for 1 hour. After cooling to room temperature by

natural cooling the magnetite nanoparticles were precipitated by adding ethanol and collected *via* centrifugation (9000 rpm, 10 min).

Surface functionalisation of magnetite nanoparticles

Magnetite nanoparticles (50 mg) were dispersed in cyclohexane (10 mL) with the aid of sonification. Tetramethylammonium hydroxide (10 mL) was added and the reaction mixture was treated with sonification for 1 h. The nanoparticles were precipitated by adding acetone and separated via centrifugation (9000 rpm, 10 min). The nanoparticles were redispersed in Milli-Q water (MQW) and washed two more times before using in catalysis experiments.

Synthesis of pseudobrookite nanoparticles

Iron (II) acetate (173.0 mg, 0.1 mmol) was dissolved in ethylene glycol (6 mL) under stirring. Titanium(IV) isopropoxide (0.34 mL, 1.1 mmol) was added dropwise under stirring. The solution was treated with sonification for one hour (Emmi 40HC of EMAG-Technologies with the maximum of power 250 W). The solution was centrifuged (9000rpm, 10 min). The residue was heated up to 600 °C in an electric oven for two hours.[90]

3.4.3. Characterisation and methods

XRD

The powder x-ray diffraction measurements were conducted on a STOE Stadi P X-ray diffractometer of STOE & Cie GmbH (Darmstadt, Germany) equipped with a MYTHEN 1 K detector of Dectris. As radiation source a Mo-K_α cathode was used. The data were analysed by using the software *Match!* 3 with the database COD REV218120 2019.09.10 and plotted with *OriginPro8*.

TEM

The TEM measurements were conducted after applying the sample to a graphite-coated TEM mesh (Cu-300 mesh, Electron Microscopy Sciences, Hatfield, PA) on a Tecnai G2 Spirit from FEI with an acceleration voltage of 120 kV. It is equipped with a twin objective lens, a LaB_6 cathode and a CCD (charge coupled device) camera (2k x 2k). The evaluation was performed with the software *ImageJ*.

For the electron microscopic analysis of the nanoparticles, they were dispersed in ethanol in case of the hematite and pseudobrookite nanoparticles, and in case of the magnetite nanoparticles in cyclohexane after synthesis but before the surface functionalisation was executed with the aid of sonification (concentration 1 mg mL^{-1}). 20 µL of the sample were applied to a TEM grid. After evaporation of the solvent at room temperature the samples were measured.

High resolution TEM (HR-TEM)

HR-TEM measurements were carried out with a FEI TECNAI F30 S-TWIN transmission electron microscope equipped with a field emission gun and working at 300 kV. TEM images were taken with a CCD camera (16-bit 4.096 x 4096 GATAN ULTRASCAN4000) and acquired by Gatan Digital Micrograph software.

BET

The BET surfaces of the used nanoparticles were measured with a 3P Micro 300 (3P Instruments). For this the nanoparticle samples were dried under vacuum. Nitrogen was used as measuring gas. The data was analysed using the software Surface Area & Pore Size Analyser System (Version: 10.03.02).

UV-Vis

The scanning kinetic measurements using ABTS and TMB as well as the scan measured of the nanoparticle samples were conducted on a Varian Cary5G UV/Vis spectrometer between 200 nm and 800 nm.

The Michaelis-Menten kinetic measurements were conducted on an Agilent Cary3500 UV/Vis spectrometer.

ABTS and TMB Assay

Scanning kinetics: Solutions were used with following concentrations: acetate buffer 0.2 M, pH 4.2, ABTS 10 mM in MQW, TMB 10 mM in DMSO, nanoparticle dispersion in water 1 mg/mL, hydrogen peroxide 35 %. The measurements were executed with a total volume of 3000 µL in a quartz glass cuvette with a thickness of 1cm. First the acetate buffer (2550 µL) was mixed with ABTS or TMB (250 µL) and the nanoparticles dispersion (magnetite and pseudobrookite nanoparticles,

100 µL) and homogenised by stirring. With adding hydrogen peroxide the measurement was started.

In the case of hematite nanoparticles two different amounts of nanoparticles were tested. The acetate buffer (2500 µL) was mixed with ABTS or TMB (150 µL) and the nanoparticle dispersion (150 µL or 50 µL), before the reaction was started by adding hydrogen peroxide (150 µL).

Michaelis-Menten kinetics: The Michaelis-Menten kinetic measurements were conducted by using the solutions described above.

First the acetate buffer was mixed with the nanoparticle dispersion before the dye substrate was added. Under stirring hydrogen peroxide was added and the measurement was started. The measurements were conducted for 5 minutes. For analysis only the measurements after 50 s were used because first an equilibrium had to be reached.

The amount of nanoparticles was varied keeping the amount of hydrogen peroxide (magnetite nanoparticles: 0.29 M, pseudobrookite nanoparticles: 0.87 M) and ABTS/TMB (magnetite nanoparticles: 1.25 mM, pseudobrookite nanoparticles: 2.5 mM) constant. While varying the amount of ABTS/TMB the amount of nanoparticles (50 µg) and hydrogen peroxide (magnetite nanoparticles: 0.29 M, pseudobrookite nanoparticles: 1.2 M) was kept constant. When the amount of hydrogen peroxide was varied the amount of nanoparticles (50 µg) and substrate dye was kept constant (magnetite nanoparticles: 1.25 mM, pseudobrookite nanoparticles: 2.5 mM).

The measurements with ABTS were executed at a wavelength of 420 nm, in case of TMB at 370 nm.

The data were fitted linear with Origin and the received slope was used for further calculations on the base of the Lambert-Beer equitation. The extinction coefficient of TMB at 370 nm was calculated with the measured scanning kinetic measurements.

AR Assay

The Michaelis-Menten kinetic measurements using AR were conducted on an Infinite 200 Pro plate reader from TECAN. Additionally, flat bottom black 96-well plates from Greiner bio-one were used for the assay. The excitation filter was set to 550 nm while the emission filter was set to 590 nm. The emission band width was set to 9 nm.

First the PBS buffer was mixed with the nanoparticle dispersion before the dye substrate was added. Hydrogen peroxide was added and the measurement was started. The measurements were conducted for 1 hour in the case of hematite nanoparticles and 15 minutes in the case of magnetite and pseudobrookite nanoparticles.

The amount of nanoparticles was varied keeping the amount of hydrogen peroxide (0.35 mM) and AR (50 µM) constant. While varying the amount of AR the amount of nanoparticles (25 µg) and hydrogen peroxide (0.35 mM) was kept constant. When the amount of hydrogen peroxide was varied the amount of nanoparticles (25 µg) and substrate dye was kept constant (50 µM).

3.5. Appendix

BET measurements

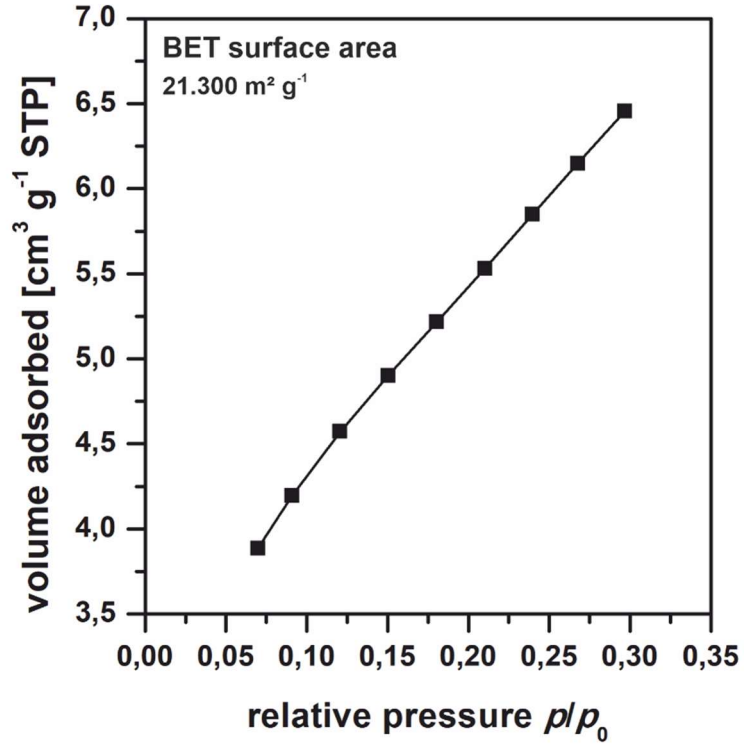

Supporting figure 1: BET measurement of hematite nanoparticles.

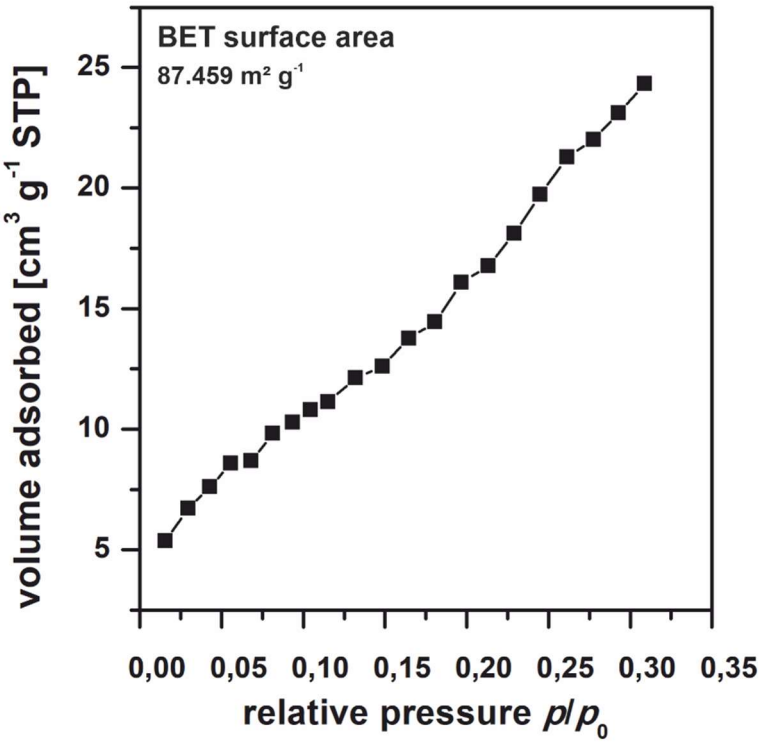

Supporting figure 2: BET measurements of magnetite nanoparticles.

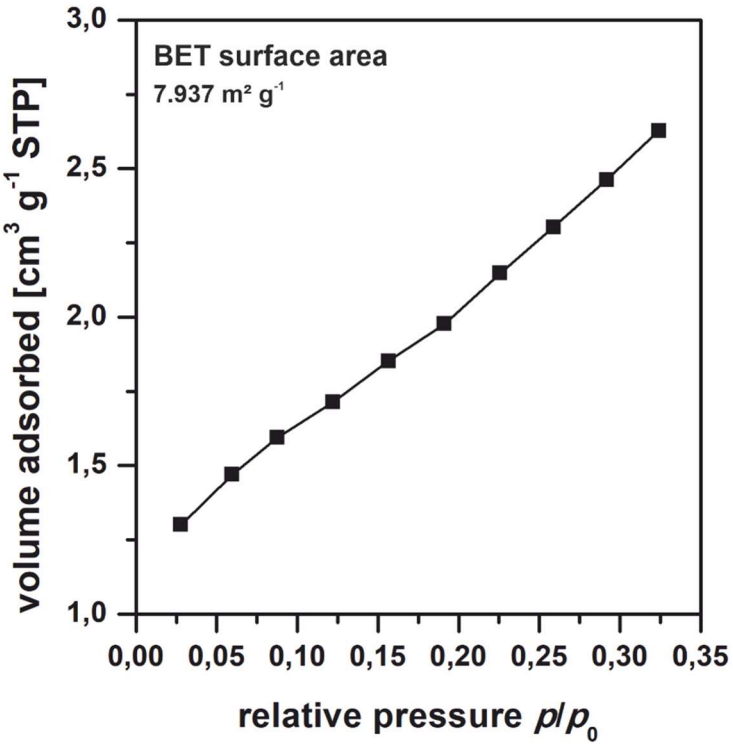

Supporting figure 3: BET measurements of pseudobrookite nanoparticles.

Reaction cascade | 4

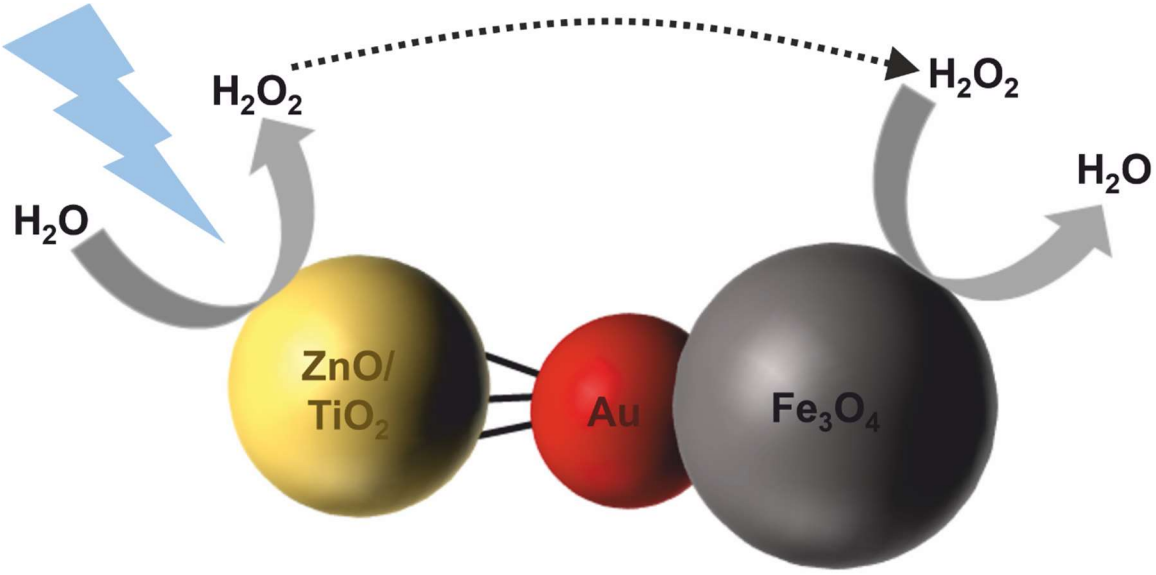

This chapter deals with the synthesis of nanoparticles with enzyme-like activity, their surface functionalisation and the formation of heterotrimeric nanoparticles to set up a reaction cascade. A bifunctional ligand with terminal thiol- and dopamine group is synthesised to connect gold–zinc oxide (Au@ZnO) Janus particles with iron(II,III) oxide (Fe_3O_4) nanoparticles, as well as gold-iron(II,III) oxide (Au@Fe_3O_4) Janus particles with titanium dioxide (TiO_2) nanoparticles.

4.1. Theoretical background

This chapter deals with the catalytic properties of Fe_3O_4 nanoparticles compared to Au@Fe_3O_4 Janus particles. For this purpose, both particle types are synthesised and their intrinsic peroxidase activity properties are compared in a TMB assay with the goal to investigate the influence of the gold domain on this property. In addition, TiO_2 and ZnO nanoparticles are investigated in respect to photocatalytic hydrogen peroxide (H_2O_2) production in aqueous medium. Furthermore the photocatalytic activity of ZnO nanoparticles will be compared to Au@ZnO Janus particles. A bifunctional ligand was synthesised *via* a multi-step organic synthesis, which will then be used to bring the Au@Fe_3O_4 Janus particles and the TiO_2 nanoparticles into close proximity to each other, as well as the Au@ZnO Janus particles and the Fe_3O_4 nanoparticles described in 3.2.3 and 3.2.4. Subsequently, a reaction cascade is imitated in which hydrogen peroxide is produced photocatalytically by ZnO respectively TiO_2 nanoparticles, this reaches the Fe_3O_4 domain of the nanoparticle system by diffusion and is converted due to the intrinsic peroxidase activity. In the following the theoretical basics of this chapter will be presented first. This includes a section on nanoparticles in general, especially Janus particles and finally a section on photocatalysis in general and photocatalytic hydrogen peroxide production using nanoparticles.

4.1.1. Nanoparticles

In general, nanoparticles can be produced by two different methods: the top-down and the bottom-up method (Figure 26).[91] In the top-down method, nanoparticles are produced from bulk materials using mechanical methods. For example, high-energy mills are used to grind particles with sizes from millimetres to micrometres into particles with sizes in the nanometre range. The bottom-up synthesis on the other hand is a chemical-physical method in which nanoparticles are generated from precursor compounds *via* atoms and molecules. E.g. this is done by thermal decomposition or redox chemical processes. The atoms or molecules assemble to form aggregates (self-organisation), which can be successively enlarged in a growth phase.[92] The theory of nanoparticle formation using the bottom-up method can be described with the *LaMer* model.

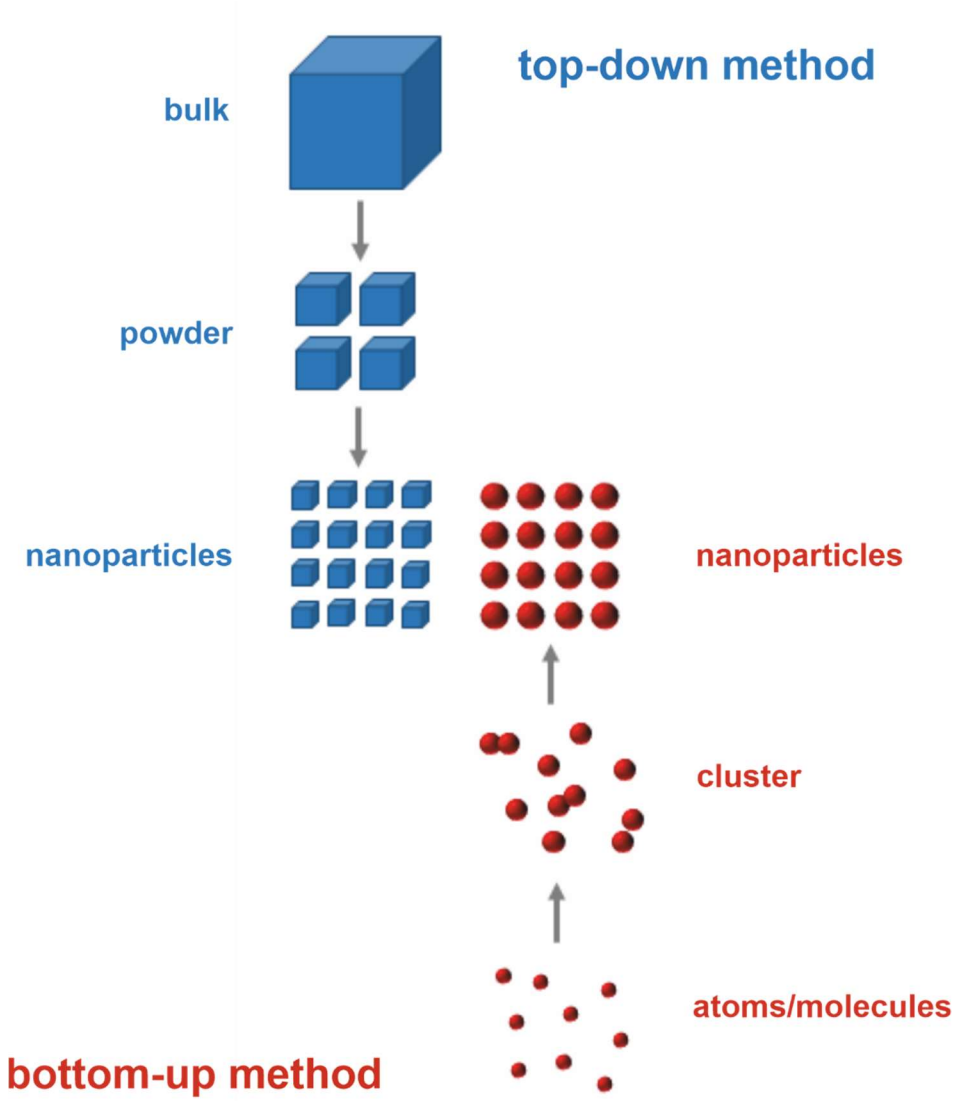

Figure 26: Schematic representation of the top-down (blue) and bottom-up method (red) for the synthesis of nanoparticles.

The advantages of the bottom-up method compared to the top-down method are that monodisperse nanoparticles can be obtained, which size can be better adjusted. Since monodispersity is often a desired goal, this strategy is very often used for the synthesis of nanoparticles. This method can be applied in gas phase or liquid phase, including precipitation processes, sol-gel processes and hydrothermal syntheses.[92]

LaMer-Modell

In 1950 *LaMer* presented a model of nucleation and growth mechanisms based on the study of monodisperse sulphur hydrosols, which is still used today as the basis for studying nucleation processes.[93] This model can be applied to many chemical

processes, such as crystallisation, but also to the synthesis of nanoparticles using the bottom-up method.

The *LaMer*-model provides three different phases: generation of atoms, nucleation phase and growth phase.

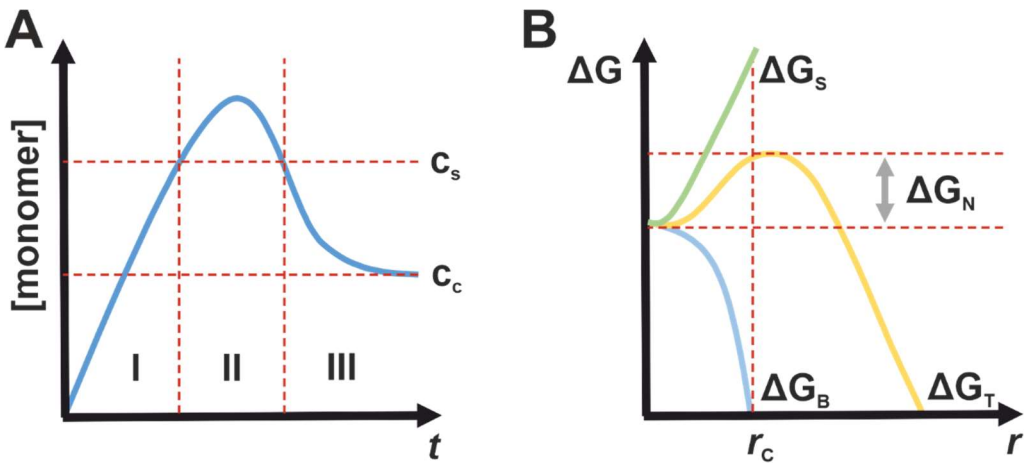

Figure 27: Schematic representation of the *LaMer* model; A: Phases of nanoparticle formation as a function of time and precursor concentration. B: Dependence of free Gibb's enthalpy on the size of the nucleus.

Figure 27A shows the monomer concentration as a function of time: In phase I atoms are generated from a precursor. Here the concentration of atoms rises and with continuous reaction progress the critical concentration c_c gets exceeded. Small unstable seeds are formed, which can dissolve again.[94] As the formation of atoms progresses, the saturation concentration c_s is exceeded and the transition to phase II takes place, in which stable particle nuclei are formed. Nucleation reduces the monomer concentration until it falls below the saturation concentration again. In phase III, the growth phase, atoms only nucleate on already formed nuclei and thus contribute to the growth of the nanoparticles.

Figure 27B shows the different free Gibb´s enthalpies involved in the process described by *LaMer* as a function of the radius *r* of the formed particles. ΔG_T represents the total free energy of the nucleation process and is composed of the sum of the free volume energy ΔG_B and the surface energy ΔG_S, with σ as surface energy.

$$\Delta G = -\Delta G_B \frac{4}{3}\pi r^3 + \sigma 4\pi r^2 \qquad \textbf{(9)}$$

ΔG_B decreases with increasing radius of the particles.

ΔG_S increases with increasing particle radius, since interfaces between two different phase states, in this case solid and liquid, require a lot of energy. This leads to the fact that formed nuclei can dissolve in favour of the liquid phases.[88,95,96]

Monodisperse nanoparticles are obtained if the nucleation combined with a high nucleation rate can be strictly separated from the growth phase, the progress which should be slow.[93,97]

Gold nanoparticles

Gold nanoparticles are of particular research interest due to their wide range of applications. In addition to their electronic application as conductors, they are also used in medicine by connecting drugs to their surface and using the gold nanoparticles themselves as transport systems.[98,99]

In addition to their wide range of applications, they are characterised by their variable size and their possible different morphologies. Examples of the morphology of gold nanoparticles are rods, cubes, octahedra or tetrahedra.[100] The morphology and the size of the nanoparticles have a great influence on their optical properties.[101] Figure 28 shows the change in the optical colour perception of spherical gold nanoparticles as a function of their size.

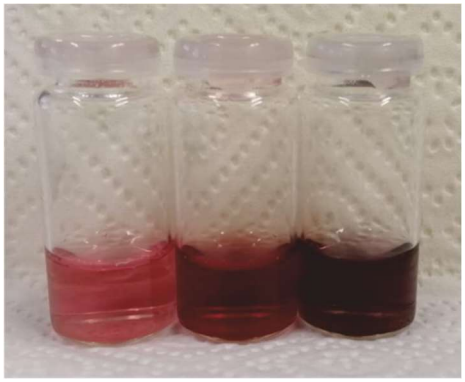

Figure 28: Gold nanoparticles and their optical colour perception with increasing diameter (from left to right) of the nanoparticles.

In the following, the structural and plasmonic properties of gold and the corresponding nanoparticles will be discussed.

Elemental gold crystallises in a face-centred cubic (fcc) structure. Since the underlying coordination polyhedron of the structure is the cube, it follows that the

sides a, b and c have the same length, with the gold specific lattice constant 4.08 Å and the angles α, β and γ are all 90 °.[102]

In the 4th century AD, the Romans made the so-called Lycurgus cup from ruby glass containing colloidal gold. The gold particles contained in the glass have a size of approximately 5 nm - 60 nm. About a special property of this cup is that it appears green in reflection, but red in transmission. This phenomenon is called dichroism.[103] The green appearance is caused from light, reflected from the cup due to Rayleigh scattering from the surface of the gold nanoparticles. Here, green light is scattered preferred compared to the rest of the light, which causes a green appearance of the cup.[103] The red colour of the cup in transmission is caused by the absorption of the green light, by the plasmon oscillation of the embedded gold nanoparticles. Thus, the cup appears in the complementary colour red. Mie first described the phenomenon of plasmons in 1908 with the Mie theory.[104]

Plasmons are a physical phenomenon and are created if electromagnetic radiation interacts with delocalised charge carriers in a metal. In this process, electrons (Au: $6s^2$) are excited from the conduction band to an energetic level directly above the Fermi level. Here they oscillate parallel to the metal surface. This is known as surface plasmon resonance (Figure 29).[105]

The surface plasmon resonance is dependent on the medium in which the nanoparticles are located, as the medium has an effect on the refraction of the light. A surface plasmon resonance can only be observed if the dispersion curves of the excited light and the surface plasmons intersect. The condition for resonance can be formulated as follows:

$$\varepsilon'(\lambda_{SPR}) = -2\varepsilon_m(\lambda_{SPR}) \quad \textbf{(10)}$$

λ_{SPR} corresponds to the wavelength of the surface plasmon resonance, ε' to the real part of the description of the dielectric function of a material, which is a proportion of the polarisation of this material by an external electric field, and ε_m to the dielectric constant of the medium.[106]

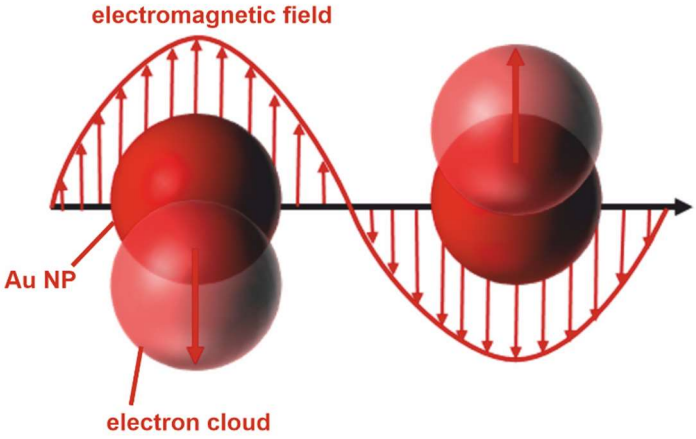

Figure 29: Schematic representation of surface plasmon resonance. The interaction of the metal nanoparticles with electromagnetic radiation excites the electrons and raises their energy above the Fermi level, where they oscillate parallel to the metal surface. Based on [107].

Gold nanoparticles have a strong absorption in the visible range of the light spectrum due to the absorption by the surface plasmons. Here the absorption maximum is typically between 510 nm and 540 nm.[106] At the same time, the intensity of the absorption depends on the size of the nanoparticles. The larger a gold nanoparticle is, the greater the electron density in the nanoparticle is. At the same time, a bathochromic shift of the absorption maximum is observed with the enlargement of the nanoparticles, starting from an approximate diameter of 20 nm.[108] This can be explained by the fact that for gold nanoparticles smaller than 20 nm, light absorption is dominated by extinction, whereas for gold nanoparticles larger than 20 nm, light scattering dominates.[109]

Since surface plasmon resonance is typical for gold nanoparticles, UV-Vis spectroscopy is a good method for characterising gold nanoparticles. In addition to UV-Vis spectroscopy, the measurement of fluorescence lifetime is also a suitable method for investigating the emission of gold nanoparticles.

Iron(II,III) oxide nanoparticles

Iron(II,III) oxide nanoparticles (Fe_3O_4 nanoparticles) have been extensively researched for a long time due to their morphological variability and their wide range of applications. In addition to spherical Fe_3O_4 nanoparticles, cube-shaped Fe_3O_4 nanoparticles have been synthesised.[73,74] These nanoparticles are used in biomedicine as magnetic resonance imaging contrast agents, tissue-specific drug delivery systems and in hyperthermia treatment.[110,111]

Iron(II,III) oxide (Fe_3O_4) or magnetite crystallises in the inverse spinel structure. The lattice constant is 8.35 Å.[102] This structure was derived from the naturally occurring mineral magnesium aluminate $MgAl_2O_4$, the spinel.[112] In the spinel structure type AB_2X_4, the X atoms form a cubically tight spherical packing. In the case of magnetite, the cubically densest sphere packing is spanned by the oxygen atoms. The normal spinel structure differs from the inverse spinel structure with regard to the arrangement of the cations within the lattice. While in the spinel structure half of the octahedral gaps are occupied by trivalent cations and one-eighth of the tetrahedral gaps are occupied by divalent cations, in the inverse spinel one quarter of the octahedral gaps are occupied by divalent cations and one quarter by trivalent cations, in this case Fe^{2+} and Fe^{3+}. One eighth of the tetrahedral gaps are occupied by trivalent cations, in the case of magnetite by Fe^{3+}.[27]

Magnetite is an inverse spinel in which two sublattices are distinguished within the fcc lattice spanned by the oxygen ions. One lattice is spanned by the trivalent iron ions, which are located in tetrahedral gaps. The other lattice is spanned by both divalent and trivalent iron ions located in octahedral gaps. Within one lattice, the spins are all aligned parallel to each other, while the spins of both lattices are aligned antiparallel to each other. The magnetic moments of the two lattices are different, resulting in a total moment. Ferrimagnetism is characteristic of spinels and thus also of the inverse spinel Fe_3O_4.[27]

Below the Curie temperature T_C, spin moments of different sizes in ferrimagnetic systems couple antiparallel within the Weiss domains, which are small magnetised domains, while above T_C this coupling disappears completely. Spin coupling results in a magnetic moment, so spontaneous magnetisation occurs, but due to the statistical distribution of magnetic moments, this only occurs if an external field is applied.[27]

In the case of nanoparticles, magnetism is size-dependent as the Weiss domains decrease with decreasing nanoparticle diameter till the whole particle can be considered as one Weiss domain for very small nanoparticles. If this size is reached, nanoparticles behave like superparamagnets.[91]

Titanium(IV) oxide and Zinc(II) oxide nanoparticles

Titanium dioxide is known in three morphologies: the thermodynamic stable rutile modification and the two metastable modifications anatase and brookite. All three modifications consist of octahedral [TiO_6]-units, which are connected differently dependent on the modification.[91] While rutile and anatase exhibit a tetragonal structure, brookite has an orthorhombic structure.[113] Brookite and rutile show a direct band gap, while anatase shows an indirect band gap, because a direct transition is not possible. A direct semiconductor is characterised by a possible direct transition of an electron from the valence band minimum to the conduction band maximum. This is not possible with an indirect semiconductor. Here, an additional impulse, usually in the form of a phonon, must be transmitted. A direct combination between electrons from the conduction band with holes of the valence band is not possible, which increases the lifetime of an electron-hole pair. The longer lifetime of the photoexcited electrons in case of anatase lead to a higher photocatalytic activity compared to the other two modifications.[114,115] The following band gaps have been published for the nanoparticles of the three titanium dioxide modifications: rutile 3.00 eV, brookite 3.13 eV and anatase 3.21 eV.[116] For more details regarding photocatalysis see 4.1.2.

Zinc oxide (ZnO) is known as zincite in nature which crystallises in wurtzite structure. ZnO is a semiconductor with a band gap of 3.4 eV.[117] It is used in sun creams as a UV blocker as well as in medicine for antiseptic applications or as pigment.[27,91,117] ZnO can be decomposed in unbuffered aqueous solution by light exposure because the anodic dissolution potential is lower than the water oxidation potential and it lies inside the band gap.[118] ZnO is soluble at low pH.[118] ZnO nanoparticles are well-known for their antibacterial properties. This effect is caused by electrostatic interactions, internalization into bacteria, Zn^{2+} release and ROS formation. The ROS formation is a photo induced process (see Figure 31 at section 4.1.2).[119]

The photocatalytic properties of TiO_2 and ZnO nanoparticles will be used in this chapter for photocatalytic production of hydrogen peroxide. In a further step the H_2O_2 will be destroyed by peroxidase mimics. The photocatalysis will be explained in detail in 4.1.2.

Janus Particles

Inspired by the two-headed figure of the Roman god Janus, *Veyssié* named amphiphilic glass spheres in 1989 as Janus spheres, which he defined as follows: "A Janus sphere is a spherical particle whose surface is half hydrophilic and half hydrophobic."[120] In 1991 *De Gennes* described Janus particles as spherical particles whose hemispheres are chemically different from each other. Today Janus particles are known in many different morphological forms. Of particular interest for research are Janus particles, which are often referred to in the literature as hetero nanoparticles, dumbbell-shaped and snowman-shaped nanoparticles, mainly due to the possibility of combining the properties of two different nanoparticles (magnetic, electrical, semiconductive, optical, optoelectronic, or catalytic properties).[121–123] They are mainly discussed for applications as optical agents in biological applications and rheological measurements, but also as catalysts and drug delivery systems in the field of nanomedicine.[124] *Schick* has already worked extensively on the synthesis of inorganic heterodimers, including Au@Fe_3O_4 Janus particles. She also investigated the functionalisation of the gold domain with mercapto compounds and the iron(II,III) oxide domain with silica.[81] On the basis of this preliminary work, the nanoparticle system for the imitation of a reaction cascade is to be developed in the present work.

The synthesis of Janus particles requires the adjustment of a very precise balance between thermodynamic and kinetic control of the reaction to obtain defined sizes and morphologies of the individual domains.[122] In addition, there are other influencing factors, such as atomic diffusion, facet-specific reactivity and the influence of interfacial strain.[125] Two different methods are often used to synthesise Janus particles. One method aims to chemically modify a manufactured nanoparticle in such a way that only one part of its surface is available for the synthesis of a Janus particle, for example by functionalising the nanoparticle surface or immobilising the nanoparticles on a horizontal surface. The other method is based on the nucleation of atoms on the nanoparticle and the subsequent epitaxial growth of the second component.[123] Since the second method is used in the present study, it should be added at this point that the heterogeneous nucleation on a submitted nanoparticle only occurs in comparison to a homogeneous nucleation if the concentration of the precursor of the second

component never reaches the supersaturation described in the *LaMer*-model and ΔG_S is negative.[93,102,126]

4.1.2. Photocatalysis

As heterogeneous photocatalysts, semiconductors are very interesting for power generation and the catalysis of photoinduced reactions. Heterogeneous photocatalysts are able to generate and separate charge carriers. This can be used in some areas.[127] In the following, the photocatalysts titanium dioxide and zinc oxide are explained and a short introduction to the band model is given.

For a better understanding of the heterogeneous photocatalysis one has to take a short look at the band model: In the band model, metals, semiconductors and isolators are distinguished from each other, with non-metals belonging to the last two categories. In the band model a distinction is made between the valence band (VB) and conduction band (CB). Also important is the Fermi energy, which indicates the highest energy level occupied by electrons in a solid state.[128] In the case of a conductor, there is no energetic difference between VB and CB. The band is partly filled with electrons, so that their mobility but also the charge transport is guaranteed. In the case of a semiconductor, the energy difference between VB and CB can be approximately between 0.5 eV and 1.5 eV. Up to the Fermi energy all bands are fully occupied. By thermal excitation electrons can be excited from the VB into the CB. In an isolator, however, the energy difference between VB and CB is more than 3 eV. Excitation of electrons from VB into CB is not possible.[129]

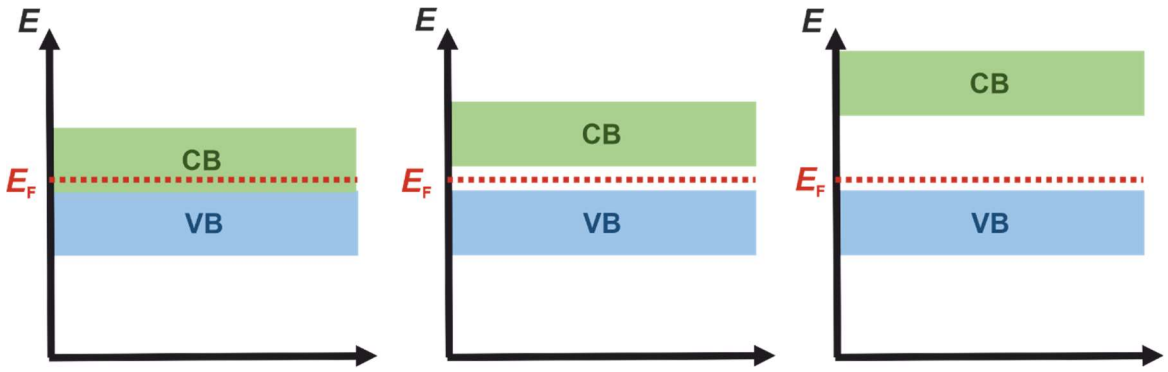

Figure 30: Schematic representation of the band structures of metal, semiconductor and isolator. Based on [129].

According to the definition explained above, all three modifications of titanium dioxide belong to the isolator category, but there are numerous publications on different titanium dioxide modifications with photocatalytic properties. This makes clear that the band gap limits mentioned are not necessarily fixed values, but rather rough guide values.

In this work, the photocatalytic generation of hydrogen peroxide is of great importance, which is shown schematically in the following figure.

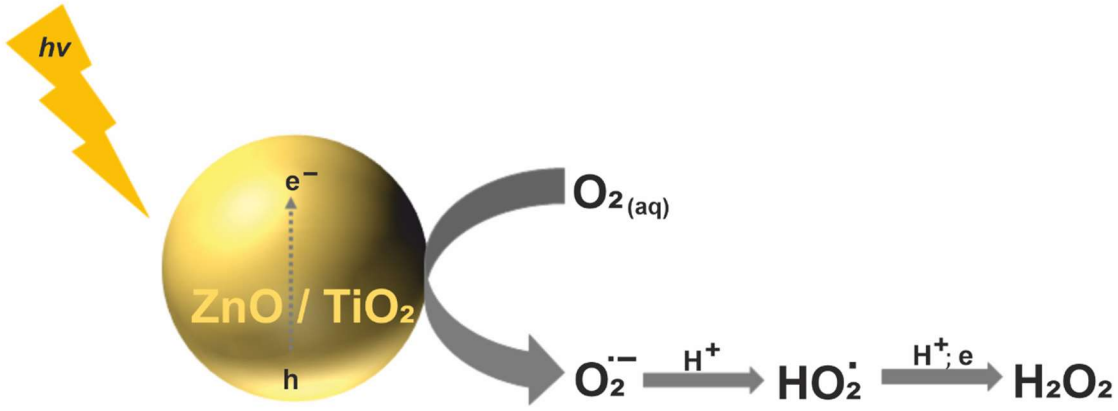

Figure 31: Schematic representation of photocatalytic hydrogen peroxide production using titanium dioxide nanoparticles in aqueous solution. Based on [130].

It has been reported that the photochemical production of hydrogen peroxide catalysed by TiO_2 and ZnO nanoparticles in aqueous solution occurs *via* the oxidation of dissolved oxygen. In this process, superoxide radical anions are generated, which are protonated in aqueous solution to form peroxo radicals. These radicals are converted to hydrogen peroxide in a further oxidation in aqueous solution. This reaction cascade will be used in the present work to produce one of the reactants required for the peroxidase reaction in situ.

4.2. Results and discussion

A heterotrimeric nanoparticle should be synthesised to mimic a reaction cascade. This was to be achieved by a combination of heterogeneous nucleation of one compound onto the surface of another nanoparticle and epitaxial growth to form a heterodimer. Afterwards surface functionalisation with a bifunctional ligand would led to a heterotrimeric nanoparticle system.

The challenge at this point was the choice of a reaction cascade that can be performed selectively and specifically. The disadvantage of nanoparticles is often that they are able to catalyse several different reactions. Therefore, the reaction cascade was chosen in a way that two different catalysis mechanisms were combined in one system. In the first step, titanium dioxide (TiO_2) nanoparticles (NPs) in the anatase modification should produce hydrogen peroxide photocatalytically. This should then be converted or decomposed by means of a redox catalysis. Magnetite nanoparticles, which have long been known for their peroxidase activity, were chosen.

First, Janus particles (JPs) consisting of gold (Au) and magnetite as well as consisting of Au and zinc oxide (ZnO) were synthesised. *Via* surface functionalisation with the aid of a bifunctional ligand, which was completely elucidated by nuclear magnetic resonance (NMR) spectroscopy, these Janus particles should be brought into close proximity with TiO_2 nanoparticles or rather Fe_3O_4 nanoparticles to build a heterotrimeric nanoparticle system.

4.2.1. Synthesis and characterisation of Au@Fe_3O_4 Janus particles

In the following chapter, the synthesis of Au@Fe_3O_4 Janus particles will be discussed, starting with the synthesis of Au nanoparticles and their characterisation. After the physical characterisation of Au@Fe_3O_4 Janus particles, their catalytic activity respective the peroxidase reaction will be discussed in comparison to the catalytic activity of magnetite nanoparticles (see 3.2.4).

Synthesis and characterisation of Au nanoparticles

Au nanoparticles were synthesised as described *Peng et al.*, with some modifications.[108] Briefly, hydrogen tetrachloroaurate(III) hydrate was dissolved in cyclohexane and oleylamine and stirred under argon. A solution containing borane-*tert*-butylamine-complex, cyclohexane and oleylamine was added and the solution was stirred for two hours. The characterisation of the obtained Au nanoparticles is concluded in Figure 32.

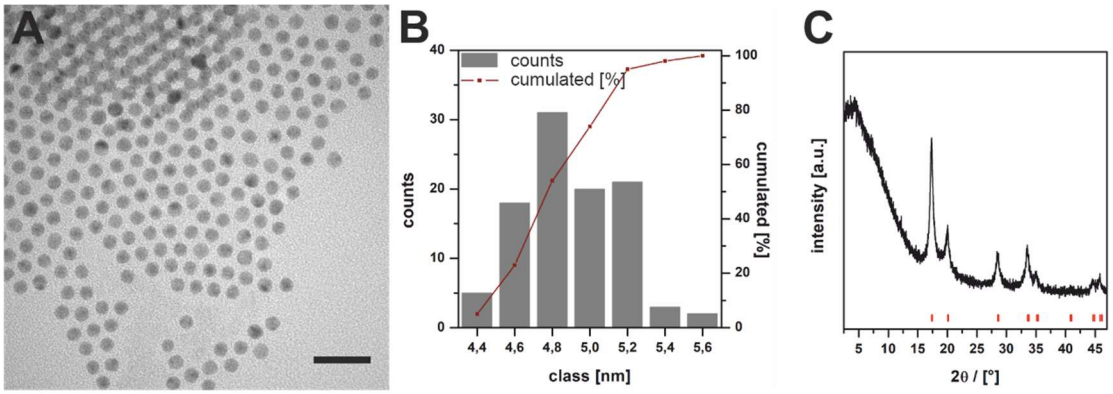

Figure 32: Characterisation of Au NPs. A: Typical TEM image of Au NPs. (scale bar 2 nm) B: Histogram of Au NPs. C: XRD pattern of Au NPs. (JCDPS card: 96-110-0139)

Figure 32 shows a typical TEM image of Au nanoparticles obtained from the synthesis route described above. The histogram shows the size distribution of the nanoparticles, which have a mean diameter of 4.8 ± 0.3 nm. The XRD pattern (Figure 32C) confirms gold as the only existing phase of the nanoparticles.

The absorption properties will be considered later in comparison to the Janus particles.

The Au nanoparticles were used as template for heterogeneous nucleation of iron(II,III) oxide to synthesise Au@Fe_3O_4 Janus particles.

Synthesis and characterisation of Au@Fe_3O_4 Janus particles

The Au@Fe_3O_4 Janus particles were synthesised by a hot injection method. Here Au nanoparticles were dispersed in 1-octadecene and mixed with oleic acid and oleylamine. The reaction mixture was heated up to 120 °C in 10 minutes. After this temperature was kept constant for 30 minutes iron(0) pentacarbonyl was injected and the temperature was increased to 310 °C. The temperature was kept constant

for one hour. After cooling to room temperature the nanoparticles were precipitated and washed.

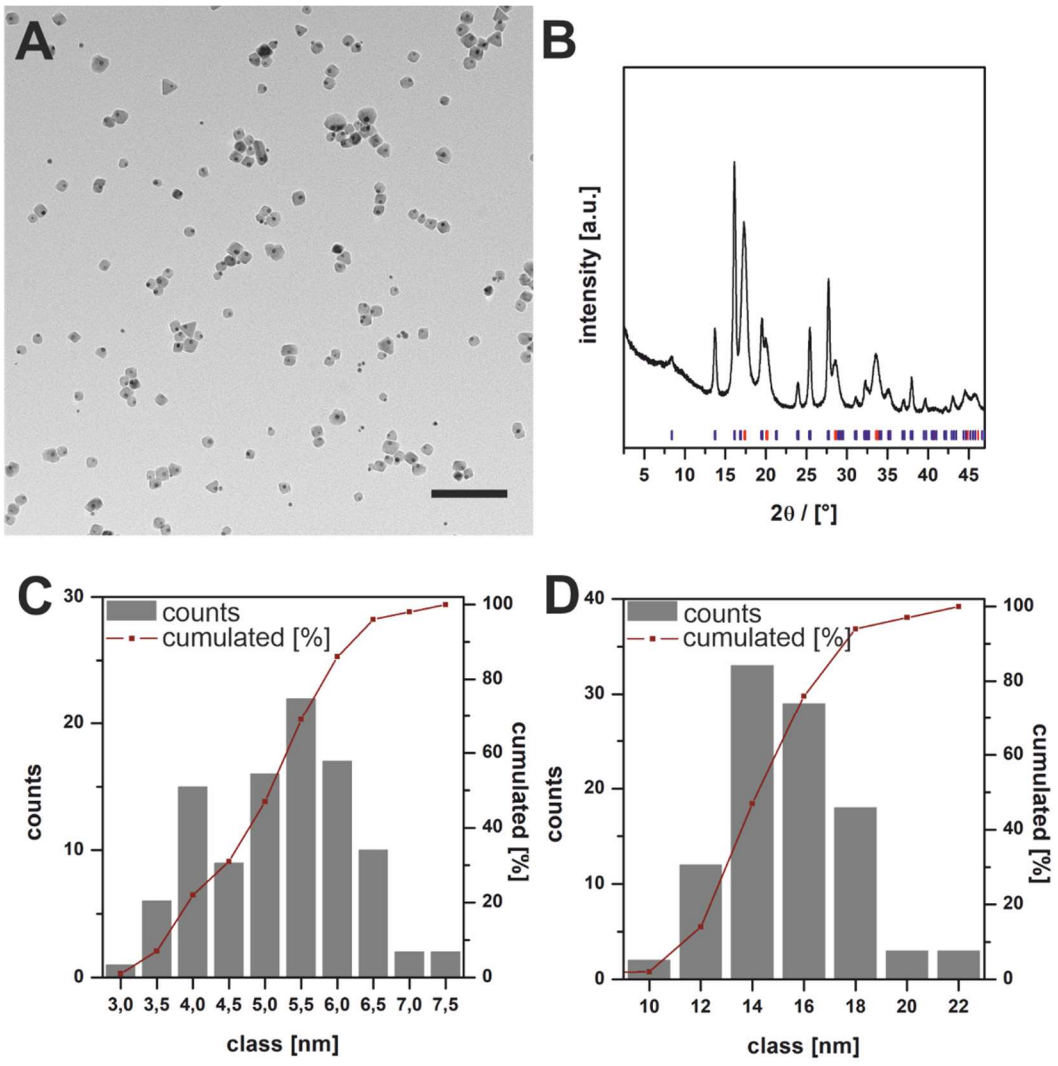

Figure 33: Characterisation of Au@Fe_3O_4 Janus particles. A: TEM image of Au@Fe_3O_4 Janus particles (scale bar 100 nm). B: XRD pattern (black) with literature reflexes (red – gold, blue – iron(II, III) oxide; JCDPS cards: 96-110-0139 and 96-900-2317). C: Histogram of Au domain of Janus particles (grey columns: counts, red line: cumulated [%]). D: Histogram of Fe_3O_4 domain of Janus particles (grey columns: counts, red line: cumulated [%]).

Figure 33 illustrates the analytic data of Au@Fe_3O_4 Janus particles. The TEM image (Figure 33A) shows the Janus particles and a few Au nanoparticles, on which no Fe_3O_4 domain is grown. The morphology of the Fe_3O_4 domains is not uniform. Some domains are more spherical, other more angled. The size distributions of both domains are shown in Figure 33C (Au) and D (Fe_3O_4). The Au domain is partly smaller and partly bigger than described in Figure 32. It can be expected that Ostwald ripening happened while heating the reaction mixture, before the nucleation process is occurred. The diameter of the Au domain is in

mean 5.0 nm ± 1.0 nm. In comparison to the Au nanoparticles in Figure 32, the domain is bigger and the deviation is also bigger. The dispersity of the Au domain is bigger than the dispersity of the isolated Au nanoparticles. The Fe_3O_4 domain has a mean size of 14.0 nm ± 2.0 nm and is smaller than the Fe_3O_4 nanoparticles synthesised with the same synthesis route without adding Au nanoparticles described in 3.2.3. The XRD pattern (Figure 33B) confirms the existence of the Au and Fe_3O_4 phase.

Additionally UV-Vis spectra of the Au nanoparticles and the Au@Fe_3O_4 Janus particles were measured, since Au nanoparticles are well known for their optical properties.

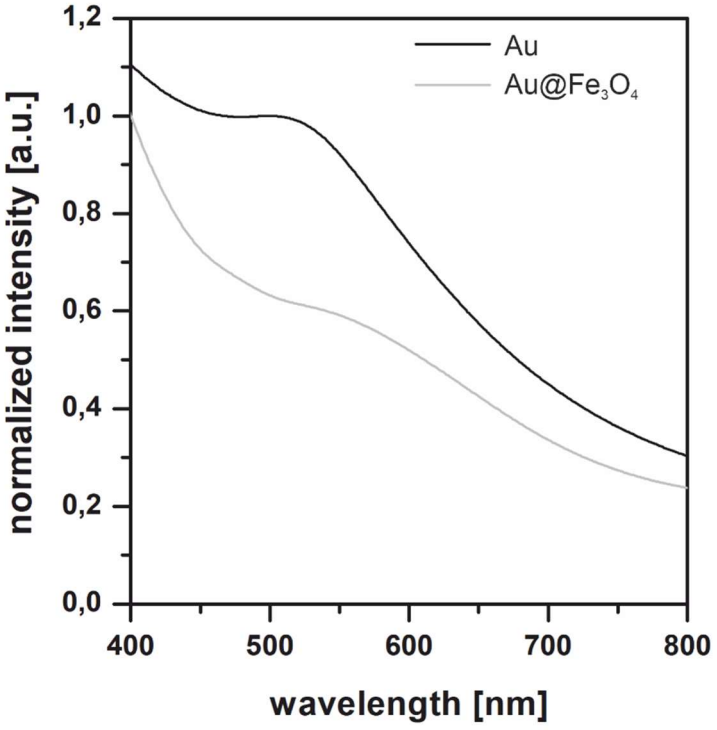

Figure 34: UV-Vis spectra of Au nanoparticles and Au@Fe_3O_4 Janus particles.

The absorption maxima of the Au nanoparticles could be detected at 502 nm, while the absorption maximum of the Au@Fe_3O_4 Janus particles is detectable at 555 nm and is clearly compressed. This bathochromic shift can be explained with electronic interaction. The Fe_3O_4 domain, which is grown on the Au nanoparticles causes an electron deficit in the Au domain. Since these electrons are essential for the plasmonic properties of the Au nanoparticles, this effect is minimised.

Kinetic properties of Au@Fe_3O_4 Janus particles

In the following the kinetic properties of Au@Fe_3O_4 Janus particles are discussed respective their peroxidase-like activity in comparison to Fe_3O_4 nanoparticles, already discussed 3.2.4 synthesised with the same synthesis approach as the Janus particles.

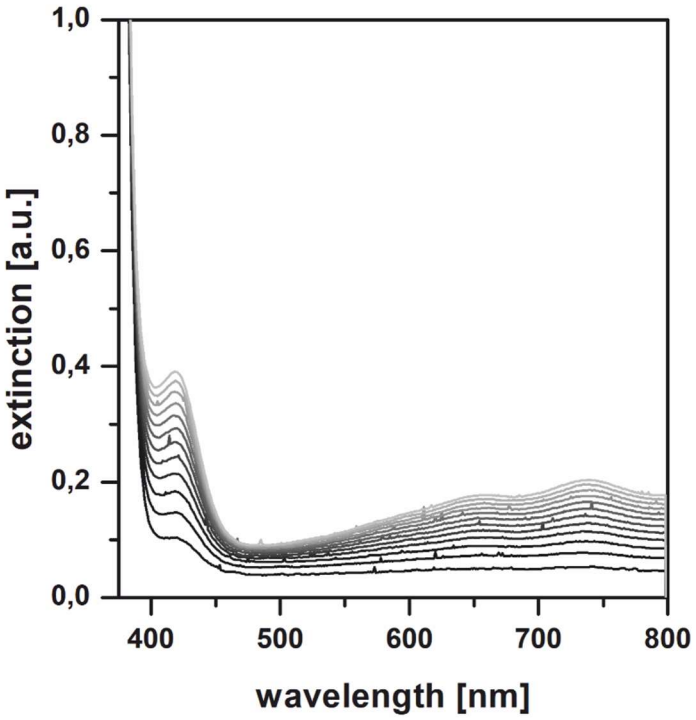

Figure 35: Scanning kinetics of Au@Fe_3O_4 Janus particles mimicking the enzyme peroxidase in an ABTS assay.

The scanning kinetic measurement of Au@Fe_3O_4 Janus particles in the ABTS assay confirms the expected peroxidase-like activity of the Janus particles. To determine the kinetic parameters K_M and v_{max} a Michaelis-Menten kinetic study was executed (see Figure 36).

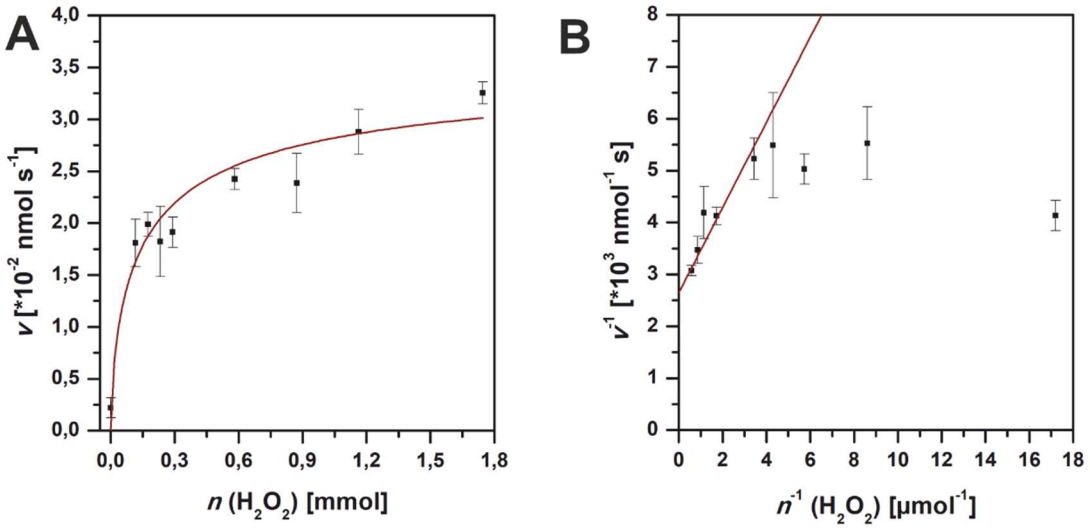

Figure 36: Michaelis-Menten (A) and Lineweaver-Burk (B) diagrams of Au@Fe_3O_4 Janus particles obtained from ABTS assay respective the hydrogen peroxide concentration.

The Michaelis-Menten diagram (Figure 36A) shows a typical hyperbolic curve. The linearised Michaelis-Menten curve results in a Lineweaver-Burk line, which can be used to determine the desired kinetic parameters. As mentioned in 3.2 not all data points will be included into the linear fit, since no further increase in slope will be detected, if v_{max} is reached.

The kinetic parameters obtained from Lineweaver-Burk fit are summarised in Table 17 in comparison to kinetic parameters of Fe_3O_4 nanoparticles from section 3.2.4.

Table 17: Kinetic parameters of Fe_3O_4 nanoparticles and Au@Fe_3O_4 Janus particles obtained from the ABTS assay with Lineweaver-Burk graphs.

	Fe_3O_4 NPs	Au@Fe_3O_4 JP
K_M	89 ± 3	0.31 ± 0.03
v_{max}	$3.51*10^{-5} \pm 0.09*10^{-5}$	0.38 ± 0.02

Regarding the kinetic parameters of the Fe_3O_4 nanoparticles and the Au@Fe_3O_4 Janus particles in Table 17 it is clear, that the Janus particles are the better catalysts. The maximum velocity of the Janus particles is bigger as well as the Michaelis-Menten constant is smaller. This implies a higher reaction rate as well as a higher affinity of the Janus particles to the hydrogen peroxide. Here, a synergistic effect as discussed by *Klünker et al*. could be the reason for the better kinetic properties. The proposed reason for the enhanced properties is an improved electron transport from the Au to the Fe_3O_4 domain.[79]

4.2.2. Synthesis and characterisation of TiO_2 nanoparticles

The used TiO_2 nanoparticles were synthesised by [redacted] in the [redacted] group. Characteristic analytic data (TEM and XRD) provided by [redacted] are presented in Figure 37.

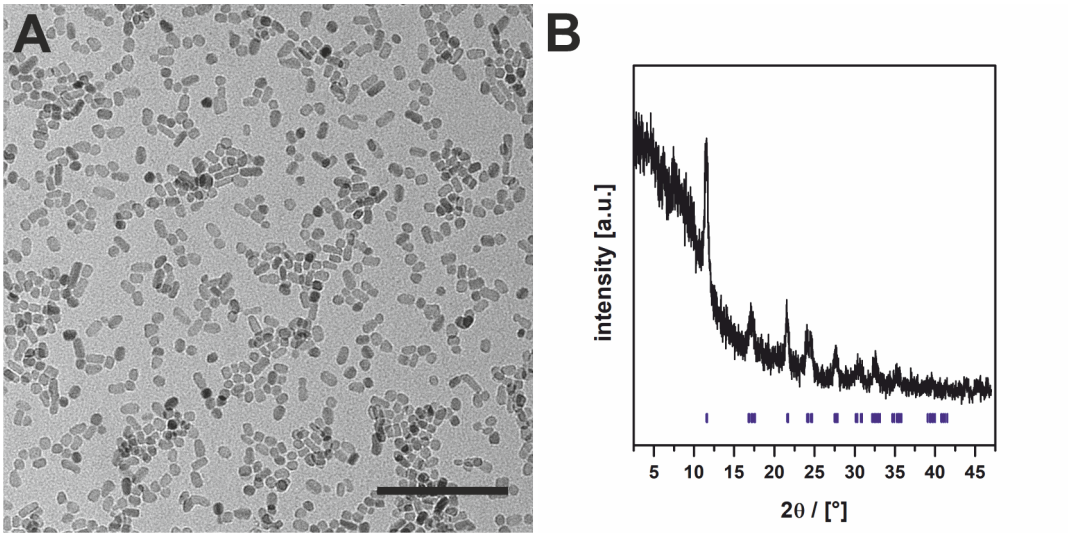

Figure 37: Characterisation of TiO_2 nanoparticles. A: TEM image (scale bar 100 nm). B: XRD pattern (black) with references (blue, JCDPS card: 96-900-8214).

Figure 37A shows a TEM image of TiO_2 nanoparticles with elongated morphology. No histogram is shown here because the nanoparticle morphology is not uniform. The XRD pattern (Figure 37B) confirms the sample as anatase.

These nanoparticles were used for further experiments (photocatalytic experiments and synthesis of heterotrimeric nanoparticles structures).

Kinetic properties of TiO_2 nanoparticles

Since a reaction cascade would be simulated by using inorganic nanoparticles, and iron containing nanoparticles as mimics for the enzyme peroxidase are already discussed, the anatase nanoparticles were examined regarding their photocatalytic hydrogen peroxide production. Therefore, the nanoparticles were surface functionalised to construct a polar surface. Aqueous nanoparticle suspensions containing different amounts of TiO_2 nanoparticles were irradiated with UV light first, before measuring the hydrogen peroxide production *via* a ferrous oxidation-xylenol orange (FOX) assay. The FOX Assay is based on a colour reaction. A solution containing xylenol orange (XO) is mixed with an acidic solution

containing iron(II). The yellow solution is added to a centrifuged aliquot of the sample solution. In the presence of hydrogen peroxide the ferrous ions are oxidised to ferric ions. These form a blue complex with the dye XO, which can be detected photometrically at a wavelength of 590 nm. The amount of hydrogen peroxide produced can be determined by external calibration.

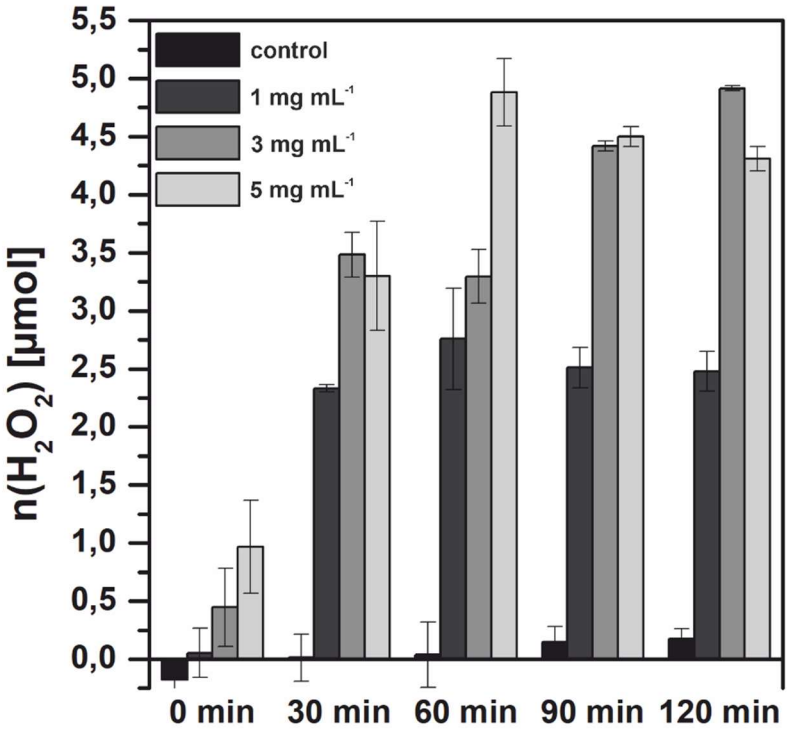

Figure 38: Photocatalytic hydrogen peroxide production by titanium dioxide nanoparticles using a FOX assay.

The concentration of produced hydrogen peroxide was determined time-dependent. Figure 38 shows the results of this assay. At the beginning of the experiment an increasing amount of hydrogen peroxide with increasing nanoparticle concentration is detectable. The short preparation time, in which the samples are exposed to daylight is already sufficient to generate hydrogen peroxide. For the sample with 1 mg mL^{-1} anatase nanoparticles the maximum of hydrogen peroxide production is already after 30 minutes, while the production in the samples with a higher nanoparticle concentration is still increasing after 30 minutes. Eventually a maximum of produced hydrogen peroxide concentration is reached too and thus limits the production. It can be expected that the nanoparticles lost their surface functionalisation since they precipitated while irradiation. It can assumed, that the produced hydrogen peroxide oxidised the

surface ligand tetramethylammonium. With the oxidation of the ligand the nanoparticles lost their polar properties and precipitated in the water. To answer this question further experiments have to be done, e.g. NMR spectroscopy. Here a surface-functionalised TiO_2 nanoparticles can be examined before and after photocatalysis. If the surface functionalisation gets lost a difference in ^{1}H-NMR would be detectable.

4.2.3. Synthesis and characterisation of ZnO nanoparticles and Au@ZnO Janus particles

The ZnO nanoparticles were synthesised like described by *Tahir et al.* Briefly, zinc(II) acetate dihydrate was dissolved in benzyl alcohol and oleylamine and heated up to 180 °C in 30 minutes. Here, the temperature was hold for 30 minutes too. The full characterisation can be seen in Figure 39.[131]

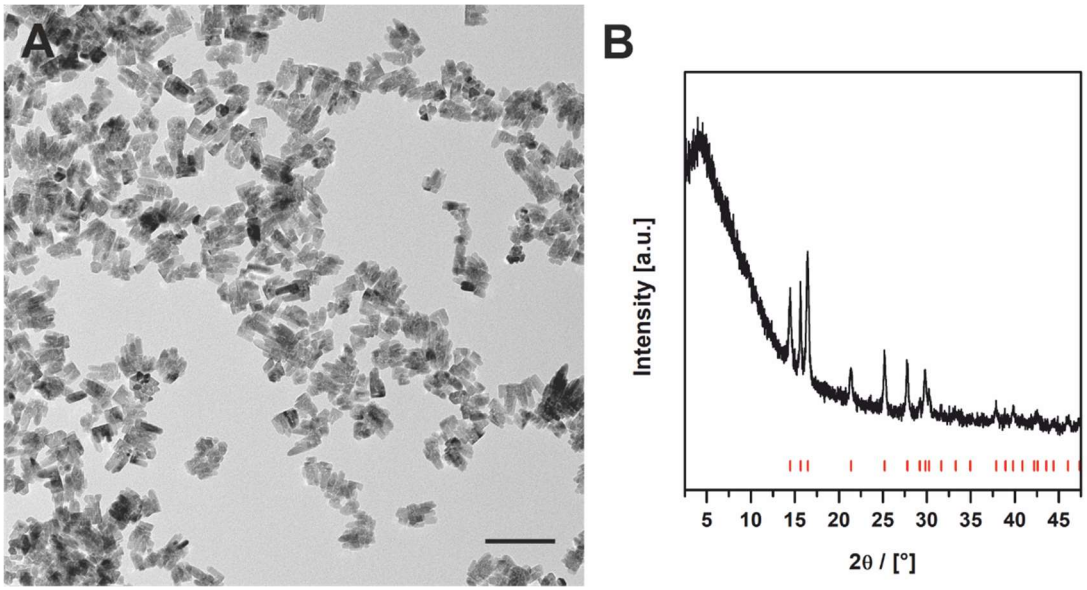

Figure 39: Characterisation of ZnO nanoparticles. A: TEM image of the synthesised ZnO nanoparticles (scale bar 100 nm). B: XRD pattern (black) of ZnO nanoparticles with reference reflexes (red) (JCDPS card: 96-210-7060).

Figure 39A shows a typical TEM image of the ZnO nanoparticles. The nanoparticles show rod-shaped morphology. However, it also appears as if several rods have grown together. This makes it difficult to determine the size of the nanoparticles, which is why an exact size determination is omitted here. Figure 39B shows the XRD pattern of the ZnO nanoparticles and confirms the existence of zincite as only phase of the nanoparticles.

The synthesis of Au@ZnO Janus particles described by *Nawaz et al.* was taken as basis for the synthesis of Au@ZnO Janus particles used in this work.[131] They reported that a relation between the polarity of the solvent mixture and the morphology of the heterodimers exists. The different polarities were generated by using different amounts of benzyl alcohol (BA) and 1-octadecene (1-ODE) as solvent, resulting in linear and branched heterodimers. While using benzyl alcohol as the only solvent they obtained branched Au@ZnO nanoparticles and by using benzyl alcohol and 1-octadecen in a ratio of 2:1 they obtained linear Au@ZnO nanoparticles. Their experimental procedure was applied to synthesise Au@ZnO nanoparticles with different ratios of benzyl alcohol and 1-octadecene.

Table 18: Reaction approaches for the synthesis of Au@ZnO nanoparticles using different ratios of benzyl alcohol to 1-octadecene.

sample	benzyl alcohol	1-octadecene	oleylamine
A	4 mL	2 mL	3 mL
B	5 mL	1 mL	3 mL
C	3 mL	3 mL	3 mL
D	2 mL	4 mL	3 mL
E	4 mL	2 mL	2 mL
F	5 mL	1 mL	2 mL
G	3 mL	3 mL	2 mL
H	2 mL	4 mL	2 mL

The morphologies of the nanoparticles resulting from the synthesis approaches described in Table 18 are characterised by using TEM. The results are shown in Figure 40 and Figure 41.

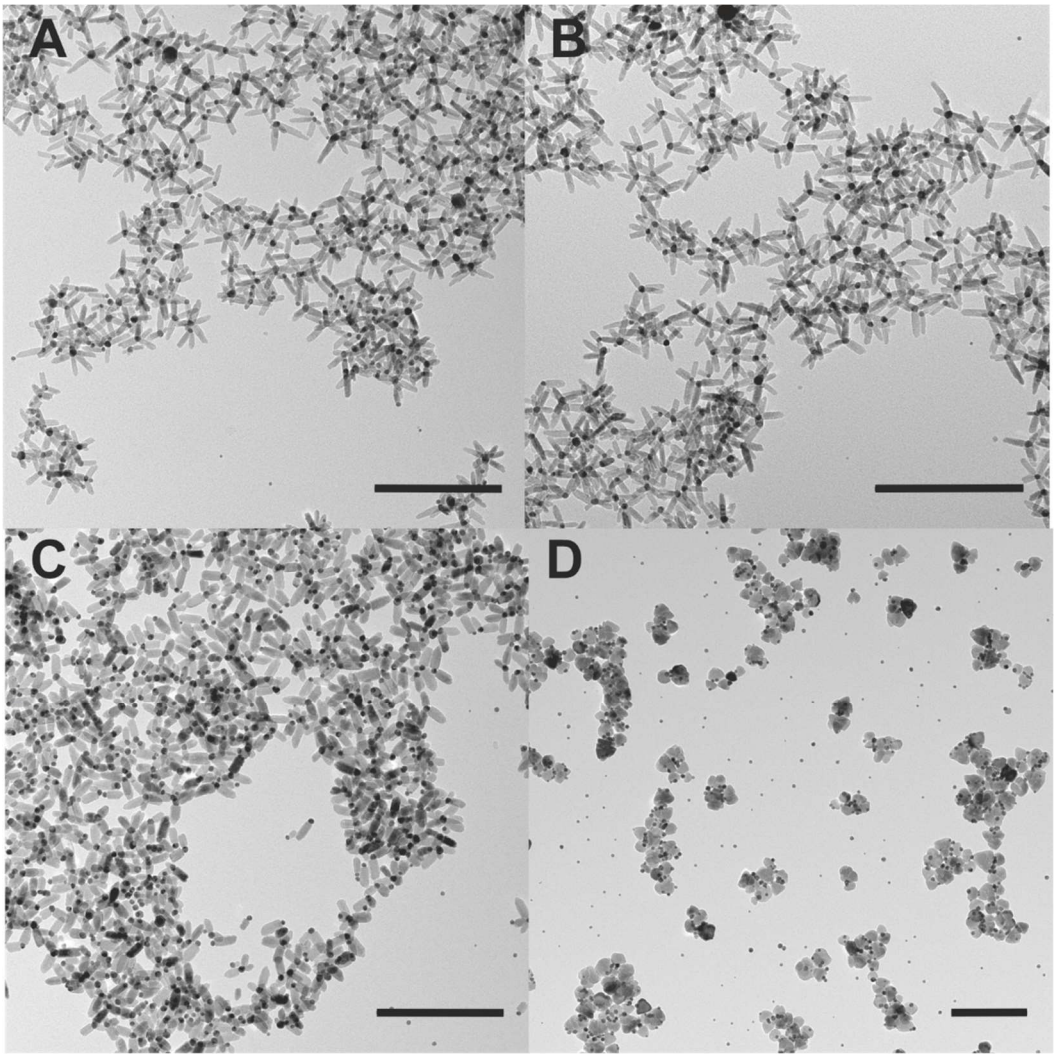

Figure 40: TEM images of Au@ZnO nanoparticles using different ratios of BA to 1-ODE while using 3 mL of oleylamine. A: 4 mL BA : 2 mL 1-ODE. B: 5 mL BA : 1 mL 1-ODE. C: 3 mL BA : 3 mL 1-ODE. D: 2 mL BA : 4 mL 1-ODE. (scale bars 200 nm)

The reaction mixture A (see Table 18) described by *Tahir et al*. should result in linear Au@ZnO nanoparticles. As seen in Figure 40, branched Au@ZnO nanoparticles were obtained in this case. The solvent ratios were varied in order to examine the influence of the polarity on the morphology of the nanoparticles. Like described in the publication it was expected that with increasing polarity the nanoparticles get more branched and with decreasing the polarity the nanoparticles get more linear. Sample B shows an example in which the polarity is increased. In comparison to sample A, no significant difference can be observed. Decreasing the polarity leads to less branched nanoparticles. Some nanoparticles show the obtained linear morphology, but no uniform morphology could be observed. An unexpected observation could be made after further decrease in polarity (sample D). Instead of only linear nanoparticles, a new morphology could

be observed. Since the synthesis did not lead to uniform dumbbell-like heteroparticles and some single Au nanoparticles could still be observed, the influence of oleylamine was scrutinised. Known from the synthesis of Au nanoparticles described in 4.2.1, oleylamine acts as stabilising ligand at the surface of Au nanoparticles. Also known from the synthesis of magnetite nanoparticles described in 3.2.3 oleylamine can also act as reducing agent. For heterogeneous nucleation the stabilisation of nanoparticles surfaces is of great importance as well as the stoichiometry between the reducing agent and the precursor (in this case hydrogen tetrachloroaurate(III) trihydrate) which influences the size of the gold nanoparticles, which should serve as nucleation template, in according to the *LaMer* model (see 4.1.1). All four synthesis approaches were repeated again with a lower amount of oleylamine to get more control over the synthesis of the Au nanoparticles regarding their size and to reduce the surface stabilising effect. The results are shown in Figure 41.

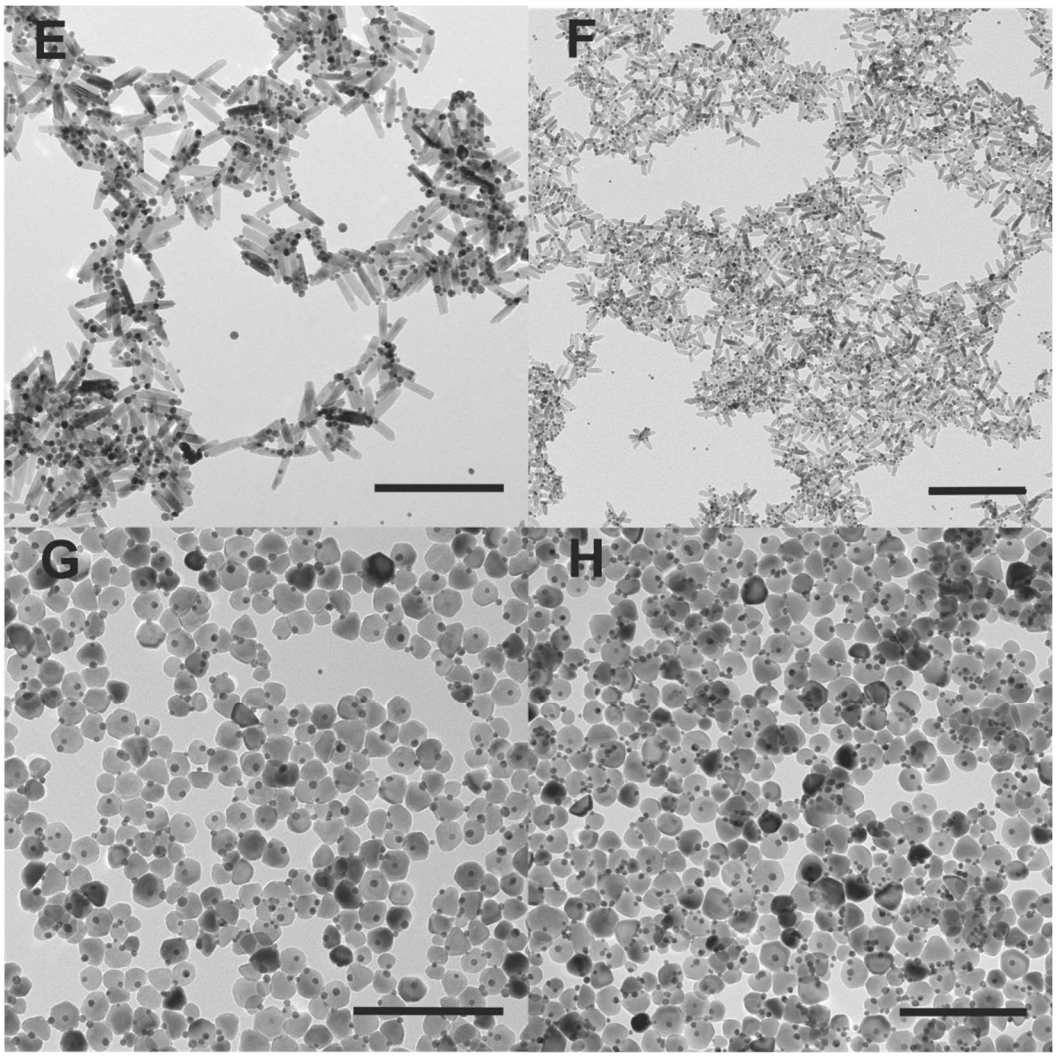

Figure 41: TEM images of Au@ZnO nanoparticles using different ratios of BA to 1-ODE while using 2 mL of oleylamine. E: 4 mL BA : 2 mL 1-ODE. F: 5 mL BA : 1 mL 1-ODE. G: 3 mL BA : 3 mL 1-ODE. H: 2 mL BA : 4 mL 1-ODE. (scale bars 200 nm)

Figure 41E shows the synthesis of Au@ZnO nanoparticles with the same solvent ratio as approach A with a lower amount of oleylamine. It is obvious that the synthesised nanoparticles are no longer branched. It also seems like there are only isolated nanoparticles in which a ZnO domain is grown on an Au nanoparticle. In most cases it looks like ZnO rods next to Au nanoparticles. Another observation is the difference in size of the ZnO rods. While the particle length in sample A is about 20 – 30 nm and the width about 7 – 10 nm, the nanoparticle structures in sample E show a length of 45 – 55 nm and a width of 14 – 19 nm. Comparing sample A and B no significant change in the morphology of the synthesised nanoparticles could be observed, a significant morphology change comparing sample E and F could be seen. While in sample E it seems like the zinc oxide is not grown onto the surface of the Au nanoparticles, it seems different in sample F. Here, also rather

branched nanoparticles could be observed. This conforms to the publication of *Tahir et al.* – as higher the polarity of the solvent mixture as more branched the nanoparticles are. By comparing sample C to sample G, the largest difference could be noted. While sample C shows mainly linear Au@ZnO heterostructures, sample G shows already dumbbell-like heterostructures which were expected for sample H. Instead, sample H shows less uniform heterostructures. Some single Au nanoparticles could be observed next to the Au@ZnO heterostructures. In consideration of all syntheses, the synthesis of sample G was used further for Au@ZnO heterostructures to obtain a comparable nanoparticle morphology to the other heteromeric nanoparticle system described in 4.2.1.

The Au@ZnO nanoparticles used for further studies were synthesised by dissolving hydrogen tetrachloroaurate(III) trihydrate and zinc(II) acetate dihydrate in 2 mL BA, 4 mL 1-ODE and 2 mL oleylamine. This mixture was heated up to 120 °C in 10 minutes and the temperature was hold for 20 minutes before it was increased to 180 °C in 10 minutes. The temperature was kept constant for further 30 minutes. The full characterisation of the Au@ZnO Janus particles is shown in Figure 42.

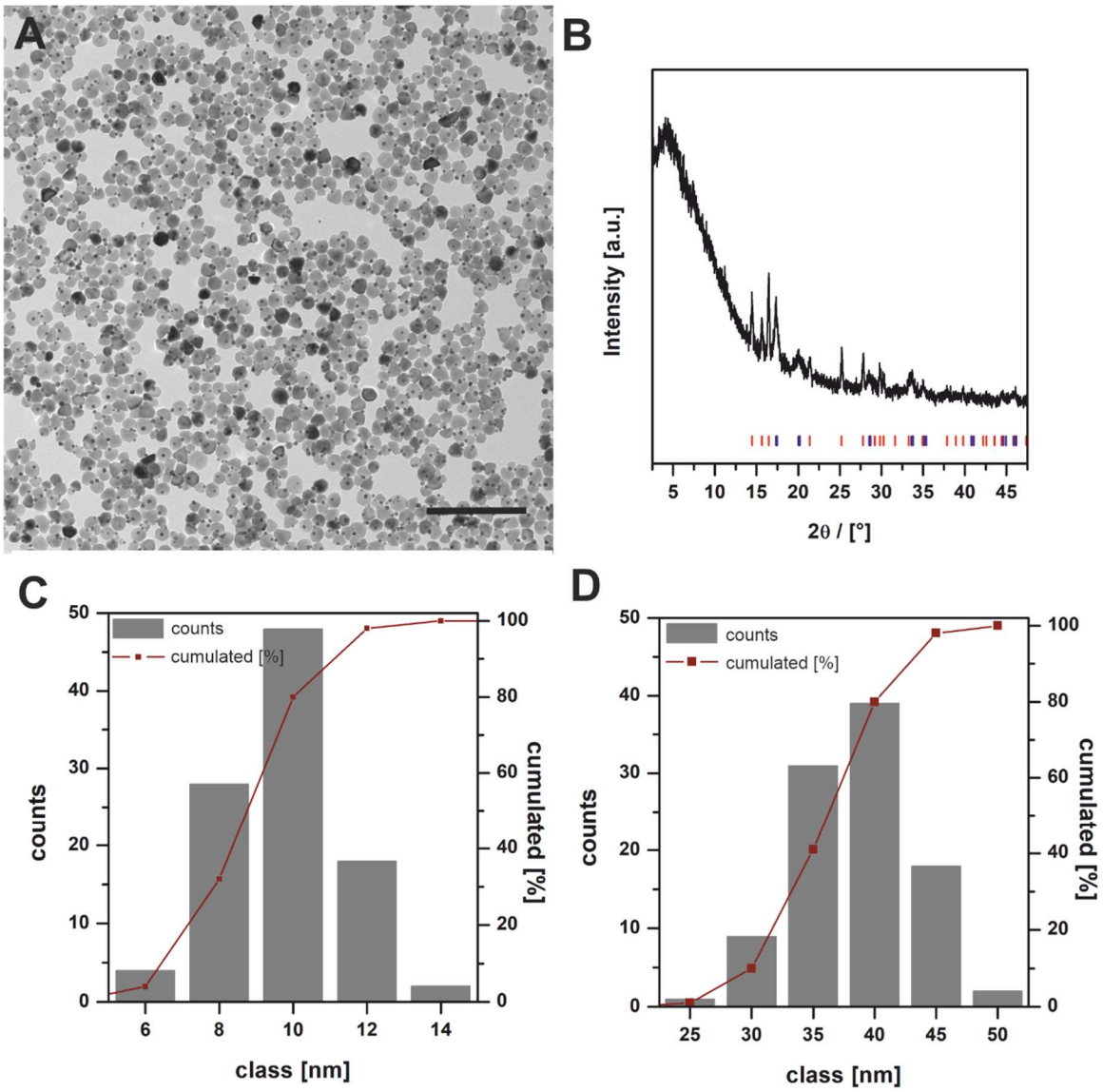

Figure 42: Characterisation of Au@ZnO nanoparticles. A: TEM image of the synthesised nanoparticles (scale bar 250 nm). B: XRD pattern (black) with literature reflexes (blue – Au and red – ZnO) (JCDPS cards 96-110-0139 and 96-210-7060). C: Histogram of the Au domain of the Au@ZnO nanoparticles. D: Histogram of the ZnO domain of the Au@ZnO nanoparticles.

Figure 42 A shows a typical TEM image of Au@ZnO Janus particles described above. The Au domain as well as the ZnO domain of the Janus particles show nearly spherical morphology. The size distributions of both domains is shown in the histograms (Au - Figure 42C and ZnO - Figure 42D). The Au domain has a diameter of 8.7 nm ± 1.6 nm and the ZnO domain of 36.1 nm ± 4.5 nm. The XRD pattern (Figure 42B) confirms the existence of a gold phase next to zincite phase.

To proof that the ZnO domain is grown onto the Au nanoparticle UV-Vis spectra were measured to compare the plasmon band of the Au@ZnO Janus particles with

the plasmon band of Au nanoparticles. The reference Au nanoparticles were synthesised analogue to the Au@ZnO Janus particles without the addition of zinc(II) acetate dihydrate. The UV-Vis spectra are shown in Figure 43A as well as the results of the FOX assay of the Au@ZnO Janus particles compared to the synthesised ZnO nanoparticles described above.

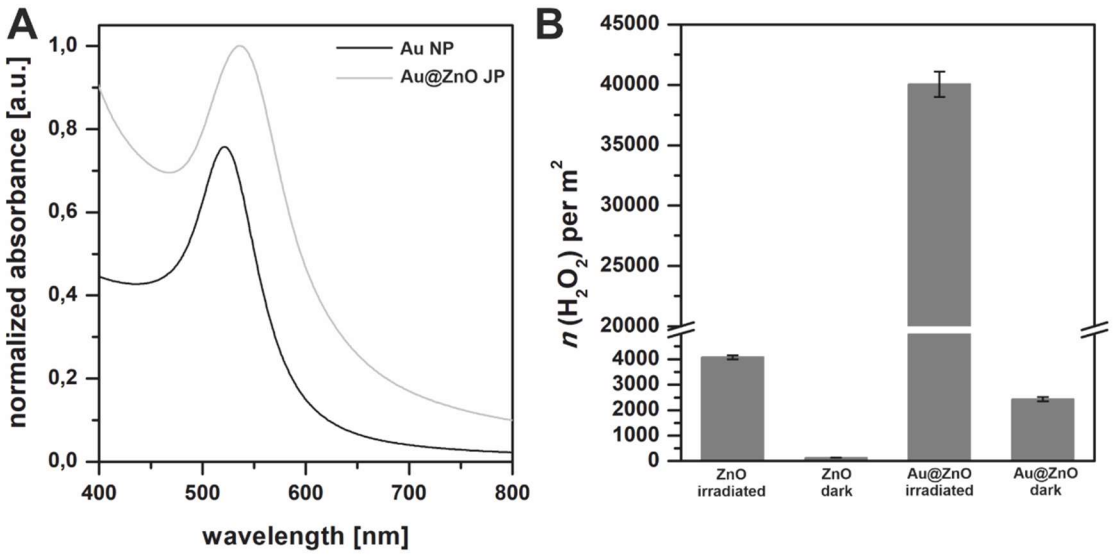

Figure 43: A. UV-Vis spectra of Au nanoparticles and Au@ZnO Janus particles. B. Photocatalytic production of hydrogen peroxide of ZnO nanoparticles and Au@ZnO Janus particles.

Figure 43 A shows the UV-Vis spectra of Au nanoparticles and Au@ZnO Janus particles. Au nanoparticles are prominent for their plasmon band which position is dependent on the size, morphology and coating of the surface of the nanoparticles.[101,131] The plasmon band of the Au nanoparticles has the maximum at 521 nm. The Au@ZnO Janus particles also show a plasmon band, but the maximum is at 535 nm. This bathochromic shift can be explained with electronic effects. If zinc oxide is nucleating on the [111] surface of gold nanoparticles by thermal decomposition and epitaxial growth is following, a polarisation of the gold nanoparticle is caused. The electrons of the gold nanoparticles orient along the [111] surface if ZnO nucleates which causes an electron deficit at the other outer surface planes of the gold nanoparticles.[131]

4.2.4. Synthesis of the bifunctional ligand 4-(11-mercaptoundecyl)benzene-1,2-diol

The bifunctional ligand for functionalisation of Janus particles and single nanoparticles to form heterotrimeric nanostructures, was prepared in a five-step synthesis. The 11-bromundecanoic acid was converted to the corresponding acid chloride by chlorination. Subsequent Friedel-Crafts acylation was used to produce the intermediate product 11-bromo-1-(3,4-dimethoxyphenyl)undecan-1-one. The keto group was reduced and the thioacetate residue introduced by means of a nucleophilic substitution. Subsequent ether cleavage using boron tribromide and acid hydrolysis led to the desired product 4-(11-mercaptoundecyl)benzene-1,2-diol.

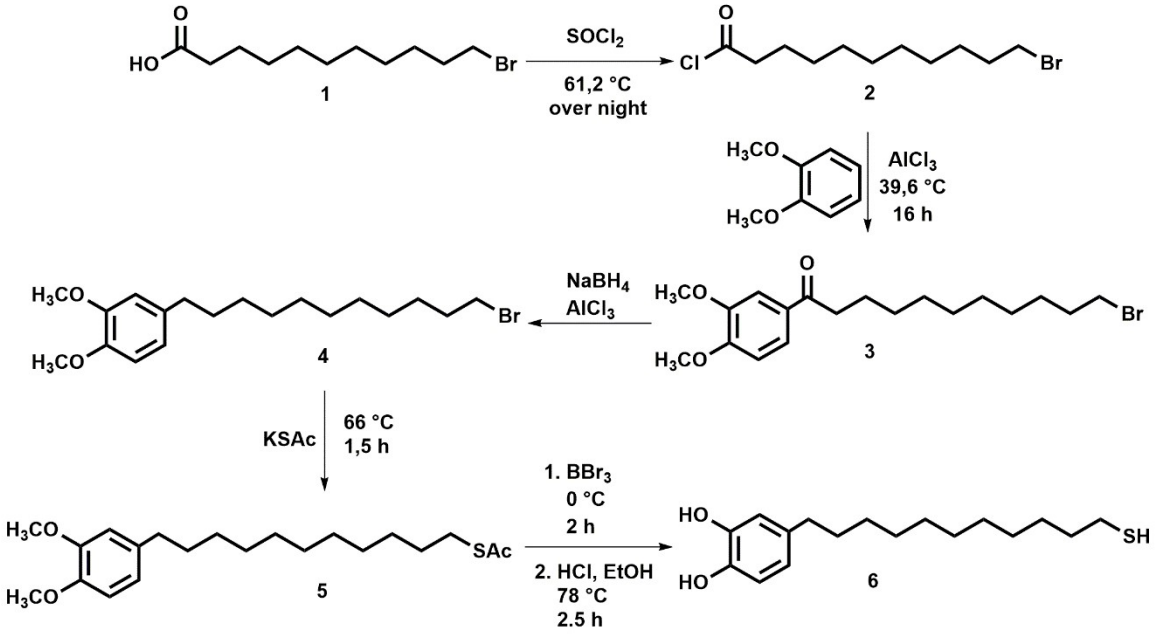

Figure 44: Synthesis scheme of the bifunctional ligand 4-(11-mercaptoundecyl)benzene-1,2-diol.

In the following, the synthesis of the bifunctional ligand is explained in detail and the structures of the respective intermediates and the final product are completely elucidated by infrared (IR) and NMR spectroscopy.

Synthesis of 11-bromoundecanoyl chloride

In the first reaction step, thionyl chloride ($SOCl_2$) is used to produce the respective acid chloride from the undecanoic acid derivate. Acid chlorides are among the most reactive carbonyl compounds and are suitable for use in Friedel-Crafts acylations.

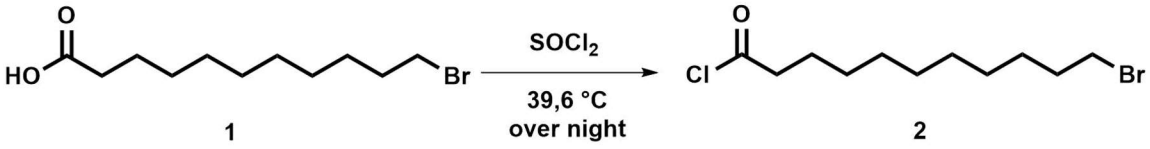

Figure 45: Reaction scheme of the synthesis of 11-bromoundecanoyl chloride.

The IR spectrum shows all expected characteristic bands. It can also be seen that the band of the C=O valence oscillation is shifted towards higher wavenumbers, indicating that the carboxylic acid has been converted to an acid chloride.

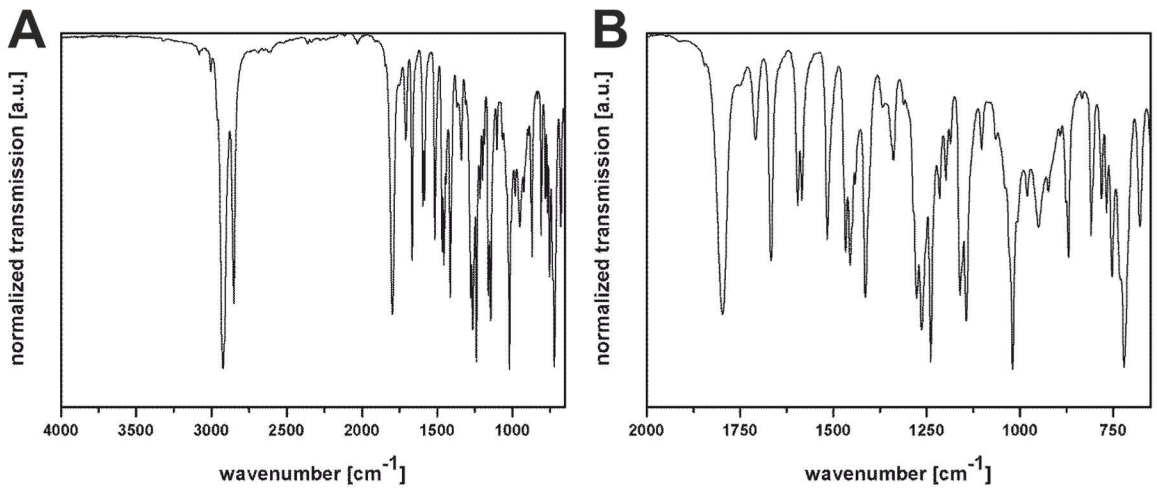

Figure 46: IR-spectra of 11-bromoundecanoyl chloride. A: full spectrum. B: zoom in.

In the following the prominent bands are assigned to the respective oscillation.

Table 19: Assignment of the prominent oscillations of 11-bromoundecanoyl chloride.

wavenumber [cm^{-1}]	assignment
2923	-CH_2 valence
2851	-CH_2 valence
1797	-C=O valence of carboxylic acid halogenide
722	-C-Br valence

Using ^{1}H-NMR spectroscopy all signals could be identified and assigned. The negative inductive effect of the bromine and the acid chloride group leads to the shielding of the adjacent methylene groups, so that their signals are deeply shifted. The unambiguous assignment of the signals was carried out by means of coupling experiments (^{1}H-^{13}C-heteronuclear single bond coherence (HSQC)-spectroscopy, ^{1}H-^{13}C-heteronuclear multiple bond correlation (HMBC)-spectroscopy, see 4.5).

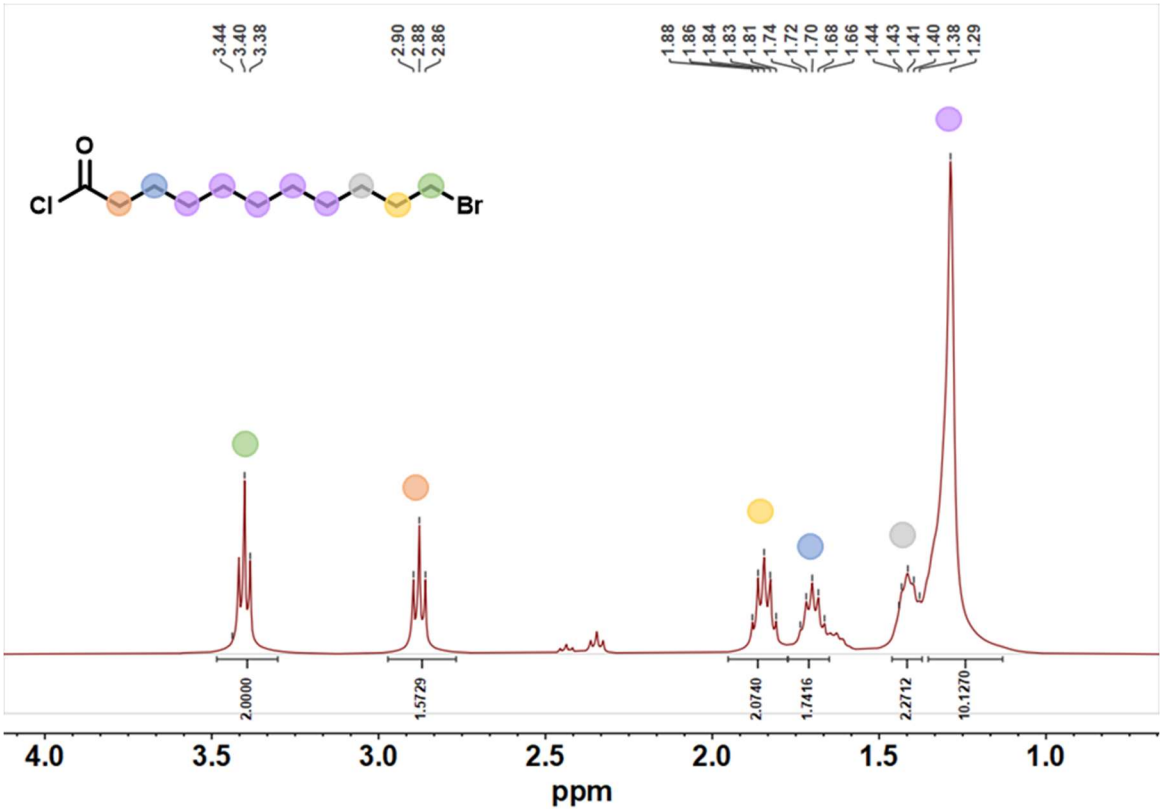

Figure 47: ^{1}H-NMR of 11-bromoundecanoyl chloride. For the full spectra see 4.5.

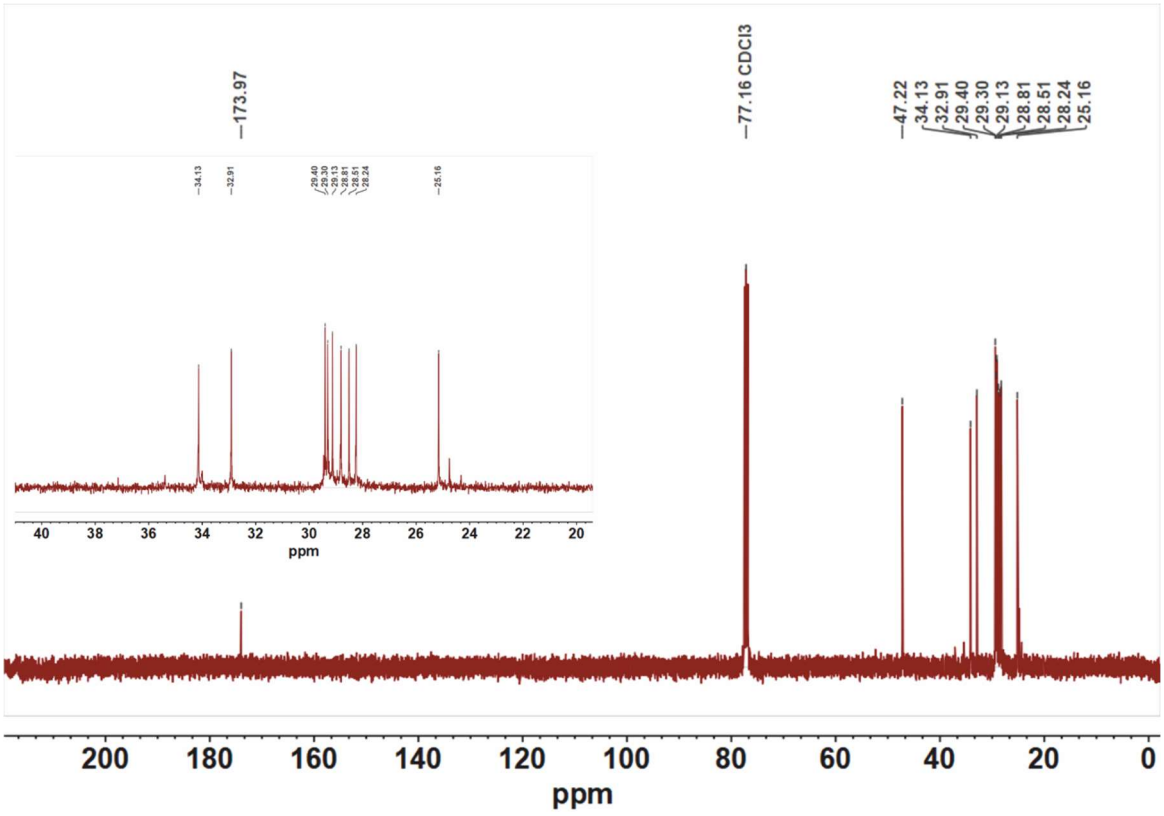

Figure 48: ^{13}C-NMR of 11-bromoundecanoyl chloride.

With the help of ^{13}C-NMR spectroscopy it could be proven that a carbonyl species is present after the reaction and no other product that also contains a carbonyl group (e.g. unreacted educt).

An exact allocation of the signals to the carbons present in each case is dispensed with in this case, since the allocation can only be made unambiguously to the terms of the alkyl chain. The middle methylene groups cannot be clearly assigned due to their chemical similarity.

After sufficient analysis of the data, the product was implemented in the next step in a Friedel-Crafts acylation.

Synthesis of 11-bromo-1-(3,4-dimethoxyphenyl)undecan-1-one

In a typical Friedel-Crafts acylation, the first stage 11-bromoundecanoyl chloride product was reacted with 1,2-dimethoxybenzene with the Lewis acid aluminium(III) chloride, which acts as a catalyst in this case.

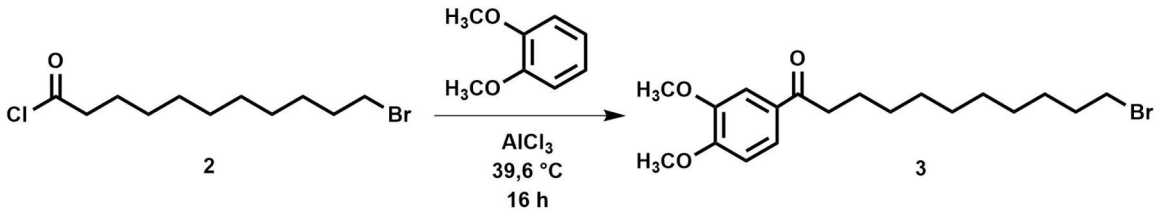

Figure 49: Reaction scheme of the synthesis of 11-bromo-1-(3,4-dimethoxyphenyl)undecan-1-one.

The IR spectrum shows all expected prominent bands which could be identified and assigned. Above all, the shift of the band of the C=O valence oscillation towards lower wavenumbers must be emphasised. This is an indication that Friedel-Crafts acylation was successful.

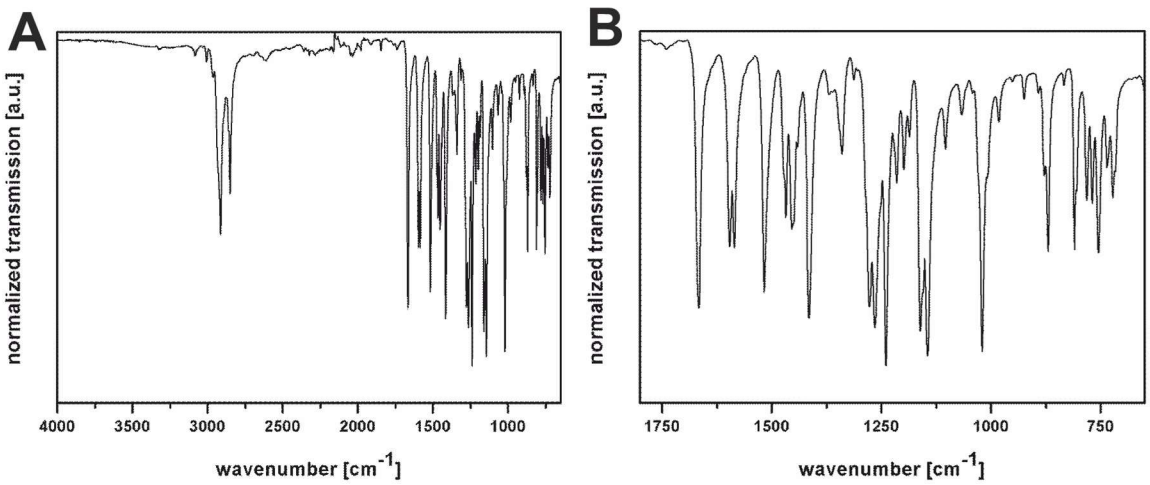

Figure 50: IR-spectra of 11-bromo-1-(3,4-dimethoxyphenyl)undecan-1-one.

In the following the relevant bands are assumed and assigned to the corresponding bonds of the product. In this reaction step it was important to detect a shift of the oscillation of the carbonyl group to prove the change of the chemical environment of this group. This indicates the success of the reaction.

Table 20: Assignment of the prominent oscillations of 11-bromo-1-(3,4-dimethoxyphenyl)undecan-1-one.

wavenumber [cm^{-1}]	assignment
3000	aromatic =C-H valence
2963	aliphatic –CH3 valence
2914	aliphatic –CH2 valence
2851	aliphatic –CH2 valence
1666	aromatic keton -C=O valence
1596	ring vibration
1279	ether C-O-C valence
1265	ether C-O-C valence
755	1,2- disubstituted benzene, =C-H deformation
722	-C-Br valence

Using ^{1}H- and ^{13}C-NMR spectroscopy it could be shown that the synthesis was successful. Coupling experiments were also performed (^{1}H-^{1}H-correlation spectroscopy (COSY), ^{1}H-^{13}C-HSQC, ^{1}H-^{13}C-HMBC, see 4.5). The ^{1}H-NMR spectrum only shows three signals for aromatic hydrogen atoms, which indicates a substitution on the aromatic ring. The signals of the hydrogen atoms of the

methylene group adjacent to the carbonyl group are slightly more deeply shifted compared to the used educt, indicating an exchange of the chloride for another substituent, in this case an aromatic.

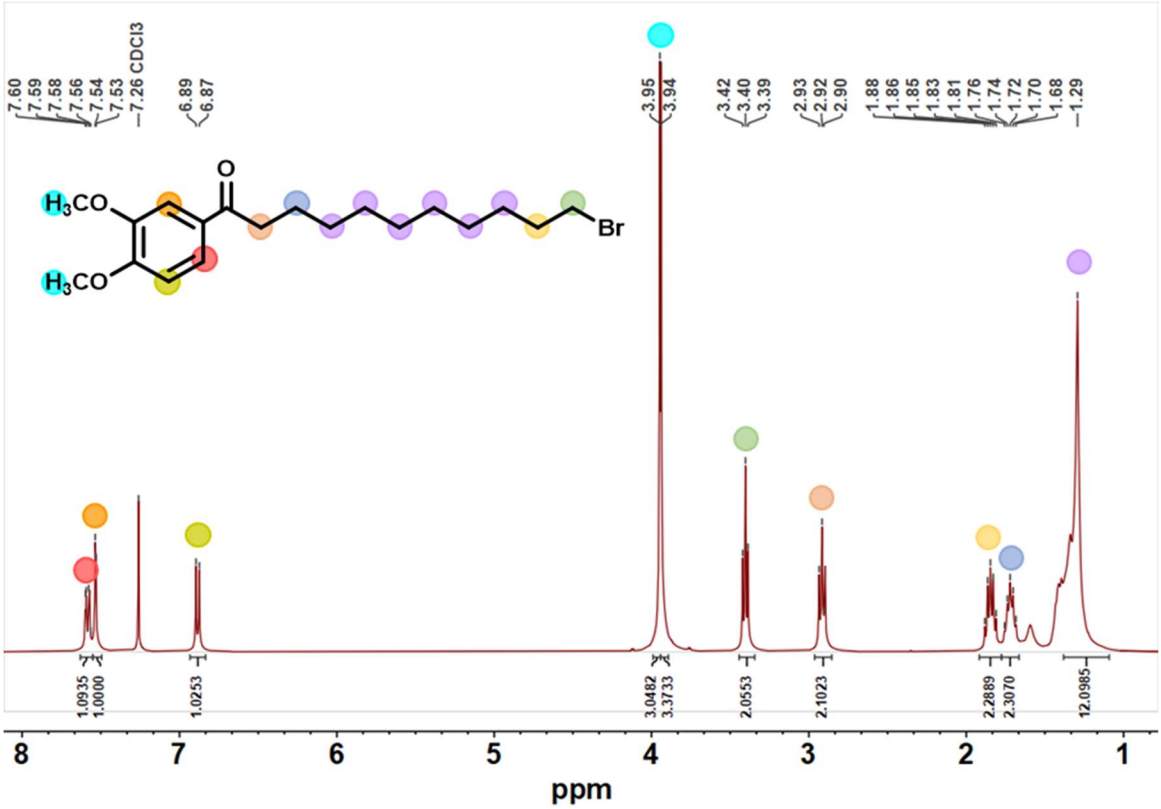

Figure 51: ^{1}H-NMR of 11-bromo-1-(3,4-dimethoxyphenyl)undecan-1-one. For the full spectra see 4.5.

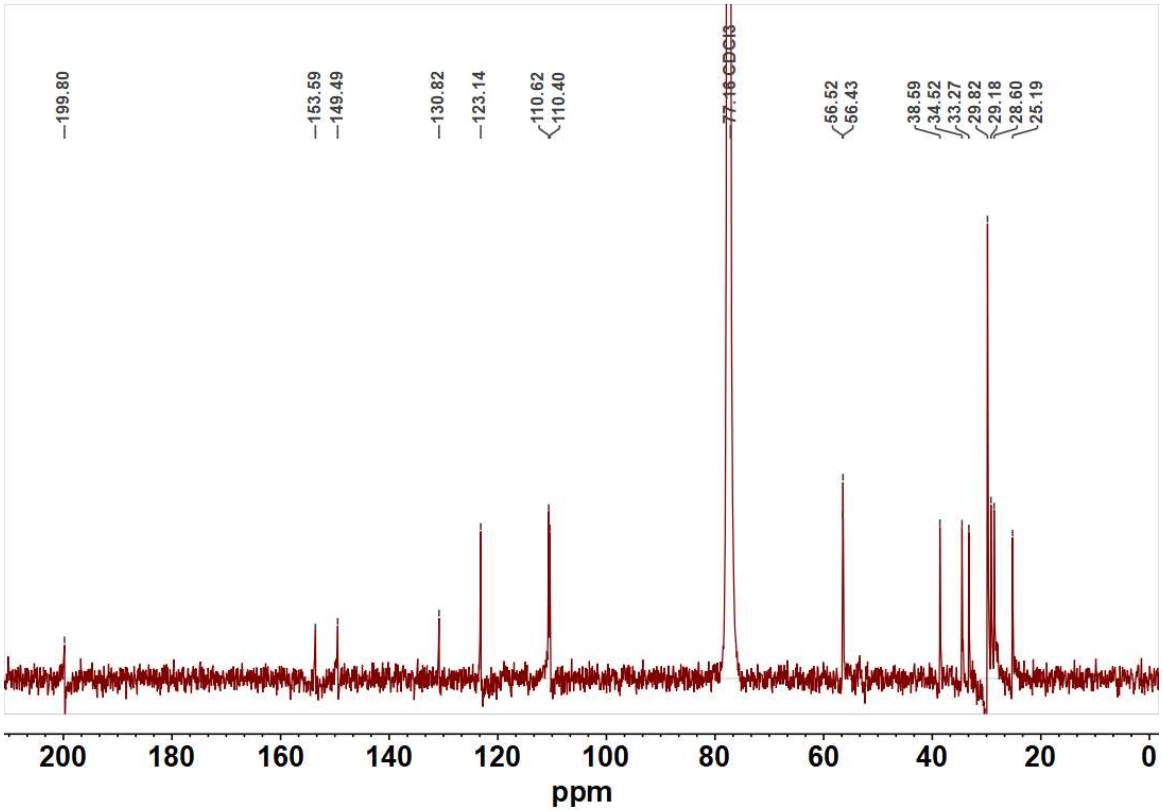

Figure 52: ^{13}C-NMR of 11-bromo-1-(3,4-dimethoxyphenyl)undecan-1-one.

The significant deep field shift of the ^{13}C signal of the carbonyl group (199.80 ppm) indicates a chemical change. It can be assumed that the electrophilic aromatic substitution was successful.

The obtained product was implemented in the subsequent synthesis stage.

Synthesis of 4-(11-bromoundecyl)-1,2-dimethoxybenzene

By means of a reduction using sodium borohydride ($NaBH_4$) and $AlCl_3$, 11-bromo-1-(3,4-dimethoxyphenyl)undecan-1-one was converted to 4-(11-bromoundecyl)-1,2-dimethoxybenzene.

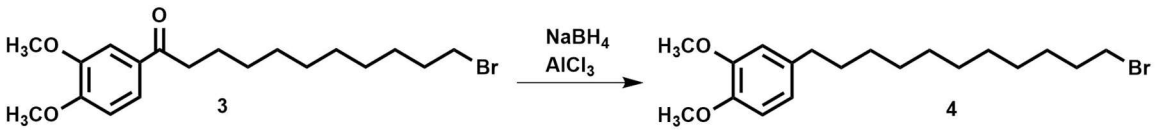

Figure 53: Reaction scheme of the synthesis of 4-(11-bromoundecyl)-1,2-dimethoxybenzene.

By means of the IR spectrum the reduction of the carbonyl group could be detected. A typical oscillation band in the range of 1600 - 1800 cm^{-1} is no longer observable.

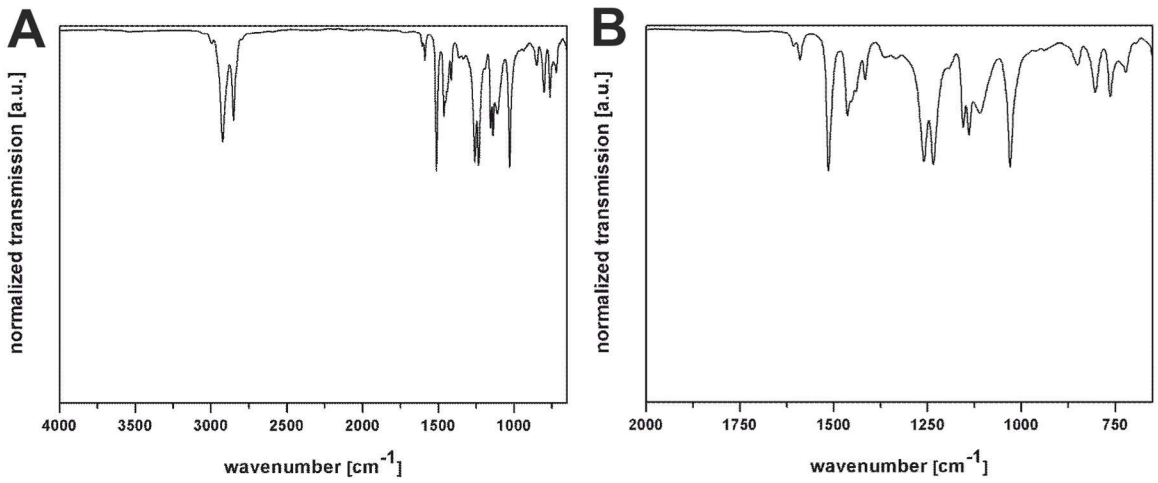

Figure 54: IR-spectra of 4-(11-bromoundecyl)-1,2-dimethoxybenzene.

Furthermore the expected structure can be confirmed by the observed bands listed in Table 21. Not listed is a band that shows up as a shoulder at 2830 cm^{-1}, which indicates an -O-CH_3-valence oscillation of a methyl ether. Since this signal cannot be represented unambiguously, but merely appears as the shoulder of another signal, it is not included in the following list.

Table 21: Assignment of the prominent oscillations of 4-(11-bromoundecyl)-1,2-dimethoxybenzene.

wavenumber [cm^{-1}]	assignment
2998	aromatic =C-H valence
2924	aliphatic –CH_2 valence
2851	aliphatic –CH_2 valence
1462	aliphatic –CH_2 and –CH_3 deformation
1261, 1234 and 1028	aromatic ether C-O-C valence
849	=C-H deformation of 1,4-disubstituted benzene
802	-C-Br valence
763	=C-H deformation of 1,2-disubstituted benzene

Using NMR spectroscopy, the structure of the resulting product could be completely elucidated. In addition to ^{1}H- and ^{13}C-NMR spectra, further spectra from coupling experiments were used (^{1}H-^{1}H-COSY, ^{1}H-^{13}C-HSQC, ^{1}H-^{13}C-HMBC, see 4.5). An important observation resulting from the ^{1}H spectrum is the additional signal at 2.54 ppm, which represents a triplet and can be assigned to the methylene group with the help of further experiments, formed by the reduction.

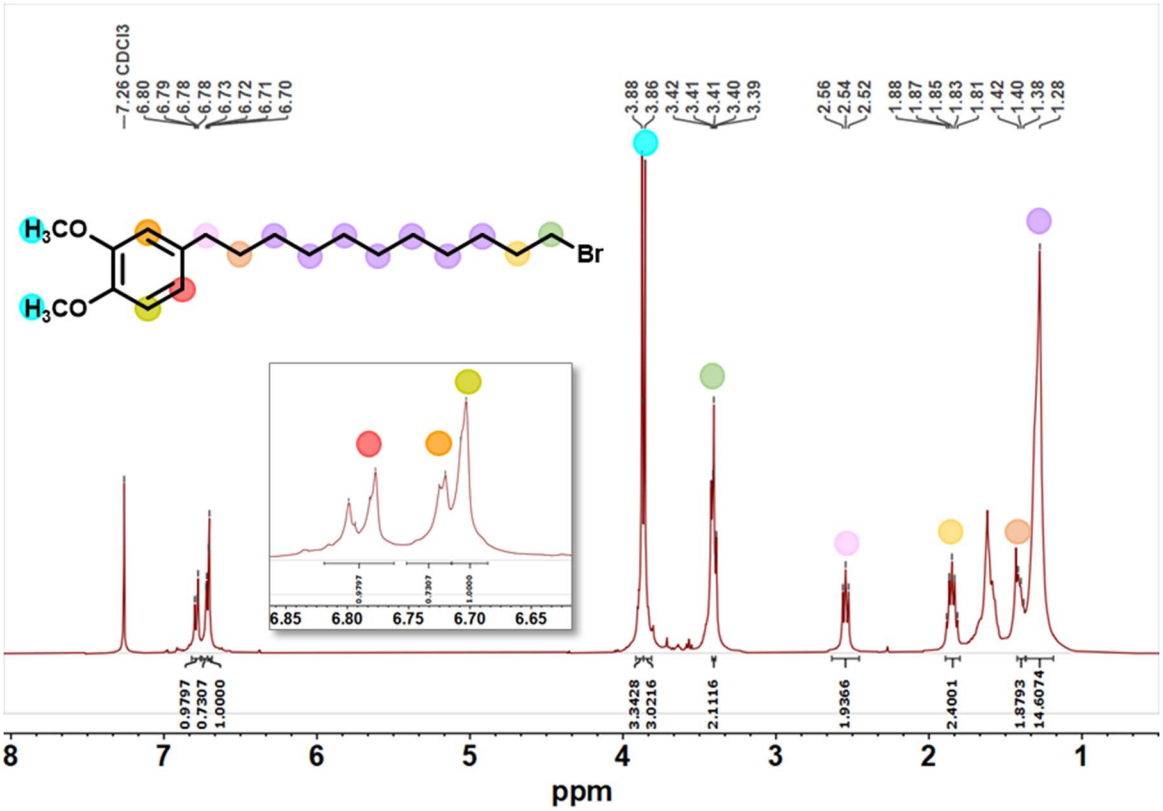

Figure 55: ^{1}H-NMR of 4-(11-bromoundecyl)-1,2-dimethoxybenze. For the full spectra see 4.5.

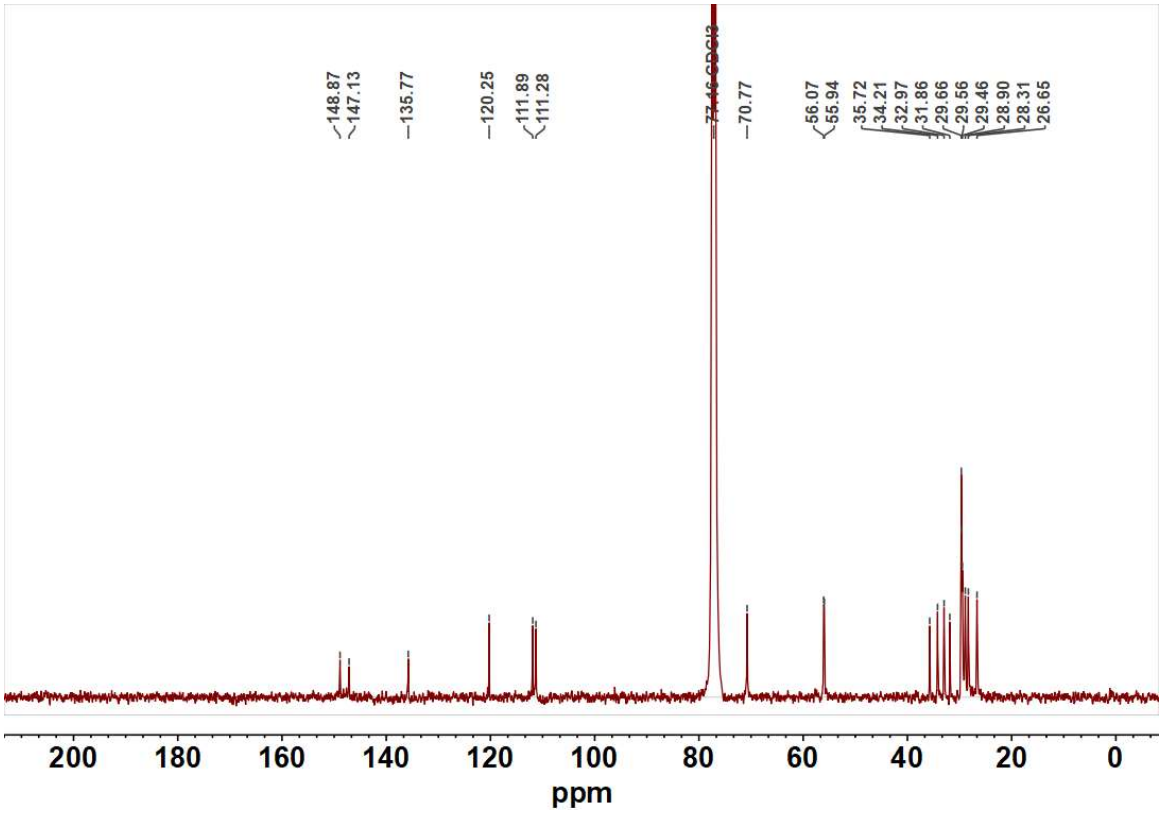

Figure 56: ^{13}C-NMR of 4-(11-bromoundecyl)-1,2-dimethoxybenze.

In the ^{13}C NMR spectrum, no C signal can be detected that indicates the presence of a carbonyl group. This confirms the success of the reduction.

Synthesis of 11-(3,4-dimethoxyphenyl)undecyl ethanethioate

In a nucleophilic substitution, the molecule 4-(11-bromoundecyl)-1,2-dimethoxybenze obtained in the previous synthesis was converted with potassium thioacetate (KSAc) to the product 11-(3,4-dimethoxyphenyl)undecyl ethanethioate.

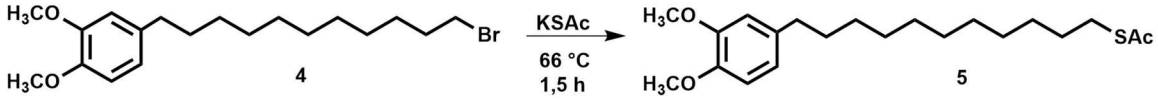

Figure 57: Reaction scheme of 11-(3,4-dimethoxyphenyl)undecyl ethanethioate.

Using IR spectroscopy, the presence of a carbonyl group could be detected by a band at 1691 cm^{-1}. In addition, a -C-S valence oscillation was detected with a band at 625 cm^{-1}, so that it can be assumed that the desired molecule could be obtained.

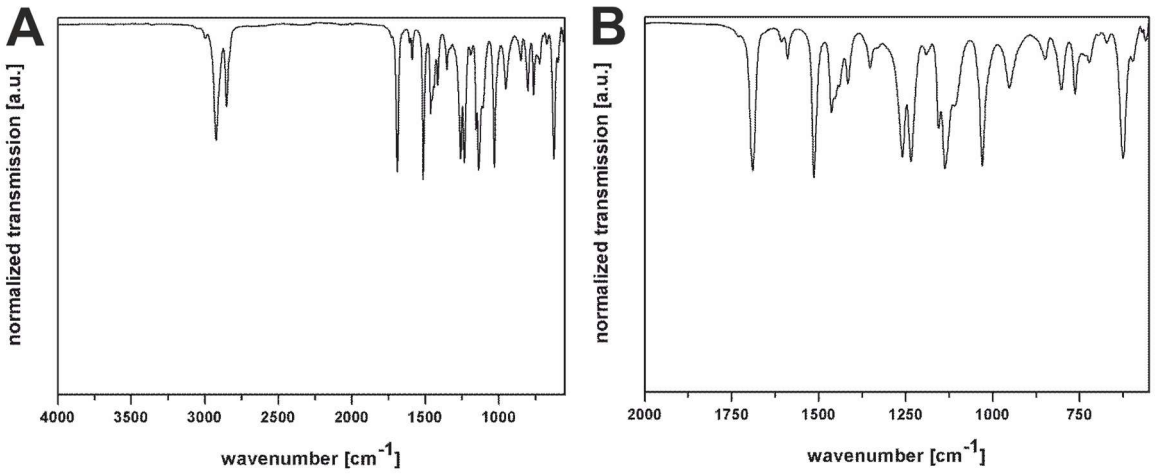

Figure 58: IR-spectra of 11-(3,4-dimethoxyphenyl)undecyl ethanethioate.

Further bands in the IR spectrum could be clearly assigned to the desired structure. (see Table 22). As in the previous case, a signal at 2832 cm^{-1} is indicated which is not listed but can be assigned to an -O-CH_3 valence vibration of a methyl ether.

Table 22: Assignment of the prominent oscillations of 11-(3,4-dimethoxyphenyl)undecyl ethanethioate.

wavenumber [cm^{-1}]	assignment
2997	aromatic =C-H valence
2922	aliphatic $–CH_2$ valence
2851	aliphatic $–CH_2$ valence
1691	-C=O valence of a carbonyl
1462	aliphatic $–CH_2$ and $–CH_3$ deformation
1258, 1235 and 1029	aromatic ether C-O-C valence
848	=C-H deformation of 1,4- disubstituted benzene
763	=C-H deformation of 1,2-disubstituted benzene
625	-C-S valence of organic sulphur compound

With the help of ^{1}H-NMR spectroscopy a new signal, which presents itself as a singlet at 2.32 ppm, can be detected and assigned to the newly introduced methyl group of the acetate residue. At the same time, a high field shift of the signal of the methylene group α-constituent to sulphur can be observed (see Figure 59, green marked methylene group), caused by the new chemical environment due to the synthesis. The previous substituent, the bromine atom, has reduced the electron density at this methylene group due to its comparatively high electronegativity, which has led to a deep field shift. However, the exchange of the substituent now changes the electronic conditions. Compared to bromine, sulphur is slightly less electronegative, so that the electron pull on the methylene group is somewhat reduced. At the same time, the sulphur terminates the strong -M and -I effect of the carbonyl group, so that they no longer have any effect on the methylene group. This composition of conditions is expressed in the high field shift of the signal of the methylene group in ^{1}H-NMR.

The complete structure could be completely elucidated with the help of ^{1}H and ^{13}-C spectra and further coupling experiments (^{1}H-^{1}H-COSY, ^{1}H-^{13}C-HSQC, ^{1}H-^{13}C-HMBC, see 4.5).

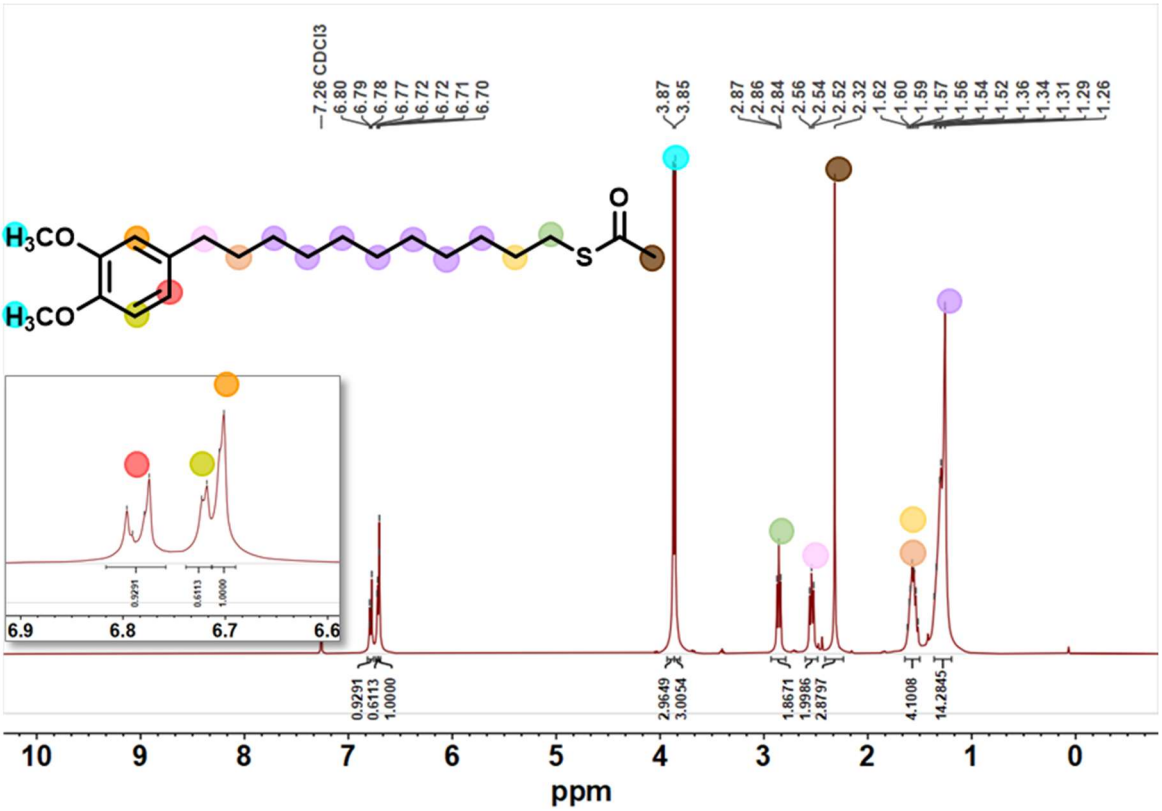

Figure 59: ^{1}H-NMR of 11-(3,4-dimethoxyphenyl)undecyl ethanethioate. For the full spectra see 4.5.

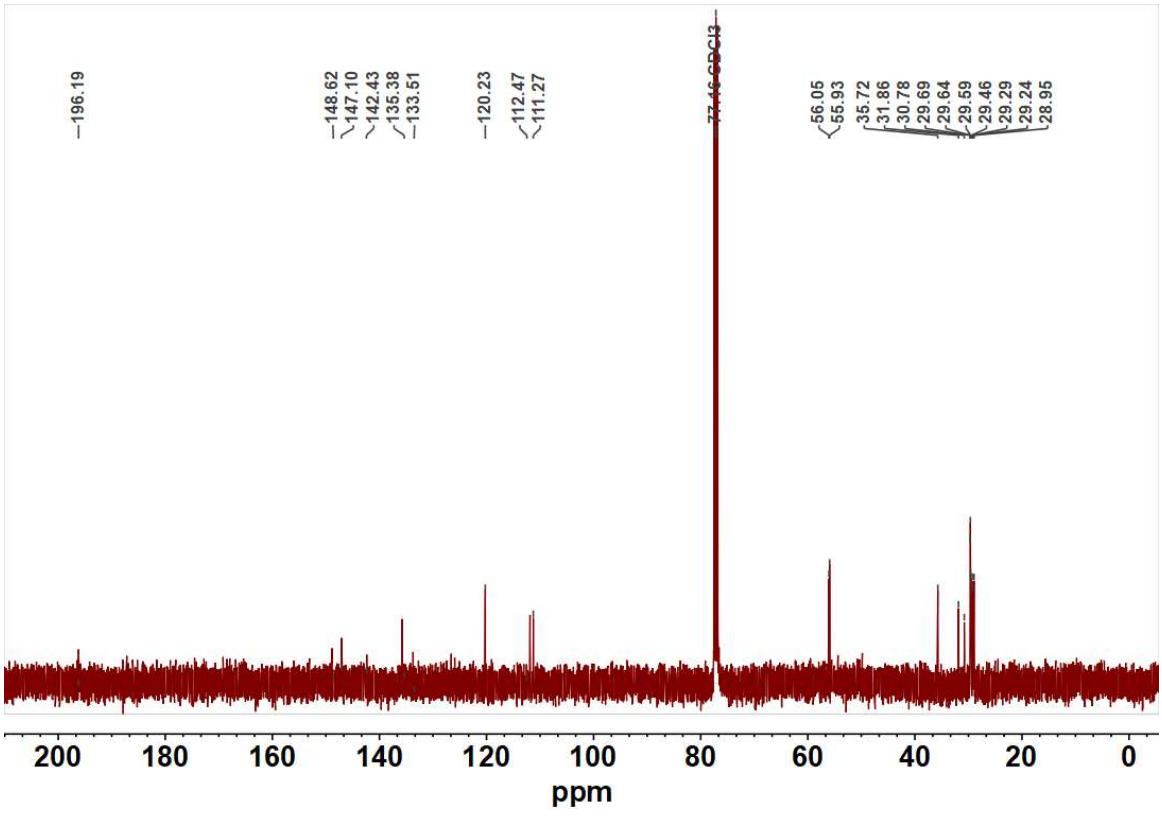

Figure 60: ^{13}C-NMR of 11-(3,4-dimethoxyphenyl)undecyl ethanethioate.

The ^{13}C spectrum shows a newly added signal at 196.19 pm, which can be assigned to a carbonyl carbon and also confirms the nucleophilic substitution.

Synthesis of 4-(11-mercaptoundecyl)benzene-1,2-diol

In the last reaction step, the aromatic methyl ethers were split with the aid of boron tribromide (BBr_3), and then the thioacetate was converted to thiol by acidic hydrolysis.

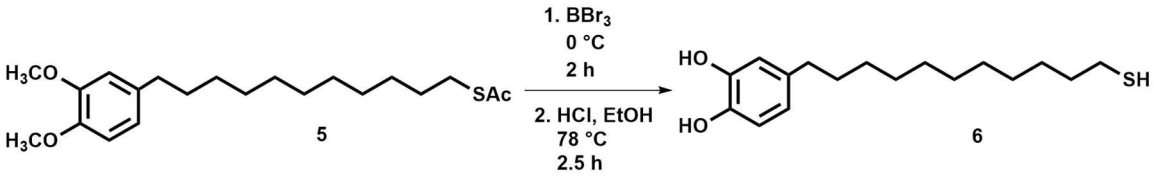

Figure 61: Reaction scheme of 4-(11-mercaptoundecyl)benzene-1,2-diol.

Using IR spectroscopy, the presence of aromatic hydroxyl groups could be detected by bands at 3352 cm^{-1} and 1210 cm^{-1}. Additionally, the carbonyl valence vibration at 1691 cm^{-1} of the protected thiol of the educt is no longer detectable.

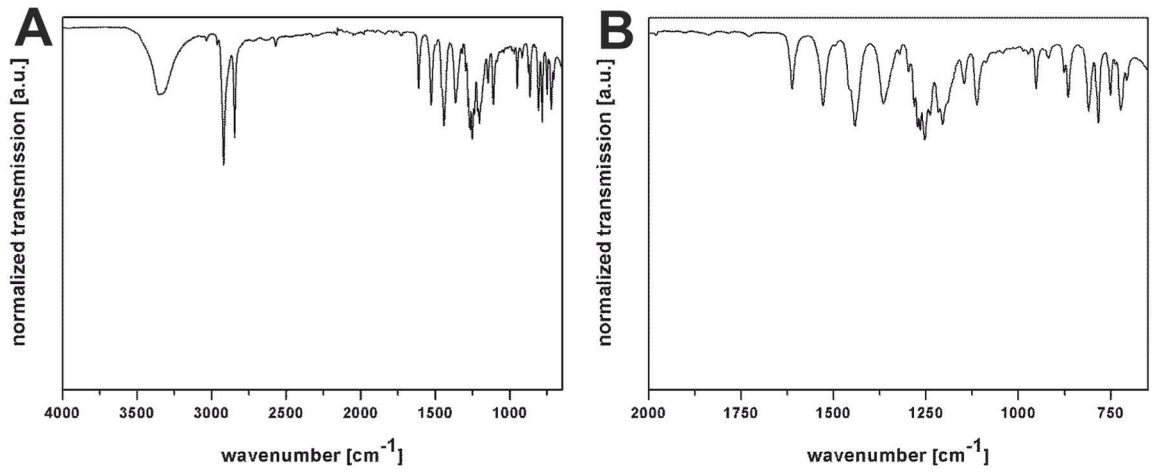

Figure 62: IR-spectra of 4-(11-mercaptoundecyl)benzene-1,2-diol.

Further bands in the IR spectrum could be clearly assigned to the desired structure (see Table 23).

Table 23: Assignment of the prominent oscillations of 4-(11-mercaptoundecyl)benzene-1,2-diol.

wavenumber [cm^{-1}]	assignment
3352	-O-H valence of phenol
3032	aromatic =C-H valence
2918 and 2847	aliphatic $–CH_2$ valence
2569	-S-H valence of thiol
1612	ring vibration
1443	aliphatic $–CH_2$ deformation
1210	-C-O valence of a phenol
810	=C-H deformation of 1,4- disubstituted benzene
782 and 707	=C-H deformation of 1,3-disubstituted benzene
750	=C-H deformation of 1,2-disubstituted benzene

Using NMR spectroscopy, the structure of the target molecule could be completely elucidated. In addition to the ^{1}H- and ^{13}C- spectra, further coupling experiments were used (^{1}H-^{1}H-COSY, ^{1}H-^{13}C-HSQC, ^{1}H-^{13}C-HMBC, see 4.5).

After the reaction, no signals for the methoxy groups of the aromatic ethers and the methyl group of the thioacetate can be detected in ^{1}H-NMR, which is a clear indication of successful ether cleavage and acid hydrolysis. At the same time, the methylene groups become more chemically similar to each other, so that the number of signals in ^{1}H-NMR decreases, but the multiplicity of signals increases. The signals can therefore only be assigned with the help of coupling experiments.

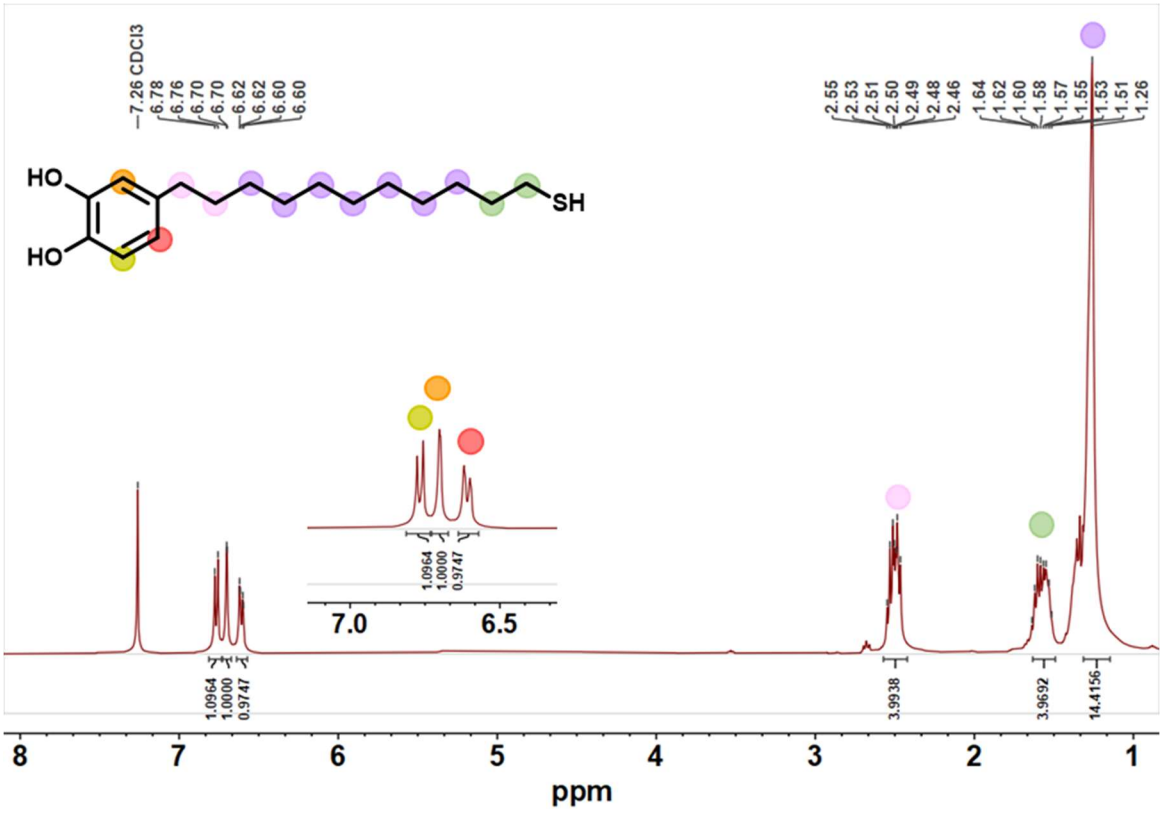

Figure 63: ^{1}H-NMR of 4-(11-mercaptoundecyl)benzene-1,2-diol. Full spectrum see 4.5.

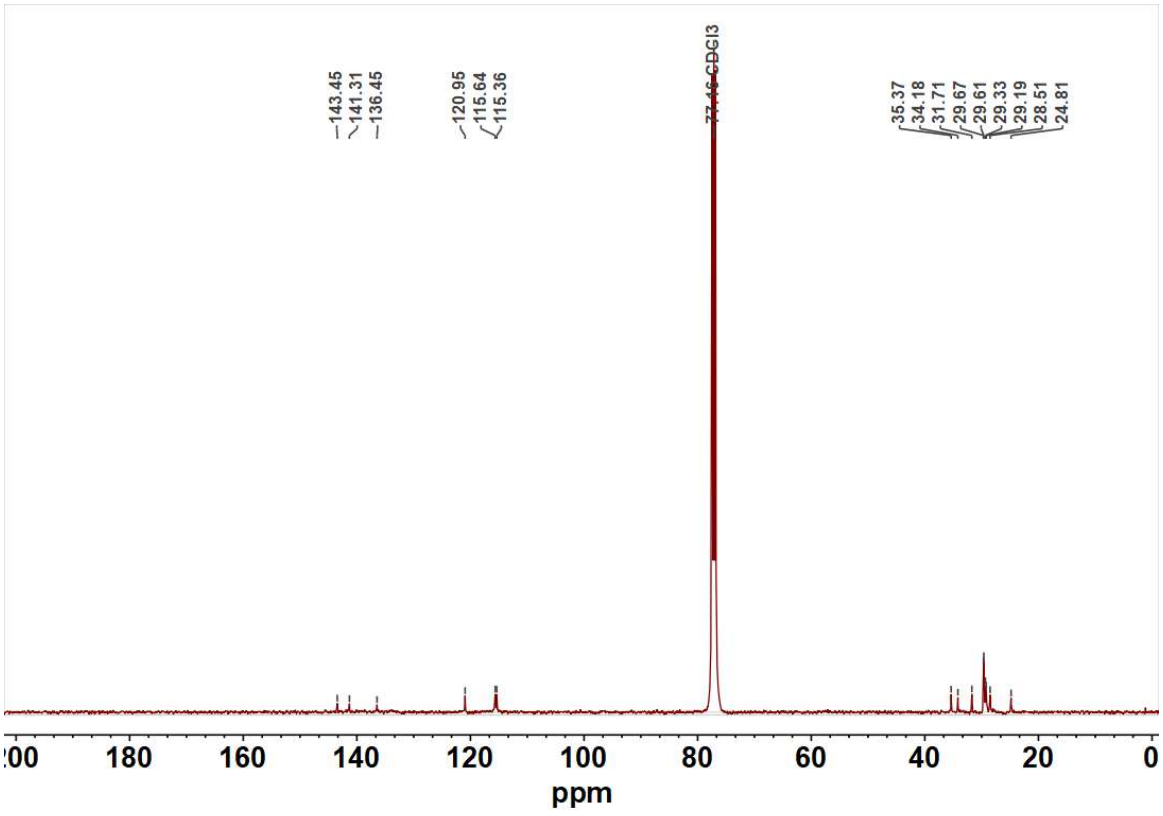

Figure 64: ^{13}C-NMR of 4-(11-mercaptoundecyl)benzene-1,2-diol.

Since the ^{13}C spectrum shows no longer the signals at 55.93 ppm and 56.05 ppm, which were assigned to the C atoms of the methyl groups, it can be assumed, that the deprotection of the hydroxyl groups was successful. Also the signal at 196.19 ppm of the protecting group is no longer apparent.

To substantiate the discussed results, a mass spectroscopy was executed.

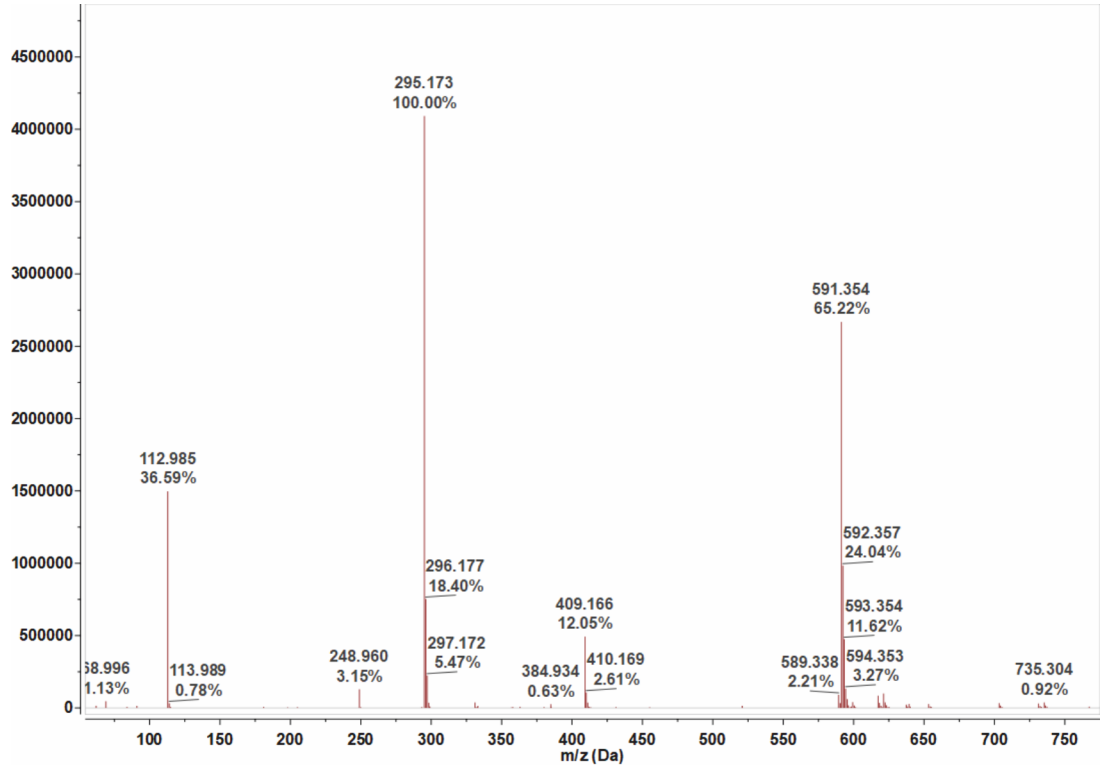

Figure 65: Mass spectra of 4-(11-mercaptoundecyl)benzene-1,2-diol.

The expected molar mass of 4-(11-mercaptoundecyl)benzene-1,2-diol is calculated 296.5 g mol^{-1}. The mass spectra (Figure 65) shows the most intensive peak at a m/z of 295.173 Da. This corresponds to 4-(11-mercaptoundecyl)benzene-1,2-diol. Another intensive peak is detectable at a m/z of 591.354 Da, which can be explained with the dimerised 4-(11-mercaptoundecyl)benzene-1,2-diol.

4.2.5. Synthesis and characterisation of heterotrimeric nanoparticles

In a further step, heterotrimeric nanoparticles should be synthesised. One strategy was to nucleate a second compound onto the surface of the Au domain of already synthesised Janus particles (TiO_2 onto Au@Fe_3O_4 and Fe_3O_4 onto Au@ZnO). The

other strategy was to connect Janus particles with single nanoparticles *via* surface functionalisation with the aid of the synthesised bifunctional molecule 4-(11-mercaptoundecyl)benzene-1,2-diol. Both strategies will be discussed with the aim to synthesise TiO_2@Au@Fe_3O_4 and ZnO@Au@Fe_3O_4 heterotrimeric nanoparticles.

Synthesis of TiO_2@Au@Fe_3O_4 nanoparticles

Like described by *Seh et al*. a synthesis of Au@TiO_2 Janus particles was executed. To achieve this, Au nanoparticles were synthesised using a citrate reduction method. After surface functionalisation with hydroxypropyl cellulose the reaction was pursued by adding titanium diisopropoxide bis(acetylacetonate).[132] Several approaches led to following results:

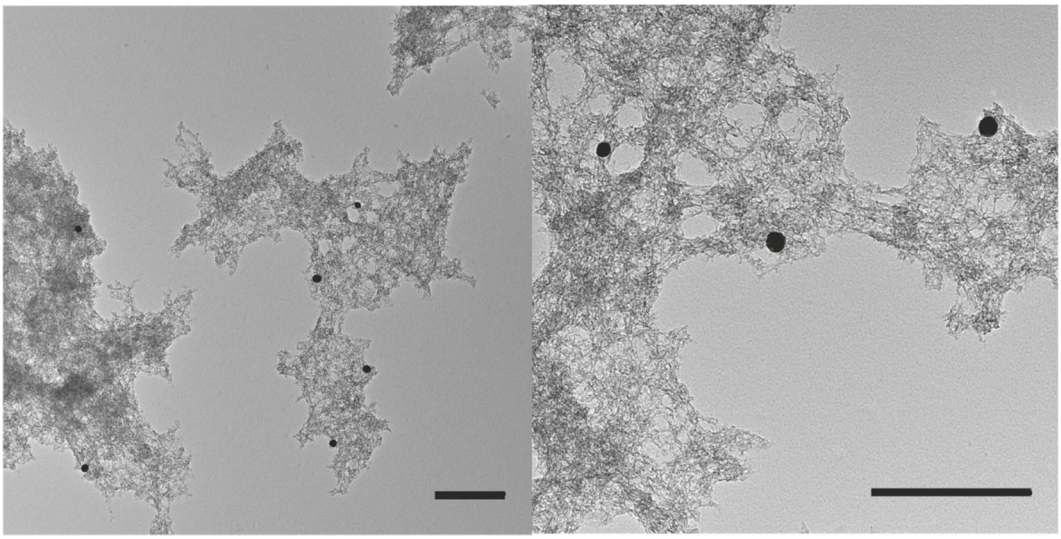

Figure 66: Typical TEM images of syntheses executed like described by [132] (scale bar 250 nm).

It seems that the hydrolysis of the titanium precursor is too fast and uncontrolled. After dilution of titanium precursor to a 100 mM solution and adding in four portions the following results were obtained:

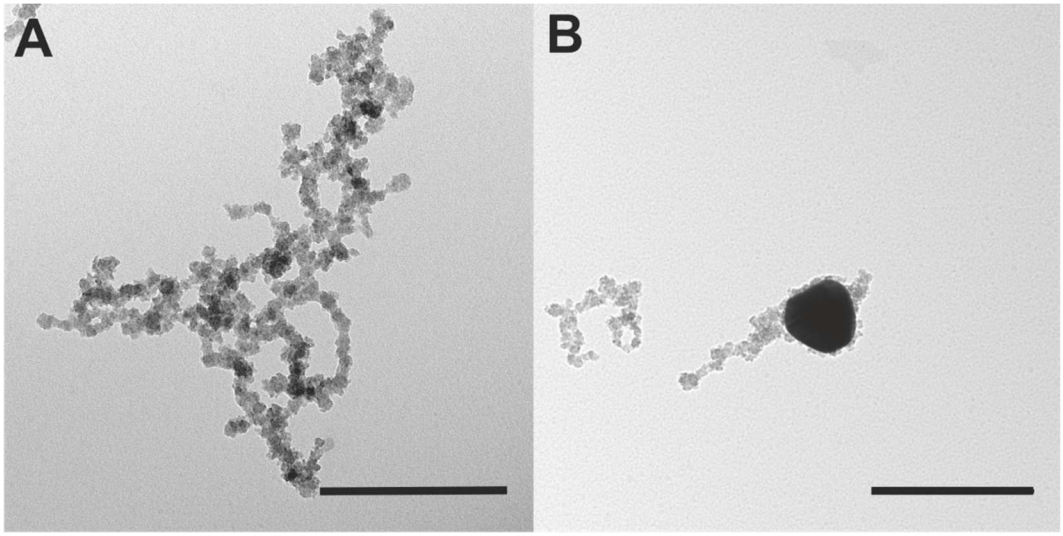

Figure 67: Typical TEM images of syntheses executed like described by [132] with modification of titanium precursor concentration and addition procedure (scale bar 250 nm).

The modifications of the synthesis led to more controlled procedure. A heterogeneous nucleation of the titanium compound onto the surface of the gold nanoparticles could be observed, but no epitaxial growth. Rather, the whole nanoparticle gets coated so that the results more be like core-shell nanoparticles. This result is not desired, since a third compound, the Fe_3O_4 domain, should still be grown onto the Au nanoparticle.

In order to still synthesise the heterotrimeric TiO_2@Au@Fe_3O_4 nanoparticles the anatase nanoparticles were surface functionalised with the bifunctional ligand 4-(11-mercaptoundecyl)benzene-1,2-diol, which could be observed by changing of the colour of the reaction mixture while functionalisation. The titanium(IV) dioxide nanoparticles can be surface functionalised with catechol derivates, while Au nanoparticles can be functionalised with thiol compounds.[133,134] Then, the functionalised anatase nanoparticles were dropped to a solution containing the Au@Fe_3O_4 Janus particles.

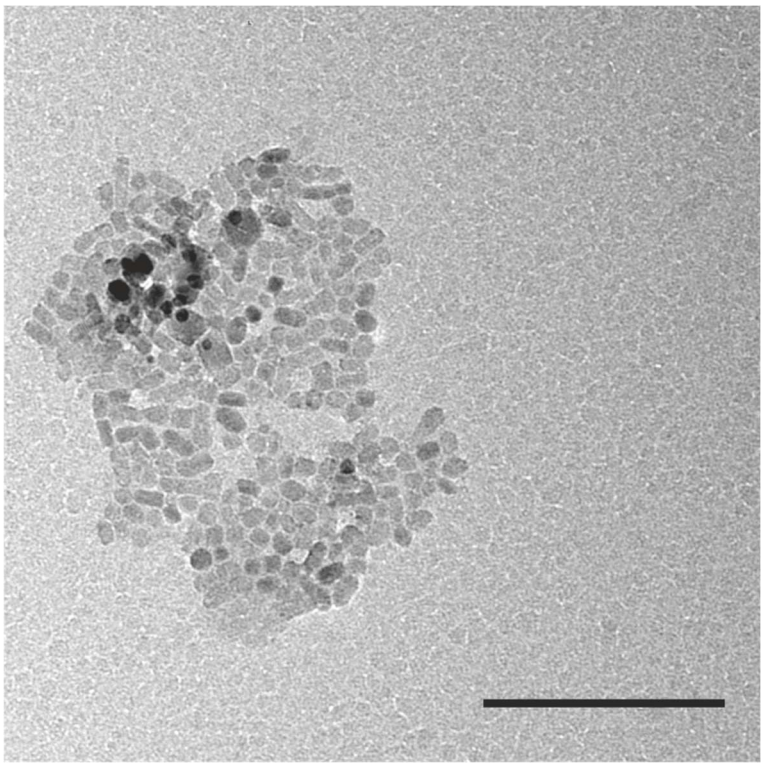

Figure 68: TEM image of TiO_2@Au@Fe_3O_4 synthesis approach (scale bar 100 nm).

The TEM image shows a typical result of an approach in which the anatase nanoparticles should be connected with Au@Fe_3O_4 Janus particles. It can be seen, that the two types of nanoparticles could be brought into close contact with each other. In addition, agglomerates with many TiO_2 nanoparticles were built. It seems like the functionalisation grade of the nanoparticles is too high, so that too many ligands are on the surface of the nanoparticles and no targeted connection can be constructed. Despite several reaction approaches with different concentrations of ligand no isolated heterotrimeric nanoparticle systems could be obtained.

Since the Au@Fe_3O_4 Janus particles and the bifunctional ligand 4-(11-mercaptoundecyl)benzene-1,2-diol could be synthesised successfully, the functionalisation procedure should be optimised. Although the ligand concentration was decreased no satisfying results were obtained. To optimise the procedure TiO_2 nanoparticles could be immobilised transitionally before surface functionalisation. The functionalisation would occur directionally and only present one direction for connection with the Au domain of the Janus particles.

Synthesis of ZnO@Au@Fe_3O_4 nanoparticles

As described above the goal was to synthesise a heterotrimeric nanoparticle system with the aid of the bifunctional ligand 4-(11-mercaptoundecyl)benzene-1,2-diol. Therefore, the synthesis strategy has to be changed. First the Fe_3O_4 nanoparticles have to be functionalised before dropping them into a dispersion containing Au@ZnO Janus particles.

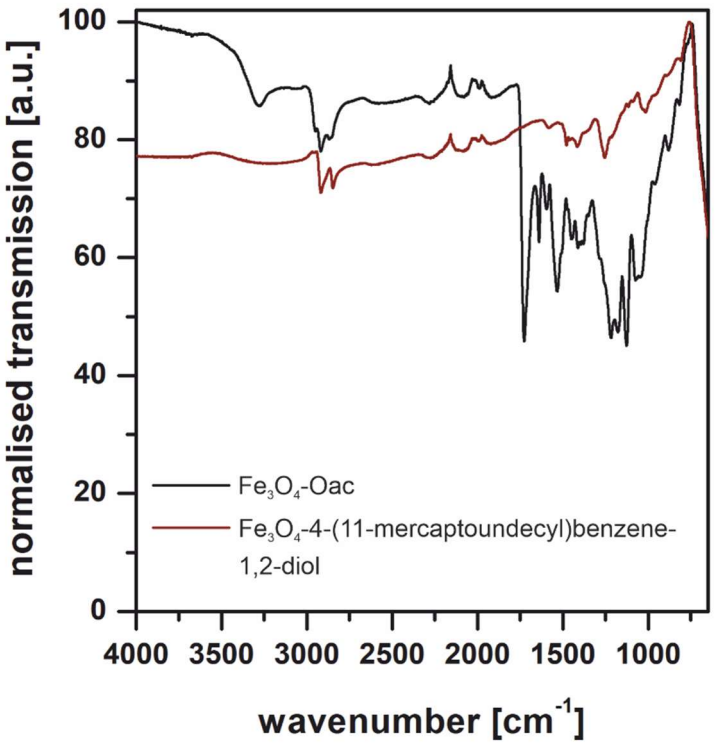

Figure 69: IR spectra of Fe_3O_4 nanoparticles obtained from non-polar synthesis (black) and of surface functionalised Fe_3O_4 nanoparticles (red) with 4-(11-mercaptoundecyl)benzene-1,2-diol.

The IR spectra (Figure 69) shows the spectra of Fe_3O_4 nanoparticles before (black) and after (red) surface functionalisation. While the nanoparticles exhibit a strong band at 1727 cm^{-1} before functionalisation, which can be assigned to -C=O valence vibration of carbonyl groups of oleic acid, they do not longer show this band after functionalisation. Since the background of the measurement of the functionalised nanoparticles is prominent no explicit assignment of the IR bands can be made, but the IR spectra show clearly, that the surface coating changed. Additionally, no IR bands of hydroxyl groups are detectable, so for the case that the ligand exchange was successful the interaction was like expected.

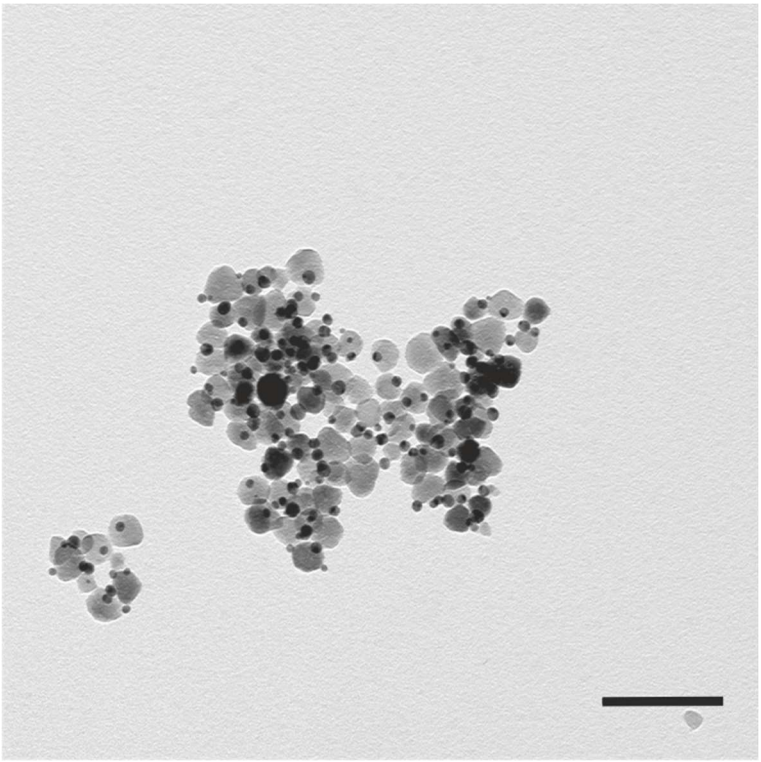

Figure 70: Typical TEM image of a synthesis approach of ZnO@Au@Fe_3O_4 *via* surface functionalisation with 4-(11-mercaptoundecyl)benzene-1,2-diol (scale bar 100 nm).

As can be seen in Figure 70 the synthesis approach *via* surface functionalisation did not led to the desired isolated heterotrimeric nanostructures. Here, agglomerates of nanoparticles are observable. Despite several approaches no ZnO@Au@Fe_3O_4 nanoparticles could be synthesised. The surface functionalisation process should be improved like discussed above.

To combine the advantages of both Janus particle types (Au@Fe_3O_4 and Au@ZnO), the most clever strategy is to connect all three compounds *via* heterogeneous nucleation and epitaxial growth. The improved properties of the Au@ZnO Janus particles compared to the ZnO nanoparticles, as well as the better kinetic properties of Au@Fe_3O_4 compared to Fe_3O_4 nanoparticles could be explained by electronic synergistic effects.[79] To achieve this effect, an interface between the Au domain and the ZnO as well as the Fe_3O_4 domain is essential. As discussed in 4.2.1 a nucleation of a compound onto the surface of Au nanoparticles led to an electron deficit in the Au domain, which influences the synthesis of another domain and the nucleation process of this compound onto the surface of the Au domain. Also, it can influence the kinetic properties, which are not assessable. Nevertheless, some attempts have been made to synthesise a

heterotrimeric nanoparticle system with the compounds ZnO, Au and Fe_3O_4 *via* heterogeneous nucleation and epitaxial growth. The most prominent examples are shown in Figure 71.

Standard procedure:

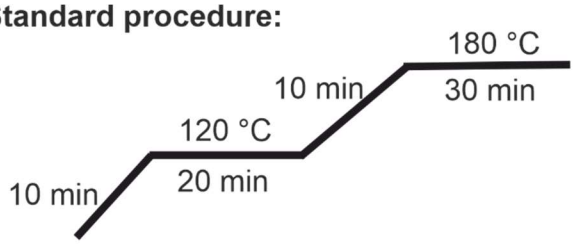

20 mg $HAuCl_4 \cdot 3\ H_2O$
109 mg $Zn(ac)_2 \cdot 2\ H_2O$
2 mL benzyl alcohol
4 mL 1-octadecen
2 mL oleylamine

A
standard procedure
+ addition of iron(III) acetylacetonate
+ 2 mL oleic acid

scale bar: 200 nm

B
standard procedure
+ addition of iron(0) pentacarbonyle
after 30 minutes

scale bar: 100 nm

C
standard procedure
+ addition of iron(III) oleate

scale bar: 100 nm

D
standard procedure
+ addition of iron(III) acetylacetonate
+ 2 mL oleic acid
after 30 minutes; up to 200 °C in 5 min
for 1 h

scale bar : 200 nm

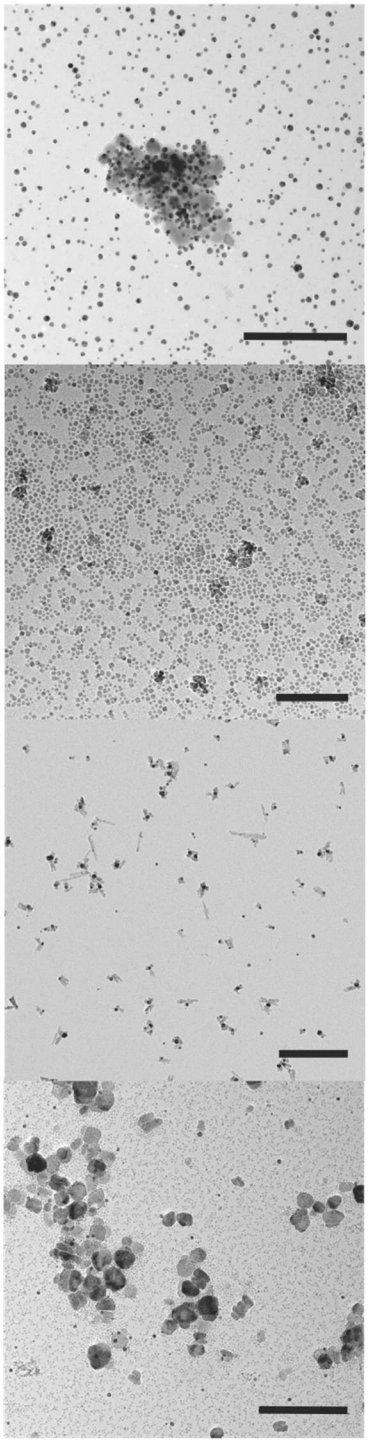

Figure 71: Overview about some synthesis approaches for the synthesis of ZnO@Au@Fe_3O_4 *via* heterogeneous nucleation.

As can be seen in Figure 71 depending on the iron precursor different synthesis results are obtained. The most promising is synthesis approach A. Here, Janus particles are formed, but no heterotrimeric nanostructures, while in the other cases no defined Janus particles are obtained. When using iron(0) pentacarbonyl as iron precursor only one type of nanoparticle is observable. In case of using iron(III) oleate as precursor some structures can be obtained, which seem to be heterostructures built by heterogeneous nucleation. Since approach A was the most promising, synthesis different variations of this were conducted, e.g. the addition of iron(III) acetylacetonate ($Fe(acac)_3$) in oleic acid after 30 minutes, to separate the synthesis of Au nanoparticles. As can be seen in Figure 71D this synthesis do not led anymore to uniform Janus particles as in approach A. A follow up reaction can be expected, since Janus particles were obtained when adding $Fe(acac)_3$ before starting the reaction and with standard heating program.

Here, further experiments on basis of approach A have to be conducted to obtain heterotrimeric ZnO@Au@Fe_3O_4 nanostructures. When obtained, these nanostructures have to be tested respective their catalytic activity, since the catalytic properties of all single compounds could be proven. On basis of presented results the simulation of a reaction cascade should be possible.

4.3. Conclusion

To mimic reaction cascades it is desirable to build up multimeric nanoparticle systems with different compounds, which catalyse different reaction step within a reaction cascade. Here the synthesis of model systems, like TiO_2@Au@Fe_3O_4 and ZnO@Au@Fe_3O_4 was attempted. The photocatalytic production of hydrogen peroxide with the aid of TiO_2 and ZnO nanoparticles could be proved as well as the peroxidase-like activity of Au@Fe_3O_4 Janus particles. The synthesis of Au@TiO_2 Janus particles as described in the literature failure. A synthesis of the heterotrimeric system TiO_2@Au@Fe_3O_4 *via* surface functionalisation was executed, but has to be improved.

Since it could be shown that Au@Fe_3O_4 Janus particles exhibit better kinetic properties respective their peroxidase-like catalysis compared to Fe_3O_4 nanoparticles, and Au@ZnO Janus particles produce tenfold more hydrogen

peroxide photocatalytically compared to ZnO nanoparticles, it is of great interest to combine these three compounds in one nanoparticle system. The synthesis of the heterotrimeric nanoparticle system ZnO@Au@Fe_3O_4 *via* surface functionalisation was executed, but has to be improved as well. To obtain a nanoparticle system with the best kinetic properties a system like ZnO@Au@Fe_3O_4, which is synthesised by heterogeneous nucleation and epitaxial growth, is desirable. Here the optimised kinetic properties could be used, since the isolated nanoparticles show less good kinetic properties.

To synthesise this system, more synthesis approaches should be done, in which Fe_3O_4 should nucleate on the Au surface of Au@ZnO Janus particles with variation of the concentrations of the surface ligands oleylamine and oleic acid. The ratio of both is crucial for the generation of ZnO@Au@Fe_3O_4. If too much oleic acid is used, the synthesis of Fe_3O_4 nanoparticles is promoted, since their stabilisation is increased. In case of an oleylamine concentration which is too low, the stabilisation of the Au domain of the Janus particles is decreased and the domain can underlie the Ostwald ripening. To avoid side reactions an iron precursor should be chosen, which decomposes at a temperature near the temperature, where the Au@ZnO Janus particles were prepared (180 °C), e.g. iron(III) acetylacetonate.

Besides the topic of prebiotic chemistry, such a system could be interesting in combination of ZnO@Au@CeO_{2-x} or TiO_2@Au@CeO_{2-x}. Cerium(IV) oxide nanoparticles are prominent for their haloperoxidase-like activity, which can reduce biofouling.[54] As this catalytic activity is dependent on hydrogen peroxide, it would be a benefit to combine CeO_{2-x} nanoparticles with another compound, which can produce this photocatalytically. The synthesis of Au@CeO_{2-x} is already reported by *Piella et al*.[135] Since CeO_{2-x} nanoparticles should be applied in marine environment the TiO_2@Au@CeO_{2-x} system should be preferred, as ZnO dissolves in water in long-term.[118,136]

4.4. Experimentals

4.4.1. Materials

(9*Z*)-Octadecenoic acid (oleic acid, OAc, $C_8H_{34}O_2$, technical grade 90 %, Sigma-Aldrich), 1,2-dimethoxybenzene ($C_8H_{10}O_2$, >99 %, TCI), 11-bromoundecanoic acid ($C_{11}H_{21}BrO_2$, 98+%, Fisher), 1-octadecene ($C_{18}H_{36}$, 90 %, Sigma-Aldrich), acetone (C_3H_6O, technical grade, Sigma-Aldrich), aluminium(III) chloride ($AlCl_3$, >98 %, TCI), ammonia (NH_3, 25 %, VWR), ammonium ferrous sulphate hexahydrate ($(NH_4)_2Fe(SO_4)_2 \cdot 6H_2O$, 99+ %, Acros), benzyl alcohol (BA, C_7H_8O, anhydrous, 99.8 %, Sigma-Aldrich), Bis(2,4-pentanedionato)bis(2-propanolato)titanium(IV) ($C_{16}H_{28}O_6Ti$, 75% in isopropanol, TCI) borane-tert-butylamine complex (TBAB, $C_4H_{14}NB$, 97 %, Sigma-Aldrich), boron tribromide (BBr_3, ≥ 99 %, Fisher), cyclohexane (C_6H_6, 99.5 %, Fisher), dichlormethane (CH_2Cl_2, ≥99.8 %, Fisher), diethyl ether ($(C_2H_5)_2O$, ≥99.5 %, Fisher), D-sorbitol ($C_6H_{14}O_6$, ≥ 98 %, Sigma-Aldrich), ethanol (C_2H_5OH, Fisher, 99 %), ethyl acetate ($C_4H_8O_2$, ≥99.8 %, Fisher), hydrochloric acid (HCl, 37 %, VWR), hydrogen tetrachloroaurate(III) hydrate ($HAuCl_4 \cdot 3H2O$, 99,99 %, Alfa Aesar), imidazole ($C_3H_4N_2$, ≥99.5 %, Sigma-Aldrich), iron(III) acetylacetonate ($Fe(C_5H_7O_2)_3$, ≥97 %, Sigma-Aldrich), iron(0) pentacarbonyl ($Fe(CO)_5$, Sigma-Aldrich; >99.99% trace metals basis), isopropanol (C_3H_7OH, 100 %, VWR), magnesium sulphate ($MgSO_4$, 97 %, Acros), methanol (CH_3OH, ≥ 99.8 %, Fisher), oleylamine ($C_{18}H_{37}N$, > 50 %, TCI), potassium thioacetate (C_2H_3KOS, 98 %, Acros), sodium borohydride ($NaBH_4$, 99 %, Acros), sodium hydrogen carbonate ($NaHCO_3$, ACS, Sigma-Aldrich), sodium oleate ($C_{18}H_{33}NaO_2$, ≥82 %, Sigma-Aldrich), sulphuric acid (H_2SO_4, 95 %, Fisher), tetrahydrofuran (THF, C_4H_8O, 99.8 %, Fisher), thionyl chloride ($SOCl_2$, ≥99 %, Fluka), trisodium citrate dihydrate ($C_6H_5Na_3O_7 \cdot 2H_2O$, ≥99 %, Merck), xylenol orange tetrasodium salt (XO, $C_{31}H_{28}N_2Na_4O_{13}S$, Merck), zinc(II) acetate dihydrate ($Zn(ac)_2 \cdot 2\ H_2O$, ACS, Acros).

4.4.2. Synthesis

Synthesis of gold nanoparticles

The gold nanoparticles were synthesised as described by *Peng et al.* with some modifications.[108] Hydrogen tetrachloroaurate(III) hydrate (118.1 mg, 0.30 mmol)

was dissolved in oleylamine (10 mL) and cyclohexane (10 mL) in a 100 mL three-necked round bottom flask and stirred for ten minutes under argon at room temperature (400 rpm). The borane-tert-butylamine complex (52.3 mg, 0.60 mmol) was dissolved in cyclohexane (1 mL) and oleylamine (1 mL) using sonification and then saturated with argon at room temperature for two minutes. This solution was added to the orange hydrogen tetrachloroaurate(III) hydrate solution and stirred for two hours under argon at room temperature. From the dark red reaction solution, the gold nanoparticles were precipitated with an ethanol-methanol mixture (1:1) containing 10 % oleylamine and centrifuged (9000 rpm, 10 min). The nanoparticles were washed with the ethanol-methanol mixture containing 10 % oleylamine and redispersed in cyclohexane.

Synthesis of Au@Fe_3O_4 Janus particles

Gold nanoparticles (20 mg, 0.10 mmol) were dissolved in 1-octadecene (20 mL), oleylamine (7 mL) and oleic acid (7 mL) in a 100 mL three-neck flask under argon and stirred (400 rpm) at room temperature. The solution was then heated up to 120 °C within ten minutes and was kept at a constant temperature for 20 minutes. Iron(0) pentacarbonyl (0.1 mL, 0.74 mmol) was added and the mixture was heated up to 310 °C within 30 minutes. The temperature was kept constant for one hour. After cooling the reaction solution to room temperature, the Janus particles were precipitated with an isopropanol-acetone mixture (1:1) and washed with this mixture after centrifugation (9000 rpm, 10 min). The Janus particles were redispersed in cyclohexane.

Synthesis of ZnO nanoparticles

The ZnO nanoparticles were synthesised as described by *Tahir et al*.[131] Zinc(II) acetate dihydrate (109.0 mg, 0.5 mmol) was dissolved in benzyl alcohol (7 mL) and oleylamine (2 mL). The solution was stirred (400 rpm) and heated up to 180 °C within 30 minutes. This temperature was kept constant for 30 minutes. After cooling to room temperature the ZnO nanoparticles were precipitated by adding ethanol, centrifuged (9000 rpm, 10 minutes) and washed with ethanol. The obtained nanoparticles were dried in an electric oven at 70 °C for 24 hours.

Synthesis of Au@ZnO Janus particles

The Au@ZnO Janus particles used in further experiments were synthesised as described by *Tahir et al.* with some modifications.[131] See Table 18 for all variations. Hydrogen tetrachloroaurate(III) hydrate (20 mg, 0.05 mmol) and zinc(II) acetate dihydrate (109.0 mg, 0.5 mmol) were dissolved in benzyl alcohol (2 mL), oleylamine (2 mL) and 1-octadecene (4 mL). The solution was stirred (400 rpm), heated up to 120 °C within 10 minutes and kept at this temperature for 20 minutes. Afterwards the temperature was increased to 180 °C within 10 minutes and stirred here for 30 minutes. After cooling to room temperature, the Janus particles were precipitated by adding ethanol. After centrifugation (9000 rpm, 10 minutes), the nanoparticles were washed with ethanol and dried in an electric oven at 70 °C for 24 hours.

Other synthesis approaches described in 4.2.3 were executed like described here with other compositions (see Table 18).

Surface functionalisation of ZnO nanoparticles and Au@ZnO Janus particles

The surface functionalisation was carried out as described by *Nawaz et al*. with some modifications.[131] The nanoparticles/ Janus particles were dispersed in cyclohexane (1 mg mL^{-1}) *via* sonification. A solution containing imidazole and chloroform (1 mg mL^{-1}) was prepared. Both were combined in a ratio of 1:1. After stirring (1000 rpm) for one hour at room temperature, the particles were centrifuged (9000 rpm, 10 min). After washing, the nanoparticles were stored in water.

Synthesis of TiO_2 nanoparticles

The synthesis of TiO_2 nanoparticles was carried out by [redacted] of the [redacted] group as described by *Dinh et al*. with small modifications described by *Schechtel et al*.[133,137]

Synthesis of 11-bromoundecanoyl chloride[138]

11-Bromoundecanoic acid (12.58 g, 0.05 mol) and thionyl chloride (13.76 mL, 0.19 mol) were dissolved in dichlormethane (CH_2Cl_2, 120 mL). The reaction mixture was heated to reflux and stirred (400 rpm) overnight. After cooling to room

temperature the solution was concentrated *in vacuo* to yield the product (12.9 g, 96 %).

^{1}H NMR (400 MHz, Chloroform-*d*): δ 3.40 (t, *J* = 6.8 Hz, 2H), 2.88 (t, *J* = 7.2 Hz, 2H), 1.84 (qi, *J* = 7.0 Hz, 2H), 1.70 (qi, *J* = 7.2 Hz, 2H), 1.41 (qi, *J* = 7.0, 5.1 Hz, 2H), 1.29 (s, 10H).

Synthesis of 11-bromo-1-(3,4-dimethoxyphenyl)undecan-1-one[138]

1,2-dimethoxybenzene (5.58 mL, 0.4 mol) and aluminium(III) chloride (6.39 g, 0.5 mmol) were added to a solution of 11-bromoundecanoyl chloride (12.36 g, 0.4 mol) and dichlormethane (215 mL) under inert argon atmosphere. The solution was heated to reflux for 19 h. After cooling to room temperature the mixture was poured in 5 M hydrochloric acid (100 mL). The solution was washed with water three times before the solvent was removed. The product was purified using column chromatography with cyclohexane:ethyl acetate (2:1) to obtain the product (10.1 g, 58 %).

^{1}H NMR (400 MHz, Chloroform-*d*): δ 7.58 (dd, *J* = 6.4 Hz, 1H), 7.53 (d, *J* = 2.0 Hz, 1H), 6.88 (d, *J* = 8.4 Hz, 1H), 3.95 (s, 3H), 3.94 (s, 3H), 3.40 (t, *J* = 6.8 Hz, 2H), 2.92 (d, *J* = 7.3 Hz, 2H), 1.85 (qi, *J* = 7.0 Hz, 2H), 1.72 (qi, *J* = 7.3 Hz, 2H), 1.29 (s, 12H).

^{13}C NMR (400 MHz, Chloroform-*d*): δ 199.80, 153.59, 149.49, 130.82, 123.14, 110.62, 110.40, 56.52, 56.43, 38.59, 34.52, 33.27, 29.82, 29.18, 28.60, 25.19.

Synthesis of 4-(11-bromoundecyl)-1,2-dimethoxybenzene[138]

4-(11-bromoundecyl)-1,2-dimethoxybenzene, sodium borohydride (4.91 g, 130 mmol) and aluminium(III) chloride (5.29 g, 21.9 mmol) were dissolved in THF (160 mL) in a three-neck flask. The mixture was stirred (400 rpm) and cooled down to 0 °C. 11-bromo-1-(3,4-dimethoxyphenyl) undecan-1-one (10 g, 25.9 mmol) was added. The mixture was stirred (400 rpm) for three days at room temperature. The solution was poured in dichlormethane and afterwards poured into a saturated sodium hydrogen carbonate solution. The organic layer was separated and extracted with dichlormethane (CH_2Cl_2). The combined organic extracts were washed with brine, dried over magnesium sulphate ($MgSO_4$) and concentrated *in vacuo* to obtain the product (6.27 g, 65 %).

^{1}H NMR (400 MHz, Chloroform-*d*): δ 6.82 – 6.76 (m, 1H), 6.72 (d, *J* = 2.0 Hz, 1H), 6.71 (d, *J* = 1.8 Hz, 1H), 3.88 (s, 3H), 3.86 (s, 3H), 3.42 – 3.39 (m, *J* = 2.3 Hz, 2H), 2.54 (t, *J* = 7.8 Hz, 2H), 1.85 (qi, *J* = 6.9 Hz, 2H), 1.40 (m, *J* = 7.1 Hz, 2H), 1.28 (s, 14H).

^{13}C NMR (400 MHz, Chloroform-*d*): δ 148.87, 147.13, 135.77, 120.25, 111.89, 111.28, 70.77, 56.07, 55.94, 35.72, 34.21, 32.97, 31.86, 29.66, 29.56, 29.46, 28.90, 28.31, 26.65.

Synthesis of 11-(3,4-dimethoxyphenyl)undecyl ethanethioate[138]

Potassium thioacetate (2.88 g, 25.2 mmol) and 4-(11-bromoundecyl)-1,2-dimethoxybenzene (6.27 g, 16.9 mmol) were dissolved in THF (100 mL) in a round-bottomed flask. The mixture was heated under reflux for 2 h while stirring (400 rpm). Afterwards it was left to stir at room temperature overnight. The reaction mixture was poured into water and extracted with diethyl ether (Et_2O). The combined organic extracts were washed with water, dried over $MgSO_4$ and concentrated *in vacuo*. The obtained solution was purified by column chromatography using cyclohexane:ethyl acetate (10:1) to yield the product (2.6 g, 45 %).

^{1}H NMR (400 MHz, Chloroform-*d*): δ 6.79 (d, *J* = 8.7 Hz, 1H), 6.72 (d, *J* = 1.8 Hz, 1H), 6.70 (s, 1H), 3.87 (s, 3H), 3.85 (s, 3H), 2.86 (t, *J* = 7.4 Hz, 2H), 2.54 (t, *J* = 8.0 Hz, 2H), 2.32 (s, 3H), 1.57 – 1.52 (m, 4H), 1.28 (m, 14H).
^{13}C NMR (400 MHz, $CDCl_3$): δ 196.19, 148.62, 147.10, 142.43, 135.38, 133.51, 120.23, 112.47, 112.27, 56.05, 55.93, 35.72, 31.86, 30.78, 29.69, 29.64, 29.59, 29.46, 29.29, 29.24, 28.95.

Synthesis of 4-(11-mercaptoundecyl)benzene-1,2-diol

(11-(3,4-dimethoxyphenyl)undecyl) ethanethioate (2.33 g, 6.6 mmol) was dissolved in CH_2Cl_2 (45 mL) and cooled to 0 °C. Boron tribromide (BBr_3, 12.5 g, 49.9 mmol) was added slowly while stirring (400 rpm). The mixture was stirred additionally for two hours at room temperature. Water was added until no more gas evolution was observable. The mixture was poured into water and extracted with Et_2O. The combined organic extracts were washed with water, dried over $MgSO_4$ and concentrated *in vacuo*. The obtained brown powder was dissolved in ethanol (EtOH, 6.5 mL) and hydrochloric acid (10 M, 6.5 mL) and heated to reflux while

stirring. The temperature was kept for 2.5 hours. After cooling to room temperature, the mixture was diluted with Et_2O, washed with water, dried over $MgSO_4$ and concentrated *in vacuo* to obtain the product (1.7 g, 76 %).

^{1}H NMR (400 MHz, Chloroform-*d*): δ 6.77 (d, *J* = 8.0 Hz, 1H), 6.70 (d, 1H), 6.61 (d, *J* = 8.0 Hz, 1H), 2.55 – 2.46 (m, 4H), 1.64 – 1.51 (m, 4H), 1.26 (m, 14H).

^{13}C NMR (400 MHz, $CDCl_3$): δ 143.45, 141.31, 136.45, 120.95, 115.64, 115.36, 35.37, 34.18, 31.71, 29.67, 29.61, 29.33, 29.19, 28.51, 24.81.

Synthesis of Au@TiO_2 Janus particles

First, Au nanoparticles were synthesised like described by *Bastús et al*. with some modifications.[139] A solution containing trisodium citrate dihydrate (48.55 mg, 0.17 mmol) and MQW (75 mL) was prepared and heated up to 100 °C while stirring (1000 rpm). After 15 minutes of boiling a solution containing hydrogen tetrachloroaurate(III) hydrate (0.5 mL, 25 mM) was added. The temperature was kept constant for additional 10 minutes and then decreased to 90 °C. A trisodium citrate dihydrate solution (0.5 mL, 60 mM) was added and after 2 minutes a hydrogen tetrachloroaurate(III) hydrate solution (0.5 mL, 25 mM). The solution was stirred for 30 minutes at 90 °C. This procedure was repeated eight times.

After cooling to room temperature the obtained Au nanoparticles dispersion (10 mL) was added to a solution containing hydroxypropyl cellulose (10 mL, 17 wt%) and stirred (400 rpm) overnight at room temperature. Isopropanol (40 mL) was added as well as ammonia (1.25 mL, 25 wt%). Titanium diisopropoxide bis(acetylacetonate) (2mL) was dissolved in isopropanol (4 mL) and this solution was added to the Au nanoparticles dispersion. The reaction mixture was stirred (500 rpm) for 5 days.

The concentration of titanium diisopropoxide bis(acetylacetonate) solution as well as the adding procedure were varied to optimise the results.

Synthesis of heterotrimeric nanoparticles (TiO_2@Au@Fe_3O_4 and ZnO@Au@Fe_3O_4) *via* surface functionalisation

A solution of 4-(11-mercaptoundecyl)benzene-1,2-diol in chloroform (10 mL, 1 mg mL^{-1}) was dropped slowly to a dispersion containing TiO_2 or Fe_3O_4 nanoparticles (10 mL, 1 mg mL^{-1}) under stirring (1000 rpm). The mixture was stirred

overnight at room temperature. After centrifugation (9000 rpm, 10 minutes) the nanoparticles were washed with cyclohexane:chloroform (1:1) several times.

The surface functionalised nanoparticles were redispersed in chloroform and dropped slowly under stirring (1000 rpm) to a dispersion containing Au@Fe_3O_4 (in case of TiO_2 nanoparticles) or Au@ZnO Janus particles (in case of Fe_3O_4 nanoparticles). The nanostructures were collected by centrifugation (9000 rpm, 10 minutes) and washed with cyclohexane:chloroform (1:1).

Synthesis of iron(III) oleate

The iron(III) oleate was synthesised like described by *Park et al*. with some modifications.[74] Sodium oleate (36.5 g, 120 mmol) and iron(III) chloride hexahydrate (10.8 g, 40 mmol) were dissolved in MQW (60 mL), ethanol (80 mL) and cyclohexane (140 mL). The solution was heated to 70 °C under stirring (400 rpm) for 4 hours. After cooling to room temperature, the organic layer was separated and washed with MQW three times. The organic layer was concentrated in *vacuo* to obtain the product.

Synthesis of heterotrimeric nanoparticles (ZnO@Au@Fe_3O_4) *via* heterogeneous nucleation

The synthesis of ZnO@Au@Fe_3O_4 nanoparticles was executed like the synthesis of Au@ZnO Janus particles with some modifications. One approach included additionally $Fe(acac)_3$ (50.0 mg, 0.14 mmol) and oleic acid (2 mL), another Fe(III) oleate (44.6 mg; 0.05 mmol), while in two other synthesis approaches the iron precursor was added after 30 minutes. In one approach iron(0) pentacarbonyl (0.025 mL, 0.19 mmol) in oleic acid (2 mL) and in the other $Fe(acac)_3$ (52.7 mg, 0.15 mmol) in oleic acid (2 mL) was added. The last approach was heated after 30 minutes up to 200 °C in 5 minutes and this temperature was kept constant for one hour. The nanoparticles were precipitated after cooling to room temperature by adding ethanol, collected *via* centrifugation (9000 rpm, 10 min) and washed with ethanol.

4.4.3. Characterisation and kinetic measurements

XRD

The powder x-ray diffraction measurements were conducted on a STOE Stadi P X-ray diffractometer of STOE & Cie GmbH (Darmstadt, Deutschland) equipped with a MYTHEN 1 K detector of Dectris. As radiation source a Mo-K_α cathode was used. The data were analysed by using the software *Match!* 3 with the database COD REV218120 2019.09.10 and plotted with *OriginPro8*.

The data of the XRD pattern of anatase nanoparticles was provided by [redacted] of the [redacted] group.

TEM

The TEM measurements were conducted after applying the sample to a graphite-coated TEM mesh (Cu-300 mesh, Electron Microscopy Sciences, Hatfield, PA) on a Tecnai G2 Spirit from FEI with an acceleration voltage of 120 kV. It is equipped with a twin objective lens, a LaB_6 cathode and a CCD (charge coupled device) camera (2k x 2k). The evaluation was performed with the software *ImageJ*.

For the electron microscopic analysis of the nanoparticles, they were dispersed in cyclohexane in case of the Au and ZnO nanoparticles and Au@Fe_3O_4 and Au@ZnO Janus particles after synthesis but before the surface functionalisation was executed with the aid of sonification (concentration 1 mg mL^{-1}). 20 µL of the sample were applied to a TEM grid. After evaporation of the solvent at room temperature the samples were measured.

The TEM image of anatase nanoparticles were took and provided by [redacted] of the [redacted] group.

BET

The BET surfaces of the used nanoparticles were measured with a 3P Micro 300 (3P Instruments). For this the nanoparticle samples were dried under vacuum. Nitrogen was used as measuring gas. The data was analysed using the software Surface Area & Pore Size Analyser System (Version: 10.03.02).

UV-Vis

The nanoparticle scans were conducted on a Varian Cary5G UV/Vis spectrometer between 200 nm and 800 nm in a quartz glass cuvette (Hellma, type no. 110-QS).

First a cyclohexane baseline then the spectra of the nanoparticles (0.1 – 0.15 mg mL^{-1}) were measured.

FOX assay

A MilliQ water sample and nanoparticle dispersions (concentrations see Table 24) were prepared and irradiated for one hour with two LEDs (SSC VIOSYS CUN66B1B on Star Platine, LED-Tech, 365 nm). After radiation the dispersions were centrifuged to separate the nanoparticles. The supernatant (20 µL) was mixed with a solution containing of two solutions mixed in a ratio of 1:100. The first solution was containing of $(NH_4)_2Fe(SO_4)_2$ (25 mM) and sulphuric acid (2.5 M) while the second solution was containing of xylenolorange (125 µM) and sorbitol (100 mM). The mixture was incubated for 30 min at room temperature before measuring the extinction at 590 nm on an Infinite 200 Pro plate reader from TECAN. Additionally, flat bottom black 96-well plates from Greiner bio-one were used. For data analysis an external calibration with hydrogen peroxide was measured simultaneously.

Table 24: Concentration of nanoparticles dispersion for FOX assay.

Sample	Concentration mg mL^{-1}
TiO_2	1/3/5
ZnO	0.1
Au@ZnO	0.01

NMR

The NMR experiments were recorded on a Bruker DRX 400 MHz spectrometer. The samples were prepared in chloroform-*d*. The processing of the data was carried out with *Topspin* 1.3 and the evaluation of the spectra was done using *MestReNova* 10.0.2.

Infrared (IR) – spectroscopy

All IR measurements were carried out on the infrared spectrometer Thermo Scientific Nicolet iS10 FTIR Smart IR with Platinum-ATR (diamond crystal, one reflection) and the measurement software OMNIS 8.1.210. The evaluation of the measurement data was carried out with the software OriginPro8.

Mass spectrometry

The mass spectrometry measurement was conducted on an Agilent 6545 QTOF-MS.

4.5. Appendix

BET measurements of ZnO nanoparticles and Au@ZnO Janus particles

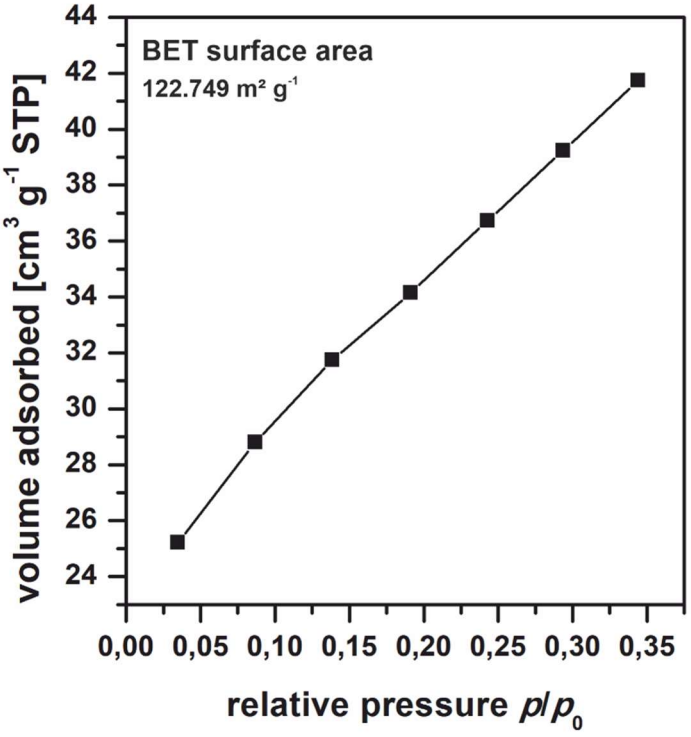

Supporting figure 4: BET measurement of ZnO nanoparticles.

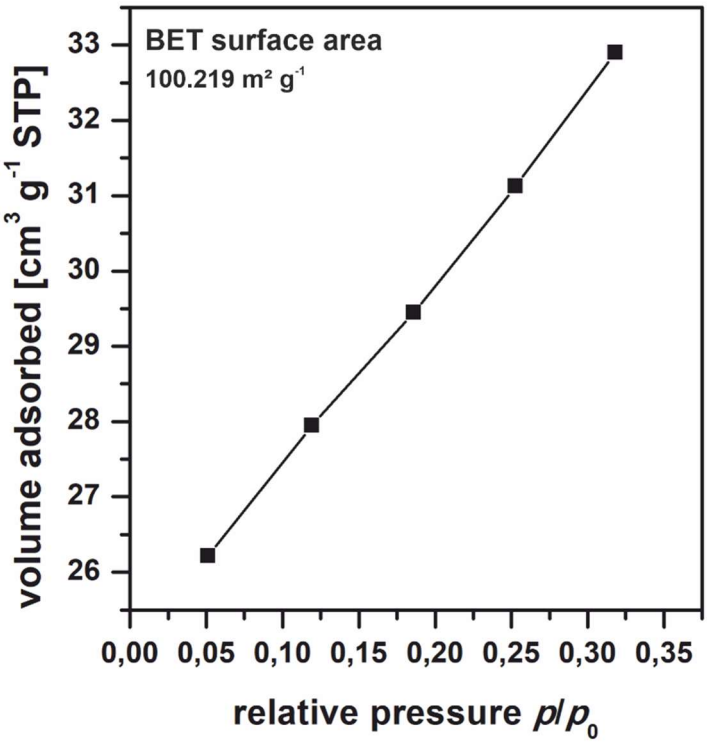

Supporting figure 5: BET measurement of Au@ZnO Janus particles.

FOX assay external calibration

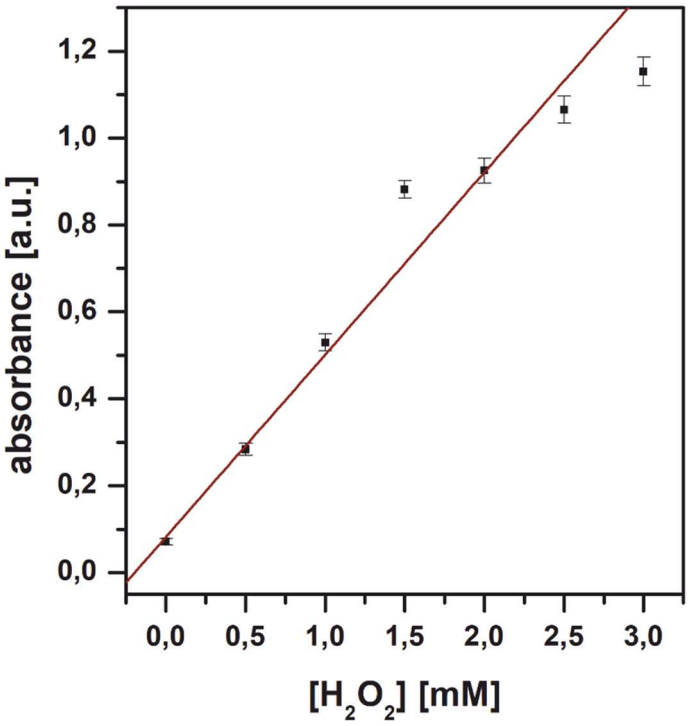

Figure 72: External seven point calibration of FOX assay with hydrogen peroxide for quantification of photocatalytic hydrogen peroxide production of anatase nanoparticles.

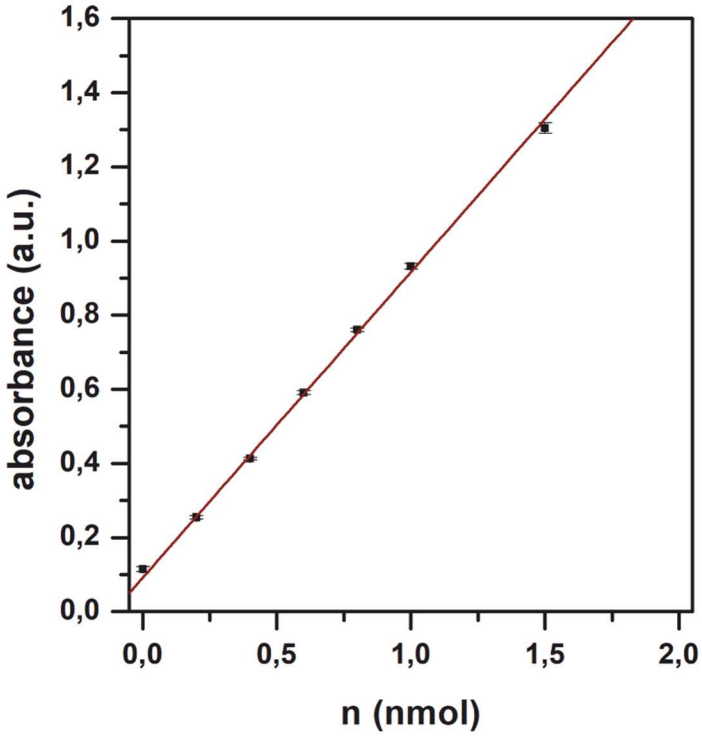

Figure 73: external seven-point calibration for FOX assay with hydrogen peroxide for measurement of hydrogen peroxide production of ZnO and Au@ZnO.

Additional spectra of 11-bromoundecanoyl chloride

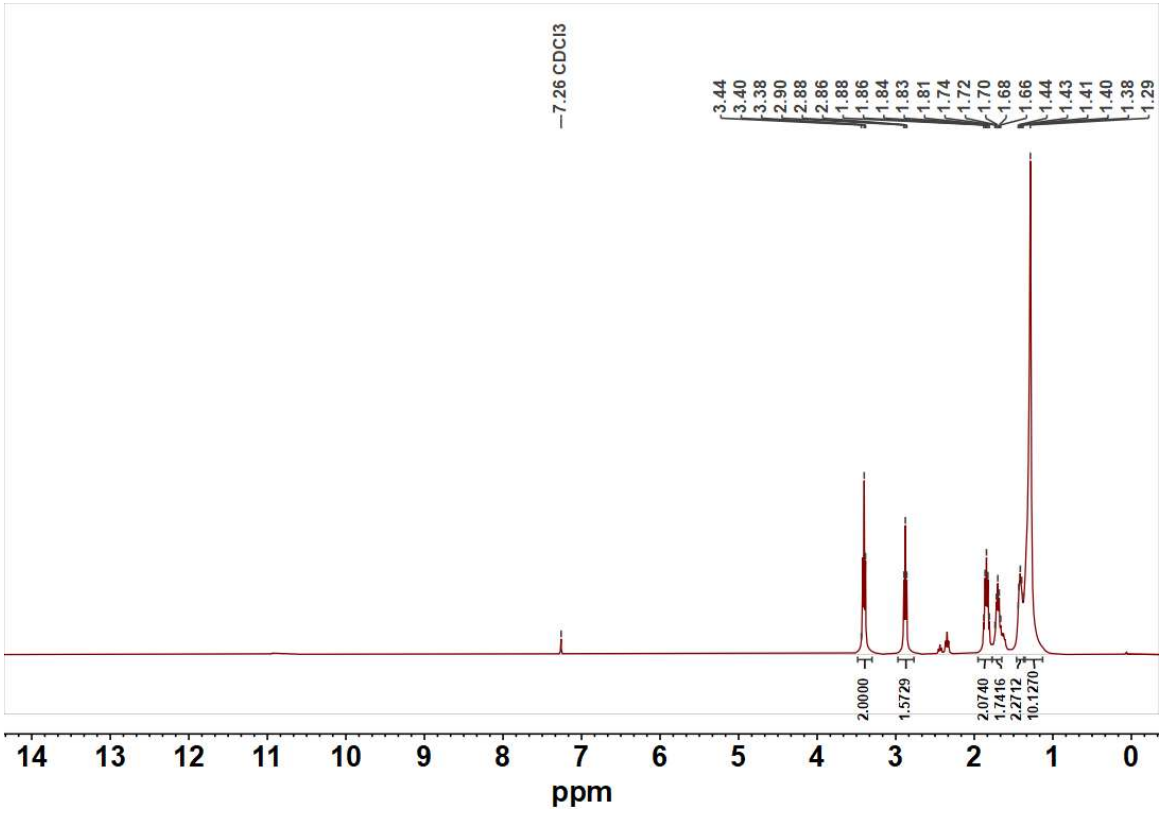

Supporting figure 6: ^{1}H-NMR of 11-bromoundecanoyl chloride.

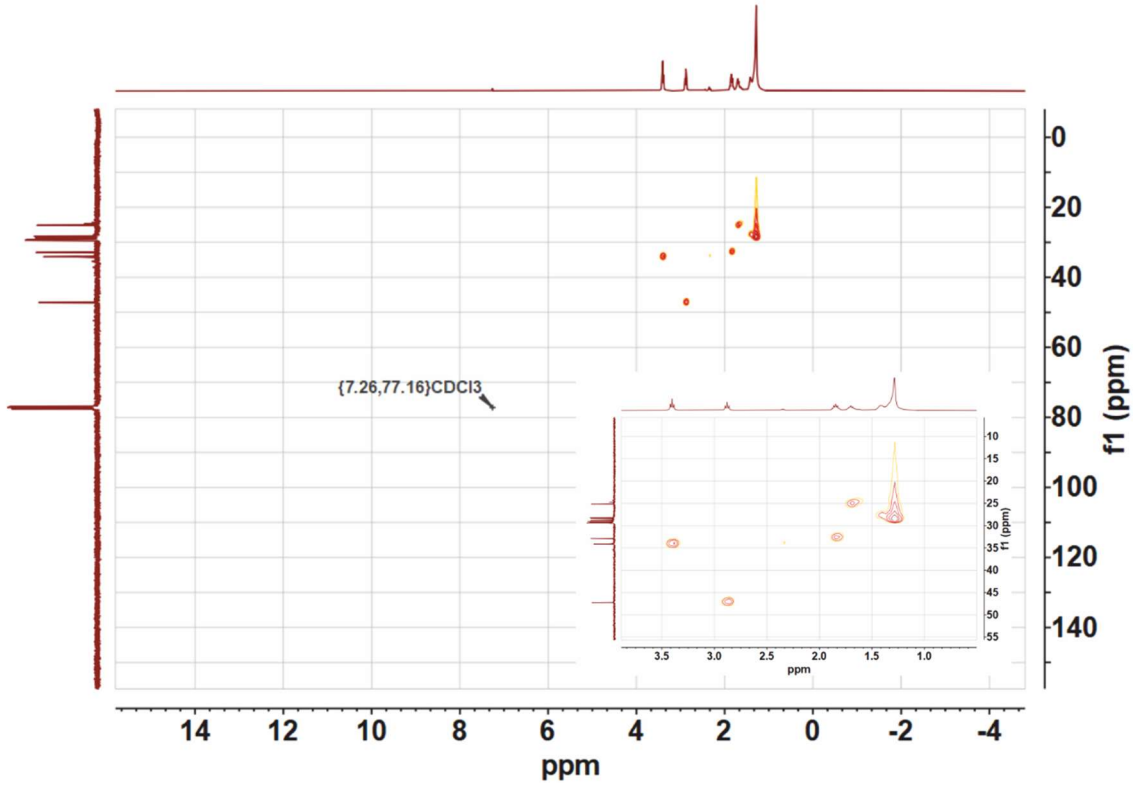

Supporting figure 7: ^{1}H-^{13}C-HSQC of 11-bromoundecanoyl chloride.

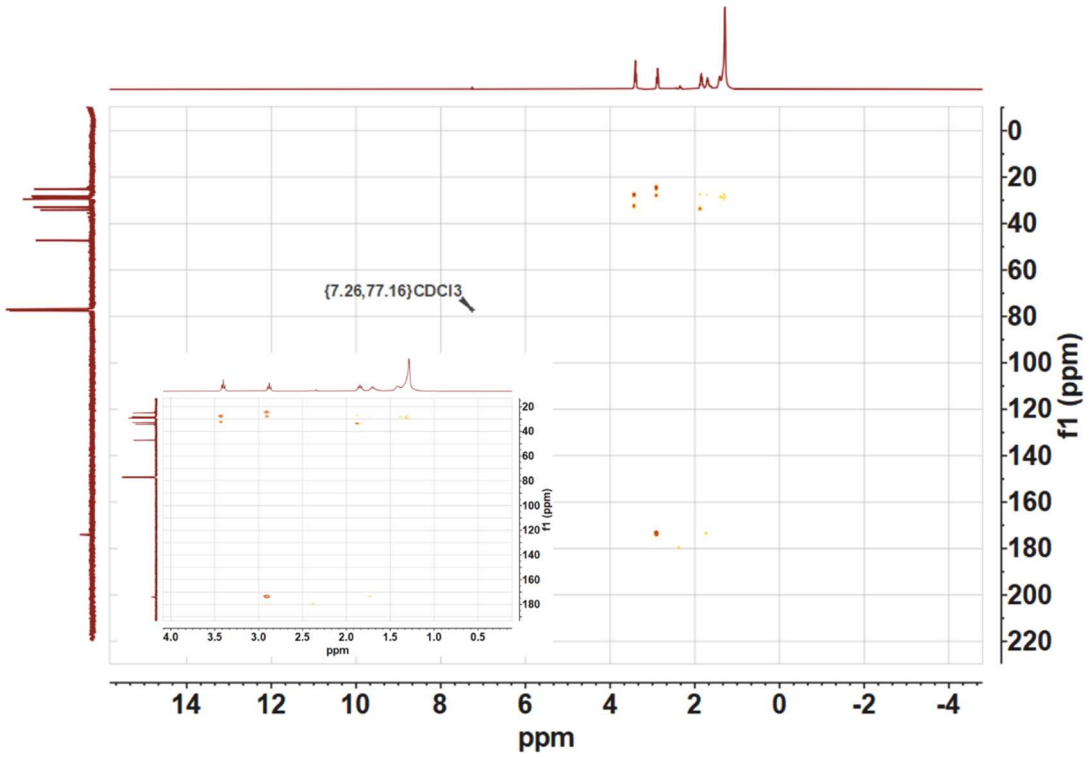

Supporting figure 8: ^{1}H-^{13}C-HMBC of bromoundecanoyl chloride.

Additional spectra of 11-bromo-1-(3,4-dimethoxyphenyl)undecan-1-one

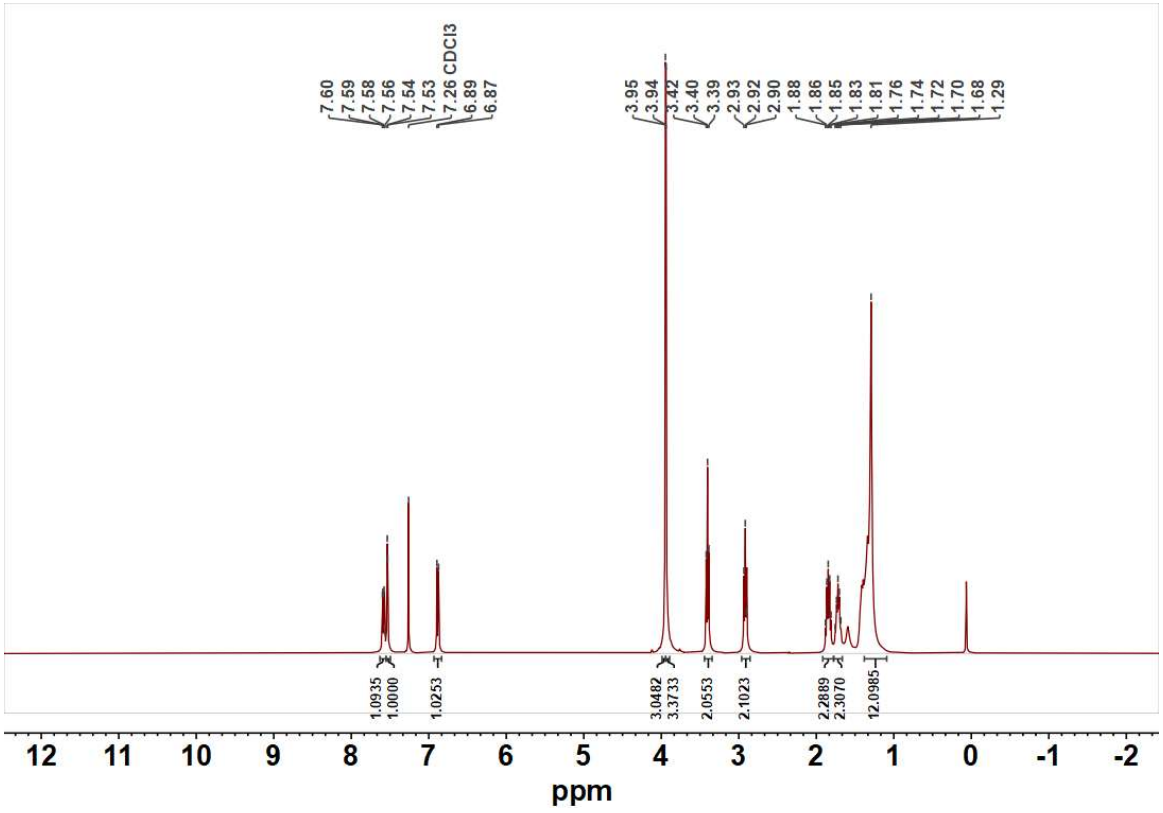

Supporting figure 9: ^{1}H-NMR of 11-bromo-1-(3,4-dimethoxyphenyl)undecan-1-one.

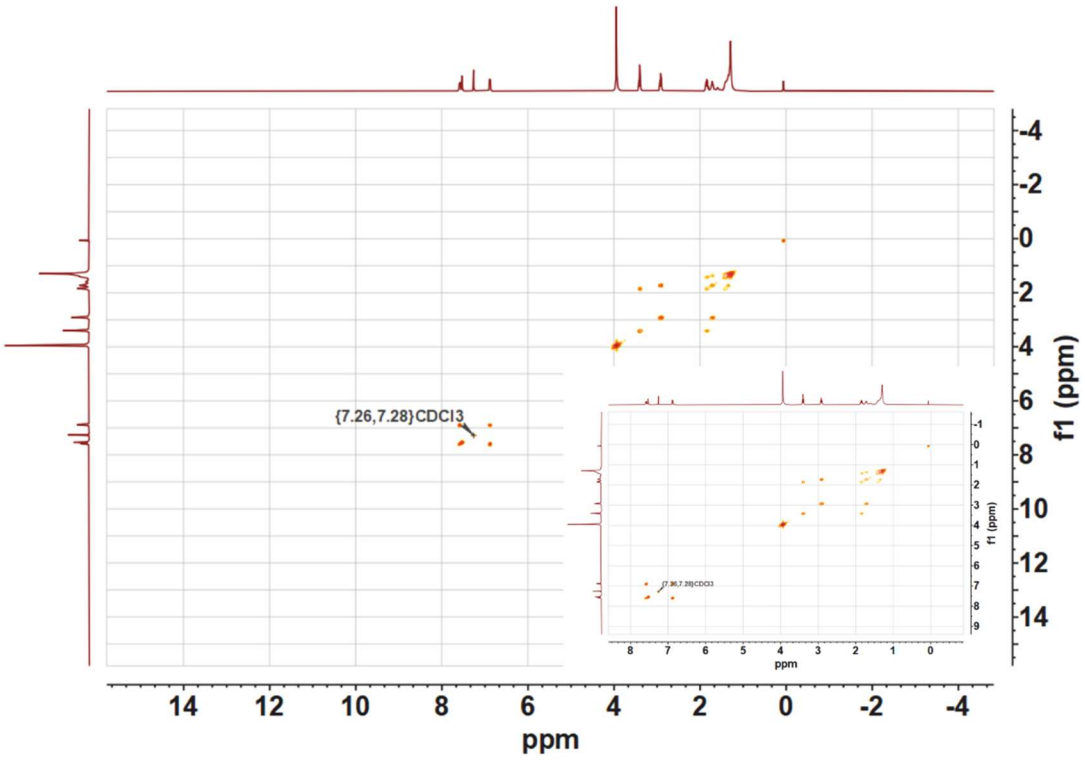

Supporting figure 10: ^{1}H-^{1}H-COSY of 11-bromo-1-(3,4-dimethoxyphenyl)undecan-1-one.

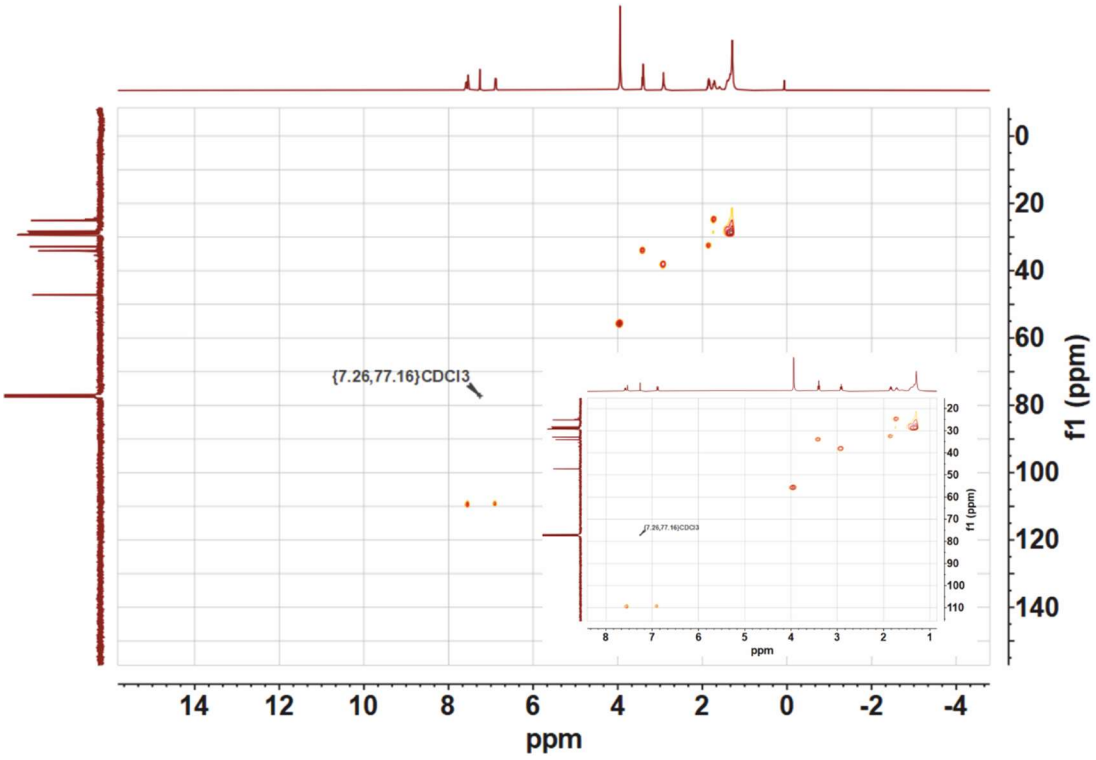

Supporting figure 11: ^{1}H-^{13}C-HSQC of 11-bromo-1-(3,4-dimethoxyphenyl)undecan-1-one.

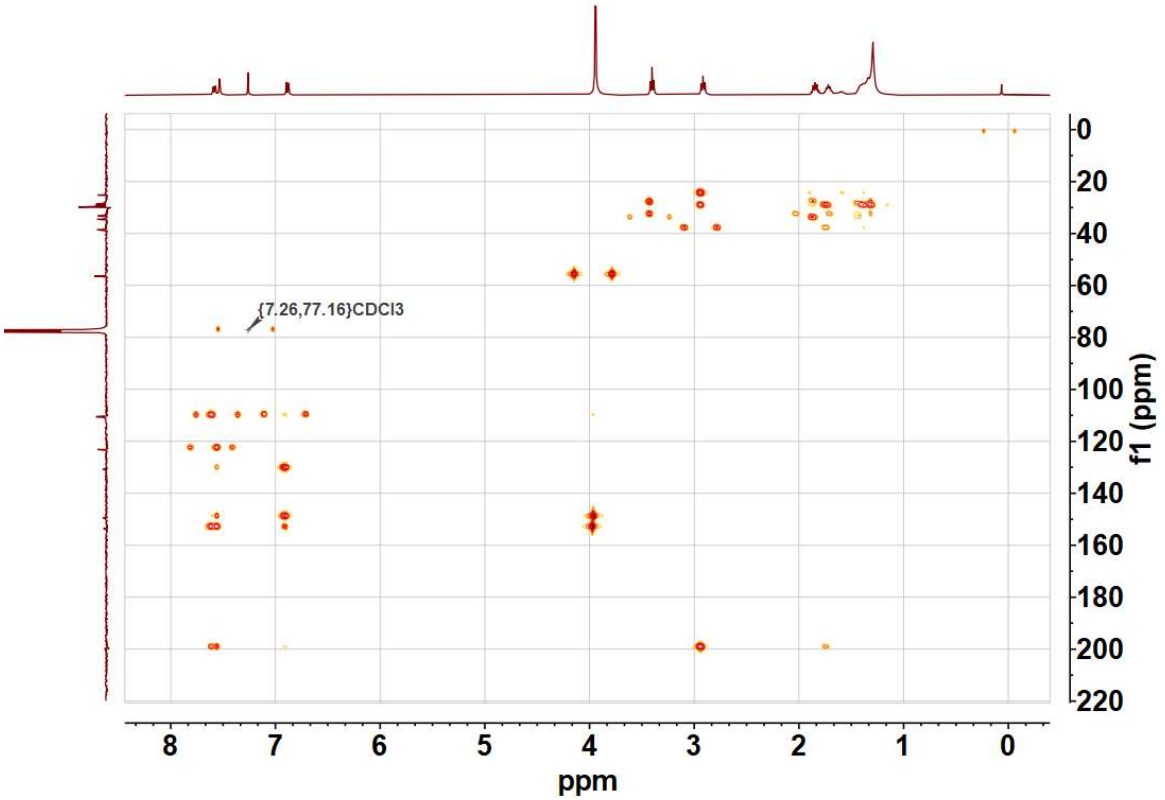

Supporting figure 12:^{1}H-^{13}C-HMBC of 11-bromo-1-(3,4-dimethoxyphenyl)undecan-1-one.

Additional spectra of 4-(11-bromoundecyl)-1,2-dimethoxybenzene

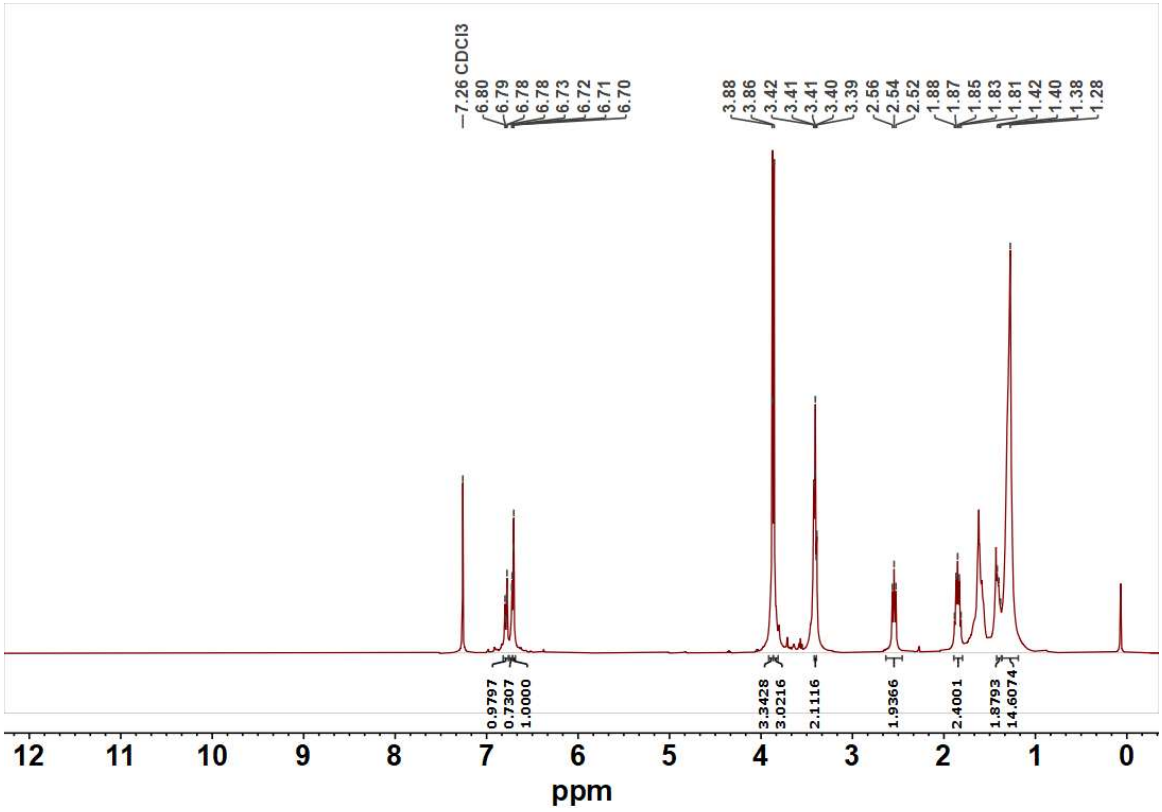

Supporting figure 13: ^{1}H-NMR of 4-(11-bromoundecyl)-1,2-dimethoxybenze.

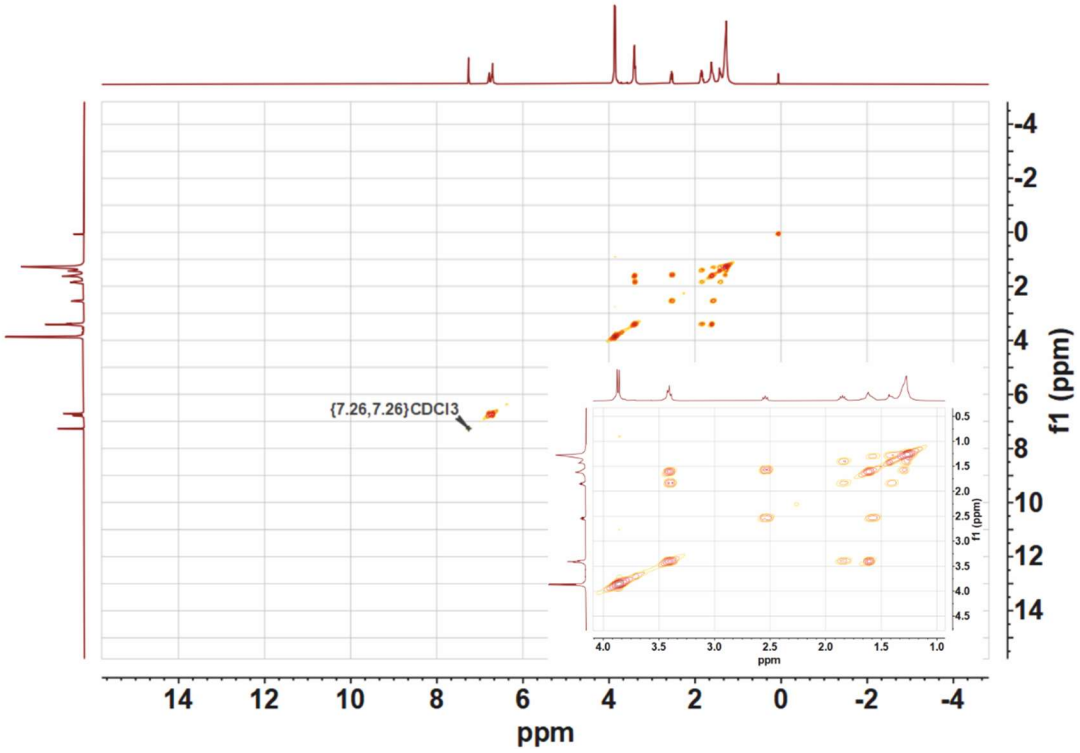

Supporting figure 14:^{1}H-^{1}H-COSY of 4-(11-bromoundecyl)-1,2-dimethoxybenzene.

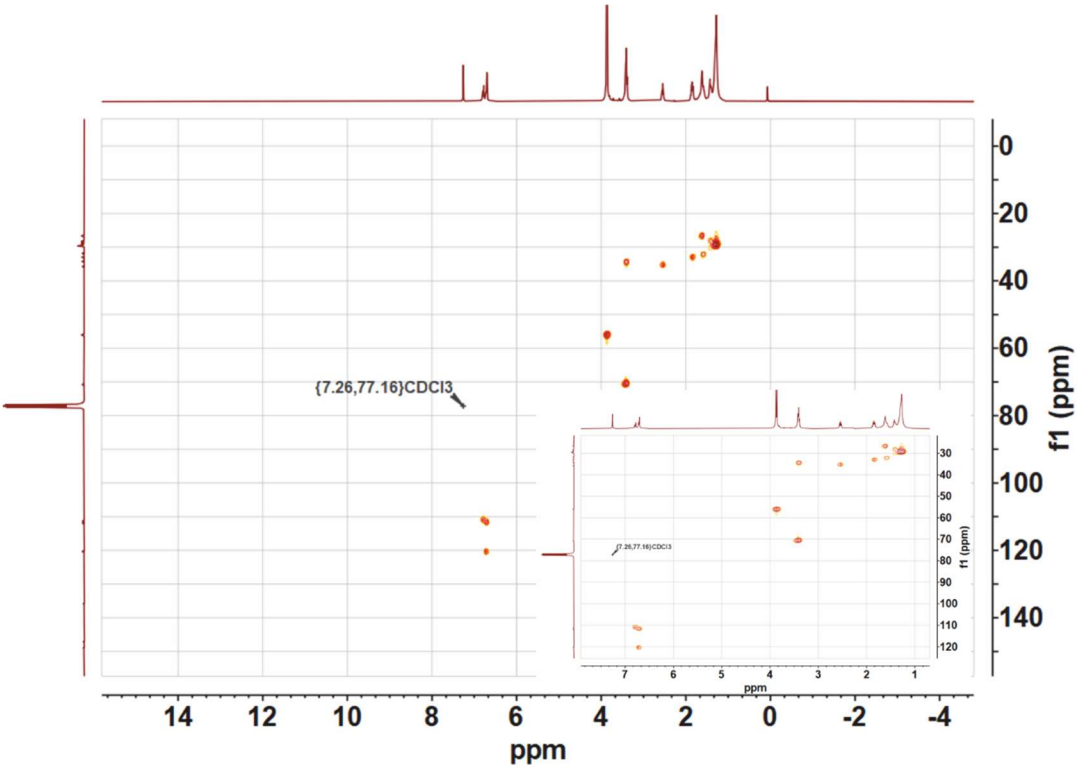

Supporting figure 15:^{1}H-^{13}H-HSQC of 4-(11-bromoundecyl)-1,2-dimethoxybenzene.

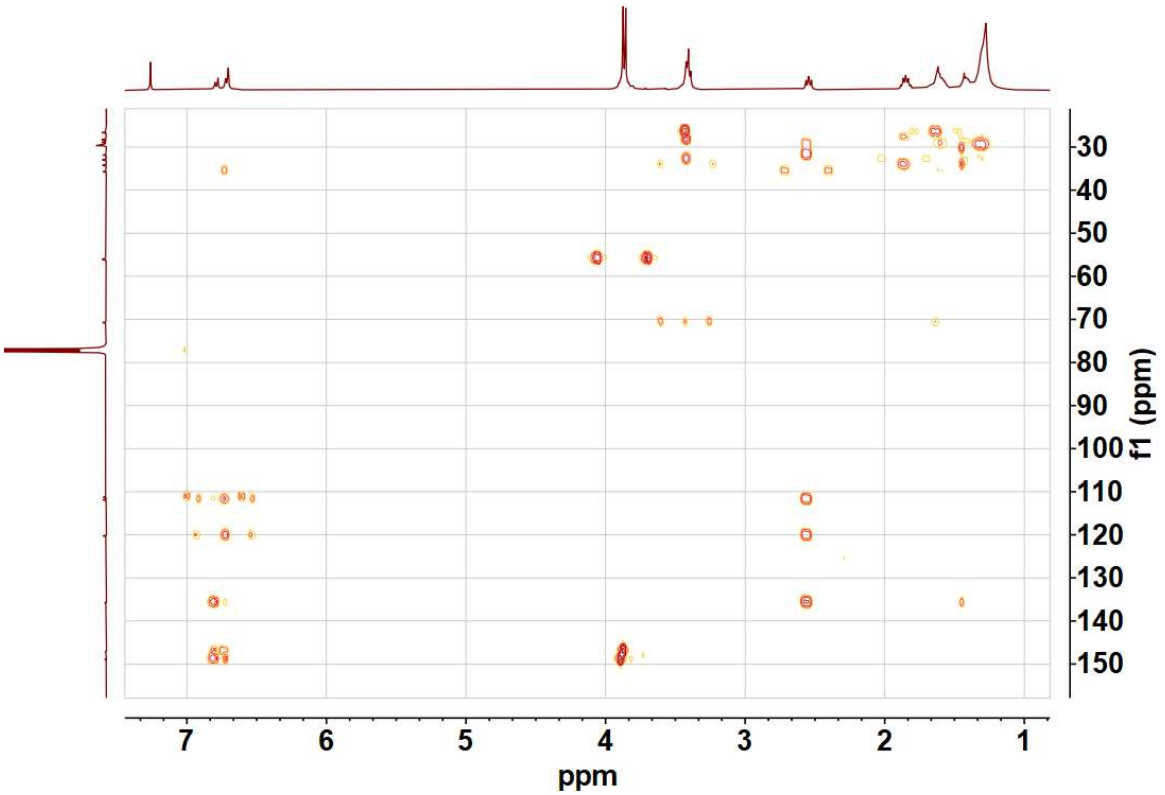

Supporting figure 16: ^{1}H-^{13}H-HMBC of 4-(11-bromoundecyl)-1,2-dimethoxybenzene.

Additional spectra of 11-(3,4-dimethoxyphenyl)undecyl ethanethioate

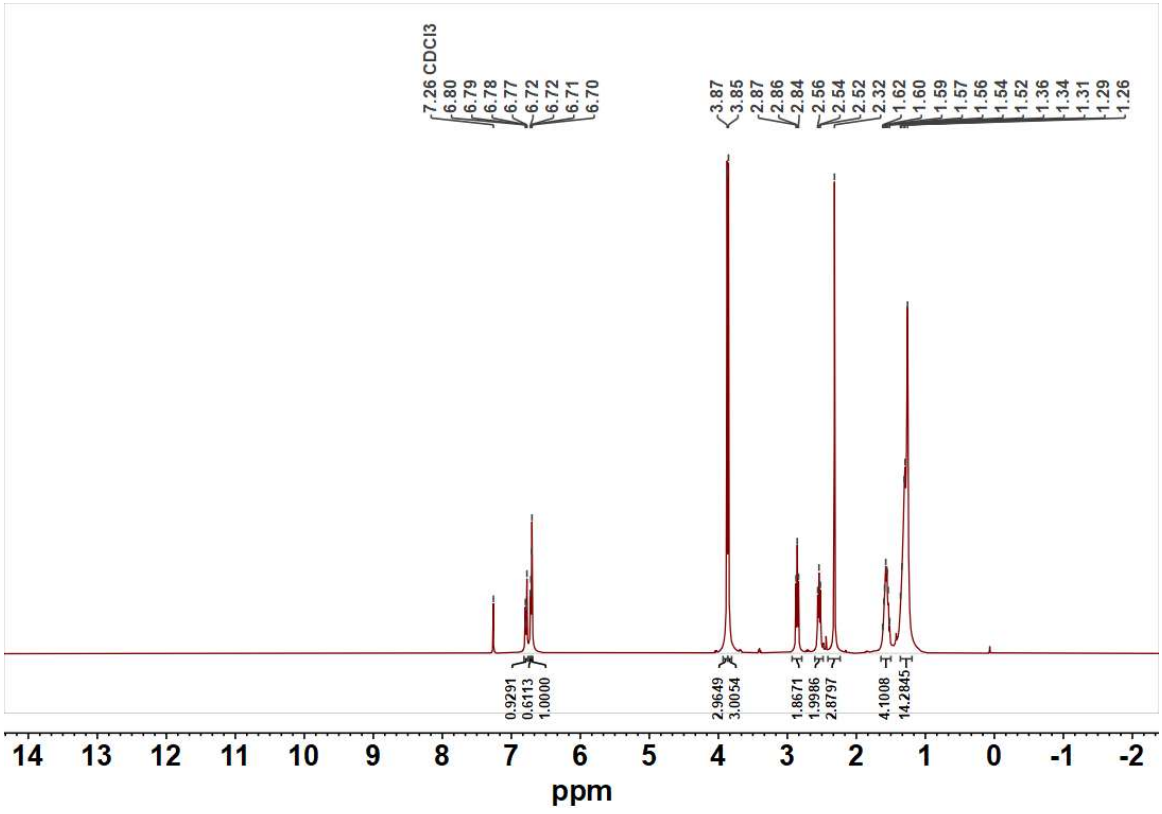

Supporting figure 17: ^{1}H-NMR of 11-(3,4-dimethoxyphenyl)undecyl ethanethioate.

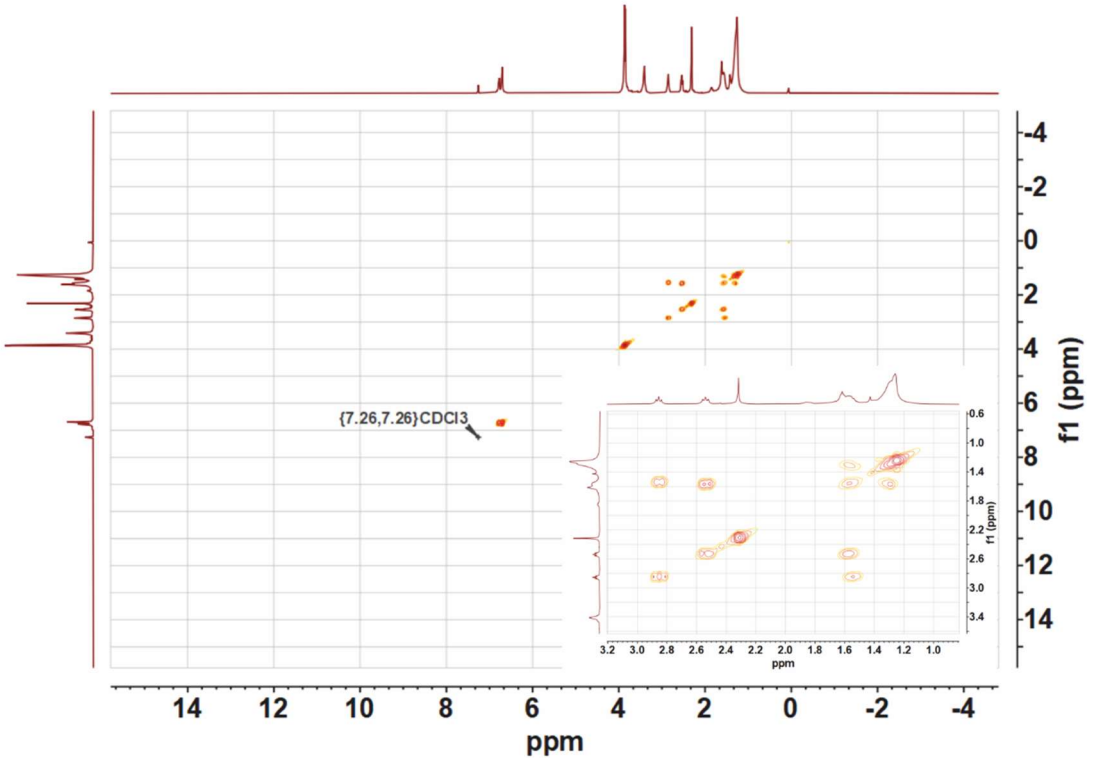

Supporting figure 18: ^{1}H-^{1}H-COSY of 11-(3,4-dimethoxyphenyl)undecyl ethanethioate.

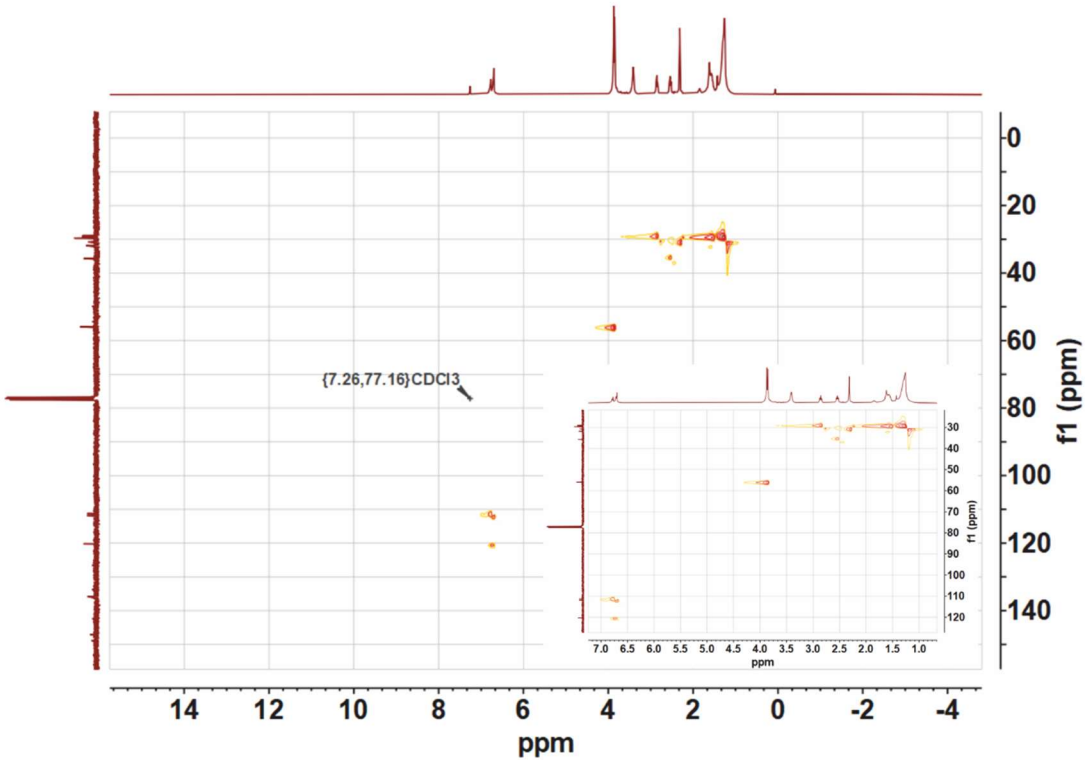

Supporting figure 19: ^{1}H-^{13}C-HSQC of 11-(3,4-dimethoxyphenyl)undecyl ethanethioate.

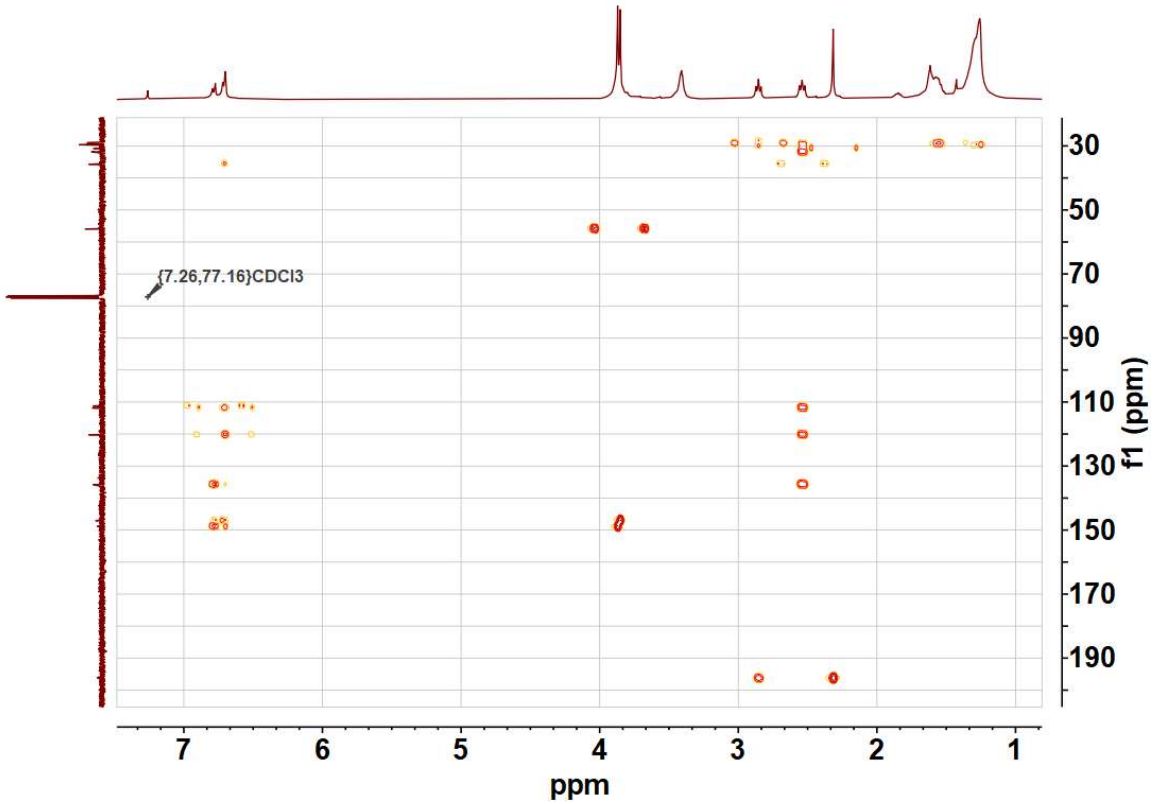

Supporting figure 20: ^{1}**H-**^{13}**C-HMBC of 11-(3,4-dimethoxyphenyl)undecyl ethanethioate.**

Additional spectra of 4-(11-mercaptoundecyl)benzene-1,2-diol

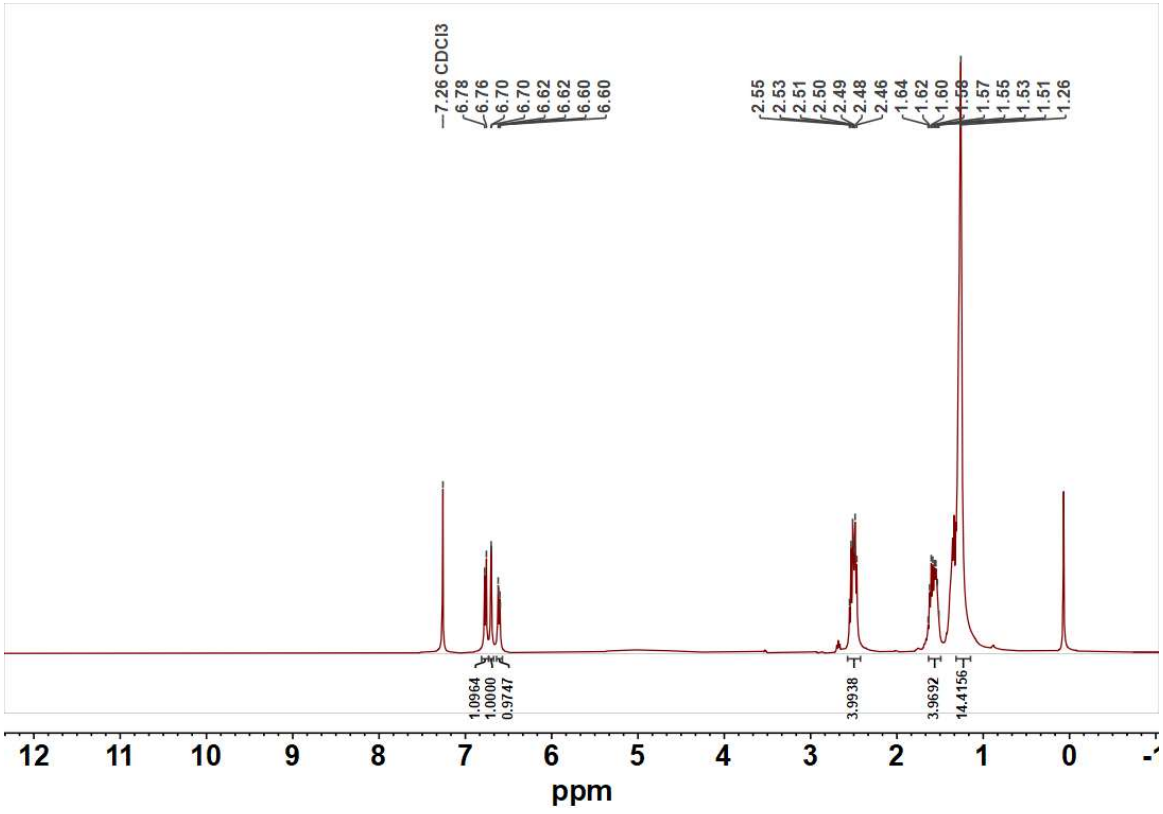

Supporting figure 21: ^{1}**H-NMR of 4-(11-mercaptoundecyl)benzene-1,2-diol.**

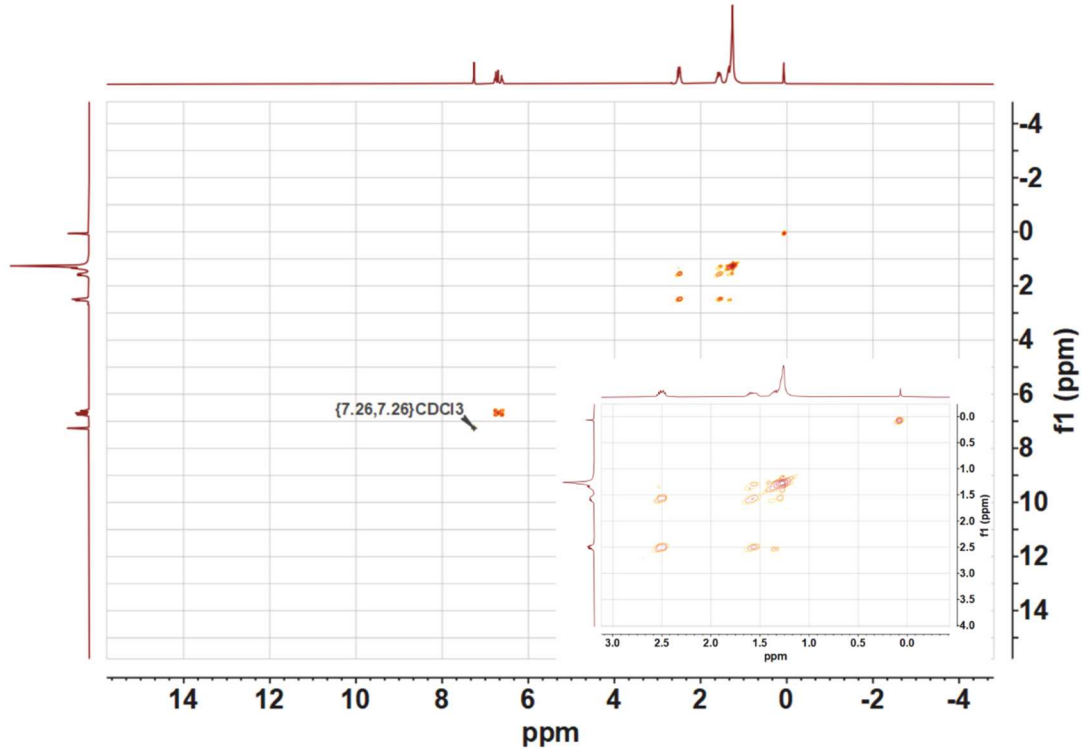

Supporting figure 22: ^{1}H-^{1}H-COSY of 4-(11-mercaptoundecyl)benzene-1,2-diol.

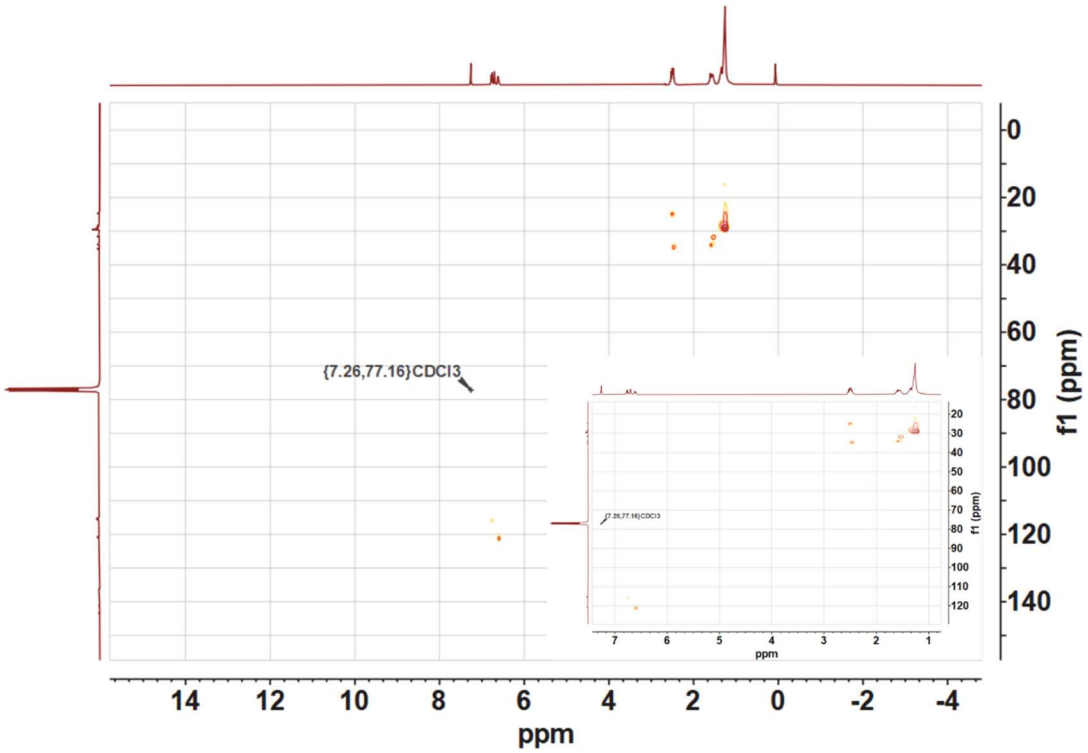

Supporting figure 23: ^{1}H-^{13}C-HSQC of 4-(11-mercaptoundecyl)benzene-1,2-diol.

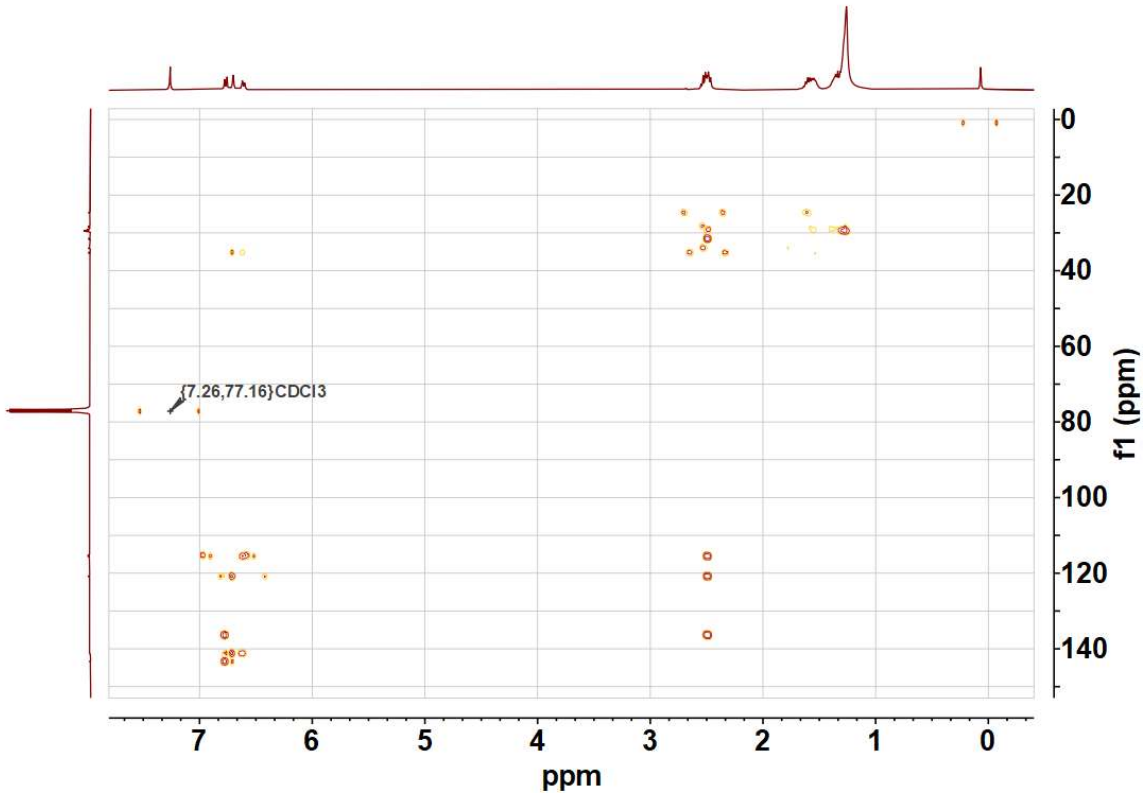

Supporting figure 24: ^{1}H-^{13}C-HMBC of 4-(11-mercaptoundecyl)benzene-1,2-diol.

Nanorattles

5

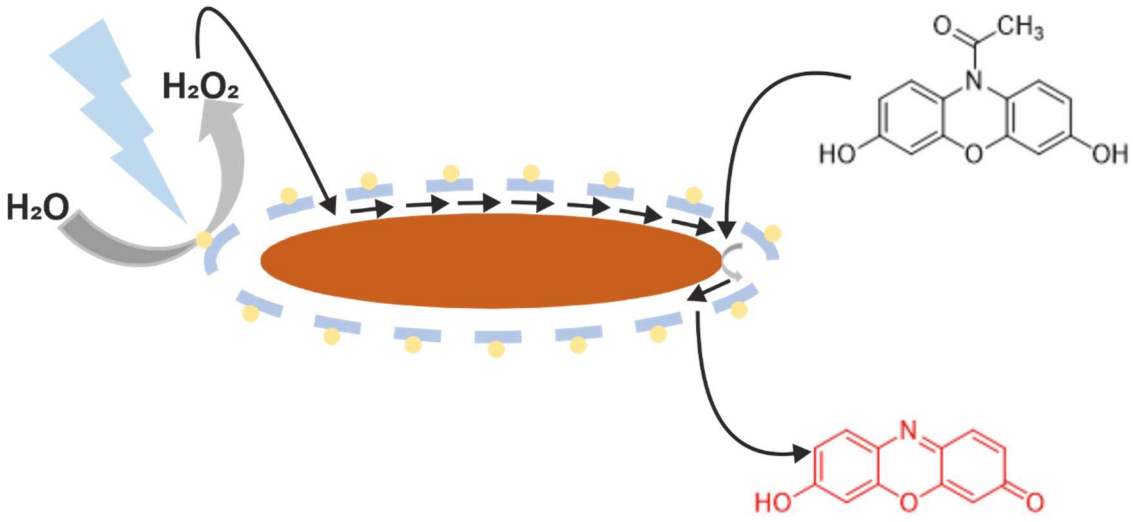

This chapter discusses nanorattles as models for prebiotic cell structures. The synthesis of heterodimeric nanostructures, called nanorattles, consisting of a hematite nanoparticle and a porous silica shell is performed. The hematite nanoparticle serves as a peroxidase mimic. Catalysis takes place through the silica shell as a diffusion barrier, which represents a mass transfer with the external environment.

5.1. Theoretical background

This chapter deals with so-called nanorattles as a model system for prebiotic cell structures. For this purpose, nanorattles are synthesised, consisting of a hematite nanoparticle as core and a porous silica shell, which is supposed to simulate the cell membrane. As discussed in chapter 3, the hematite nanoparticles are a mimic for the enzyme peroxidase. A material exchange between the external environment and the interior of the nanorattle takes place by diffusion, so that material conversion takes place inside the shell. The silica shell represents a diffusion barrier that is comparable to the cell membrane. For a better understanding, cells and, in general, cell structures of living beings of the three great empires (Figure 3) are explained at the beginning and the cell membrane of archaebacteria is discussed. For catalysis, chapter 3 is assumed.

5.1.1. Nanorattles

Nanorattles, also called yolk-shell particles, are nanoparticles encapsulated in a shell. Here they have to be distinguished from core-shell particles, where the shell has grown on the core, so that a connection exists between the two materials. In case of the nanorattles, the core is not always located in the centre of the entire particle system, but it is assumed that the core can move freely within the shell.[140] While in TEM experiments it is usually observed that the core of a nanorattles is apparently sticked to the shell, *Sun et al.* could show in a TEM experiment that the core in an Au/Ag@Au/Ag rattle has a core movement. For this purpose they prepared the samples as follows: The nanorattles dispersed in a solvent were applied to a TEM grid and a TEM grid rotated by 70° compared to the former and held in this position during the entire drying process. After complete drying, the TEM measurements were performed. This experiment shows a difference in the distribution of the localisation of the core particles. While in the rotated samples a large part of the core particles could be localised at the bottom of the shell, no significant difference in localisation could be observed in the non-rotated samples.[141]

The interesting thing about this type of nanoparticles is that it is also possible to enclose several nanoparticles in one shell, or to construct several shells around one nanoparticle. It is often observed that the shells have the outer morphology of the core nanoparticle used.[140] Furthermore, it is possible to functionalise the shell surface to make the nanorattles interesting for use as drug delivery systems.[142] For example, a nanorattle system was developed in which magnetic magnetite nanoparticles were encapsulated in a mesoporous silica shell functionalised with polyethylene glycol (PEG) and folic acid. Subsequently, the shell structure was loaded with doxorubicin as the active substance, whereby it can theoretically be used as a bio carrier.[143] Further applications can be found in form of nanoreactors. Since the present work is also concerned with nanorattles in catalysis, the focus in the following is primarily on examples with catalytic application. Interesting examples are electrocatalysis, heterogeneous catalysis and photocatalysis. Au@Pt nanorattles have been studied, for example, as electrocatalysts in the oxidation of methanol to CO_2. It could be observed that the catalytic activity of Au@Pt nanorattles is significantly higher compared to the respective core-shell nanoparticles, hollow Pt or Pt nanoparticles as well as commercial Pt/C. Furthermore, this nanostructure has a significantly higher CO tolerance compared to the other structures.[144] Another interesting system is Pd@CeO_2, where CeO_2 is a mesoporous hollow structure. After calcination of this structure, these nanorattles were capable of CO oxidation at 110 °C with 100% conversion rate. Furthermore, the trend could be observed that the particle activity increased with the calcination temperature. CeO_2 nanoparticles did not catalyse the reaction at all. Pd@SiO_2 nanoparticles were also able to catalyse this reaction, but only at much higher temperatures. It is therefore assumed that there is a synergistic effect between the Pd and CeO_2 content of the nanorattles, that their catalytic activity could be achieved.[145]

With regard to photocatalysis it is interesting that $NiTiO_3$ nanoparticles are able to degrade methylene blue photocatalytically. However, comparing its catalytic activity with that of the respective nanorattles $NiTiO_3$@SiO_2, an 68 % higher activity of $NiTiO_3$@SiO_2 could be observed. This seems confusing at first glance, because it cannot be assumed that the silica shell has a photocatalytic activity. However, taking into account further investigations regarding the photocatalytic activity of

nanorattles, it can be assumed that the significantly increased activity can be explained by the fact that the light is multi-reflected within the nanorattles. While light that occurs on the surface of a spherical nanoparticle is reflected according to the principle "angle of incidence equals angle of exit", it can penetrate a hollow nanoparticle. There, the light can penetrate the particle as an extension of the incident light beam, or be reflected inside the particle when it hits the inner surface, so that the beam does not completely exit the hollow nanoparticle again. In the case of the nanorattles, however, the light beam can be reflected not only on the inner surface of the shell, but also on the surface of the integrated core particle. This increases the probability that the light is reflected several times within the nanorattle structure before the light beam exits, thus increasing the efficiency of using light. Consequently, the observation is not based on a more active $NiTiO_3$ nanoparticle, but on the more efficient use of photons by the nanorattle structure.[146,147]

However, the most interesting example in the context of the present work is the example of the reaction cascade. *Yang et al.* synthesised a nanorattle with a core particle that carries amino groups on its surface and sulfonate groups on the outer surface of the shell. Thus they combined an acidic and a basic functional group in one system. With this system they produced a catalyst that can catalyse the Henry reaction cascade. Normally this reaction has to be carried out in two steps, since the first reaction step - the deacetalisation, in the acidic and the second reaction step - the nitroaldol reaction, in the basic have to be performed. These two reaction steps are normally not combinable with each other, since the catalytically added acid and base would neutralise each other. In this case, however, the catalytic units are spatially fixed and do not come into direct contact with each other. This allows a two-stage synthesis to be carried out within one reaction step.[148,149] However, it must be remembered that this two-stage reaction is highly dependent on the diffusion of the molecules. Therefore, it is not easy to develop such a system, as it must be ensured that the molecules do not undergo any side reactions.

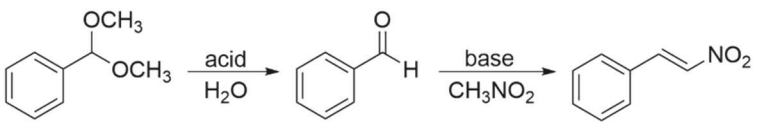

Figure 74: Reaction scheme of Henry reaction described by [149].

Nanorattle - substructures

Looking at these already well-known examples, it becomes very clear that research on nanorattle is not only innovative but also future-oriented. But the synthesis of such systems is not trivial. To be able to plan the syntheses better and make them more successful, one must be aware of the functions of the two components (core and shell).

While in the case of core-shell particles the core particle is located in the centre and surrounded by the shell, in the case of nanorattles it is usually not in the centre and is also presumably freely movable.[140,141] In many cases, the inner part of the particle is the relevant component for the application (e.g. the example of photocatalysis with $NiTiO_3$). It must be taken into account that in the case of catalytic applications, for example, the core particle is freed from possible surface ligands in order not to reduce its catalytic activity.[150]

An important task is also assigned to the cavity between the core particle and the shell. Depending on the application, this cavity can be made hydrophilic or hydrophobic by selecting the ligands that form the cavity.[151] Thus, depending on the application, in the case of porous shells the penetration of surrounding molecules can be specifically promoted or prevented. The size of the cavity can also be controlled by the choice of ligands, which can then also have an effect on the reactions taking place within the nanorattle.[152] For example, this determines the distance a molecule must put aside *via* diffusion to the catalytically active particle, but also the capacity of how many substrate molecules can be incorporated into a nanorattle structure.

The shell determines central properties of the nanorattles. On the one hand, it protects the core from external influences, for example during the processing of the synthesised structures (e.g. sintering).[153] On the other hand, it also plays a central role in the exchange with the environment. The shell can be closed or porous and thus enable or prevent mass transfer. For example, mass transfer is indispensable in catalytically active nanorattles, where the core is the catalytically active part of the nanorattle.[147] If a nanorattle system with magnetic properties – presented in the particle core- would be synthesised, the shell could also be closed, because a mass transfer is not necessarily required for this. However, the shell

can also represent a defined space. For example, as a depot for pharmaceuticals, so that nanorattles can be used as drug delivery systems.[142] This defined space can also represent a defined reaction space in order to synthesise nanorattles. For example, precursor compounds can be introduced into a hollow particle, which only form the core particle of the nanorattle in a subsequent reaction step by means of a chemical reaction.[140] The synthesis strategies will be discussed in more detail below.

Synthesis strategies

One strategy for the synthesis of nanorattles is the template method. Here, a structural unit of the nanorattle is specified and, based on its structure, a synthesis is aimed which is oriented towards the template. A distinction is made between hard and soft template synthesis. Hard templates include the structural units of the nanorattle, i.e. the core particle or the shell, while soft templates are, for example, surfactants and polymers, which provide a structure for the synthesis through their interaction with the molecules and structures present in the synthesis solution.

In the following Figure 75 the synthesis according to the hard template method is shown schematically.

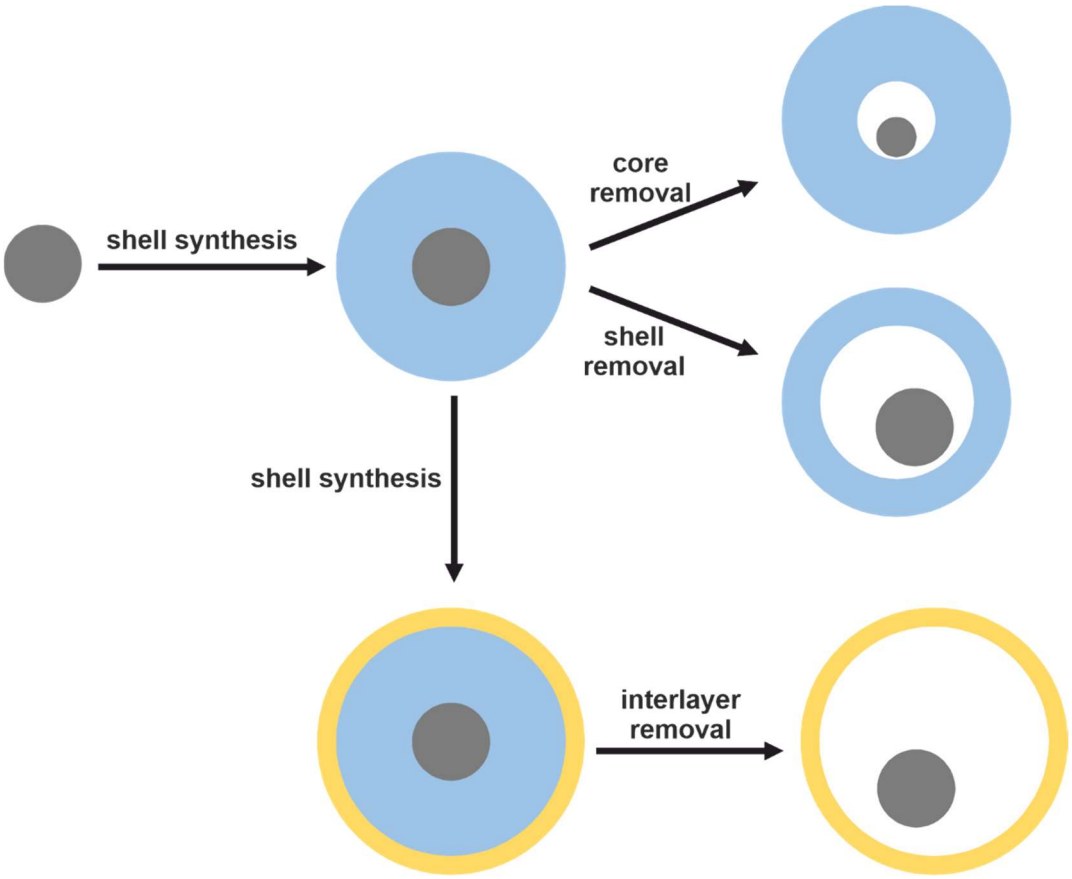

Figure 75: Schematic illustration of the hard template method for the synthesis of nanorattles.

As can be seen in Figure 75, there are different strategies for the synthesis of nanorattles in hard template synthesis. Usually, they all start with the synthesis of the core particle, which is then presented as a hard template. In the first synthesis step, a shell is synthesised on top of the core particle. The result is a core-shell particle. Then either a part of the core particle or a part of the shell is selectively dissolved.[140] However, this strategy also involves certain difficulties, for example in stoichiometry. In this case it is difficult to make a synthesis reproducible so that both, the core and the shell have the same diameter or thickness each time. When dissolving the shell, it is also a difficulty to dissolve the shell from the inside out. If it is only dissolved from the outside, the result is a core-shell particle in which only the shell thickness has been reduced. Therefore, there is also the possibility to synthesise a third layer, which is chemically different from the first and second layer, and then to dissolve the middle layer.[143] This is perhaps the most clever strategy, but it is also very difficult, because three different chemical structures have to be found which can be synthetically combined in such a synthesis and grow heterogeneously on top of each other. It must also be controlled that after the

heterogeneous nucleation there is no epitaxial growth leading to the Janus particles already discussed, but that the heterogeneous nucleation is preferred here until a complete shell is formed, which then serves the homogeneous nucleation and growth of the shell.

As already mentioned, there is also the possibility of soft template synthesis. This is mainly performed as a microemulsion method. This method makes use of micelle-forming molecules, which determine the shape and size of the nanorattles through micelle formation, and also makes it possible to control and adjust these two parameters simultaneously. In the following figure the different possibilities of the microemulsion method are shown schematically.

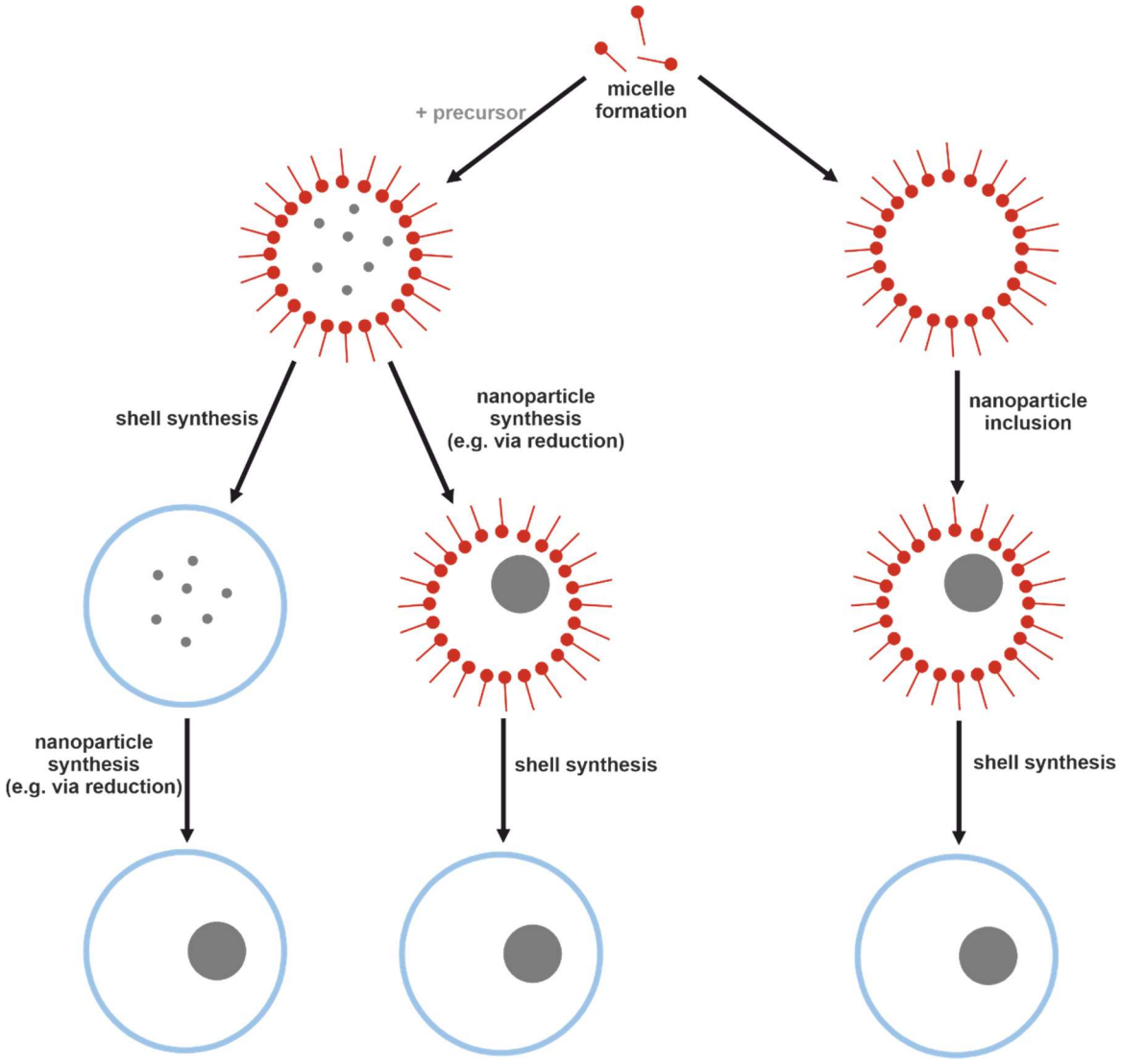

Figure 76: Schematic representation of the synthesis of nanorattles using a soft template method, in particular the microemulsion method.

This method makes use of surface-active substances that form micelles in a two-component system due to their amphiphilic properties. Mainly oil in water systems are used, but water in oil systems can also be used in reverse microemulsions. To simplify the explanation, everything is explained here using oil in water systems. To introduce the core particle, a precursor compound can be dissolved in the organic phase (also oil phase). This results in micelles in which the precursor compound is trapped. This step can be followed by shell formation, or by the synthesis step in which the core particle is synthesised from the precursor compound, for example by reduction. This is followed by the missing synthesis step. In the case of the preceding shell synthesis, the synthesis of the core particle follows, in the case of the preceding core particle synthesis the shell synthesis follows.[154,155] Alternatively, it is also possible to introduce a completely synthesised core particle into the micelle system at the beginning by dispersing the desired core particles in the organic phase. The synthesis of the shell can follow after.[156]

The advantage of this synthesis method is the strict separation of core and shell by using two different phases. At the same time, this can also be a disadvantage, as the properties of the individual structural units are thus also fixed and not every application can be made possible. If, for example, a catalyst is to be enclosed in a mesoporous silica shell and this is done in a microemulsion synthesis, the synthesis starts with a nanoparticle that is dispersible in an organic solvent or with its precursor compound that is soluble in this solvent. The core particle thus has hydrophobic and lipophilic properties. The synthesis of the silica shell thus takes place in the aqueous phase. To the outside, the nanorattle structure has hydrophilic properties and can be easily dispersed in water. If, however, this nanorattle is planned for catalysis in an aqueous solvent, with the core particle representing the catalytically active part, catalysis will not take place, because the core particle has hydrophobic properties and no interaction with the solvent will take place.

In cases where the nanorattles are synthesised from the inside out, i.e. the core particle is presented and then the shell is synthesised, this is called a bottom-up method, while the reverse is called a top-down method.

5.1.2. Structures of Archaebacteria

By informing about cells and their structural composition, one repeatedly encounters the terms prokaryotes and eukaryotes, which are single-celled and multi-cellular organisms. Prokaryotes include all archaebacteria and also many bacteria. Eukaryotes are mainly plants and animals, whereby their cell structure differs again due to their different habitats. Taking into account the phylogenetic tree (Figure 3), which shows that eukaryotes were formed and developed after the realm of archaebacteria, it can be assumed that the origin of life at the cellular level developed from a single-celled organism.

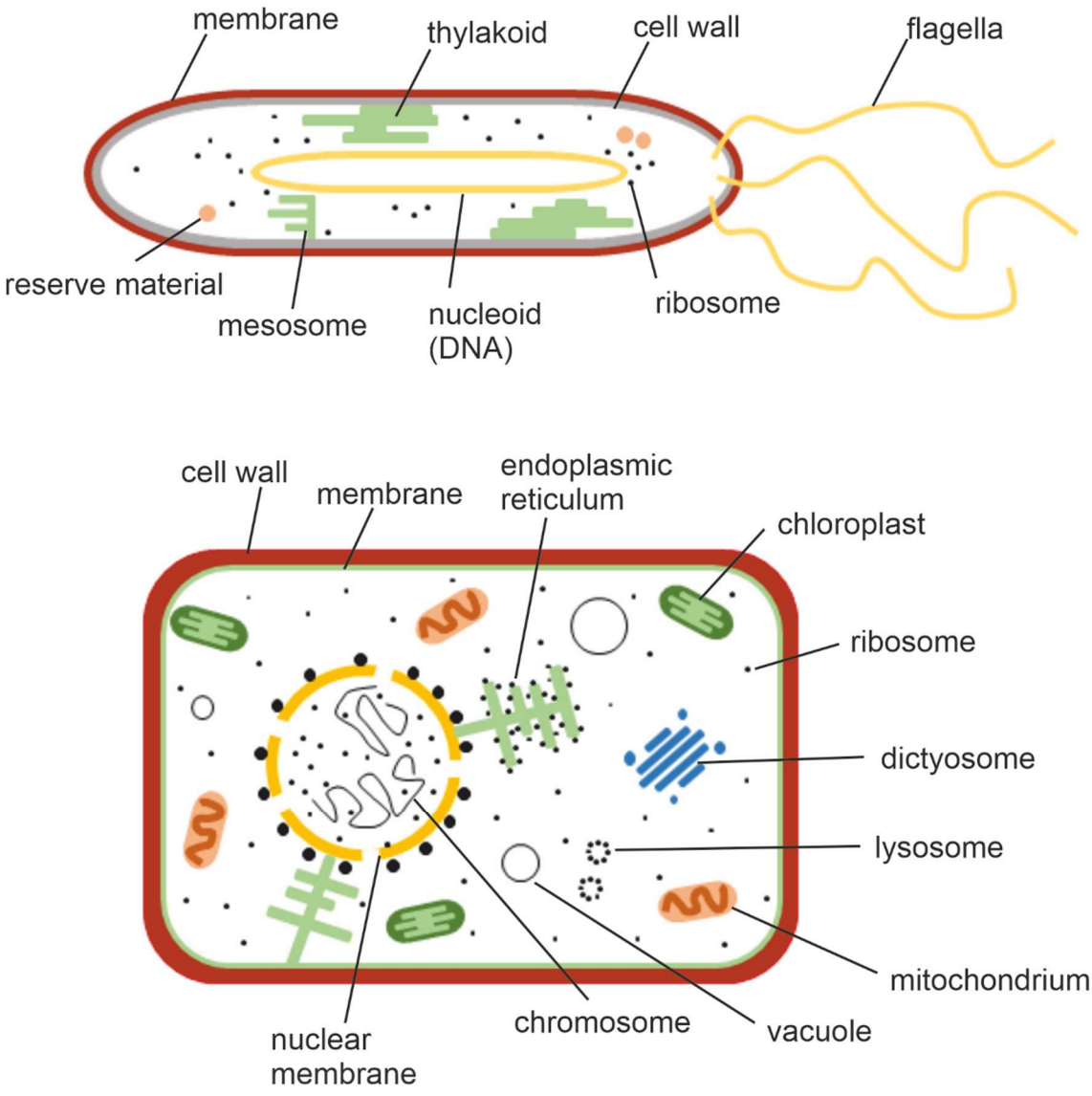

Figure 77: Schematic representation of the cell structure of prokaryotes (top) and eukaryotes using the example of a plant cell (bottom). Based on [157].

Prokaryotes are known from bacteria and archaea while eukaryotes are known from e.g. animals. Figure 77 shows a schematic representation of both cell structures. It is obvious that both types of cells differ from each other. While the cell structure of prokaryotes seems simple, the structure of eukaryotes is more complex. The main differences are the presence (eukaryotes) respectively the absence (prokaryotes) of a nucleus, which has the function to protect the DNA from enzymatic degradation. Another striking difference is the compartmentalisation of the eukaryotes in comparison to the prokaryotes.

Prokaryotes are impressive organisms. They live in several environments, some are known as aerob, some as anaerob. Some practise photosynthesis, other feed on inorganic matter. Prokaryotes are very versatile. But on a molecular-biological basis prokaryotes have to be subclassified into eubacteria and archaebacteria. Most eubacteria known in everyday life are bacteria which make organisms ill or which live in the soil. But archaebacteria can also live in extreme environments like concentrated brine or hot, acidic springs. Some environments are comparable to the conditions on Early Earth, why archaebacteria are discussed as first cellular living organisms.[158]

In the realm of archaebacteria *Euryarchaeota* have to be distinguished from *Crenarchaeota*. The *Euryarchaeota* include methanogens like psychrophiles, mesophiles and thermophiles, reaching from organisms living in subzero, aquatic environment to organisms living in extreme heat, up to 70 °C, extreme halophiles and extreme acidophilic thermophiles.[159–161] With one known exception, all Crenarchaeota live at 70 °C.[159] From today's perspective, these environmental conditions are unimaginable in terms of human life. Nevertheless, there are archaebacteria that still live under the conditions described above. Here the question arises how the archaebacteria differ from all other known life forms that they are viable under such conditions. An important reason for this is the structure of their cell membrane. The cell membranes of eukaryotes consist mainly of phosphoglycerides, on whose phosphate group an alcohol may be condensed and whose two other hydroxyl groups of glycerol are esterified with one fatty acid each.[36] Archaebacteria have not incorporated fatty acids into this basic structure, but have ether bridges with long-chained, branched alkyl chains at these two hydroxyl groups of the glycerol unit.[162] The ether bonds compared to the ester

bonds are clearly more hydrolysis stable and the branching of the alkyl chains compared to linear alkyl chains additionally protects against oxidations at the C-backbone. Compared to many bacteria and the eukaryotes, many archaebacteria have a lipid monolayer instead of a bilayer structure.[162]

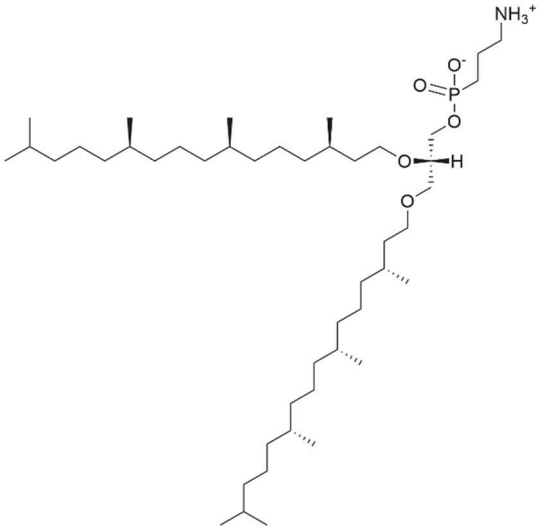

Figure 78: Membrane lipid of methanococcus jannaschii as example of a membrane lipid of an archaebacteria. Based on [36].

5.2. Results and discussion

This chapter discusses the synthesis of nanorattles and their catalytic properties. The hematite nanoparticles known from chapter 3 were used for this purpose. For this reason, reference is made at this point to the results from chapter 3 and will be briefly presented again below, but not discussed further. Only the AR assay is used in this chapter, due to the advantages of working with hematite nanoparticles explained in chapter 3.

5.2.1. Synthesis and characterisation of the nanorattles

For the synthesis of nanorattles hematite nanoparticles discussed in 3 were used. For further analytic data see chapter 3.2.1 and 3.2.2.

The synthesis used in this work is a soft template method with lauryl sulfobetaine (LSB) and sodium dodecyl benzenesulfonate (SDBS) as templates. These tensides are able to coat nanoparticles by building up micelles. With the aid of their sulfonate groups an interaction with the amino group of (3-Aminopropyl)triethoxysilane (APTES) is possible, which acts as linker for tetraethyl orthosilicate (TEOS). TEOS can then be hydrolysed and build up a shell around the nanoparticles. After washing out the ligands the nanoparticle can move freely in the silica shell. The synthesis strategy is illustrated in Figure 79.

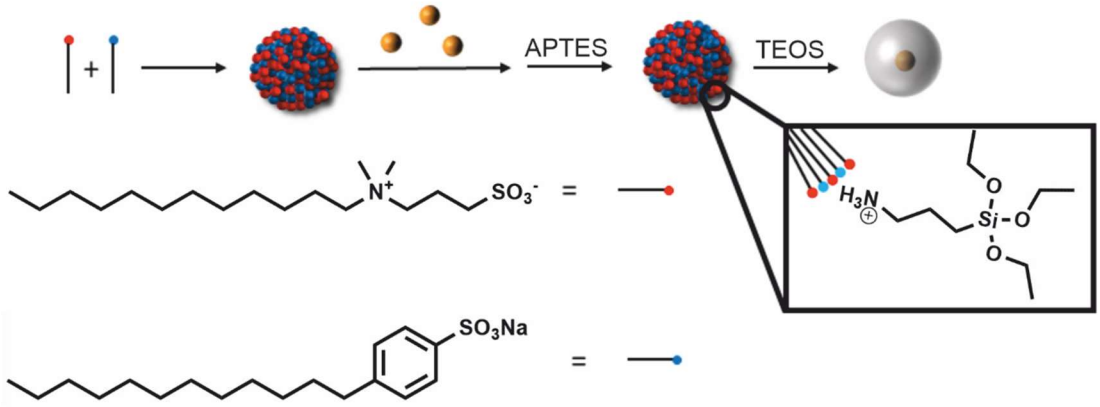

Figure 79: Schematic illustration of the synthesis of nanorattles used here. Based on [163].

Fe_2O_3@SiO_2, nanorattles were synthesised using a soft template method described by *Wu and Xu* with some modifications.[163] Hematite nanoparticles were

dispersed in water and mixed with a solution containing of lauryl sulfonate betaine (LSB) and sodium dodecyl benzenesulfonate (SDBS). The reaction mixture was heated up to 40 °C under stirring. 3-Aminopropyl triethoxysilane (APTES) and tetraethyl orthosilicate (TEOS) were added. After one additional hour the temperature was increased up to 80 °C. After washing the nanorattles with water they were stirred in diluted hydrochloric acid to wash out the ligand molecules.

To synthesise nanorattles, first all effects of concentration variation of every compound of the synthesis was tested. In the following tables all synthesis approaches and in all figures representative TEM images of the synthesis approaches are presented.

The experiments were started with the variation of TEOS.

Table 25: Synthesis approaches for variation of TEOS.

compound	m [mg]	n [mmol]	V [µL]	c [mol/L]
Fe_2O_3 NP	75,00	-	-	-
LSB	8,35	0,025	-	0,0025
SDBS	8,70	0,025	-	0,0025
APTES	22,33	0,101	23,50	0,0101
TEOS	variation	variation	variation	variation
A	47,00	0,226	50,00	0,0226
B	94,00	0,451	100,00	0,0451
C	141,00	0,677	150,00	0,0677
D	188,00	0,902	200,00	0,0902
E	235,00	1,128	250,00	0,1128
F	282,00	1,354	300,00	0,1354
G	470,00	2,256	500,00	0,2256
H	940,00	4,512	1000,00	0,4512

The TEOS concentration was varied because of the expectation to influence the thickness of the shell by increasing the TEOS concentration. In the same way the minimum concentration of TEOS should be determined for building up shells around the hematite nanoparticles.

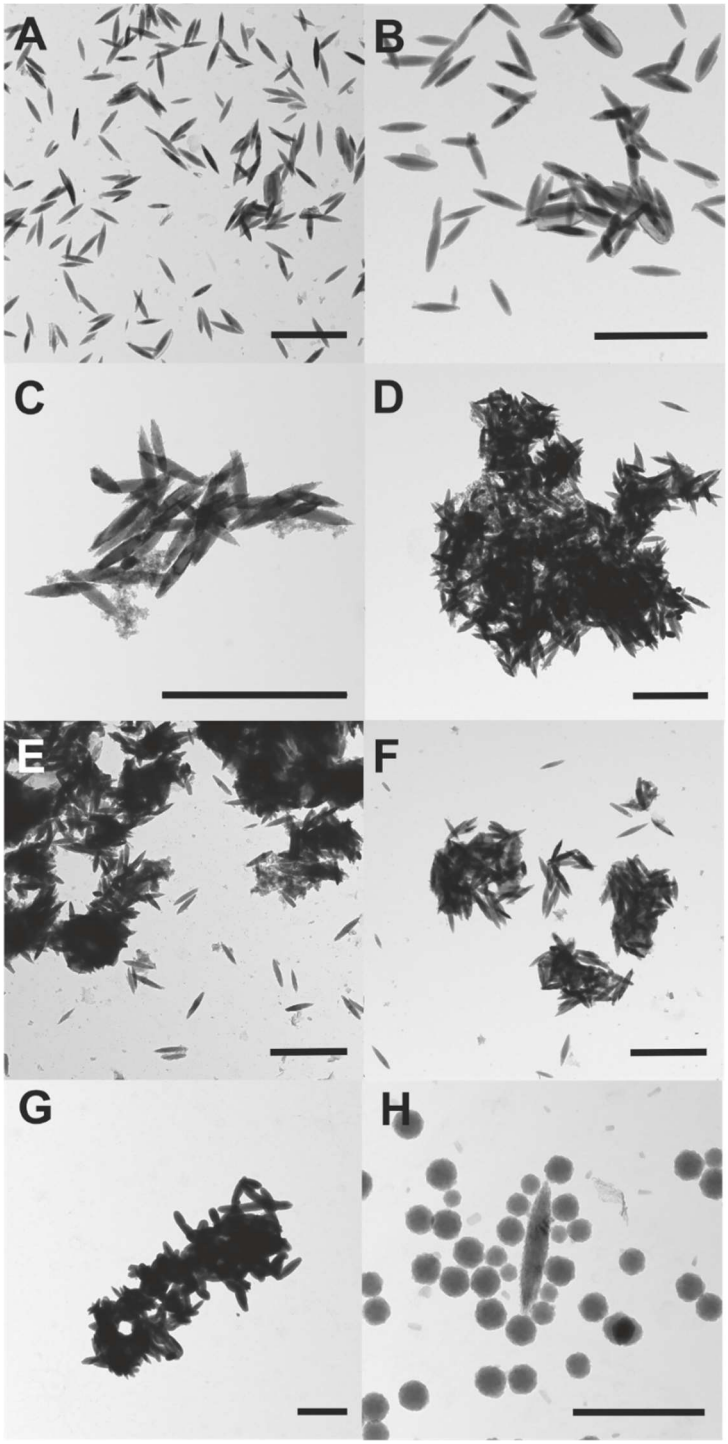

Figure 80: TEM images of variation of TEOS concentration in the synthesis of Fe_2O_3@SiO_2 nanorattles. (scale bar A-G: 1 µM, H: 500 nm)

Figure 80 shows TEM images of the different synthesis approaches described in Table 25. If the TEOS concentration is too low only some hematite nanoparticles can be included into a silica shell but also core-shell nanoparticles can be observed (see Figure 80 A and B). In contrast, if the TEOS concentration is too high it results in spherical silica nanoparticles and no shell formation occurs. Synthesis approach G shows some hematite nanoparticles encapsulated into a silica shell. But it seems that the silica shells are hydrolysed together. Also, not in all cases nanorattles are observable, but core-shell particles. Figure 80 C – F show different synthesis approaches, where no shell formation occurs. It looks like silica is hydrolysed onto the surface of hematite nanoparticles without any order. This results in agglomerates, where condensed silica connects the hematite nanoparticles. Summarised it is possible to build up nanorattles like observed in synthesis approaches A and B. At this point no excess of TEOS in form of free silica could be observed. But increasing the TEOS concentration does not lead to nanorattles, like expected. This indicates that the concentration of APTES or the concentration of ligand is too low.

If the concentration of ligands is too low, the hematite nanoparticles cannot be coated completely. Consequently, the template for silica hydrolysis is not fully built up. If the concentration of APTES is too low no connection between the ligands and TEOS can be built up. Only segments of a shell can be synthesised or TEOS hydrolysed without any order.

To find the best APTES concentration for this synthesis some approaches with different concentrations of APTES were done.

Table 26: Synthesis approaches for variation of APTES.

compound	m [mg]	n [mmol]	V [µL]	c [mol/L]
Fe_2O_3 NP	75,00	-	-	-
LSB	8,35	0,025	-	0,0025
SDBS	8,70	0,025	-	0,0025
APTES	variation	variation	variation	variation
TEOS	141,00	0,677	150,00	0,0677
A	5,58	0,025	5,88	0,0025
B	11,16	0,050	11,75	0,0050
C	22,33	0,101	23,50	0,0101
D	44,65	0,202	47,00	0,0202
E	89,30	0,403	94,00	0,0403
F	178,60	0,807	188,00	0,0807
G	357,20	1,614	376,00	0,1614
H	714,40	3,227	752,00	0,3227
I	1428,80	6,454	1504,00	0,6454

It can be expected that in case of APTES concentration, which is too low no nanorattles will be built up, while in case of a too high concentration additional silica particles will be synthesised next to the nanorattles.

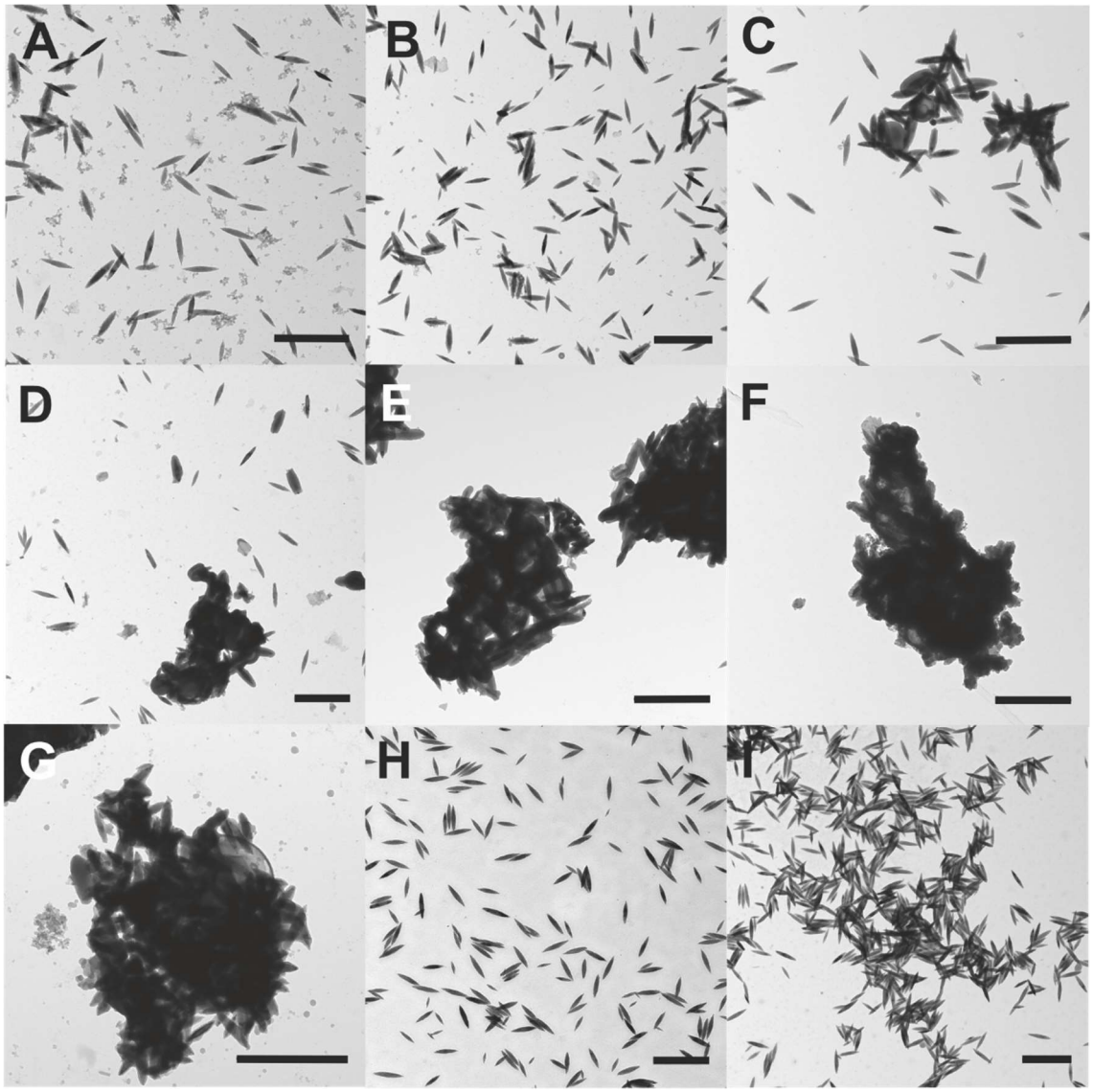

Figure 81: TEM images of variation of APTES concentration in the synthesis of Fe_2O_3@SiO_2 nanorattles. (scale bar A-H: 1 µM)

Figure 81 shows TEM images of the in Table 26 described synthesis approaches with variation of APTES concentration. In Figure 81A the synthesis with the lowest APTES concentration is shown. No nanorattles can be observed. The TEOS is hydrolysed in connection to the hematite nanoparticles, but no shells are built. In this case it seems like the APTES concentration is too low to coat the full nanoparticles. With increasing the APTES concentration (Figure 81B and C) a few nanorattles are observable but also many hematite nanoparticles without shells. With even larger amounts of APTES (Figure 81 D to G) silica without a connection to the hematite nanoparticles can be observed, also agglomerates of connected nanorattles. It is obvious that the APTES concentration in this cases is too high.

The synthesis approaches shown in Figure 81 H and I are confusing at first. It can be expected that no nanorattles are synthesised here. The only explanation, why no silica nanoparticles can be observed, is that the built silica nanoparticles are small and were not collected *via* centrifugation. No additional precipitants were used, since the nanorattles were collectable without any precipitation.

Since no sample could be prepared, in which almost nanorattles are presented the influence of the ligand mixture containing of LSB and SDBS was examined. Stock solutions (60 mM) of both ligands were prepared and mixed in equivalent rates. Water was added to a final volume of 5 mL. Further experimental details see Table 27, Table 28 and 5.4.2.

Table 27: General synthesis approaches for variation of ligand mixture (LSB and SDBS).

compound	m [mg]	n [mmol]	V [µL]	c [mol/L]
Fe_2O_3 NP	75,00	-	-	-
LSB	variation	variation	-	variation
SDBS	variation	variation	-	variation
APTES	22,33	0,101	23,50	0,0101
TEOS	141,00	0,677	150,00	0,0677

Table 28: Ligand mixtures for synthesis of nanorattles.

	compound	m [mg]	n [mmol]	V_{stock} [mL]	c [mol/L]	V_{water}
A	LSB	3,3555	0,0100	0,1667	0,0010	2,3333
	SDBS	3,4848	0,0100	0,1667	0,0010	2,3333
B	LSB	6,7110	0,0200	0,3333	0,0020	2,1667
	SDBS	6,9696	0,0200	0,3333	0,0020	2,1667
C	LSB	8,3888	0,0250	0,4167	0,0025	2,0833
	SDBS	8,7120	0,0250	0,4167	0,0025	2,0833
D	LSB	10,0665	0,0300	0,5000	0,0030	2,0000
	SDBS	10,4544	0,0300	0,5000	0,0030	2,0000
E	LSB	16,7775	0,0500	0,8333	0,0050	1,6667
	SDBS	17,4240	0,0500	0,8333	0,0050	1,6667
F	LSB	25,1663	0,0750	1,2500	0,0075	1,2500
	SDBS	26,1360	0,0750	1,2500	0,0075	1,2500
G	LSB	33,5550	0,1000	1,6667	0,0100	0,8333
	SDBS	34,8480	0,1000	1,6667	0,0100	0,8333
H	LSB	41,9438	0,1250	2,0833	0,0125	0,4167
	SDBS	43,5600	0,1250	2,0833	0,0125	0,4167
I	LSB	50,3325	0,1500	2,5000	0,0150	0,0000
	SDBS	52,2720	0,1500	2,5000	0,0150	0,0000

The ligand concentrations were varied to achieve the best coating of the nanoparticles. If the ligand concentration is too low, no full coating can be achieved, while a concentration, which is too high leads to micelles, which act as template for TEOS hydrolysis.

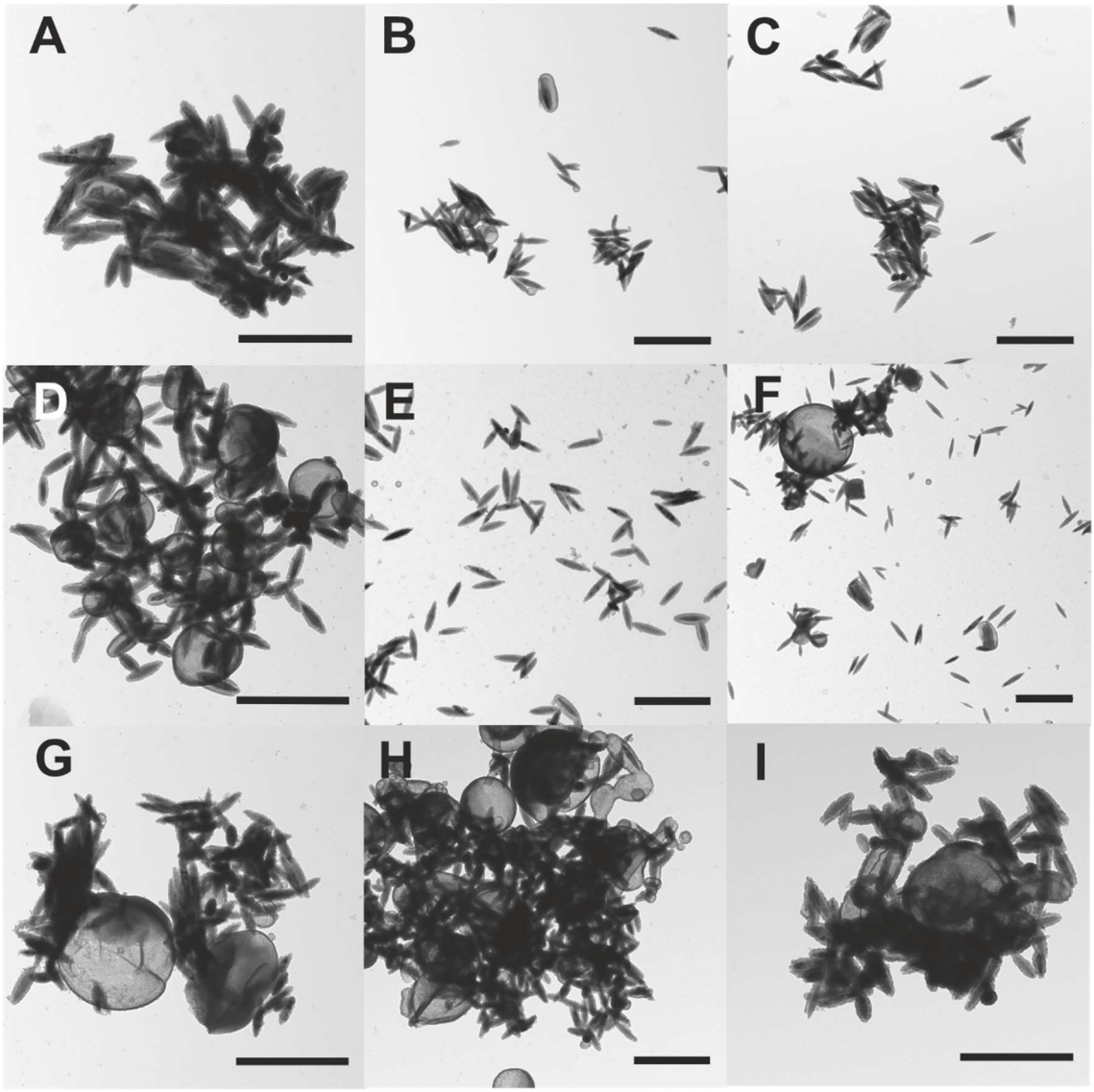

Figure 82: TEM images of variation of ligand mixture (SDBS and LSB) concentration in the synthesis of Fe_2O_3@SiO_2 nanorattles. (scale bar A-H: 1 µM)

Figure 82 shows the TEM images of different synthesis approaches of the variation of the ligand mixture. In approach A primary core-shell nanoparticles are observable, while in Figure 82B and C already some nanorattles are presented. In all three cases the concentration of the ligands is too low. The hematite nanoparticles cannot be coated completely to build up a shell around all nanoparticles. Approach D contains some nanorattles but also some silica spheres

built because of ligand micelles next to nanoparticles. In approach E, however, free silica is observable. All concentrations higher lead to silica spheres and agglomerates of nanorattles.

To obtain nanorattles the optimised parameters of the three synthesis series were combined (TEOS approach C, APTES approach C and ligands approach E). Since some nanoparticles were not included in silica shells and free silica could be observed the ligand concentration was increased (approach F). Results are shown in Figure 83.

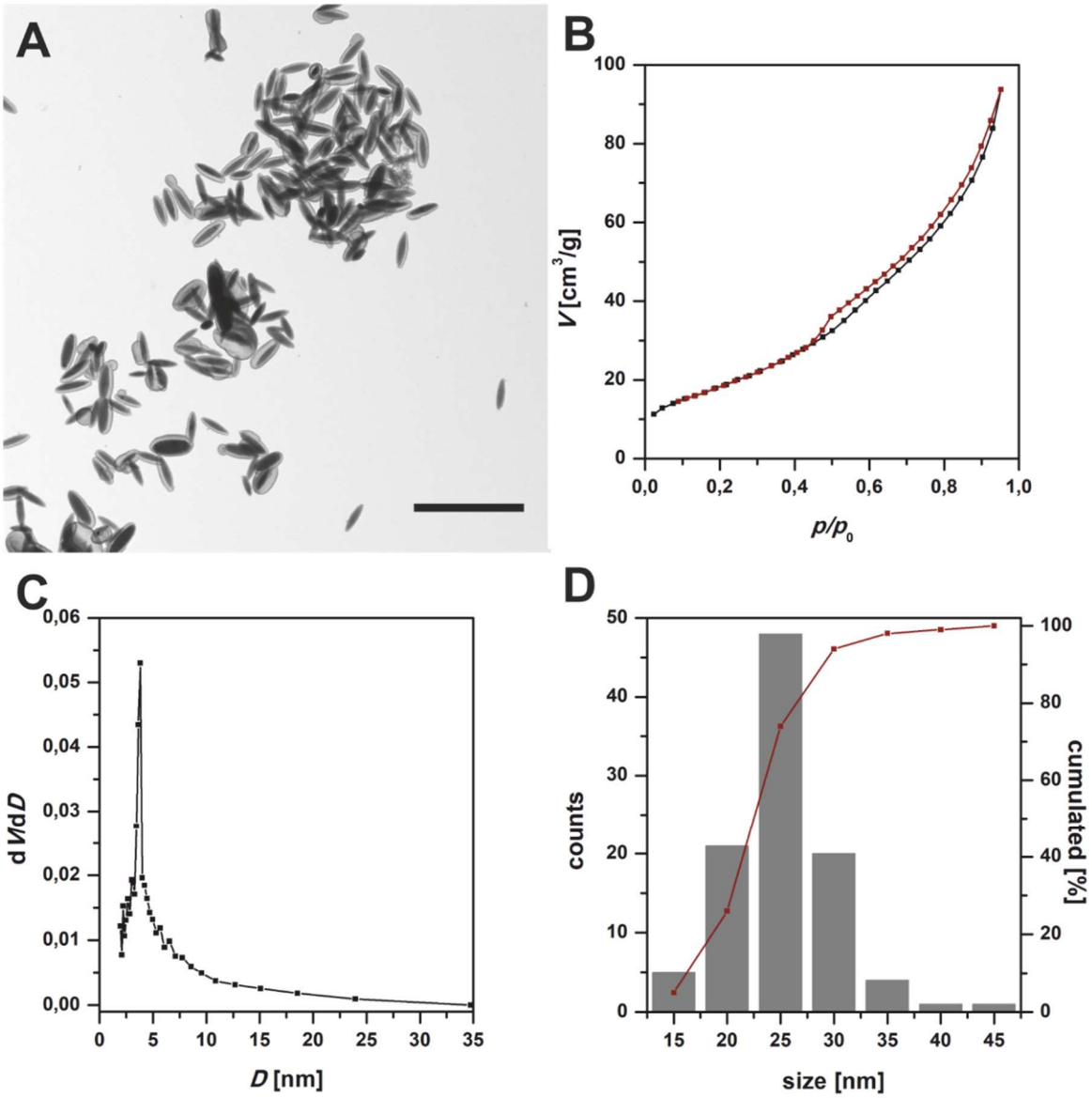

Figure 83: A: TEM image of Fe_2O_3@SiO_2 nanorattles (scale bar 2 µm). B: BET measurement of the nanorattles (black line: adsorption, red line: desorption). C: Pore size distribution obtained from BET measurements. D: Histogram of silica shell thickness (grey columns: counts, red line: cumulated [%]).

Figure 83A shows a typical TEM image of synthesised Fe_2O_3@SiO_2 nanorattles. From the TEM image it is not obvious if the silica shell is porous or not, so Brunauer-Emmett-Teller (BET) measurements were performed (Figure 83B). A typical type II physisorption isotherm could be observed. The observed isotherm can be clearly distinguished from a type III isotherm, because the observable slope between measuring point 1 and 2 is larger than between measuring point 2 and 3. Additionally a H3 hysteresis loop could be detected. This hysteresis type is known from samples with complex pore structures, e.g. large pores connected to the environment by thin pore necks. Here, large pores remain filled until the thinner necks are emptied at lower vapour pressures.[164] The pore size distribution is presented in Figure 83C. The distribution is very narrow with a maximum at a pore size of 3.8 nm. The silica shell thickness is 23 ± 5 nm. The related histogram is presented in Figure 83D.

To compare the peroxidase-like activity of the hematite NPs and the Fe_2O_3@SiO_2 nanorattles the AR assay was performed. For this purpose, the time dependent change in the fluorescence intensity was analysed, using different amounts of nanoparticles.

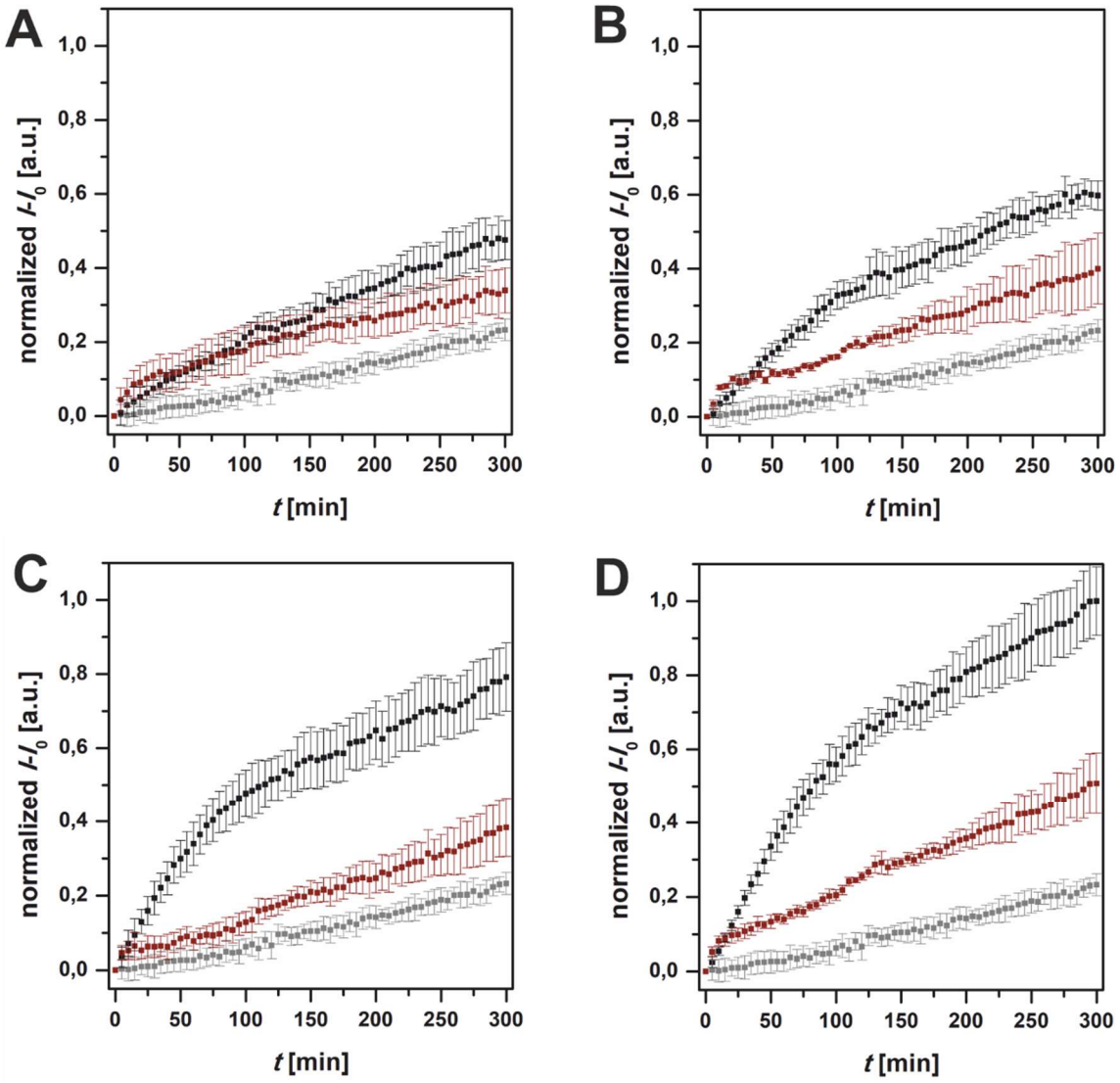

Figure 84: Time course of fluorescence increase during the AR assay with different amounts of Fe_2O_3 NPs (black) or Fe_2O_3@SiO_2 nanorattles (red) – A: 25 µg ml^{-1}, B: 50 µg ml^{-1}, C: 125 µg ml^{-1} and D: 250 µg ml^{-1}. In addition, the fluorescence intensity increase in an AR sample to determine the blind activity (grey).

Comparing the catalysis of the peroxidase reaction in the AR assay between the hematite nanoparticles and the nanorattles, it is evident that, regardless of the concentration of particles used, the hematite nanoparticles convert more dye per unit time than the nanorattles. The measured values are normalised to the maximum of the conversion with the highest concentration of hematite nanoparticles. All measurements of hematite nanoparticles show a hyperbolic trend. However, the turnover of the dye in the presence of the nanorattles is in all four cases linear dependent on time. This can be explained by diffusion. By encapsulating the catalytic active hematite nanoparticles in a silica shell, a diffusion

barrier has been incorporated into the system. In the model, this barrier should be comparable to the membrane of a primitive organism. The peroxidase-like reaction is therefore no longer limited by the catalyst, but by the diffusion rate. Nevertheless, the conversion rate also increases with the increasing concentration of nanorattles, since the diffusion paths become shorter due to the increase in concentration. All measurements with the addition of nanoparticles or nanorattles show a higher turnover of the dye molecule than the blind measurement.

5.2.2. Synthesis and characterisation of heterotrimeric Fe_2O_3@SiO_2@TiO_2 nanorattles

To build up a reaction cascade, titanium dioxide was applied to the silica shell by means of a hydrolysis reaction followed by calcination described by *Li et al.*[165] Energy dispersive X-ray spectroscopy (EDX) confirmed the presence of titanium on the surface of the nanoparticles (Figure 85).

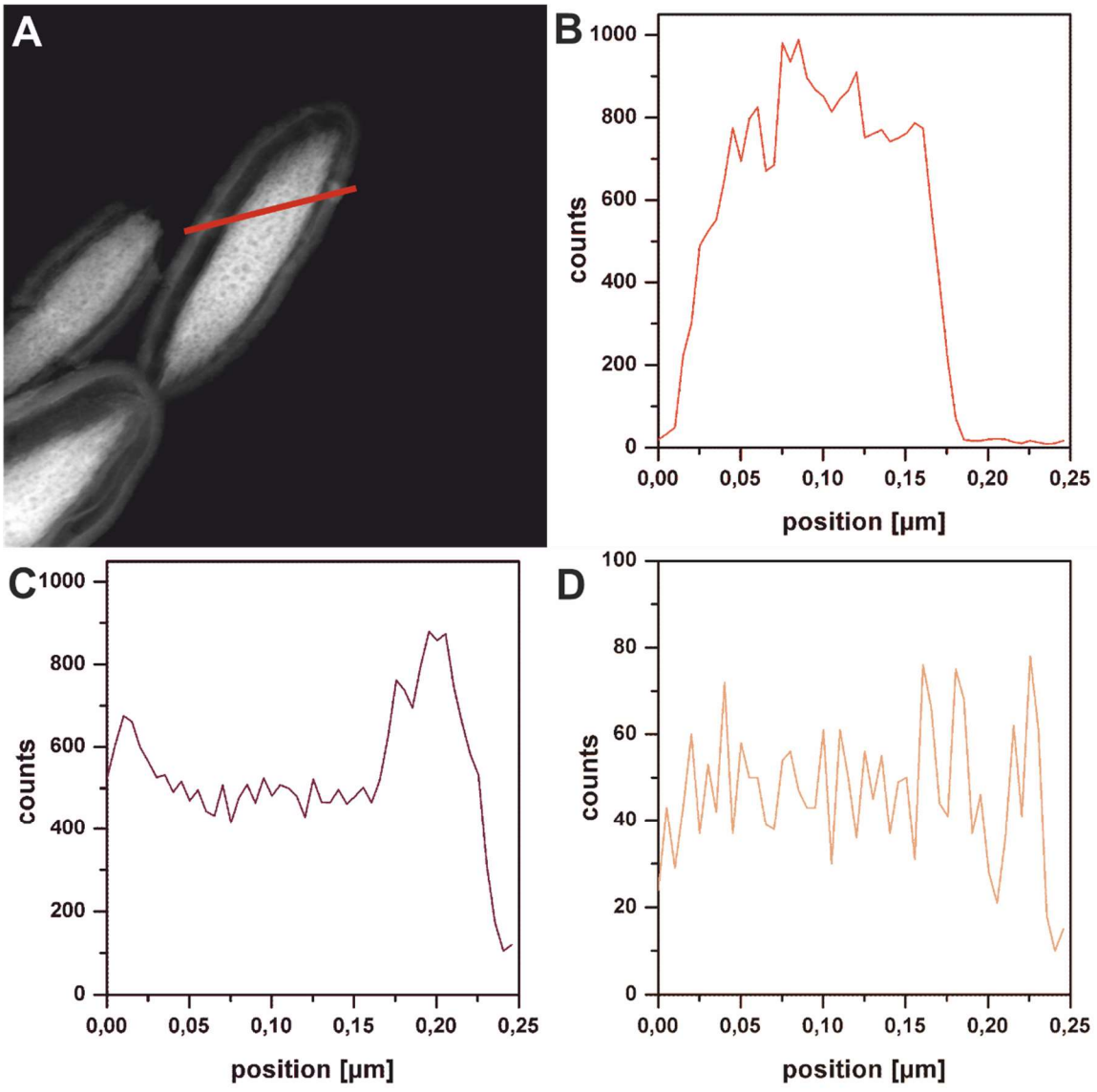

Figure 85: A: HR-TEM image of Fe_2O_3@SiO_2@TiO_2 in STEM mode with EDX measurement line (red). B: EDX line scan of iron. C: EDX line scan of silicon. D: EDX line scan of titanium.

Figure 85A shows a high resolution (HR)-TEM image of a titanium dioxide coated nanorattle. The red line shows the course of the EDX measurement. The hematite nanoparticle can be seen in the image, which is surrounded by a silica shell. In comparison to the previous TEM image (Figure 85A), individual points of higher

contrast can be seen, which can be assigned to titanium dioxide. Figure 85B, C and D show the EDX spectra related to iron (Figure 85B), silicon (Figure 85C) and titanium (Figure 85D). The titanium and silicon signals show continuous counts over the particles with an abrupt dip at the edge of the nanoparticles. The counts of the titanium signal are significantly lower compared to the other two measurements and the observable dip further at the edge of the particle, which is also consistent with the observations in the HR-TEM image. Here, no continuous signal is detectable, since the applied titanium dioxide are a single sphere and not a continuous film.

To set up a reaction cascade, hydrogen peroxide was generated by photocatalysis. The quantification of generated hydrogen peroxide was done by using the FOX assay. To mimic the reaction cascade the turnover of AR after photocatalytic generation of hydrogen peroxide was performed too.

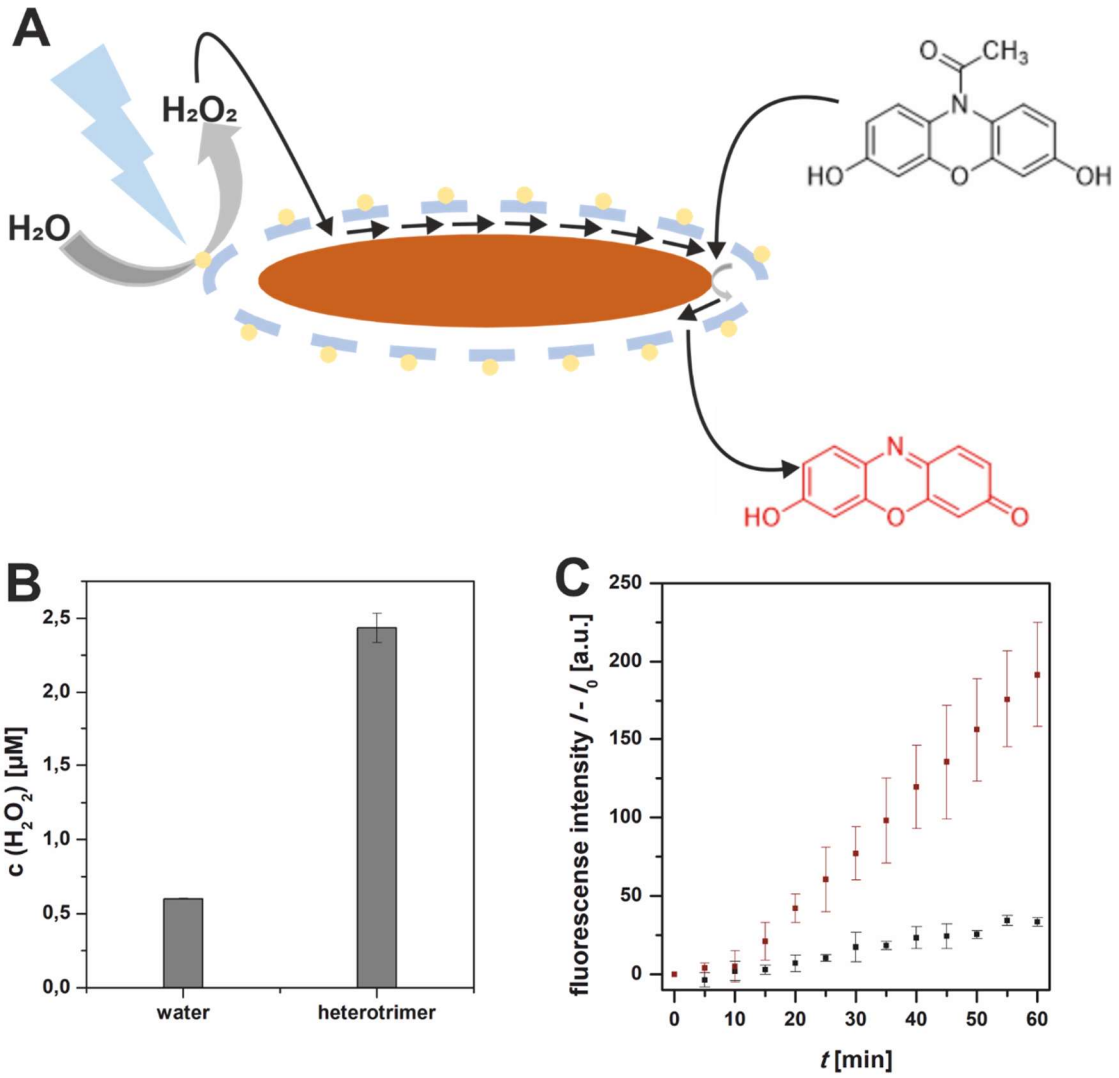

Figure 86: A: Schematic representation of the reaction cascade performed. B: Photocatalytically produced amount of hydrogen peroxide as detected by the FOX assay in an irradiated MilliQ water sample and the heterotrimeric nanorattles dispersed in water. C: Turnover of the AR after previous irradiation in the water sample (black) and the sample with heterotrimeric nanorattles (red).

Figure 86A schematically shows the desired reaction cascade. The hematite nanoparticles, which are characterised by an intrinsic peroxidase-like activity, are coated by a silica layer to form a nanorattle. It is a model system for an inorganic protocell. Outside the protocell, on the outer surface of the silica shell, is titanium dioxide, which is photocatalytic active. Under irradiation with UV light, titanium dioxide in the anatase modification is able to generate hydrogen peroxide in aqueous dispersions. This is utilised as follows: the photocatalytically produced hydrogen peroxide reaches the inside of the protocell by diffusion through the porous silica shell. The AR molecule enters the protocell by the same route. At the surface of the hematite nanoparticle, the peroxidase-like activity of the nanoparticle

converts AR and hydrogen peroxide into the fluorescent resorufin molecule. This molecule diffuses through the pores of the silica shell into the surrounding medium where it can be detected by fluorescence measurements. The reaction cascade therefore consists of two sub-steps which were observed in sequence.

Anticipated, no additional XRD pattern are shown in the following figure, because the silica shell is amorphous so no reflex could be detected. The titanium compound on the outer surface of the silica shell would also be not detected in the XRD pattern, because the particles on the surface are very small, so that no defined reflexes would be detectable.

Figure 86B shows the amount of photocatalytically produced hydrogen peroxide in comparison to the heterotrimeric nanorattles using the FOX assay (see 4.2.2), both in an irradiated water environment. In the sample containing nanorattles almost five times the amount of hydrogen peroxide is formed photocatalytically compared to the water sample.

Subsequently, it was tested whether it is possible to convert the produced hydrogen peroxide in a peroxidase-like reaction inside the nanorattles. To do this, both molecules involved in the synthesis - hydrogen peroxide and AR - have to diffuse through the silica shell into the interior of the nanorattle in order to react on the surface of the hematite nanoparticles. The resulting resorufin molecule must then diffuse through the silica shell back into the surrounding medium in order to be detected. For this purpose, fluorescence measurements were performed on the two irradiated samples. After irradiation, AR was added to the sample in phosphate buffered saline (PBS) and the increase in fluorescence intensity over time was measured. Figure 86C shows the significantly stronger fluorescence increase in the case of the nanorattles sample compared to the water sample. This clearly shows that resorufin was formed. The direct comparison with the irradiated water sample also shows that the conversion of the AR to resorufin is caused by the present nanorattles. Since a smaller increase in fluorescence intensity can be observed in the first ten minutes of the measurement than afterwards, it can be assumed that the diffusion time of the AR after the addition into the interior of the nanorattle and the subsequent outward diffusion can be observed. This confirms that a reaction cascade consisting of photocatalytic hydrogen peroxide production

and subsequent reaction on a nanoparticle with peroxidase-like activity through a diffusion barrier could be successfully imitated.

5.3. Conclusion

A heterotrimeric nanoparticle system that is characterised by two catalytic units could be developed. The system combines redox-active hematite nanoparticles with photocatalytic active titanium dioxide. The system is characterised by an interior and an exterior, which makes it possible to separate the two catalytic active units. At the same time, the separation in form of a porous silica shell provides a diffusion barrier comparable to a simple membrane. With the help of this heterotrimeric nanoparticle system, a reaction cascade could be imitated that was previously only possible with enzymes. With this system, a model that makes it possible to establish theories on the origin of the first life forms including inorganic matter was created. With the encapsulated hematite nanoparticles, a model for an inorganic protocell could be presented, whereby the hematite nanoparticles are enzyme-like systems. They represent the inorganic matter at the time of the formation of the first life forms and may well have been possible as an early protective function of developing life forms against oxidative pollutants.

In addition to nanoparticle architecture, the model provides new food for thought for influencing and enabling the emergence of the first life forms.

5.4. Experimentals

5.4.1. Materials

3-Aminopropyl triethoxysilane (APTES, $C_9H_{23}NO_3Si$, ≥98%, Sigma-Aldrich), ammonium ferrous sulphate hexahydrate ($(NH_4)_2Fe(SO_4)_2 \cdot 6H_2O$, 99+ %, Acros), amplifu™ Red (AR, $C_{14}H_{11}NO_4$, ≥98 %, Sigma-Aldrich), D-sorbitol ($C_6H_{14}O_6$, ≥ 98 %, Sigma-Aldrich), hydrochloric acid (HCl, 37 wt%, VWR), *N*-dodecyl-*N*,*N*-dimethyl-3-ammonio-1-propanesulfonate (LSB, $C_{18}H_{29}SO_3Na$, ≥98%, Alfa Aesar), hydrogen peroxide (H_2O_2, 35 %, pure, Roth), iron(III) chloride hexahydrate ($FeCl_3 \cdot 6H_2O$, 97 %, abcr), phosphate buffered saline (PBS, Sigma-Aldrich), potassium dihydrogen phosphate (KH_2PO_4, 99 %, Sigma-Aldrich), Sodiumdodecyl benzenesulfonate (SDBS, $C_{18}H_{29}SO_3Na$, technical grade, Sigma-Aldrich), sulphuric acid (H_2SO_4, 95 %, Fisher), tetraethyl orthosilicate (TEOS, $SiC_8H_{20}O_4$, reagent grade, 98%, Sigma-Aldrich), tetrahydrofurane (THF, C_4H_8O, 99.8 %, Fisher), xylenolorange tetrasodium salt (XO, $C_{31}H_{28}N_2Na_4O_{13}S$, Merck).

5.4.2. Synthesis

Synthesis of hematite – silica nanorattles

The nanorattles were synthesised like described elsewhere with some modifications:[163] LSB and SDBS were mixed (1.25 mL, 60 mM stock solution) with water (2.5 mL). Hematite nanoparticles (75 mg) were dispersed in water (5 mL) *via* sonification and added to the ligand solution. The reaction mixture was stirred (250 rpm) at 40 °C for 2 h. APTES (23.5 µL, 0.101 mmol) and TEOS (100 µL, 0.45 mmol) were added and the mixture was additional stirred for 1 h before the reaction temperature was increased to 80 °C. After stirring over night the reaction mixture was naturally cooled to room temperature and the product was collected *via* centrifugation (9000 rpm, 10 min), washed with water and ethanol and dried overnight in an electric oven at 70 °C. The nanorattles were stirred in diluted hydrochloric acid for 3 hours.

Coating of hematite – silica nanorattles with titanium dioxide

The coating of the nanorattles was done like described elsewhere.[165] Fe_2O_3@SiO_2 nanorattles (20 mg) were dispersed in Ethanol (20 mL) *via* sonification. MilliQ water (0.5 mL) was added before titanium isopropoxide (100 µL) was added. The reaction mixture was stirred overnight. The nanorattles were collected *via* centrifugation (9000 rpm, 10 min) and washed three times with ethanol. The nanoparticles were dried in an electric oven at 70 °C for 3 hours before they were calcined at 550 °C for 3 hours.

Kinetic analysis

AR assay

To measure the conversion of AR by using hematite nanoparticles in comparison to nanorattles, the different amounts of nanoparticles/nanorattles (stock solution 1 mg mL^{-1} ; 0 µL, 5 µL, 10 µL, 25 µL and 50 µL) were mixed with PBS buffer (160 µL, 155 µL, 150 µL, 135 µL and 110 µL) and AR (500 µM; 20 µL) before starting the reaction by adding hydrogen peroxide (10 mM; 20 µL).

The measurements were conducted on an Infinite 200 Pro plate reader from TECAN in flat bottom black 96-well plates from Greiner bio-one. The excitations wavelength was set to 550 nm, the emission wavelength at 590 nm, while the excitation band width was set to 9 nm.

FOX assay

A MilliQ water sample and a Fe_2O_3@SiO_2@TiO_2 nanorattle dispersion (5 mg mL^{-1}, in water) was prepared and irradiated for one hour with two LEDs (SSC VIOSYS CUN66B1B on Star Platine, LED-Tech, 365 nm). After radiation the dispersion was centrifuged to separate the nanorattles. The supernatant (20 µL) was mixed with a solution containing of two solutions mixed in a ratio of 1:100. The first solution was containing of $(NH_4)_2Fe(SO_4)_2$ (25 mM) and sulphuric acid (2.5 M) while the second solution was containing of xylenolorange (125 µM) and sorbitol (100 mM). The mixture was incubated for 30 min at room temperature before measuring the extinction at 590 nm. For data analysis an external 5-point calibration with hydrogen peroxide was measured simultaneously (Supporting figure 25).

Reaction cascade using AR

For measuring the conversion of AR in a reaction cascade a MilliQ water sample and a Fe_2O_3@SiO_2@TiO_2 nanorattle dispersion (5 mg mL^{-1}, in water) were prepared and radiated for one hour with a two LEDs (SSC VIOSYS CUN66B1B on Star Platine, LED-Tech, 365 nm). The samples (50 µL) were mixed with PBS buffer (130 µL) in a flat bottom black 96-well plates from Greiner bio-one. Before starting the measurement AR was added (20 µL, 500 µM). The measurements were conducted for one hour on an Infinite 200 Pro plate reader from TECAN. The excitations wavelength was set to 550 nm, the emission wavelength at 590 nm, while the excitation band width was set to 9 nm.

Nanoparticle Characterisation

Powder X-ray diffraction (XRD)

The solid-state analysis of the pure hematite nanoparticles was conducted on a STOE Stadi P (Germany) diffractometer using Mo $K_{\alpha1}$ radiation. The data was analysed with *MATCH3!* (*JCDPS card 99-504-2341*).[166]

Transmission electron microscopy (TEM)

The TEM measurements were conducted after applying the sample to a graphite-coated TEM mesh (Cu-300 mesh, Electron Microscopy Sciences, Hatfield, PA) on a Tecnai G2 Spirit from FEI with an acceleration voltage of 120 kV. It is equipped with a twin objective lens, a LaB_6 cathode and a CCD (charge coupled device) camera (2k x 2k). The evaluation was performed with the software *ImageJ*.

High resolution TEM and EDX (HR-TEM and EDX)

HR-TEM and EDX measurements were carried out with a FEI TECNAI F30 S-TWIN transmission electron microscope equipped with a field emission gun and working at 300 kV. TEM images were taken with a CCD camera (16-bit 4.096 x 4096 GATAN ULTRASCAN4000) and acquired by Gatan Digital Micrograph software. Scanning transmission electron microscopy (STEM) images and EDX spectra were collected by a FISCHIONE high-angular annular dark field (HAADF) detector / FP 5402/00 EDX detector and acquired by Emispec ES Vision software.

BET

The BET measurements of the used nanorattles were conducted on a 3P Micro 300 (3P Instruments). For this the nanorattle samples were dried under vacuum. Nitrogen was used as measuring gas. The data was analysed using the software Surface Area & Pore Size Analyser System (Version: 10.03.02).

5.5. Appendix

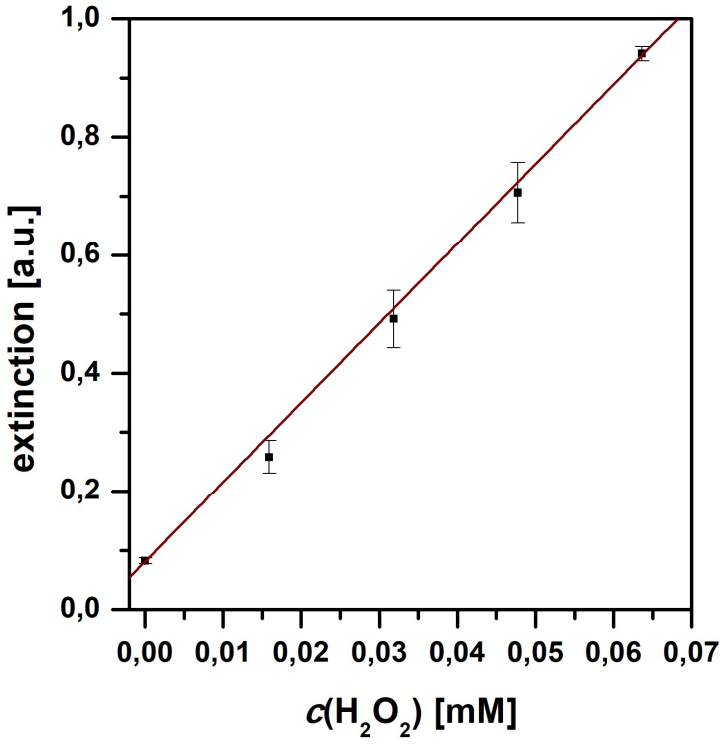

Supporting figure 25: External 5-point calibration of FOX-assay.

Conclusion 6

This doctoral thesis describes the successful presentation of a reaction cascade using inorganic nanoparticles in view of a prebiotic background.

An overview of different theories on the emergence of first life forms could be given. Experiments such as the Miller-Urey experiment, but also theories such as those of Wächterhäuser, who established a connection between the emergence of life and the formation of pyrite, as well as modern approaches such as those of Schreiber and Meyer were presented. Research sites that still exist today, such as black and white smokers and Lost City systems, were also described.

The work deals intensively with nanoparticles as enzyme mimics and here primarily with the mimicry of the enzyme peroxidase. Peroxidase is a vital enzyme that strictly regulates the existence of hydrogen peroxide in living organisms. With regard to the known assays for the investigation of peroxidase activity, some studies have been carried out that critically examine their use. The known and published assays are designed for use in the investigation of enzymatic systems, but not for the investigation of inorganic nanoparticles. Nevertheless, they can be used for this purpose. However, the comparability of the results must be questioned. The assays are excellent for evaluating and comparing own nanoparticle samples, provided that they do not interact with the dye molecule used. However, a comparison of the catalytic properties with foreign nanoparticles that were not examined under the same conditions is invalid. The present results should sensitise to critically question the catalytic parameters of foreign samples and to make a comparison with them only if work was done under the same conditions and interactions can be excluded.

Janus particles such as Au@Fe_3O_4 and Au@ZnO were synthesised to represent a reaction cascade involving the photocatalytic generation of hydrogen peroxide and its conversion on a peroxidase mimetic. Of particular interest were the improved catalytic parameters of the Janus particles compared to their individual components in the form of Fe_3O_4 and ZnO nanoparticles. Attempts were made to extend the synthesised Janus particles to heterotrimeric systems such as TiO_2@Au@Fe_3O_4 and ZnO@Au@Fe_3O_4. For this purpose, a bifunctional ligand 4-(11-mercaptoundecyl)benzene-1,2-diol was prepared. In addition to a thiol group

for functionalisation of the Au domain, this ligand has a catechol group that is suitable for functionalisation of Fe_3O_4 and TiO_2 nanoparticles. With the help of this ligand, an attempt was made to synthesise heterotrimeric nanostructures. Since it seemed that the ligand concentration in the experiments was too high, which led to the formation of nanoparticle agglomerates, work must be done to improve the implementation. By working with lower ligand concentrations or a mixture of two ligands consisting of the bifunctional ligand and a monofunctional ligand, the degree of functionalisation of the TiO_2 or Fe_3O_4 nanoparticles could be reduced, thus enabling the formation of heterotrimeric nanoparticles. The synthesis of heterotrimeric nanostructures consisting of ZnO, Au and Fe_3O_4 seems possible with the synthesis of Au@ZnO Janus particles using $Fe(acac)_3$ as iron precursor. Further experiments should be carried out here in the future by varying the ratio of oleic acid to oleylamine. If ZnO@Au@Fe_3O_4 heteroparticles have been synthesised, their catalytic properties should be investigated and it should be checked whether a synergistic effect can also be observed on these particles. The synthesis of TiO_2@Au@CeO_{2-x} nanoparticles for use against marine biofouling would then be particularly interesting. Here, the TiO_2 domain would be able to generate hydrogen peroxide under the influence of sunlight, which the CeO_{2-x} domains convert in a haloperoxidase-like reaction. This could reduce biofouling.

Nanorattles consisting of hematite and a mesoporous silica shell could be synthesised. It was shown that catalysis with the help of the hematite nanoparticles is possible through a diffusion barrier and can also be measured at the same time. Here, an expected linear behaviour between the colour reaction and the time was shown, due to the diffusion. These nanorattles could be extended by a third type of particle - the TiO_2 on the outside of the nanorattles, condensed onto the silica shell. This made it possible to generate hydrogen peroxide photocatalytically outside the nanorattle, which diffuses through the mesoporous silica shell into the interior to the hematite nanoparticle. At the surface of the hematite nanoparticle, it was then converted in a peroxidase-like reaction. This model system has an analogy with archaea. A life form whose origin is assumed to be close to the origin of life. Archaea are living organisms that are viable under extreme conditions and consciously seek their habitat there (e.g. strong acidic environments, sulphurous

habitats). In analogy to the cell membrane of archaea, which is characterised by a higher robustness against external influences compared to the cell membranes of today's mammals, the mesoporous silica shell was chosen as the nanorattle shell. Since extreme environmental conditions are assumed at the time of the emergence of the first life forms, the existence of hydrogen peroxide is likely, assuming an aerobic environment. Since hydrogen peroxide is considered toxic in high concentrations within a living being, protective mechanisms, such as the enzymes known today, have been essential for all living beings since the beginning of their emergence. The model system presented here shows an exemplary representation of the regulation of the hydrogen peroxide concentration of a life form that did not yet have enzymes in interaction with inorganic matter.

Literature

[1] G. S. Smith, *Am. J. Phys.* **2005**, *73*, 590–597.

[2] P. Fara, *Philos. Trans. R. Soc. A Math. Phys. Eng. Sci.* **2015**, *373*, DOI 10.1098/rsta.2014.0213.

[3] W. Martin, J. Baross, D. Kelley, M. J. Russell, *Nat. Rev. Microbiol.* **2008**, *6*, 805–814.

[4] K. Dose, *Chemie unserer Zeit* **1987**, *21*, 177–185.

[5] A. I. Oparin, *The Origin of Life on the Earth*, **1957**.

[6] S. L. Miller, J. William Schopf, A. Lazcano, *J. Mol. Evol.* **1997**, *44*, 351–353.

[7] M. Di Giulio, *J. Theor. Biol.* **2010**, *266*, 569–572.

[8] G. Fuchs, in *Allg. Mikrobiol.*, **2014**, p. 31.

[9] M. C. Weiss, F. L. Sousa, N. Mrnjavac, S. Neukirchen, M. Roettger, S. Nelson-Sathi, W. F. Martin, *Nat. Microbiol.* **2016**, *1*, 1–8.

[10] C. R. Woese, *Proc. Natl. Acad. Sci. U. S. A.* **2000**, *97*, 8392–8396.

[11] E. V. Koonin, *Nat. Rev. Microbiol.* **2003**, *1*, 127–136.

[12] C. Woese, *Proc. Natl. Acad. Sci. U. S. A.* **1998**, *95*, 6854–6859.

[13] T. M. McCollom, *Annu. Rev. Earth Planet. Sci.* **2013**, *41*, 207–229.

[14] X. Xie, D. Backman, A. T. Lebedev, V. B. Artaev, L. Jiang, L. L. Ilag, R. A. Zubarev, *Sci. Rep.* **2015**, *5*, 1–8.

[15] M. Ferus, F. Pietrucci, A. M. Saitta, A. Knížek, P. Kubelík, O. Ivanek, V. Shestivska, S. Civiš, *Proc. Natl. Acad. Sci. U. S. A.* **2017**, *114*, 4306–4311.

[16] G. Wächtershäuser, *Syst. Appl. Microbiol.* **1988**, *10*, 207–210.

[17] G. Wächtershauser, *Proc. Natl. Acad. Sci. U. S. A.* **1990**, *87*, 200–204.

[18] B. Kaim, W.; Schwederski, *Bioanorganische Chemie*, **2005**.

[19] W. Martin, M. J. Russell, *Philos. Trans. R. Soc. B Biol. Sci.* **2007**, *362*, 1887–1925.

[20] G. Wächtershäuser, *Am. Soc. Microbiol.* **1988**, *52*, 452–484.

[21] M. Colín-García, A. Heredia, G. Cordero, A. Camprubí, A. Negrón-Mendoza, F. Ortega-Gutiérrez, H. Beraldi, S. Ramos-Bernal, *Bol. la Soc. Geol. Mex.* **2016**, *68*, 599–620.

[22] "Hydrothermalquellen," can be found under https://www.spektrum.de/lexikon/biologie/hydrothermalquellen/33127, **1999**.

[23] "White smoker," **n.d.**

[24] "mafisch," can be found under https://www.spektrum.de/lexikon/geowissenschaften/mafisch/9863, **2000**.

[25] "ultramafisch," can be found under https://www.spektrum.de/lexikon/geowissenschaften/ultramafisch/17189, **2000**.

[26] N. Hollemann, A.F., Wiberg, *Lehrbuch Der Anorganischen Chemie*, Walther DeGruyter, **2007**.

[27] C. Riedel, E.; Janiak, *Anorganische Chemie*, DeGruyter, **2011**.

[28] M. Schulte, D. Blake, T. Hoehler, T. McCollom, *Astrobiology* **2006**, *6*, 364–376.

[29] M. J. Russell, A. J. Hall, W. Martin, *Geobiology* **2010**, *8*, 355–371.

[30] University of Washington, "Lost City Research," can be found under http://www.lostcity.washington.edu/questions/recentlyasked.html, **2009**.

[31] A. Y. Mulkidjanian, *Biol. Direct* **2009**, *4*, 1–39.

[32] "Verwerfung," **2000**.

[33] U. Schreiber, O. Locker-Grütjen, C. Mayer, *Orig. Life Evol. Biosph.* **2012**, *42*, 47–54.

[34] T. Tassaing, R. Oparin, Y. Danten, M. Besnard, *J. Supercrit. Fluids* **2005**, *33*, 85–92.

[35] C. Mayer, U. Schreiber, M. J. Dávila, *Orig. Life Evol. Biosph.* **2015**, *45*, 139–

148.

[36] J. L. Stryer, L; Berg, J.M.; Tymoczko, *Biochemie*, **2013**.

[37] B. Zhang, R. Breslow, *J. Am. Chem. Soc.* **1997**, *119*, 1676–1681.

[38] X. Cao, S. P. Teong, D. Wu, G. Yi, H. Su, Y. Zhang, *Green Chem.* **2015**, *17*, 2348–2352.

[39] F. Cramer, W. Kampe, *J. Am. Chem. Soc.* **1965**, *87*, 1115–1120.

[40] A. Corma, *Catal. Rev. - Sci. Eng.* **2004**, *46*, 369–417.

[41] R. R. French, P. Holzer, M. G. Leuenberger, W. Woggon, *Organomet. Chem.* **2000**, 1267–1269.

[42] E. A. Doherty, J. A. Doudna, *Annu. Rev. Biophys. Biomol. Struct.* **2001**, 597–615.

[43] D. Hewett-Emmett, R. E. Tashian, *Mol. Phylogenet. Evol.* **1996**, *5*, 50–77.

[44] C. Obinger, *Arch. Biochem. Biophys.* **2010**, *500*, 1–2.

[45] A. Góth, L; Rass, P.; Páy, *Mol. Diagn.* **2004**, *8*, 141–149.

[46] A. Butler, *Curr. Opin. Chem. Biol.* **1998**, *2*, 279–285.

[47] I. A. Abreu, D. E. Cabelli, *Biochim. Biophys. Acta - Proteins Proteomics* **2010**, *1804*, 263–274.

[48] L. Gao, J. Zhuang, L. Nie, J. Zhang, Y. Zhang, N. Gu, T. Wang, J. Feng, D. Yang, S. Perrett, X. Yan, *Nat. Nanotechnol.* **2007**, *2*, 577–583.

[49] B. K. Burgess, D. J. Lowe, *Chem. Rev.* **1996**, *96*, 2983–3011.

[50] H. Wei, E. Wang, *Chem. Soc. Rev.* **2013**, *42*, 6060–6093.

[51] R. Ragg, M. N. Tahir, W. Tremel, *Eur. J. Inorg. Chem.* **2016**, *2016*, 1906–1915.

[52] R. Ragg, A. M. Schilmann, K. Korschelt, C. Wieseotte, M. Kluenker, M. Viel, L. Völker, S. Preiß, J. Herzberger, H. Frey, K. Heinze, P. Blümler, M. N. Tahir, F. Natalio, W. Tremel, *J. Mater. Chem. B* **2016**, *4*, 7423–7428.

[53] M. Hu, K. Korschelt, P. Daniel, K. Landfester, W. Tremel, M. B. Bannwarth,

ACS Appl. Mater. Interfaces **2017**, *9*, 38024–38031.

[54] K. Herget, P. Hubach, S. Pusch, P. Deglmann, H. Götz, T. E. Gorelik, I. A. Gural'skiy, F. Pfitzner, T. Link, S. Schenk, M. Panthöfer, V. Ksenofontov, U. Kolb, T. Opatz, R. André, W. Tremel, *Adv. Mater.* **2017**, *29*, 1–8.

[55] J. Hou, M. Vázquez-González, M. Fadeev, X. Liu, R. Lavi, I. Willner, *Nano Lett.* **2018**, *18*, 4015–4022.

[56] Y. Meng, W. Li, X. Pan, G. M. Gadd, *Environ. Sci. Nano* **2020**, *4*, DOI 10.1039/c9en01089k.

[57] F. Natalio, R. André, A. F. Hartog, B. Stoll, K. P. Jochum, R. Wever, W. Tremel, *Nat. Nanotechnol.* **2012**, *7*, 530–535.

[58] D. Jiang, D. Ni, Z. T. Rosenkrans, P. Huang, X. Yan, W. Cai, *Chem. Soc. Rev.* **2019**, *48*, 3683–3704.

[59] S. Hashimoto, R. Nakajima, I. Yamazaki, T. Kotani, S. Ohtaki, T. Kitagawa, *FEBS Lett.* **1989**, *248*, 205–209.

[60] P. A. Wood, Z.A.; Poole, L.B.; Karplus, *Science (80-.).* **2003**, *300*, 650–653.

[61] M. Zámocký, S. Hofbauer, I. Schaffner, B. Gasselhuber, A. Nicolussi, M. Soudi, K. F. Pirker, P. G. Furtmüller, C. Obinger, *Arch. Biochem. Biophys.* **2015**, *574*, 108–119.

[62] N. C. Veitch, *Phytochemistry* **2004**, *65*, 249–259.

[63] R. Fenna, J. Zeng, C. Davey, *Arch. Biochem. Biophys.* **1995**, *316*, 653–656.

[64] A. O. Falade, U. U. Nwodo, B. C. Iweriebor, E. Green, L. V. Mabinya, A. I. Okoh, *Microbiologyopen* **2017**, *6*, 1–14.

[65] Y. Orii, *J. Biol. Chem.* **1982**, *257*, 9246–9248.

[66] J. N. Rodríguez-López, D. J. Lowe, J. Hernández-Ruiz, A. N. P. Hiner, F. García-Cánovas, R. N. F. Thorneley, *J. Am. Chem. Soc.* **2001**, *123*, 11838–11847.

[67] M. Mahmoudi, A. Simchi, A. S. Milani, P. Stroeve, *J. Colloid Interface Sci.* **2009**, *336*, 510–518.

[68] C. Shundo, H. Zhang, T. Nakanishi, T. Osaka, *Colloids Surfaces B Biointerfaces* **2012**, *97*, 221–225.

[69] L. Yang, X. Ren, F. Tang, L. Zhang, *Biosens. Bioelectron.* **2009**, *25*, 889–895.

[70] F. Bødker, M. F. Hansen, C. B. Koch, K. Lefmann, *Phys. Rev. B* **2000**, *61*, 6826–6838.

[71] R. M. Cornell, in *Corros. Rev.*, **1997**, pp. 533–559.

[72] N. Singh, G. J. S. Jenkins, R. Asadi, S. H. Doak, *Nano Rev.* **2010**, *1*, 5358.

[73] K. Wichmann, Synthese, Funktionalisierung Und Anwendung von Magnetischen Eisenoxidnanopartikeln, **2016**.

[74] J. Park, K. An, Y. Hwang, J. E. G. Park, H. J. Noh, J. Y. Kim, J. H. Park, N. M. Hwang, T. Hyeon, *Nat. Mater.* **2004**, *3*, 891–895.

[75] Y. Zhang, N. Kohler, M. Zhang, *Biomaterials* **2002**, *23*, 1553–1561.

[76] K. M. Min, K. S. Park, A. H. Lim, J. C. Kim, D. W. Kim, *Ceram. Int.* **2012**, *38*, 6009–6013.

[77] M. Dondi, F. Matteucci, G. Cruciani, G. Gasparotto, D. M. Tobaldi, *Solid State Sci.* **2007**, *9*, 362–369.

[78] B. R. E. Childs, W. G. Bardsley, *Biochem. J.* **1975**, *145*, 93–103.

[79] M. Kluenker, M. Nawaz Tahir, R. Ragg, K. Korschelt, P. Simon, T. E. Gorelik, B. Barton, S. I. Shylin, M. Panthöfer, J. Herzberger, H. Frey, V. Ksenofontov, A. Möller, U. Kolb, J. Grin, W. Tremel, *Chem. Mater.* **2017**, *29*, 1134–1146.

[80] D. Josephy, T. Eling, R. Mason, *J. Biol. Chem.* **1982**, *257*, 3669–3675.

[81] I. Schick, Design of Multifunctional Janus Particles for Biomedical Applications, **2014**.

[82] C. W. Lee, Y. C. Chen, A. Ostafin, *J. Biomed. Nanotechnol.* **2009**, *5*, 477–485.

[83] C. S. Karamitros, J. Lim, M. Konrad, *Anal. Biochem.* **2014**, *445*, 20–23.

[84] B. Zhao, F. A. Summers, R. P. Mason, *Free Radic. Biol. Med.* **2012**, *53*, 1080–1087.

[85] C. J. B. Alejo, C. Fasciani, M. Grenier, J. C. Netto-Ferreira, J. C. Scaiano, *Catal. Sci. Technol.* **2011**, *1*, 1506–1511.

[86] M. Zhou, Z. Diwu, N. Panchuk-Voloshina, R. P. Haugland, *Anal. Biochem.* **1997**, *253*, 162–168.

[87] O. Kreft, M. Prevot, H. Möhwald, G. B. Sukhorukov, *Angew. Chemie - Int. Ed.* **2007**, *46*, 5605–5608.

[88] P. Daniel, Synthesis and Functionalization of Iron Oxide Nanoparticles and Their Application in Hybrid Materials, **2017**.

[89] A. Lejus, A.M.; Goldberg, D.; Revcolevschi, *C.R. Seances Acad. Sci.* **1966**, *Ser. C*, 1223–1226.

[90] S. Anandan, T. Lana-Villarreal, J. J. Wu, *Ind. Eng. Chem. Res.* **2015**, *54*, 2983–2990.

[91] R. Janiak, C.; Meyer, H.-J.; Gudat, D.; Alsfasser, *Moderne Anorganische Chemie*, **2012**.

[92] M. Nentwich, *Nanotrust Dossiers* **2010**, *3*, 1–4.

[93] V. K. LaMer, R. H. Dinegar, *J. Am. Chem. Soc.* **1950**, *72*, 4847–4854.

[94] F. Fievet, J. P. Lagier, M. Figlarz, *MRS Bull.* **1989**, *14*, 29–34.

[95] Y. Wang, J. He, C. Liu, W. H. Chong, H. Chen, *Angew. Chemie* **2015**, *127*, 2046–2079.

[96] J. Van Embden, A. S. R. Chesman, J. J. Jasieniak, *Chem. Mater.* **2015**, *27*, 2246–2285.

[97] M. G. Murray, C.B.; Kagan, C.R.; Bawendi, *Annu. Rev. Mater. Sci.* **2000**, *30*, 545–610.

[98] S. D. Brown, P. Nativo, J. A. Smith, D. Stirling, P. R. Edwards, B. Venugopal, D. J. Flint, J. A. Plumb, D. Graham, N. J. Wheate, *J. Am. Chem. Soc.* **2010**, *132*, 4678–4684.

[99] P. Chandra, J. Singh, A. Singh, A. Srivastava, R. N. Goyal, Y. B. Shim, *J. Nanoparticles* **2013**, *2013*, 1–12.

[100] T. K. Sau, C. J. Murphy, *J. Am. Chem. Soc.* **2004**, *126*, 8648–8649.

[101] J. Pérez-Juste, I. Pastoriza-Santos, L. M. Liz-Marzán, P. Mulvaney, *Coord. Chem. Rev.* **2005**, *249*, 1870–1901.

[102] H. Yu, M. Chen, P. M. Rice, S. X. Wang, R. L. White, S. Sun, *Nano Lett.* **2005**, *5*, 379–382.

[103] U. Leonhardt, *Nat. Photonics* **2007**, *1*, 207–208.

[104] G. Mie, *Ann. Phys.* **1908**, *330*, 377–445.

[105] M. C. Daniel, D. Astruc, *Chem. Rev.* **2004**, *104*, 293–346.

[106] L. Cademartiri, G. A. Ozin, *Concepts of Nanochemistry*, Wiley-VCH, **2009**.

[107] K. Lance Kelly, E. Coronado, L. L. Zhao, G. C. Schatz, *J. Phys. Chem. B.* **2003**, *107*, 668–677.

[108] S. Peng, Y. Lee, C. Wang, H. Yin, S. Dai, S. Sun, *Nano Res.* **2008**, *1*, 229–234.

[109] Y. Xia, N. J. Halas, G. Editors, *MRS Bull.* **2005**, *30*, 338–348.

[110] S. Yan, X. Zhang, Y. Sun, T. Wang, X. Chen, J. Yin, *Colloids Surfaces B Biointerfaces* **2014**, *113*, 302–311.

[111] K. C. Barick, S. Singh, D. Bahadur, M. A. Lawande, D. P. Patkar, P. A. Hassan, *J. Colloid Interface Sci.* **2014**, *418*, 120–125.

[112] R. Robl, *Angew. Chemie* **1958**, 367–371.

[113] F. Scarpelli, T. F. Mastropietro, T. Poerio, N. Godbert, in *Titan. Dioxide Mater. a Sustain. Environ.*, **2018**, pp. 57–80.

[114] J. Zhang, P. Zhou, J. Liu, J. Yu, *Phys. Chem. Chem. Phys.* **2014**, *16*, 20382–20386.

[115] “direkter Halbleiter,” can be found under https://www.spektrum.de/lexikon/physik/direkte-

halbleiter/3156#:~:text=direkte Halbleiter%2C Halbleiter mit einer,das am Valenzbandmaximum liegt%2C rekombinieren., **1998**.

[116] D. Reyes-Coronado, G. Rodríguez-Gattorno, M. E. Espinosa-Pesqueira, C. Cab, R. De Coss, G. Oskam, *Nanotechnology* **2008**, *19*, DOI 10.1088/0957-4484/19/14/145605.

[117] C. Klingshirn, *Phys. Stat. Sol.* **2007**, *244*, 3027–3073.

[118] A. A. Khodja, T. Sehili, J.-F. Pilichowski, P. Boule, *J. Photochem. Photobiol. A Chem.* **2001**, *141*, 231–239.

[119] A. Sirelkhatim, S. Mahmud, A. Seeni, *Nano-Micro Lett.* **2015**, *7*, 219–242.

[120] N. Müller, C. Heinrich, K. Abersfelder, G. Kickelbick, *Chemie Unserer Zeit* **2016**, *50*, 392–399.

[121] A. Perro, S. Reculusa, S. Ravaine, E. Bourgeat-Lami, E. Duguet, *J. Mater. Chem.* **2005**, *15*, 3745–3760.

[122] I. Schick, S. Lorenz, D. Gehrig, S. Tenzer, W. Storck, K. Fischer, D. Strand, F. Laquai, W. Tremel, *Beilstein J. Nanotechnol.* **2014**, *5*, 2346–2362.

[123] J. Hu, S. Zhou, Y. Sun, X. Fang, L. Wu, *Chem. Soc. Rev.* **2012**, *41*, 4356–4378.

[124] A. Walther, A. H. E. Müller, *Soft Matter* **2008**, *4*, 663–668.

[125] L. Carbone, P. D. Cozzoli, *Nano Today* **2010**, *5*, 449–493.

[126] C. Wang, C. Xu, H. Zeng, S. Sun, *Adv. Mater.* **2009**, *21*, 3045–3052.

[127] S. Kisch, H.; Lindner, W.Chemie, *Chemie unserer Zeit* **2001**, *4*.

[128] R. Hoffmann, *Angew. Chemie* **1987**, *26*, 846–878.

[129] W. Tremel, R. Seshadri, E. Wolfgang Finckh, *Chemie Unserer Zeit* **2001**, *35*, 42–58.

[130] J. Schneider, M. Matsuoka, M. Takeuchi, J. Zhang, Y. Horiuchi, M. Anpo, D. W. Bahnemann, *Chem. Rev.* **2014**, *114*, 9919–9986.

[131] M. N. Tahir, F. Natalio, M. A. Cambaz, M. Panthöfer, R. Branscheid, U. Kolb,

W. Tremel, *Nanoscale* **2013**, *5*, 9944–9949.

[132] Z. W. Seh, S. Liu, M. Low, S. Y. Zhang, Z. Liu, A. Mlayah, M. Y. Han, *Adv. Mater.* **2012**, *24*, 2310–2314.

[133] E. Schechtel, R. Dören, H. Frerichs, M. Panthöfer, M. Mondeshki, W. Tremel, *Langmuir* **2019**, *35*, 12518–12531.

[134] P. Ionita, A. Volkov, G. Jeschke, V. Chechik, *Anal. Chem.* **2008**, *80*, 95–106.

[135] J. Piella, A. Gónzalez-Febles, J. Patarroyo, J. Arbiol, N. G. Bastús, V. Puntes, *Chem. Mater.* **2019**, *31*, 7922–7932.

[136] M. Hu, K. Korschelt, M. Viel, N. Wiesmann, M. Kappl, J. Brieger, K. Landfester, H. Thérien-Aubin, W. Tremel, *ACS Appl. Mater. Interfaces* **2018**, *10*, 44722–44730.

[137] C. Dinh, T. Nguyen, F. Kleitz, T. Do, *ACS Nano* **2009**, *3*, 3737–3743.

[138] Y. Jie, J. R. Niskala, A. C. Johnston-Peck, P. J. Krommenhoek, J. B. Tracy, H. Fan, W. You, *J. Mater. Chem.* **2012**, *22*, 1962–1968.

[139] N. G. Bastús, J. Comenge, V. Puntes, *Langmuir* **2011**, *27*, 11098–11105.

[140] M. Priebe, K. M. Fromm, *Chem. - A Eur. J.* **2015**, *21*, 3854–3874.

[141] Y. Sun, B. Wiley, Z. Y. Li, Y. Xia, *J. Am. Chem. Soc.* **2004**, *126*, 9399–9406.

[142] H. Wu, G. Liu, S. Zhang, J. Shi, L. Zhang, Y. Chen, F. Chen, H. Chen, *J. Mater. Chem.* **2011**, *21*, 3037–3045.

[143] B. Liu, J. Wang, S. Sun, X. Wang, M. Zhao, W. Zhang, H. Zhang, X. Yang, *RSC Adv.* **2013**, *3*, 18506–18518.

[144] L. Kuai, S. Wang, B. Geng, *Chem. Commun.* **2011**, *47*, 6093–6095.

[145] C. Chen, X. Fang, B. Wu, L. Huang, N. Zheng, *ChemCatChem* **2012**, *4*, 1578–1586.

[146] H. Li, Z. Bian, J. Zhu, D. Zhang, G. Li, Y. Huo, H. Li, Y. Lu, *J. Am. Chem. Soc.* **2007**, *129*, 8406–8407.

[147] W. Dong, Y. Zhu, H. Huang, L. Jiang, H. Zhu, C. Li, B. Chen, Z. Shi, G. Wang,

J. Mater. Chem. A **2013**, *1*, 10030–10036.

[148] S. Shylesh, A. Wagener, A. Seifert, S. Ernst, W. R. Thiel, *Angew. Chemie* **2010**, *122*, 188–191.

[149] Y. Yang, X. Liu, X. Li, J. Zhao, S. Bai, J. Liu, Q. Yang, *Angew. Chemie - Int. Ed.* **2012**, *51*, 9164–9168.

[150] N. Yan, Q. Chen, F. Wang, Y. Wang, H. Zhong, L. Hu, *J. Mater. Chem. A* **2013**, *1*, 637–643.

[151] T. Zeng, X. Zhang, Y. Ma, S. Wang, H. Niu, Y. Cai, *Chem. Commun.* **2013**, *49*, 6039–6041.

[152] Z. M. Cui, Z. Chen, C. Y. Cao, L. Jiang, W. G. Song, *Chem. Commun.* **2013**, *49*, 2332–2334.

[153] P. M. Arnal, C. Weidenthaler, F. Schüth, *Chem. Mater.* **2006**, *18*, 2733–2739.

[154] S. H. Wu, C. T. Tseng, Y. S. Lin, C. H. Lin, Y. Hung, C. Y. Mou, *J. Mater. Chem.* **2011**, *21*, 789–794.

[155] M. Priebe, K. M. Fromm, *Part. Part. Syst. Charact.* **2014**, *31*, 645–651.

[156] Y. S. Lin, S. H. Wu, C. T. Tseng, Y. Hung, C. Chang, C. Y. Mou, *Chem. Commun.* **2009**, 3542–3544.

[157] S. Junker, R., Scherer, *Evolution: Ein Kritisches Lehrbuch*, **2006**.

[158] B. Alberts, *Lehrbuch Der Molekularen Zellbiologie*, **2014**.

[159] J. L. C. M. Van de Vossenberg, A. J. M. Driessen, W. N. Konings, *Extremophiles* **1998**, *2*, 163–170.

[160] H. Koffler, *Bacteriol. Rev.* **1957**, *21*, 227–240.

[161] J. W. Deming, *Curr. Opin. Microbiol.* **2002**, *5*, 301–309.

[162] S. V. Albers, B. H. Meyer, *Nat. Rev. Microbiol.* **2011**, *9*, 414–426.

[163] X. J. Wu, D. Xu, *J. Am. Chem. Soc.* **2009**, *131*, 2774–2775.

[164] M. Thommes, K. Kaneko, A. V. Neimark, J. P. Olivier, F. Rodriguez-Reinoso, J. Rouquerol, K. S. W. Sing, *Pure Appl. Chem.* **2015**, *87*, 1051–1069.

[165] X. Li, J. He, *ACS Appl. Mater. Interfaces* **2013**, *5*, 5282–5290.

[166] R. . Blake, R. E. Hessevick, *Am. Mineral.* **1966**, *51*, 123–129.

List of figures

List of tables

List of supporting figures